



저작자표시-비영리-변경금지 2.0 대한민국

이용자는 아래의 조건을 따르는 경우에 한하여 자유롭게

- 이 저작물을 복제, 배포, 전송, 전시, 공연 및 방송할 수 있습니다.

다음과 같은 조건을 따라야 합니다:



저작자표시. 귀하는 원저작자를 표시하여야 합니다.



비영리. 귀하는 이 저작물을 영리 목적으로 이용할 수 없습니다.



변경금지. 귀하는 이 저작물을 개작, 변형 또는 가공할 수 없습니다.

- 귀하는, 이 저작물의 재이용이나 배포의 경우, 이 저작물에 적용된 이용허락조건을 명확하게 나타내어야 합니다.
- 저작권자로부터 별도의 허가를 받으면 이러한 조건들은 적용되지 않습니다.

저작권법에 따른 이용자의 권리는 위의 내용에 의하여 영향을 받지 않습니다.

이것은 [이용허락규약\(Legal Code\)](#)을 이해하기 쉽게 요약한 것입니다.

[Disclaimer](#)

공학박사학위논문

**Shear characteristics of a rock discontinuity
under various thermal, hydraulic and
mechanical conditions**

다양한 열, 수리, 역학적 조건 하에서
암석 불연속면 전단 거동 특성에 관한 연구

2017년 2월

서울대학교 대학원
에너지시스템공학부
김 태 현

**Shear characteristics of a rock discontinuity under
various thermal, hydraulic and mechanical conditions**

다양한 열, 수리, 역학적 조건 하에서
암석 불연속면 전단 거동 특성에 관한 연구

지도교수 전 석 원

이 논문을 공학박사학위논문으로 제출함
2016년 10월

서울대학교 대학원

에너지시스템공학부

김 태 현

김태현의 박사학위논문을 인준함
2016년 12월

위 원 장	<u>송 재 준</u>	(인)
부 위 원 장	<u>전 석 원</u>	(인)
위 원	<u>민 기 복</u>	(인)
위 원	<u>엄 정 기</u>	(인)
위 원	<u>박 정 욱</u>	(인)

Abstract

Shear characteristics of a rock discontinuity under various thermal, hydraulic and mechanical conditions

Taehyun Kim

Department of Energy Systems Engineering

The Graduate School

Seoul National University

Discontinuities in rock mass behave as weak planes, and thus, understanding the behaviors of discontinuities is crucial to assess the stability of underground structures. At great depth, shear characteristics of discontinuities are more affected by the interaction among overburden depending on the depth, tectonic stresses, water pressure by ground water level and high temperature than at the near surface environment. Many researchers have studied the combined effect on shear characteristics, however, the results were varied with rock types, surface roughness, normal stress, and the degree of temperature and water pressure. Furthermore, most studies examined earth crustal behavior and hence, testing conditions such as normal stress, temperature and water pressure were extremely high. Thus, it is necessary to evaluate the variations of the frictional properties of various rock types which can be suitable for the engineering problems.

A series of shear tests were performed under various thermal, hydraulic

and mechanical conditions. Three types of rocks including a single saw-cut surface were used, Daejeon granite, Goheung diorite, and Linyi sandstone. The testing conditions were determined considering the situation in the vicinity of underground structures such as a disposal facility for radioactive waste, enhanced geothermal system, and oil reservoir. The friction angle was analyzed based on Mohr-Coulomb failure criterion, which remains the most widely used one in geotechnical practice.

The friction angle of the three different types of rock decreased when water pressure was applied on the saw-cut surfaces. Different mechanisms affect the reduction of the friction angle. In XRD analysis and SEM observation, layer lattice minerals were found in Daejeon granite and Goheung diorite, which can reduce the friction angle by readily adsorption of water. For Linyi sandstone, in SEM observation, a large amount of pulverized fine grain was observed after the tests when water pressure was applied. Thus, it can be deduced that detached soft powdered grains may reduce the shear strength of the saw-cut surfaces. On the contrary, the effect of temperature at 80°C was not significant on the shear behavior.

In addition to the tests on saw-cut specimens, the effect of surface roughness on shear characteristics was examined. Cement-mortar was used to reproduce identical rough discontinuities, and two kinds of rough discontinuities were prepared (JRC=2.05 and 11.63). Due to asperity degradation, friction angles were analyzed at low and high normal stress separately based on Patton's failure criterion. When water pressure was applied, the friction angle of rough discontinuities showed a larger decrease at low normal stress below than 10 MPa. The decrease might be caused by the weakening of tensile strength under wet conditions. Thus, it can be concluded that the adverse effect of water on friction angle and shear

strength increases on the rougher discontinuities. Whereas at high normal stress greater than 10 MPa, friction angle showed almost similar values independent on roughness, because asperities are sheared off. At an elevated temperature of 80°C, shear characteristics were not also varied in the same way as in the saw-cut specimens.

Numerical simulation using two-dimensional particle flow code was performed for the description of the shear behavior of cement-mortar specimens. Smooth joint model was used to generate a single discontinuity in the numerical model. The results showed a good agreement with the experimental results at room temperature and 80°C conditions. However, in the HM simulation, there was some discrepancy between experimental and numerical one in friction angle and dilation at low normal stress which should be resolved in the further study.

From this study, shear characteristics of different rock types and the effect of roughness were investigated along with numerical simulation. The presence of water reduced the shear strength of a rock discontinuity depending on rock type and normal stress, but temperature of 80°C did not show any clear effect. This study can contribute to the understanding of the mechanisms of the variations of shear characteristics under various thermal, hydraulic and mechanical conditions. Also, this result can be used to assess and design the stability of rock and underground rock structures, where the effect of T-H-M interaction should be considered.

Keywords: Friction angle, Shear tests, T-H-M coupled process, Triaxial compression chamber, DEM, Bonded particle model, Smooth joint model.

Student ID: 2007-21247

CONTENTS

ABSTRACT	i
CONTENTS	iv
LIST OF TABLES	vii
LIST OF FIGURES	ix
1. Introduction	1
1.1 Motivation	1
1.2 Research objectives	6
1.3 Outline of dissertation	7
2. Background theory and literature review	8
2.1 Prediction models of shear strength	8
2.2 Effect of temperature on shear strength	14
2.3 Effect of water on shear strength	22
3. Laboratory testing	30
3.1 Specimen preparation	30
3.1.1 Saw-cut specimens	30
3.1.2 Cement-mortar specimens	35
3.2 Testing apparatus and testing conditions	40
3.2.1 Testing apparatus	40
3.2.2 Testing method for saw-cut specimens	43
3.2.3 Testing method for cement-mortar specimens	49

4. Experimental results	52
4.1 Saw-cut Daejeon granite	58
4.1.1 Test results at room temperature and dry conditions	58
4.1.2 Test results at 80°C	65
4.1.3 Test results at room temperature with water pressure	66
4.1.4 Test results at 80°C with water pressure	68
4.2 Saw-cut Goheung diorite	70
4.2.1 Test results at room temperature and dry conditions	70
4.2.2 Test results at 80°C	75
4.2.3 Test results at room temperature with water pressure	76
4.3 Saw-cut Linyi sandstone	78
4.3.1 Test results at room temperature and dry conditions	78
4.3.2 Test results at 80°C	83
4.3.3 Test results at room temperature with water pressure	84
4.4 Cement-mortar including a smooth discontinuity	86
4.4.1 Test results at room temperature and dry conditions	86
4.4.2 Test results at 80°C	95
4.4.3 Test results at room temperature with water pressure	96
4.5 Cement-mortar including a rough discontinuity	98
4.5.1 Test results at room temperature and dry conditions	98
4.5.2 Test results at 80°C	106
4.5.3 Test results at room temperature with water pressure	107
4.6 Scanning electron microscope analysis	109
4.6.1 Goheung diorite	112
4.6.2 Linyi sandstone	115

5. Numerical simulation	119
5.1 Introduction	119
5.2 Smooth joint model	122
5.3 TM coupling simulation in PFC2D	125
5.4 HM coupling simulation in PFC2D	127
5.5 Numerical model generation	129
5.6 Simulation results	137
5.6.1 Simulation results of a smooth discontinuity	137
5.6.2 Simulation results of a rough discontinuity	149
6. Discussion	161
6.1 Effect of temperature	161
6.2 Effect of water	162
6.3 Comparison between experimental and simulation results	169
7. Conclusions	171
References	175
Appendix A Test results of saw-cut specimens	188
Appendix B Test results of cement-mortar specimens including a smooth discontinuity (JRC=2.05)	195
Appendix C Test results of cement-mortar specimens including a rough discontinuity (JRC=11.63)	210
Abstract (Korean)	223

LIST OF TABLES

Table 2.2.1	Results of literature review on the effect of temperature on shear strength and friction angle.	21
Table 2.3.1	Summary of frictional coefficients for three conditions of surface moisture (after Horn and Deere, 1962).	23
Table 2.3.2	Frictional strength data under dry and wet conditions collated by Barton (after Barton, 1973).	28
Table 2.3.3	Results of literature review: variations of friction angle depending on dry and wet conditions.	29
Table 3.1.1	Physical and mechanical properties of Daejeon granite, Goheung diorite, Linyi sandstone and cement-mortar.	34
Table 3.1.2	Mineralogy of each rock type used in this study based on XRD analyses.	35
Table 3.2.1	Number of specimens and specimen identifications (IDs).	49
Table 4.1.1	Results of shear tests by using multistage triaxial compression test method on Daejeon granite saw-cut surfaces on various testing conditions.	63
Table 4.2.1	Results of shear tests by using multistage triaxial compression test method on Goheung diorite saw-cut surfaces on various testing conditions.	74
Table 4.3.1	Results of shear tests by using multistage triaxial compression test method on Linyi sandstone saw-cut surfaces on various testing conditions.	82
Table 4.4.1	Results of shear tests on smooth discontinuities (JRC=2.05) of cement-mortar specimens on various testing conditions.	91

Table 4.5.1	Results of shear tests on rough discontinuities (JRC=11.63) of cement-mortar specimens on various testing conditions.	102
Table 5.1.1	Mechanical, thermal and hydraulic micro-properties of particles, parallel bonds and smooth joint contacts of cement-mortar specimens and the macro properties tested from the simulation of uniaxial compression test by PFC2D.	121
Table 5.6.1	Results of the numerical simulations on smooth discontinuities (JRC=2.05) at various testing conditions.	140
Table 5.6.2	Results of the numerical simulations on rough discontinuities (JRC=11.63) at various testing conditions.	151
Table 6.1.1	Summary of a series of shear tests for peak friction angle and cohesion of Daejeon granite, Goheung granite, Linyi sandstone and Cement-mortar specimens.	166
Table 6.1.2	Summary of a series of shear tests for peak friction angle depending on various testing conditions.	168

LIST OF FIGURES

Fig. 2.1.1	A schematic diagram of Patton's bilinear model of friction (redrawn after Patton (1966b)).	10
Fig. 2.2.1	Discontinuity surfaces prepared by (a) tensile fracture and (b) saw-cut (after Pakpoom, 2013).	16
Fig. 2.2.2	Relation between peak shear stress and normal stress depending on temperature: (a) saw-cut surface and (b) tensile fractured surface (after Pakpoom, 2013).	16
Fig. 2.2.3	Relation between shear stress and normal stress depending on temperature: (a) granite saw-cut (b) faulted granite and (c) faulted gabbro (after Stesky et al., 1974).	19
Fig. 2.2.4	A schematic diagram of the experiments and test results: (a) a schematic diagram inside a triaxial chamber and (b) Relation between shear stress and normal stress depending on temperature of saw-cut graywacke specimens and fractured specimens (after Lockner et al., 1982).	20
Fig. 2.2.5	Discontinuity surface including saw-tooth shape of asperities and test results: (a) discontinuity surface and (b) shear strength depending on temperature (after Zhao et al., 2016).	20
Fig. 2.3.1	Percentage of decrease in frictional strength of in-filled gouge minerals under 100 MPa of confining pressure and 10 MPa of pore pressure (after Morrow et al., 2000).	24
Fig. 2.3.2	Results of tilt tests under three different conditions (after Ulusay and Karakul, 2015).	25

Fig. 2.3.3 Experimental set-up and test results: (a) sample assembly inside a triaxial chamber and (b) relation between shear stress and effective normal stress of illite/montmorillonite gouge (after Morrow et al., 1992).	27
Fig. 3.1.1 Location of Daejeon, Goheung in Korea and Linyi in China (from Google Earth).	32
Fig. 3.1.2 Configuration of the saw-cut Daejeon granite specimen: (a) side view of the specimen with a saw-cut surface, (b) picture of the saw-cut surface with a water injection hole, and (c) schematic longitudinal-section view of the specimen ($\Theta = 28^\circ$).	33
Fig. 3.1.3 A configuration of 3 dimensional laser roughness profiling machine.	38
Fig. 3.1.4 Three dimensional profiles of discontinuities of cement-mortar specimens and the profiles of center lines (A-A') used in the numerical simulation: (a) JRC = 2.05 and (b) JRC = 11.63.	39
Fig. 3.1.5 Aluminum replica of rock joint surface and a pair of cast with lower piece of the specimen: (a) an inclined cast combined with aluminum replica of rock joint surface and (b) a cylindrical cast with lower piece made by cement-mortar.	40
Fig. 3.2.1 A schematic diagram of experiment and the view of experimental set-up of water pressure applied test: (a) a schematic diagram of experiment inside the triaxial compression chamber and (b) the view of experimental set-up inside the chamber when water pressure was applied.	42
Fig. 3.2.2 Overall view of MTS 816 system with 500D syringe pump after setup in use.	43

Fig. 3.2.3 Relation between axial stress, confining pressure and shear displacement of LY-M-1 and decision of slip point by using bilinear decay method.	47
Fig. 3.2.4 Stress path of A-M-2 (confining pressure: 10 MPa/room temperature/Dry) and A-HM-5 (confining pressure: 10 MPa/room temperature/water pressure: 2 MPa).	48
Fig. 4.1.1 Schematic diagram for calculation of normal and shear displacement on rock discontinuities: (a) a longitudinal section view of the specimen after slip with positive normal and shear direction and (b) a conceptual cross-section view before and after shearing.	56
Fig. 4.1.2 relation between stress and displacement: (a) curve of effective normal stress and normal displacement of S-M-9, R-M-8, D-M-1 and LY-M-1 specimens (confining pressure = 15 MPa / room temperature / Dry condition) and (b) graph of effective normal stress, shear stress and normal stiffness versus shear displacement of LY-M-1 specimen.	57
Fig. 4.1.3 A-M-2 specimen after the test (20°C / Dry surface): (a) powder induced by shearing on the saw-cut surface and (b) slickenside induced by shearing on the saw-cut surface.	60
Fig. 4.1.4 Relation between shear stress and effective normal stress acting on Daejeon granite saw-cut surfaces on various testing conditions.	60
Fig. 4.1.5 Peak friction angles of Daejeon granite saw-cut surfaces on various testing conditions.	61

Fig. 4.1.6 Relation between effective normal stress, shear stress and shear displacement of A-M-1 and A-M-2 at room temperature on dry condition.	61
Fig. 4.1.7 Relation between normal, shear stiffness and initial effective confining pressure of Daejeon granite saw-cut surfaces on various testing conditions: (a) normal stiffness and (b) shear stiffness.	62
Fig. 4.1.8 Relation between effective normal stress, shear stress and shear displacement of A-M-2 (20°C / Dry) and A-TM-2 (80°C / dry condition).	66
Fig. 4.1.9 Relation between effective normal stress, shear stress and shear displacement of A-M-2 (20°C / Dry) and A-HM-2, 4 and 5 (20°C / water pressure: 0.1, 0.5, 2.0 MPa).	68
Fig. 4.1.10 Relation between effective normal stress, shear stress and shear displacement of A-M-2 (20°C / Dry) and A-THM-2 and 4 (80°C / water pressure: 0.1, 0.5 MPa).	69
Fig. 4.2.1 Slickenside along the shear direction on the saw-cut surface of Goheung diorite: (a) D-M-2 specimen (room temperature/dry condition) and (b) D-HM-2 specimen (room temperature/water pressure: 1 MPa).	71
Fig. 4.2.2 Relation between shear stress and effective normal stress acting on Goheung diorite saw-cut surfaces on various testing conditions and linear regression line for peak friction angle.	71
Fig. 4.2.3 Peak friction angles of Goheung diorite saw-cut surfaces on various testing conditions.	72

Fig. 4.2.4 Relation between effective normal stress, shear stress and shear displacement of D-M-1 and D-M-2 at room temperature on dry saw-cut surfaces.	72
Fig. 4.2.5 Relation between normal, shear stiffness and initial effective confining pressure of Goheung diorite saw-cut surfaces on various testing conditions: (a) normal stiffness and (b) shear stiffness.	71
Fig. 4.2.6 Relation between effective normal stress, shear stress and shear displacement of D-M-2 at room temperature and D-TM-2 at 80°C on dry saw-cut surfaces.	76
Fig. 4.2.7 Relation between effective normal stress, shear stress and shear displacement of D-M-2 (room temperature, dry condition) and D-HM-2 (room temperature, water pressure: 1.0 MPa).	77
Fig. 4.3.1 Saw-cut surface of Linyi sandstone specimen (LY-M-1): (a) before shearing and (b) after shearing. Slickenside were observed over the whole saw-cut surface along the shear direction.	79
Fig. 4.3.2 Relation between shear stress and effective normal stress acting on Linyi sandstone saw-cut surfaces on various testing conditions and linear regression line for peak friction angle.	79
Fig. 4.3.3 Peak friction angles of Linyi sandstone saw-cut surfaces on various testing conditions.	80
Fig. 4.3.4 Relation between effective normal stress, shear stress and shear displacement of LY-M-1 and LY-M-2 at room temperature on dry saw-cut surfaces.	80

Fig. 4.3.5 Relation between normal, shear stiffness and initial effective confining pressure of Linyi sandstone saw-cut surfaces on various testing conditions: (a) normal stiffness and (b) shear stiffness.	81
Fig. 4.3.6 Relation between effective normal stress, shear stress and shear displacement of LY-M-2 at room temperature and LY-TM-2 at 80°C on dry saw-cut surfaces.	83
Fig. 4.3.7 Relation between effective normal stress, shear stress and shear displacement of LY-M-2 (at room temperature/dry condition) and LY-HM-1 (at room temperature/water pressure: 1.0 MPa).	85
Fig. 4.4.1 Discontinuity surface of S-M-10 specimen (JRC=2.05/at room temperature/dry condition/confining pressure: 10 MPa): (a) before shearing and (b) after sliding.	88
Fig. 4.4.2 Relation between shear stress and effective normal stress acting on cement-mortar specimens including smooth discontinuities (JRC=2.05) on various testing conditions and linear regression lines for peak friction angles.	89
Fig. 4.4.3 Peak friction angles of cement-mortar specimens including smooth discontinuities (JRC=2.05) depending on normal stress and various testing conditions.	90
Fig. 4.4.4 Relation between the peak friction coefficient and initial effective normal stress of cement-mortar specimens including smooth discontinuities (JRC=2.05) under various testing conditions.	90
Fig. 4.4.5 Relation between normal, shear stiffness and initial effective normal stress of cement-mortar specimens including smooth discontinuities (JRC=2.05) under various testing conditions: (a) normal stiffness and (b) shear stiffness.	93

Fig. 4.4.6	Relation between effective normal stress, shear stress, normal displacement and shear displacement of S-M-1, 3, 5, 10, 11, 13 specimens (confining pressure: 0.5, 1, 2, 10, 15, 20 MPa/20°C/dry condition): (a) effective normal stress, (b) shear stress, and (c) normal displacement along with shear displacement.	94
Fig. 4.4.7	Relation between dilation angle and effective normal stress of cement-mortar specimens including smooth discontinuities (JRC=2.05) under various testing conditions.	95
Fig. 4.5.1	Discontinuity surface of R-M-5 specimen (JRC=11.63/at room temperature/dry condition/confining pressure: 2 MPa): (a) before shearing and (b) after sliding.	99
Fig. 4.5.2	Relation between shear stress and effective normal stress acting on cement-mortar specimens including rough discontinuities (JRC=11.63) on various testing conditions and linear regression lines for peak friction angles.	100
Fig. 4.5.3	Peak friction angles of cement-mortar specimens including rough discontinuities (JRC=11.63) depending on normal stress and various testing conditions.	101
Fig. 4.5.4	Relation between the peak friction coefficient and the initial effective normal stress of cement-mortar specimens including rough discontinuities (JRC=11.63) under various testing conditions.	101
Fig. 4.5.5	Relation between normal, shear stiffness and initial effective normal stress of cement-mortar specimens including rough discontinuities (JRC=11.63) under various testing conditions: (a) normal stiffness and (b) shear stiffness.	102

- Fig. 4.5.6** Relation between effective normal stress, shear stress, normal displacement and shear displacement of R-M-1, 3, 5, 7, 10, 12 specimens (confining pressure: 0.5, 1, 2, 10, 15, 20 MPa/20°C/dry condition): (a) effective normal stress, (b) shear stress, and (c) normal displacement along with shear displacement. 105
- Fig. 4.5.7** Relation between dilation angle and effective normal stress of cement-mortar specimens including rough discontinuities (JRC=11.63) under various testing conditions. 106
- Fig. 4.6.1** Zeiss Merlin Compact Field-Emission scanning electron microscope used in this study. 110
- Fig. 4.6.2** Saw-cut surfaces after the tests and cored samples for SEM observation of Goheung diorite ((a), (b), (c)) and Linyi sandstone ((d), (e), (f)): (a) D-M-1, (b) D-HM-1, (c) cored samples of Goheung diorite, (d) LY-M-1, (e) LY-HM-1, and (f) cored samples of Linyi sandstone. 111
- Fig. 4.6.3** A coater (MSC-101) and Linyi sandstone samples for the SEM tests: (a) a coater and (b) Linyi sandstone samples after platinum spraying treatments. 112
- Fig. 4.6.4** SEM images of Goheung diorite saw-cut surfaces: (a) and (b) before test (100×/500×, respectively), (c) and (d) D-M-1 after test at room temperature and dry conditions (100×/500×, respectively), and (e) and (f) D-HM-1 after test at 3 MPa of water pressure applied conditions (100×/500×, respectively). 114
- Fig. 4.6.5** SEM images of microcracks and lattice structures in Goheung diorite saw-cut surfaces after the test at a 3 MPa of water pressure applied condition: (a) microcracks on a mineral grain (1000×) and (b) layer lattice structure mineral (20000×). 115

Fig. 4.6.6 SEM images of Linyi sandstone saw-cut surfaces: (a) and (b) before test (100×/500×, respectively), (c) and (d) LY-M-1 after test at room temperature and dry conditions (100×/500×, respectively), and (e) and (f) LY-HM-1 after test at 3 MPa of water pressure applied conditions (100×/500×, respectively).	117
Fig. 4.6.7 SEM images of Linyi sandstone saw-cut surfaces after the tests at 3 MPa of water pressure applied conditions: (a) microcracks at the saw-cut surfaces (5000×) and (b) mineral grains at a magnification of 20000.	118
Fig. 5.2.1 A schematic diagram of the particles assigned smooth joint contacts (from Mas Ivars et al., 2011).	123
Fig. 5.2.2 A numerical model used in the validation process and the result: (a) a numerical model including a flat discontinuity and (b) relationship between shear stress and effective normal stress from a multi-stage triaxial compression test and a numerical simulation on a flat discontinuity.	124
Fig. 5.4.1 A numerical model assigned a fluid network system.	128
Fig. 5.5.1 Enlarged view of particle interlocking in a smooth joint model of a flat discontinuity: (a) before shearing and (b) after 1 mm shear displacement.	130
Fig. 5.5.2 Procedure of a numerical model generation (JRC=11.63): (a) material vessels generation, (b) lower model generation, (c) upper model generation, and (d) combination of the lower and the upper model.	132

Fig. 5.5.3 Flowchart of numerical simulation at each testing conditions.	134
Fig. 5.5.4 Enlarged view of bonds between particles: (a) initial stage and (b) after hydrostatic pressure.	135
Fig. 5.5.5 Numerical models with a smooth discontinuity (JRC=2.05) and a rough discontinuity (JRC=11.63): (a) JRC=2.05 and (b) JRC=11.63.	136
Fig. 5.6.1 Effective normal stress, shear stress, normal displacement versus shear displacement of cement-mortar specimens including smooth discontinuities (JRC=2.05) when the confining pressure was 10 MPa at room temperature and dry conditions in both experimental test and the numerical simulation (PFC2D).	141
Fig. 5.6.2 Relation between effective normal stress and shear stress of cement-mortar specimens including smooth discontinuities (JRC=2.05) at various testing conditions in both experimental tests and the numerical simulation (PFC2D).	142
Fig. 5.6.3 Peak friction angles of cement-mortar specimens including smooth discontinuities (JRC=2.05) depending on normal stress and various testing conditions obtained from the numerical simulations. ...	143
Fig. 5.6.4 Effective normal stress, shear stress and cumulative crack numbers versus shear displacement of cement-mortar specimens including a smooth discontinuity (JRC=2.05) when the confining pressure was 20 MPa at room temperature and dry conditions in the numerical simulation.	143

- Fig. 5.6.5** Effective normal stress, shear stress, normal displacement versus shear displacement of cement-mortar specimens including smooth discontinuities (JRC=2.05) at various testing conditions in the numerical simulations (confining pressure: 0.5, 1, 2, 10, 15, 20 MPa/20°C/dry condition): (a) effective normal stress, (b) shear stress, and (c) normal displacement versus shear displacement. 144
- Fig. 5.6.6** Microcracks at a shear displacement of 1.2 mm on smooth discontinuities (JRC=2.05) at room temperature and dry condition depending on confining pressure: (a) 0.5 MPa, (b) 1.0 MPa, (c) 2.0 MPa, (d) 10.0 MPa, (e) 15.0 MPa, and (f) 20.0 MPa (red : tensile crack, black : shear crack). 145
- Fig. 5.6.7** Contact forces (black in compression and red in tension) at a shear displacement of 1.2 mm on smooth discontinuities (JRC=2.05) at room temperature and dry condition depending on confining pressure: (a) 0.5 MPa, (b) 1.0 MPa, (c) 2.0 MPa, (d) 10.0 MPa, (e) 15.0 MPa, and (f) 20.0 MPa. 145
- Fig. 5.6.8** Relation between normal, shear stiffness and initial effective normal stress of cement-mortar specimens including smooth discontinuities (JRC=2.05) at various testing conditions obtained from the numerical simulations.: (a) normal stiffness and (b) shear stiffness. 146
- Fig. 5.6.9** Relation between dilation angle and effective normal stress of cement-mortar specimens including smooth discontinuities (JRC=2.05) at various testing conditions obtained from the numerical simulations. 147

Fig. 5.6.10 Effective normal stress, shear stress, normal displacement versus shear displacement of cement-mortar specimens including rough discontinuities (JRC=11.63) when the confining pressure was 20 MPa at room temperature and dry conditions in both experimental test and the numerical simulation (PFC2D).	152
Fig. 5.6.11 Relation between effective normal stress and shear stress of cement- mortar specimens including rough discontinuities (JRC=11.63) at various testing conditions in both experimental tests and the numerical simulation (PFC2D).	153
Fig. 5.6.12 Peak friction angles of cement-mortar specimens including rough discontinuities (JRC=11.63) depending on normal stress and various testing conditions obtained from the numerical simulations.	154
Fig. 5.6.13 Effective normal stress, shear stress and cumulative crack numbers versus shear displacement of cement-mortar specimens including a rough discontinuity (JRC=11.63) when the confining pressure was 20 MPa at room temperature and dry conditions in the numerical simulation.	154
Fig. 5.6.14 Effective normal stress, shear stress, normal displacement versus shear displacement of cement-mortar specimens including rough discontinuities (JRC=11.63) at various testing conditions in the numerical simulations (confining pressure: 0.5, 1, 2, 10, 15, 20 MPa/20°C/dry condition): (a) effective normal stress, (b) shear stress, and (c) normal displacement versus shear displacement.	155

- Fig. 5.6.15** Microcracks at a shear displacement of 1.2 mm on rough discontinuities (JRC=11.63) at room temperature and dry condition depending on confining pressure: (a) 0.5 MPa, (b) 1.0 MPa, (c) 2.0 MPa, (d) 10.0 MPa, (e) 15.0 MPa, and (f) 20.0 MPa (red : tensile crack, black : shear crack). 156
- Fig. 5.6.16** Contact forces (black in compression and red in tension) at a shear displacement of 1.2 mm on rough discontinuities (JRC=11.63) at room temperature and dry condition depending on confining pressure: (a) 0.5 MPa, (b) 1.0 MPa, (c) 2.0 MPa, (d) 10.0 MPa, (e) 15.0 MPa, and (f) 20.0 MPa. 156
- Fig. 5.6.17** Relation between normal, shear stiffness and initial effective normal stress of cement-mortar specimens including rough discontinuities (JRC=11.63) at various testing conditions obtained from the numerical simulations.: (a) normal stiffness and (b) shear stiffness. 157
- Fig. 5.6.18** Relation between dilation angle and effective normal stress of cement-mortar specimens including rough discontinuities (JRC=11.63) at various testing conditions obtained from the numerical simulations. 158
- Fig. 6.1.1** Relation between effective normal stress and shear stress of discontinuities of Daejeon granite, Goheung diorite, Linyi sandstone and cement-mortar specimens at various testing conditions. 165
- Fig. 6.1.2** Comparison of the ratio between the friction coefficients of flat discontinuities under dry and wet conditions depending on rock types. 168

1. Introduction

1.1 Motivation

Rock mass includes discontinuities (faults, joints, bedding planes, cleavages et al.) due to various geological processes such as orogeny and folding. Discontinuities behave as weak planes, and thus, understanding the behaviors of discontinuities is crucial to assess the stability of underground structures. Numerous studies have been performed to predict shear strength of discontinuities, and in the classic view of Amonton's law of friction, shear strength is proportional to the normal load and is independent of the area of contact (Coulson, 1972; Paterson and Wong, 2005).

However, shear strength tends to change depending on various factors including the mechanical properties (friction angle, joint wall compressive strength et al.), effective normal stress, the degree of roughness and the size of discontinuities. Mainly, four models have been used to predict the shear strength of discontinuities at constant normal load condition: Coulomb model, Patton model (1966b), Barton model (1973) and Byerlee model (1978). In Coulomb model which was proposed in 1773, shear stress has a linear relationship with a given normal stress. Patton (1966b) and Goldstein et al. (1966) explained the effect of the roughness on the shear strength firstly by using a saw-tooth shaped roughness model. In Patton model, shear strength criterion has a bilinear curve depending on normal stress. After Patton model, Ladanyi and Archambault (1969), Barton (1973), Plesha (1987) and Saeb (1990) proposed various empirical and analytical non-linear models to consider the influence of asperities and the degradation of asperities on shear behavior. Among them, Barton's model (1973) is an

empirical model to describe the shear strength of rock joints through a series of shear tests using tensile fractured rocks. Barton's model has been widely applied in the field due to the simplicity, and various empirical equations were proposed based on Barton's model (Kulatilake et al., 1995; Grasselli, 2001; Xia et al., 2010). However, based on a large amount of data, Byerlee (1978) noted that shear strength should be estimated by different criteria depending on normal stress level. Barton's model is applicable only under low normal stress less than 5 MPa, but at high normal stress greater than 5 MPa, the surface roughness of a discontinuity has little or no effect on shear strength.

The four models emphasize the role of basic friction angle, normal stress, and surface roughness on shear strength in common. Those sources which can affect shear strength vary with rock types and geological conditions around rock mass. Geological conditions can be greatly affected by the location and subsurface depth. Recently, the demands of subsurface engineered underground structures such as a disposal facility for radioactive waste, enhanced geothermal system, and oil reservoir have continued to rise. At deep depth, underground rock mass condition is affected by the interaction among three-dimensional stress field induced by overburden depending on the depth, tectonic stresses, water pressure by ground water level and high temperature. These complex interactions of in situ mechanical, thermal, hydraulic, and chemical processes and their effects on system performance should be considered (Yow and Hunt, 2002).

In particular, pore pressure induced by groundwater and injection of the fluid decreases the effective normal stress on the discontinuities. Giardini (2009) stated the possibility for the generation of microearthquakes induced by fluid injection at an enhanced geothermal system. Majer et al. (2007)

reported that seismic events with the magnitude of 3.4 or less occurred during the development of an enhanced geothermal system in Basel, Switzerland. Heat emitted by the nuclear waste and caused by deep depth can generate thermal stress due to the confinement and different thermal expansion of the surrounding rocks. This resulting thermal stress will enhance shear slip and dilation in the geological repository (Min and Stephansson, 2009). However, in addition to stress perturbation which can cause shear slip along the pre-existing discontinuities, temperature and wet conditions affect the friction angle itself. Various studies were carried out in a variety of ways to investigate the effect of temperature and water on the friction angle. The results also varied depending on rock types and testing conditions.

Drennon and Handy (1971) carried out direct shear tests on the ground blocks of Bedford limestone and observed that the static friction coefficient increased with increasing temperature. Donath et al. (1972) reported the friction coefficient increased under elevated temperature for limestone and sandstone. The increasing tendency of the friction coefficient at elevated temperature conditions was also observed by Friedman et al. (1974), Stesky (1978), Lockner et al. (1986) and Pakpoom (2013). The rock types in their studies were granite and sandstone, and the temperature was varied in the range of 20 and 845°C. They explained the increase of the friction strength is caused by either the removal of adsorbed water or the formation of glass of quartz minerals.

On the other hand, Olsson (1974) found that increased temperature from 25 to 100°C has little effect on the frictional properties of faulted limestone samples. Stesky et al. (1974) reported the friction coefficient of saw-cut granite and faulted gabbro did not show any variations at 700°C. The results

of saw-cut sandstone (Lockner et al., 1982), granite (Stesky et al., 1974; Blanpied et al., 1995; Odera et al., 2001; Pakpoom, 2013; Zhao et al., 2016) showed the same tendency. Paterson and Wong (2005) stated that the shear stress needed to cause sliding along a shear fracture has not been changed or decreased by the increasing temperature up to around 427 and 527°C (700 or 800 K) based on collated data. Thus, the effect of increasing temperature on shear strength is differed by rock types and temperature range.

As for the wet condition, the effect on friction is not also still clear. Jaeger (1959) reported that the friction angle for natural joints of sandstone and granitic gneiss decreased by 2.3° and 4.0° when the surfaces were wet. The reduction of friction angle and shear strength were also found for trachyte (Hoskins et al., 1967), chalk (Gutierrez et al., 2000), sandstone (Sheng and Reddish, 2005; Lee and Chang, 2013) and Marl (Pellet et al., 2013). Ulusay and Karakul (2015) performed tilt tests for 20 rock types (andesite, travertine, basalt, granite, limestone et al.), and reported that under submerged conditions, all the tested specimens showed a decrease in the basic friction angle. Horn and Deere (1962), Nascimento (1981) and Morrow et al. (2000) investigated the basic friction angle of minerals and concluded that the basic friction angles of layer lattice minerals were reduced under wet surfaces.

Whereas Byerlee (1967), Hoskins et al. (1968), Coulson (1972), and Goodman and Ohnishi (1973) found that wet condition produces no effect or a slight increase on the frictional properties. Morrow et al. (1992) reported that under high normal pressure above 100 MPa, the friction coefficient did not change with increasing pore pressure, but the theory of effective stress induced by pore pressure was applied well on the shear

behavior.

As described above, the friction angle can change with various factors, including normal stress, roughness, temperature and wet conditions. The mechanisms for the change of friction properties at each condition have been proposed, but even in the same rock types, the effect can appear differently. Furthermore, most of the studies were carried out to examine earth crustal behavior and hence, testing conditions were extremely high. Thus, it is necessary to evaluate the variations of the frictional properties of various rock types which can be suitable for the engineering problems. Also, previous studies have been mainly conducted on the saw-cut of flat surfaces due to the difficulties of reproducing identical shear surfaces and complexity of experiments. Therefore, it is required to investigate the effect of surface roughness on shear behavior at different temperature and wet conditions. Consequently, the assessment of the frictional properties should deal with rock types, surface roughness, and normal stress conditions.

1.2 Research objectives

As discussed in the previous section, it is crucial to understand the shear characteristics to secure the stability of underground structures such as a disposal facility for radioactive waste, enhanced geothermal system, oil reservoir, etc (any mining application and civil structures).

The primary objectives of this study are:

(1) *To investigate the effect of thermal, hydraulic and mechanical conditions on shear characteristics of different rock types.* Three types of rocks (granite, diorite, sandstone) with a single saw-cut surface were selected for shear tests. The testing conditions were determined considering the situation in the vicinity of underground excavation. Shear tests were conducted inside a triaxial chamber with MTS 816 system. Various shear characteristics including friction angle and stiffness of the surface were investigated. SEM analysis is added to find the mechanisms of the variations.

(2) *To investigate the effect of thermal, hydraulic and mechanical conditions on shear characteristics of different rough discontinuities.* The samples were made of high strength cement-mortar using a mold duplicated from a natural single rock joint to reproduce same joint surfaces. In addition to the investigation of friction angle and stiffness of the discontinuities, dilation angle and peak friction coefficient were analyzed under various testing conditions. Besides shear characteristics depending on different normal stress were also investigated.

(3) *To reproduce the shear behavior using numerical simulation.* Numerical simulation was conducted to figure out the cracking mechanism during shearing. The effect of thermal, hydraulic and mechanical conditions was also investigated in the simulation using commercial discrete element method (DEM) software, PFC2D.

1.3 Outline of dissertation

This dissertation consists of seven chapters.

Chapter 2 introduces the fundamental models for prediction of shear strength and previous studies for the variations of friction angles under various thermal and hydraulic conditions. The basic mechanical properties (uniaxial compressive strength, brazilian tensile strength, Poisson's ratio et al.) of tested specimens are given in Chapter 3 and the information of testing apparatus and testing procedure are explained. Chapter 4 deals with the experimental test results of each specimen under various testing conditions. Chapter 5 presents the numerical model generation and the comparison between the results of simulation and experimental data. Summary of the results, the mechanisms of the variations and the limitations of this study is discussed in Chapter 6. Finally, Chapter 7 summarizes the major observations and results obtained in this study.

2. Background and literature review

As stated before, discontinuities have a significant effect on rock mass behavior. Various studies have been carried out to forecast shear strength of discontinuities after Amonton's law. In this chapter, some of the prediction models of shear strength will be introduced. Shear strength can be affected by various factors, and temperature and water are included in them. Therefore, previous studies considering the effect of temperature and water on shear characteristics will be summarized.

2.1 Prediction models of shear strength

Prediction of shear strength for frictional behavior has been traditionally based on the Mohr-Coulomb failure criterion, which remains the most widely used model in geotechnical practice (Griffiths, 1990). Coulomb model was firstly proposed in 1773, and in the model, shear strength has a linear relationship with normal stress. After Coulomb, Mohr suggested a modified Coulomb model based on a failure envelope derived from a series of triaxial compression tests, as shown in equation (2.1).

$$\tau_p = c + \sigma_n \tan \phi_p \quad (2.1)$$

In equation (2.1), τ_p is peak shear stress, σ_n is effective normal stress, c is apparent cohesion and ϕ_p is peak friction angle. Apparent cohesion has been recognized to be related with the roughness of discontinuities. In the residual state after the failure of the specimen or for a flat and unweathered

discontinuity, apparent cohesion is generally assumed as zero.

However, on the natural discontinuities, shear stress shows a non-linear relationship with normal stress. To overcome this problem, Patton (1966b) and Goldstein et al. (1966) suggested a new criterion based on the research of Newland and Allely (1957). Newland and Allely (1957) developed a model to predict shear stress at a certain normal stress based on the observed dilatant behavior of granular material such as sand as shown in equation (2.2) (Barton, 1973).

In equation (2.2), i denotes the inclination angle of asperity towards shear direction as shown in Fig. 2.1.1. Patton (1966b) and Goldstein et al. (1966) carried out shear tests on discontinuities including saw-tooth shape asperities. They found that equation (2.2) was valid at low normal stresses. At high normal stresses, asperities sheared off and shear behavior would follow Mohr-Coulomb relationship (Fig. 2.1.1). Thus, Patton model can be summarized as follows.

$$\tau = \sigma_n \tan(\phi_b + i) \quad \sigma_n \leq \sigma_T \quad (2.2)$$

$$\tau = c + \sigma_n \tan\phi_r \quad \sigma_n > \sigma_T \quad (2.3)$$

In equation (2.2) and (2.3), ϕ_b is basic friction angle of discontinuity, ϕ_r is residual friction angle, and σ_T is transition stress where shearing accompanying with asperity degradation starts. σ_T can be expressed as shown in equation (2.4).

$$(2.4)$$

Patton's model assumes that the behavior of sliding and shearing on discontinuity is separated. Following Patton's model, several attempts were made to consider the effect of asperity degradation on shear behavior and modified criteria were put forward.

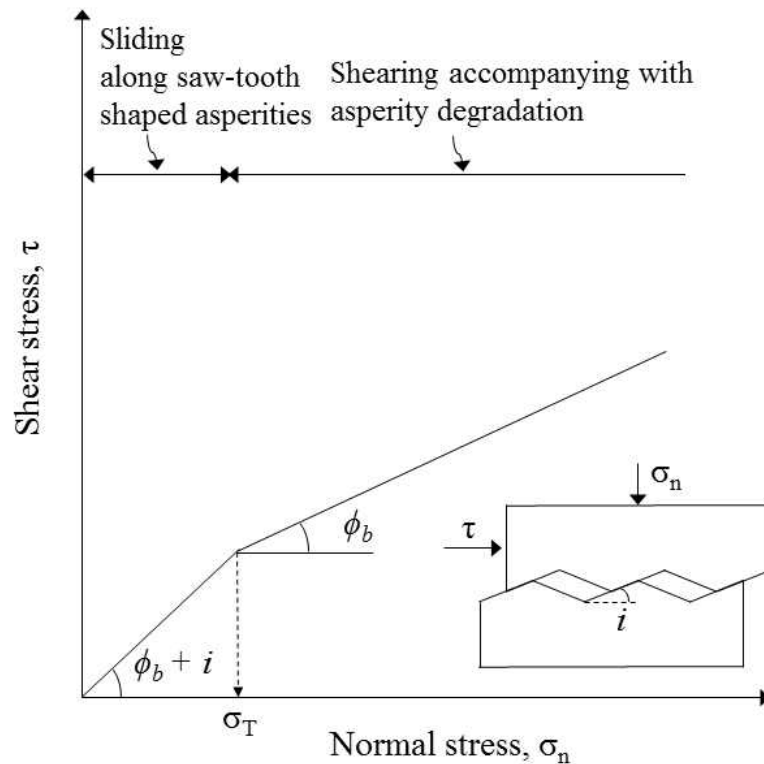


Fig. 2.1.1 A schematic diagram of Patton's bilinear model of friction (redrawn after Patton (1966b)).

Ladanyi and Archambault (1969) presumed that shear behavior is a complex combined behavior of sliding and shearing with asperity degradation, and they tried to modify Patton's model based on the assumption. They suggested a modified non-linear failure criterion considering effective normal stress, basic friction angle, and dilation of a discontinuity (equation (2.5)).

$$\tau_p = \frac{S}{A} = \frac{\sigma_n(1-a_s)(\dot{\nu} + \tan\phi_b) + a_s(\sigma_n \tan\phi_o + s_o)}{1 - (1-a_s)\dot{\nu} \tan\phi_b} \quad (2.5)$$

a_s is the ratio of the total sheared off area and the total projected shear area, $\dot{\nu}$ is dilation at peak shear stress, and $\sigma_n \tan\phi_o + s_o$ is the shear strength of flat discontinuities. When the normal stress is less than the transition stress (σ_T), a_s and $\dot{\nu}$ are assumed as follows:

$$a_s = 1 - \left(1 - \frac{\sigma_n}{\sigma_T}\right)^{k_1} \quad (2.6)$$

$$\dot{\nu} = \left[1 - \left(1 - \frac{\sigma_n}{\sigma_T}\right)^{k_2}\right] \tan i \quad (2.7)$$

where, k_1 and k_2 are 2 and 4, which are constants derived from experiments. $\sigma_n \tan\phi_o + s_o$ can be calculated by equation (2.8).

$$\sigma_n \tan\phi_o + s_o = \sigma_c \frac{\sqrt{1+n}-1}{n} \sqrt{1+n \frac{\sigma_n}{\sigma_c}} \quad (2.8)$$

In equation (2.8), σ_c is the uniaxial compressive strength and n is the ratio of tensile strength and uniaxial compressive strength of an intact rock. Ladanyi and Archambault model can express the non-linear behavior of shear strength, but the model is impractical due to the complication.

Barton (1973) carried out a series of shear tests for more than 200

tensile fractured specimens and proposed an empirical model to describe the shear strength of rock joints as shown in equation (2.9).

$$\tau = \sigma_n \tan \left[\phi_b + JRC \log_{10} \left(\frac{JCS}{\sigma_n} \right) \right] \quad (2.9)$$

In Barton's model, the shear strength is described as a function of the relationship among joint wall compressive strength (JCS), basic friction angle (ϕ_b), effective normal stress (σ_n) and joint roughness coefficient (JRC). If the surface of a discontinuity is weathered, ϕ_b is replaced with ϕ_r , and in the case of unweathered discontinuities, the uniaxial compressive strength of intact specimens can substitute JCS. Barton's shear tests were performed at relatively low normal stress, and thus, the model fits well at low normal stress. However, at very low normal stress, the log term can diverge infinitely. Therefore, the maximum limit of the tangential term is below than 70°. On the contrary, at very high normal stress, the log term can be converged to zero. Thus, the deviatoric stress of an intact specimen should replace JCS in that case.

Based on the numerous collated data, Byerlee (1978) stated that Barton's model is applicable at low normal stress less than 5 MPa. At higher normal stress, he proposed the following criterion:

$$\tau = 0.85 \sigma_n, \quad (5 \text{ MPa} \leq \sigma_n \leq 200 \text{ MPa}) \quad (2.10)$$

$$, \quad (\quad) \quad (2.11)$$

In Byerlee's model, shear strength is independent of rock types. However, the data were collated at high normal stress conditions, and the effect of roughness was excluded even at low normal stress. Therefore, it can be seen that Byerlee's model is available for the shear behavior of the earth crust.

2.2 Effect of temperature on shear strength

Drennon and Handy (1971) carried out direct shear tests on the flat ground surfaces of Bedford limestone. Normal loads were varied between 0.075 and 2.0 MPa and temperatures from 30 to 200°C were applied. They observed that the static friction coefficient increased with increasing temperature. They explained the increase resulted from the removal of adsorbed water above 100°C. As a result, with the effect of further plastic deformation due to high temperature, asperity to asperity contact areas may increase. They also found that higher temperature enhanced stick-slip behavior.

Friedman et al. (1974) carried out shear tests on sandstone saw-cut surfaces inclined at 29 to 45° to maximum principal compressive stress inside a triaxial chamber. Temperatures were from 24 to 410°C, and confining pressures were from 14 to 500 MPa. Shear strength increased with increasing temperature and the coefficient of sliding friction (the ratio of peak shear stress and normal stress) also rose from 0.58 at 25°C to 0.72 at 410°C. They found welded gouges at high temperature through scanning electron microscope (SEM) observation, and they stated that increase of the actual contact area appears to inhibit sliding. The increase of temperature also accompanied stable sliding behavior.

Lockner et al. (1986) used saw-cut granite specimens, inclined 30° to the sample axis, and artificial granite gouges were placed between the interfaces. Shear tests were conducted at a constant confining pressure of 250 MPa and temperatures in the range of 22 and 845°C. Axial stress was measuring at 2.9 mm of total displacement due to slip hardening behavior. The axial stress of gouge increased approximately 15% at 845°

C.

Bilgin and Pasamehmetoglu (1990) conducted direct shear tests using saw-cut and tensile fractured shale samples at constant normal load condition from 0.25 to 2.0 MPa and temperature from 20 to 400°C. JRC values of fractured specimens were 3, 5 and 8, respectively. Up to 200°C, shear strength increased in all specimens, while decreased above 200°C. They also explained the reduction resulted from the removal of water and the increase of contact area.

Pakpoom (2013) used the rectangular shape of granite specimens including saw-cut or tension fractured surfaces inclined 30° to loading axis. Fig. 2.2.1 shows the prepared discontinuity surfaces. The variations of shear strength were investigated at 30, 100, 300 and 500°C and the confining pressures were 1, 3, 7, 12 and 18 MPa. In the results, the shear strength of saw-cut surfaces increased with increasing temperature as shown in Fig. 2.2.2(a). He presumed that the shear strength increased due to the contact area of saw-cut surface extended caused by plastic deformation at high temperature. In Fig. 2.2.2(a), peak friction angle did not show much change, but cohesion increased. That means extended contact area presumably raise the adhesion of the surfaces. Whereas shear strength and basic peak friction coefficient of tensile fractured surface decreased when the temperature rises (Fig. 2.2.2(b)). He explained that the decrease might be related to the weakening of the mechanical properties at high temperature.

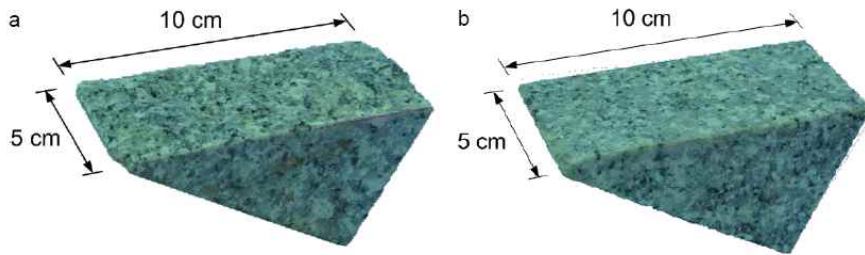


Fig. 2.2.1 Discontinuity surfaces prepared by (a) tensile fracture and (b) saw-cut (after Pakpoom, 2013).

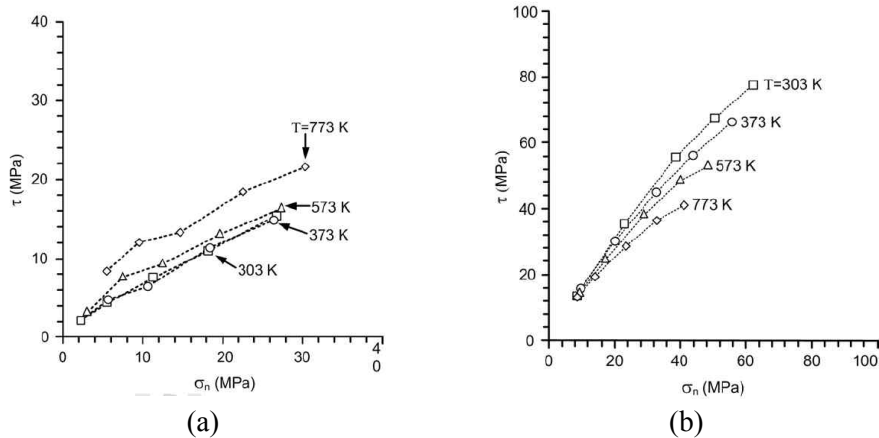


Fig. 2.2.2 Relation between peak shear stress and normal stress depending on temperature: (a) saw-cut surface and (b) tensile fractured surface (after Pakpoom, 2013).

On the other hand, Olsson (1974) found that increased temperature from 25 to 300°C has little effect on the frictional properties of faulted limestone samples. Confining pressures were from 34.5 to 138 MPa, and the peak friction angles were 26.6° at room temperature, 23.7° at 100°C, and 25.2° at 300°C.

Stesky et al. (1974) carried out a series of shear tests inside a pressure vessel. The cylindrical shape of saw-cut and faulted granite and faulted

gabbro specimens were used. Temperatures increased up to 700°C, and confining pressures were from 250 to 600 MPa. Fig. 2.2.3 shows the relation between shear stress and normal stress for each sample. Up to 300°C for granite saw-cut surfaces, 600°C for granite faulted surfaces, and 400°C for gabbro faulted surfaces, the effect of temperature on peak shear strength and friction angle was insignificant. They mentioned that frictional strength of discontinuities was less affected by temperature, and at very high temperature range, the fracture strength of intact part is less than the frictional strength of discontinuities. Therefore, failure can occur in the intact part, and it can cause the rapid decrease of peak shear stress at high temperature.

Lockner et al. (1982) carried out a series of shear tests inside a triaxial chamber for 30° saw-cut graywacke specimens and fractured specimens at confining pressures of 20 to 100 MPa and temperature of 20, 150 and 240°C. Fig. 2.2.4 shows a schematic diagram of the experimental set-up. They reported that peak friction angle shows no significant variation with temperature in all specimens (Fig. 2.2.4).

Zhao et al. (2016) conducted direct shear tests on a series of heat-treated fracture granite specimens. Discontinuity surfaces of the specimens include 45° saw-tooth shape of asperities with a height of 2 mm (Fig. 2.2.5(a)). Temperatures were 20, 100, 200, 300 and 400°C, and cyclic heating-cooling treatment was applied on the samples in an electrical furnace. Normal stress of 5 MPa was maintained during the tests. From the results, shear strength decreased up to 200°C, while increased again from 200 to 400°C (Fig. 2.2.5(b)). They presumed the increase of shear strength above 200°C might be caused by randomly distributed microcracks occurred by high temperature. Those microcracks could dissipate fracture energy, and

hence as the number of microcracks increased with rising temperature, shear strength increased again.

From the overall review, the effect of temperature on shear strength is still spotty depending on rock types and the temperature range. Many researchers presumed the increase of the shear strength results from either the removal of adsorbed water (Drennon and Handy, 1972; Bilgin and Psamehmetoglu, 1990) or the formation of glass of quartz minerals (Friedman et al., 1974; Bilgin and Psamehmetoglu, 1990; Pakpoom, 2013). The formation of glass presumably increased the contact area and caused a corresponding increase in frictional force to maintain sliding (Stesky et al., 1974). On the other hand, shear strength showed a decrease or no change, and deterioration of mechanical properties is considered as the main factor (Stesky et al., 1974; Olsson, 1974; Bilgin and Psamehmetoglu, 1990). The information of friction angle was rarely mentioned but usually did not show much change up to 400°C. Table 2.2.1 summarized the overall collated results on the variations of shear strength and friction angle depending on temperature.

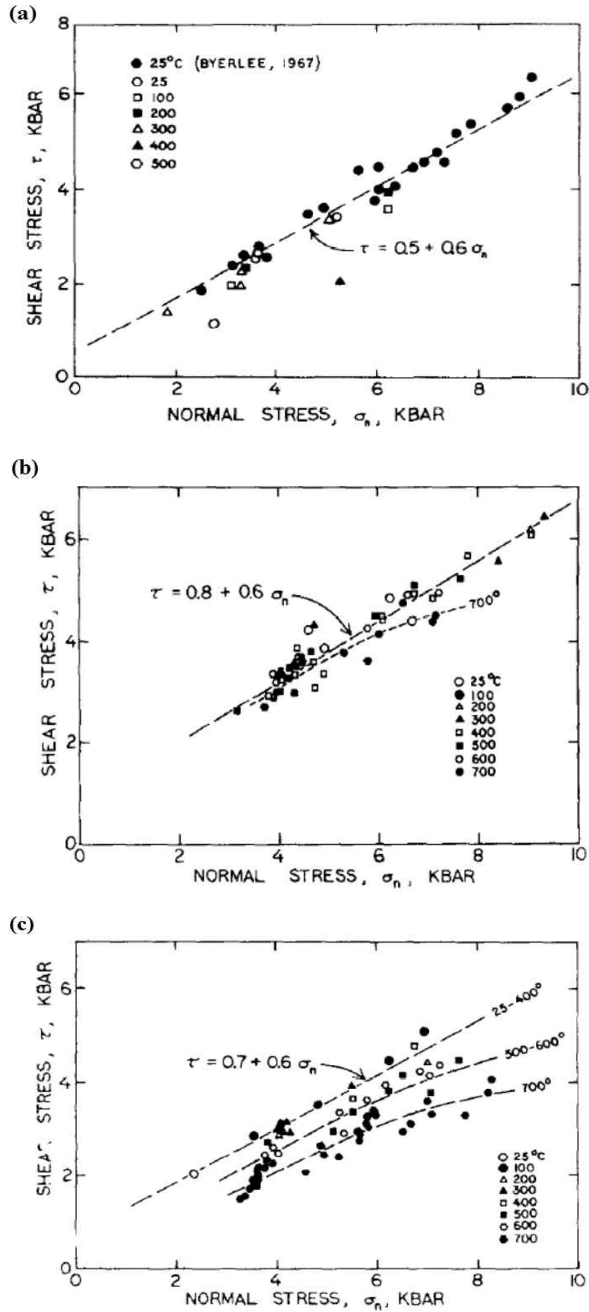


Fig. 2.2.3 Relation between shear stress and normal stress depending on temperature: (a) granite saw-cut (b) faulted granite and (c) faulted gabbro (after Stesky et al., 1974).

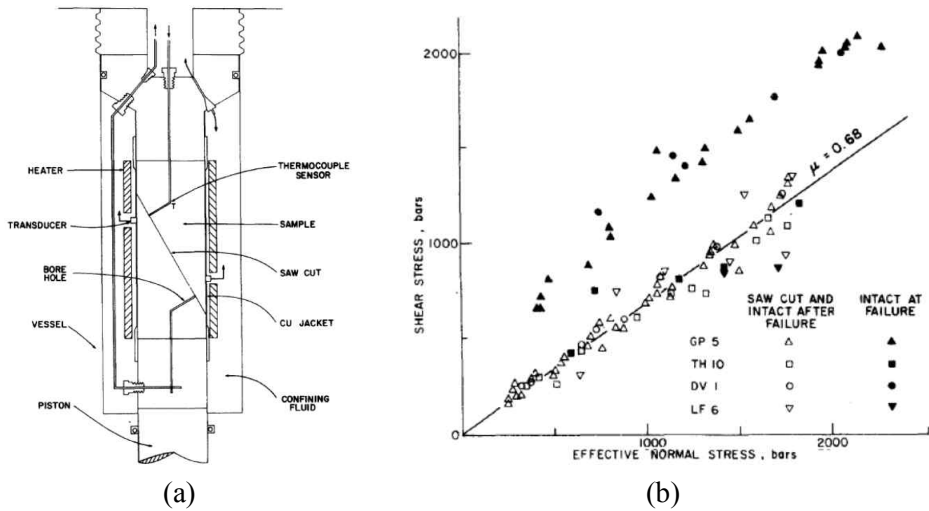


Fig. 2.2.4 A schematic diagram of the experiments and test results: (a) a schematic diagram inside a triaxial chamber and (b) Relation between shear stress and normal stress depending on temperature of saw-cut graywacke specimens and fractured specimens (after Lockner et al., 1982).

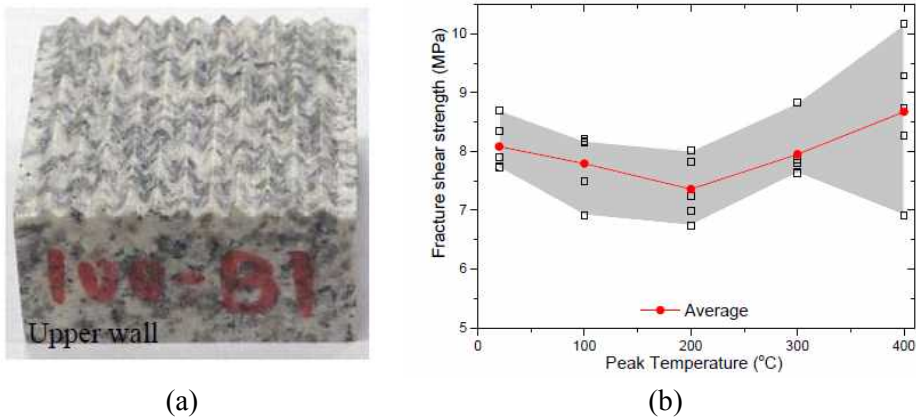


Fig. 2.2.5 Discontinuity surface including saw-tooth shape of asperities and test results: (a) discontinuity surface and (b) shear strength depending on temperature (after Zhao et al., 2016).

Table 2.2.1 Results of literature review on the effect of temperature on shear strength and friction angle.

References	Rock type	Description of discontinuity	Temperature (°C)	Normal stress (σ_n) or confining pressure (σ_3) (MPa)	Shear strength	Friction angle
Drennon and Handy, 1972	Limestone	saw-cut	20-200	σ_n : 0.075-2.0	Increase	No information
Donath et al., 1972	Sandstone	shear fracture	20-300	σ_3 : 50-200	Increase	
Friedman et al., 1974	Granite	gouge	20-410	σ_3 : 14-500	Increase	
Lockner et al., 1986	Granite	gouge	20-845	σ_3 : 250	Increase	
Bilgin and Psamehmetoglu, 1990	Shale	saw-cut/ tension fracture	20-400	σ_n : 0.25-2.0	Increase and decrease from 200°C	
Pakpoom, 2013	Granite	saw-cut	20-500	σ_3 : 1-18	Increase	No change
		tension fracture			Decrease	Decrease
Donath et al., 1972	Limestone/ Slate	shear fracture	20-300	σ_3 : 50-200	Decrease	No information
Olsson, 1974	Limestone	shear fracture	20-300	σ_n : 34.5-138	No change	No change
Stesky et al., 1974	Granite	saw-cut	20-700	σ_3 : 250-600	No change and decrease from 300°C	No information
	Granite	shear fracture			No change and decrease from 600°C	
	Gabbro	shear fracture			No change and decrease from 400°C	
Lockner et al., 1982	Graywacke	saw-cut/ shear fracture	20-240	σ_3 : 20-100	No change	
Blanpied et al., 1995	Granite	saw-cut	20-600	σ_3 : 400	No change	
Odera et al, 2001	Granite	shear fracture	20-480	σ_3 : 70-480	No change and decrease from 300°C	
Zhao et al., 2016	Granite	saw-tooth	20-400	σ_n : 5	Decrease and increase from 200°C	

2.3 Effect of water on shear strength

No clear pattern is evident for the effect of water on the friction of the sliding surfaces. Sometimes water have no effect, or possibly more often decrease the friction, while increases also have been reported (Paterson and Wong, 2005).

Jaeger (1959) performed shear tests in a triaxial vessel using a multistage triaxial compression method. Intact cylindrical samples of granitic gneiss and sandstone were fractured at a constant confining pressure of 100 MPa to make shear fractures. Shear tests were carried out at constant confining pressures of 20, 40, 60, 80 and 100 MPa, respectively, on dry and wet fractured specimens. Based on Mohr-Coulomb failure criterion, sliding friction coefficient decreased from 0.71 to 0.61 for granitic gneiss, and from 0.52 to 0.47 for sandstone when wet condition.

Horn and Deere (1962) performed direct shear tests at constant normal loads on various minerals. Normal loads were varied from 1 to 10 lb, and the sliding rate was 0.7 inch/min (equal to 0.3 mm/sec). Oven-dried samples at 105°C, oven-dried/air-equilibrated specimens, and saturated/air-equilibrated specimens were used. The term of “air-equilibrated” means the specimens were stored for several days in an opened air condition. From the results, the frictional coefficients of massive minerals including quartz, feldspar, and calcite showed an increase and those of layer lattice minerals such as muscovite, biotite, and chlorite decreased under wet conditions (Table 2.3.1). They presumed molecules of the fluid would be readily adsorbed on the surfaces of the layer lattice minerals. Therefore, water can act as a lubricant by diminishing the cohesive forces, and hence, friction might decrease.

Table 2.3.1 Summary of frictional coefficients for three conditions of surface moisture (after Horn and Deere, 1962).

Crystal structure	Mineral	Ove-dried	Oven-dried/ air-equilibrated	Saturated
Massive-structured minerals	Quartz	0.11-0.14	0.11-0.16	0.42-0.51
	Microline feldspar	0.11-0.12	0.12-0.13	0.76-0.77
	Calcite	0.14	0.14-0.21	0.60-0.68
Layer-lattice minerals	Muscovite	0.41-0.45	0.30-0.36	0.22-0.26
	Phlogopite	0.29-0.31	0.22-0.25	0.15-0.16
	Biotite	0.31	0.26	0.13
	Chlorite	0.53	0.35	0.22
	Serpentine	0.62-0.76	0.50-0.65	0.29-0.48
	Steatite	0.38	0.26	0.23
	Talc	0.36	0.24	0.16

Morrow et al. (2000) obtained the decreasing tendency of shear strength from shear tests inside the triaxial chamber using a 30° saw-cut specimen including mineral gouge layer. Confining pressure was kept constant at 100 MPa, and 10 MPa of pore pressure was applied. An impermeable fused silica block was used as a lower part of the saw-cut pair to maintain undrained condition. He reported that the friction coefficients of layer-lattice structured minerals dropped 20~60% with the addition of water, and the most remarkable decrease was observed in clay minerals (Fig. 2.3.1).

Ulusay and Karakul (2015) carried out a series of tilt tests on flat surfaces of various rock types including limestone, marble, travertines, granite and serpentinite under different testing conditions (dry, wet and

submerged). XRD analysis was also performed to investigate the effect of minerals before the tilt tests. Basic friction angles of rocks including clay minerals dropped by 0.19~8.64° (Fig. 2.3.2). Under submerged conditions, the effect of water head was also examined, and they concluded that the effect was ignorable.

The results from other researchers (chalk, Gutierrez et al. (2000); sandstone, Sheng and Reddish (2005); marl, Pellet et al. (2013); sandstone, Lee and Chang (2013)) also showed the reduction of the friction angle under wet condition. They explained that layer-lattice structured minerals readily adsorb water due to negative charged surfaces and the water could act as a water film to lubricate the sliding surface. The adsorption depends on many factors including mineral composition, surface charge, pH of the water, and pressure-temperature conditions (Morrow et al., 2000).

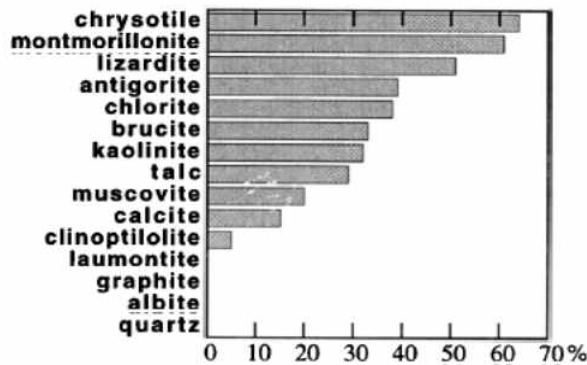


Fig. 2.3.1 Percentage of decrease in frictional strength of in-filled gouge minerals under 100 MPa of confining pressure and 10 MPa of pore pressure (after Morrow et al., 2000).

Rock type no.	Dry			Wet			Submerged		
	Basic friction angle (°)			Basic friction angle (°)			Basic friction angle (°)		
	Number of tests	Mean	Standard deviation	Number of tests	Mean	Standard deviation	Number of tests	Mean	Standard deviation
MET-2	6*	27.90	1.12	6*	29.25	0.63	9	26.98	1.31
MET-3	6*	28.35	0.68	6*	30.43	0.72	6	25.27	0.82
FC1	6*	32.02	2.26	6*	28.30	1.34	9	26.71	1.19
FC4	6*	30.85	1.75	6*	28.55	1.33	9	28.69	1.29
1	3	38.27	0.12	3	36.60	1.40	6	36.05	0.96
2	6*	28.20	0.92	3	29.73	1.97	9	28.01	1.39
3	3	32.30	0.78	3	30.33	0.58	9	31.30	1.22
4	3	32.43	0.74	3	34.77	1.52	9	29.67	1.66
5	3	35.43	0.59	3	30.23	1.25	9	34.34	1.34
6	3	36.90	0.17	3	26.27	1.35	9	33.50	1.16
8	3	31.00	0.95	3	31.17	1.61	9	27.12	2.23
9	3	25.87	0.42	3	26.70	1.70	9	25.60	0.52
10	3	31.40	1.22	3	31.57	0.38	9	26.18	0.87
11	6*	30.93	1.32	3	31.10	0.36	9	27.49	1.39
12	3	22.53	0.51	3	29.00	1.51	9	18.80	1.03
13	3	31.15	0.71	6*	28.57	1.05	9	28.18	1.81
14	3	36.73	0.75	3	35.30	1.3	9	28.09	1.40
15	6*	37.62	0.71	3	31.77	0.68	9	22.42	1.46
16	3	36.73	0.67	3	32.60	0.79	9	32.41	1.29
17	6*	34.92	0.53	6*	32.30	1.15	9	26.79	1.11
19	6*	30.53	1.58	3	27.9	0.66	9	25.60	0.47
20	6*	30.78	0.38	6*	26.10	0.84	9	26.39	0.85

Fig. 2.3.2 Results of tilt tests under three different conditions (MET-2, MET-3, FC1, FC4, 13 : Andesite / 1, 2, 8 : Travertine / 3 : Carbonated serpentinite / 4, 5, 6, 9, 15, 19 : Limestone / 10, 14, 17, 20 : Ignimbrite / 11 : Basalt / 12 : Granite / 16 : Marble) (after Ulusay and Karakul, 2015).

On the contrary, Byerlee (1967) reported that the friction coefficient of granite did not show any change under wet conditions. He prepared three types of specimens, which are ground surfaces, tensile fractured surfaces and shear fractures obtained from triaxial compression tests. For the investigation of the effect of the water, pore pressures of 0, 100 and 165 MPa were applied on the surfaces, and the confining pressures were varied from 50 to 450 MPa. The theory of effective stress law was applied well, but the friction coefficient was 0.6 in all cases.

Hoskins et al. (1968) performed shear tests at a constant normal angle load of

1.7, 3.4 and 5.1 MPa (equal to 250, 500, 750 psi). Trachyte and sandstone specimens were tested under dry and wet conditions. Based on Mohr-Coulomb criterion, the friction coefficient of trachyte decreased from 0.68 to 0.56, but that of sandstone increased from 0.51 to 0.61 under wet conditions.

Morrow et al. (1992) carried out shear tests inside a triaxial vessel using saw-cut specimens in-filled with montmorillonite and illite clays (Fig. 2.3.3(a)). The confining pressures were in the range of 100 and 300 MPa, and the pore pressures were varied from 0 to 150 MPa. The effective pressure law for friction holds under all pressure conditions, but no change was observed in the friction angle (Fig. 2.3.3(b)).

Barton (1973) collected the experiments data of the friction angle to investigate the effect of water. From the data, he concluded that shear strength of smooth polished surfaces shows no change or increased slightly when wet conditions. However, exceptions can occur when mineralogy affects the friction under wet conditions. On the contrary, the friction angle of non-planar joints was reduced due to the weakening of the tensile strength under saturated conditions. Table 2.3.2 shows the collated data recorded in the paper.

From the overall literature review, it can be seen that the variations of friction angles of flat surfaces can be influenced by rock types and minerals on the discontinuity surfaces. For rough surfaces, due to the weakened asperities, shear strength might decrease under wet conditions. However, in most of the previous studies, the information of joint roughness was not provided, and in the case of the shear fractures, it is hard to clarify the effect of water due to the different roughness. Table 2.3.3 lists the overall

results of the literature review except for the data which already provided in the figure and the table above.

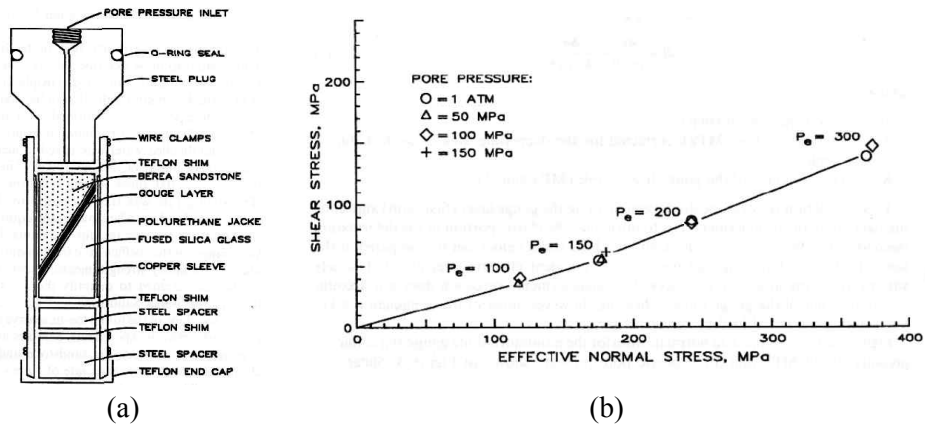


Fig. 2.3.3 Experimental set-up and test results: (a) sample assembly inside a triaxial chamber and (b) relation between shear stress and effective normal stress of illite/montmorillonite gouge (after Morrow et al., 1992).

Table 2.3.2 Frictional strength data under dry and wet conditions collated by Barton (after Barton, 1973).

Rock type	Description of discontinuity	Dry		Wet		Reference
		ϕ (°)	μ	ϕ (°)	μ	
Quartzite	artificial, planar, polished (σ_n : 30-400 kg/cm ²)					Jaeger and Rosengren (1968)
Shales, siltstones and slates	minor faults; smooth, polished or slickensided, graphite coated	No change in general				Rosengren (1968)
Shales, siltstones and slates	extension fractures; coated with limonite, pyrite, quartz					Rosengren (1968)
Reduction						
Granite, gneiss, sandstone	shear fractures from failure of intact specimens (σ_n : 100-2500 kg/cm ²)		0.71		0.61	Jaeger (1959)
			0.52		0.47	
Sandstones, carbonates	artificial, rough sawn, equivalent to residual	ϕ_r 25-34 33-39		ϕ_r 24-33 32-36		Patton (1966a)
Shales, siltstones and slates	minor fault, smooth, polished, chlorite coated		0.49		0.40	Rosengren (1968)
Dolorite	joint	52		37		Duncan (1969)
Granite	artificial surface	38		31		
Gneiss	natural schistose plane, "keyed"	49		44		
Phyllite	schistose plane	40		32		
Shale	joint	37		27		
Quartzite	joint	44		34-37		
Marble	joint	49		42		
Increase						
Sandstone	artificial, planar, polished (equivalent to slickenside)	ϕ_r 27-32		ϕ_r 30-38		Patton (1966a)
Gabbro	joint	47		48		Duncan (1969)
Oolitic limestone	joint	44		48		
Chalk (2 of 3 types)	joint	40		41		
Quartzite	artificial, planar, polished	23		30		Duncan and Scheerman-Chase (1965-66)
Basalt	artificial, planar, polished	33		35		
Schistose gneiss, granite, sandstone	artificial, planar, polished with increasing polish during shear	-	-	-	-	Coulson (1970)

Table 2.3.3 Results of literature review: variations of friction angle depending on dry and wet conditions.

References	Rock type	Description of discontinuity	Normal stress (σ_n) or confining pressure (σ_3) (MPa)	Friction angle			
				Dry		Wet	
				ϕ (°)	μ	ϕ (°)	μ
Increase							
Hoskins et al. (1967)	Sandstone	saw-cut	σ_n : 1.7-5.1	0.51	0.61		
No change							
Byerlee (1967)	Granite	ground flat	σ_3 : 50-450	0.6	0.6		
Morrow et al. (1992)	Montmorillonite /Illite	gouge	σ_3 : 100-350	-	-	-	-
Goodman and Onishi (1972)	Sandstone	saw-cut	-	34	34		
Reduction							
Gutierrez et al. (2000)	Chalk	natural fracture	σ_n : 0.5-3.0	26	15		
Sheng and Reddish (2005)	Sandstone	shear fracture	σ_3 : 1-18	-	-	-	-
Pellet et al., (2013)	Marl	flat	σ_n : 2.0-16.0	22	12		
Lee and Chang (2015)	Sandstone	saw-cut	σ_3 : 2-20	0.71	0.65		

3. Laboratory testing

3.1 Specimen preparation

3.1.1 Saw-cut specimens

In this study, Daejeon granite, Goheung diorite, and Linyi sandstone were taken as test samples considering the distinct characteristics of the area and the rock types. Granite samples were cored during site investigation at KURT (Korea Atomic Energy Research Institute Underground Research Tunnel). The size of cylindrical core samples was 47.7 mm in diameter. Diorite and sandstone were initially obtained as block samples and cored with the size of 54 mm in diameter. Diorite obtained from Goheung in the southern part of Korea, where a subsea tunnel is considered to be constructed. Sandstone was imported from Linyi in the eastern part of China and chosen as a representative of sedimentary rock. The height of all specimens were 2~2.5 times of the diameter. Granite and diorite consist of coarse grain, but sandstone are composed of relatively fine-grained minerals and shows pink color. Fig. 3.1.1 shows the location of Daejeon, Goheung, and Linyi, where samples were obtained.

A series of triaxial compression tests were performed on intact granite specimens to investigate the angle of the saw-cut surface to make shear behavior along the saw-cut surface. The angle between shear rupture surface and cylindrical core axis was 28° (Kim and Jeon, 2011). Therefore, cylindrical specimens were cut by a diamond saw to make a smooth discontinuity surface with the angle of 28° to make shear behavior along the discontinuity surface. Due to the low permeability of the specimens, water

injection holes were drilled on the top and bottom surfaces to apply water pressure directly on the discontinuity surface. The diameter was 3.0-4.0 mm, and the holes were drilled on the specimens only for the water pressure applied tests (Fig. 3.1.2).

To investigate the physical and mechanical properties, a series of uniaxial compression tests were performed and porosity, specific gravity and seismic wave velocity of the specimens were also measured. Schmidt hammer test for joint wall compressive strength (JCS) and tilt test for basic friction angle were also carried out on dry and wet specimens to investigate the effect of water on discontinuity surface. All the experiments were performed at least for five different specimens and Table 3.1.1 showed the results with average values.

In the results of all specimens, JCS decreased when the surface was wet, and reduction amounted to 9~22%. JCS is proportional to the uniaxial compressive strength and in the case of unaltered joints, uniaxial compressive strength can replace JCS. Therefore, Barton (1973) summarized previous studies about the effect of water on the uniaxial compressive and tensile strength of various rocks including sandstone (Price, 1960), shale (Colback and Wiid, 1965), gneiss (Bernaix, 1969) and granite (Broch and Franklin, 1972). Reductions of the strength amounted to approximately 10~50% in their results. JCS and the tensile strength of all the specimens also showed a decrease at a saturated condition, by 10~40%. Conversely, basic friction angle from tilt tests showed a little increase at a wet condition and the amount was 1~4°. To investigate mineralogy of each rock type used in this study, X-ray diffraction (XRD) tests were carried out at Korea Institute of Geoscience and Mineral Resources (KIGAM) (Table 3.1.2).

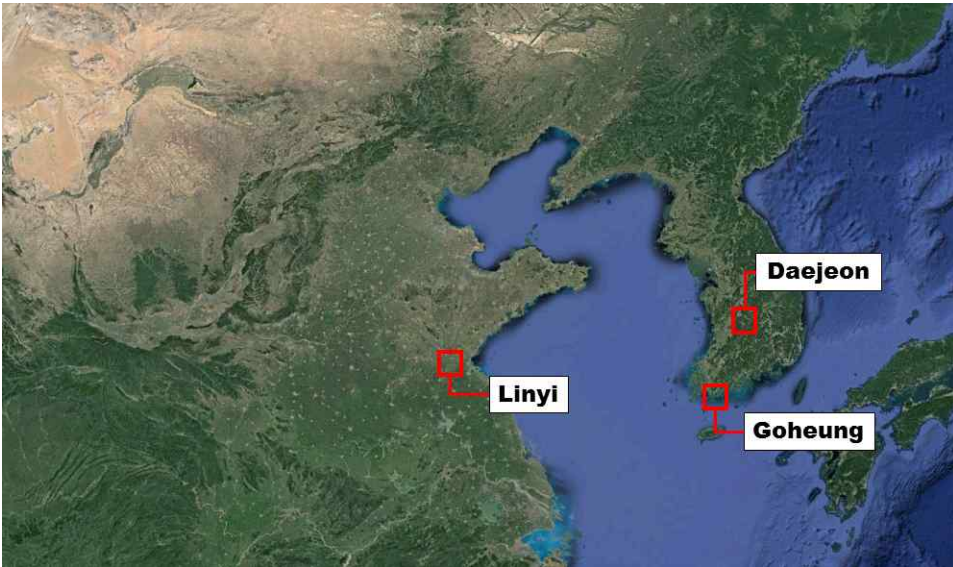


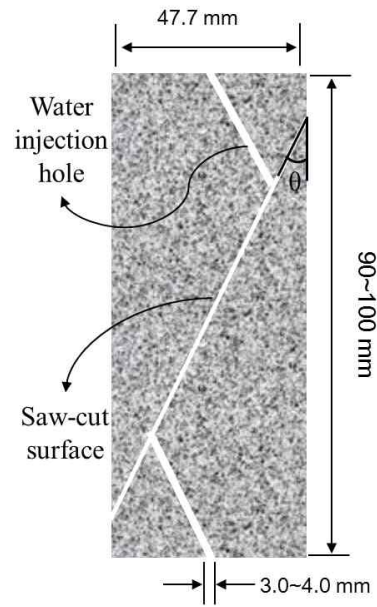
Fig. 3.1.1 Location of Daejeon, Goheung in Korea and Linyi in China (from Google Earth).



(a)



(b)



(c)

Fig. 3.1.2 Configuration of the saw-cut Daejeon granite specimen: (a) side view of the specimen with a saw-cut surface, (b) picture of the saw-cut surface with a water injection hole, and (c) schematic longitudinal-section view of the specimen ($\theta = 28^\circ$).

Table 3.1.1 Physical and mechanical properties of Daejeon granite, Goheung diorite, Linyi sandstone and cement-mortar.

		Daejeon granite	Goheung diorite	Linyi sandstone	Cement-mortar
Uniaxial compressive strength (MPa)		111.4	272.7	64.0	82.5
Young's modulus (GPa)		59.7	67.6	10.5	25.9
Poisson's ratio		0.20	0.23	0.22	0.33
Porosity (%)		0.72	0.59	8.2	9.15
Specific gravity		2.65	2.77	2.35	2.20
Seismic wave (m/sec)	P wave	4770	5600	2317	3210
	S wave	2489	2880	1531	1800
Brazilian tensile strength (MPa)	Dry	10.5	17.5	4.72	9.22
	Wet	7.76	13.0	3.66	7.32
Joint wall compressive strength (MPa)	Dry	111.4	142.7	67.4	81.5
	Wet	100.9	111.0	58.8	67.4
Basic friction angle (°)	Dry	30.0	28.5	27.6	34.4
	Wet	31.0	31.5	30.8	36.0

Table 3.1.2 Mineralogy of each rock type used in this study based on XRD analyses.

Rock type	Daejeon granite	Goheung diorite	Linyi sandstone	Cement-mortar
Mineral/ (Weight ratio, %)	Quartz (32.2)	Albite (52.1)	Albite (44.3)	Dolomite (68.6)
	Albite (29.3)	Orthoclase (13.8)	Quartz (35)	Ettringite (18.1)
	Microline (24.7)	Quartz (8.8)	Microline (13.4)	Anhydrite (7.3)
	Muscovite (9.2)	Hornblende (8.3)	Laumonite (3.5)	Calcite (5.0)
	Biotite (3.0)	Monmorillonite (4.4)	Hematite (2.2)	Quartz (1.0)
	Chlorite (1.6)	Magnetite (3.8)	Calcite (1.7)	-
	-	Talc (3.7)	-	-
	-	Biotite (3.2)	-	-
	-	Chlorite (1.7)	-	-

3.1.2 Cement-mortar specimens

High strength cement-mortar was used to make synthetic rock specimens. The uniaxial compressive strength of high strength cement-mortar showed a consistent value of 82.5 MPa when the mortar to water mixing ratio was 100:15 by weight after ten days of curing in the water. Table 3.1.1 provides the physical and mechanical properties of cement-mortar

specimens and Table 3.1.2 shows the results of XRD analyses for cement-mortar specimens. Porosity was greater than other rocks, but JCS and basic friction angle from tilt tests showed same variations depending on dry and wet conditions compared to other rock specimens.

A tensile fractured rock joint surface was used to make a duplicated mold before the test. Asan gneiss rock block was fractured by Brazilian splitting test and some part of the fractured surface was reproduced with aluminum. Two different discontinuities were duplicated to investigate the effect of joint roughness. Three-dimensional laser roughness profiling system with a Keyence sensor was used to measure the roughness quantitatively. The machine composed of laser displacement meter, positioning system and main computer for data acquisition and control (Fig. 3.1.3). The target area of the rough surface is designated as a rectangular shape in horizontal plane. Laser displacement meter moves along x and y-direction of the targeted area and measures the relative coordination in the z-direction of the surface by using the reflection of the laser. Resolution of the measuring length is 0.5 μm , and the range of measurement is within ± 9 mm around the point which is 5 cm away from the laser head.

Roughness was calculated with the method proposed by Tse and Cruden (1979). Z2 values along the lines having 0.5 mm spacing which is parallel to the shear direction were calculated by using equation (3.1). With equation (3.2) and the average value of Z2 values, joint roughness can be determined. The roughness of each discontinuity was 2.05 and 11.63 and Fig. 3.1.4 shows the three-dimensional profiles of discontinuities.

$$Z_2 = \left[\frac{1}{L} \int_{x=0}^L \left(\frac{dy}{dx} \right)^2 dx \right]^{\frac{1}{2}} \quad (3.1)$$

$$JRC = 32.2 + 32.47 \log Z_2 \quad (3.2)$$

A pair of the cylindrical cast were used to make a lower and upper piece of the specimen separately. The diameter of the specimens was 54 mm, and the height was 2~2.5 times of the diameter. The angle of rough discontinuity in the specimen was 28° from the axis of the specimen, which is the same with saw-cut rock specimens. Water injection holes were also drilled on the bottom and upper surfaces of the specimens to apply water pressure on the discontinuity surface directly. Cement-mortar specimens were prepared in the following procedure.

1) The aluminum replica of the rough surface is combined with an inclined cast to make a lower piece of the specimen (Fig. 3.1.5(a)). A releasing grease should be spread on the aluminum replica surface and the cast to easily separate the specimen from the cast before pouring cement-mortar.

2) Cement-mortar is mixed with water in a ratio of 100 : 15 by weight and pour the cement-mortar mixture into the inclined cast. After one day curing, separate the lower piece of the specimen from the cast.

3) To make an upper piece of a specimen, place the lower piece into the cylindrical cast (Fig. 3.1.5(b)). After spreading releasing agent on the discontinuity surface, pour the mixed cement-mortar into the cast.

4) After 5~6 hours, take the specimen out from the cast, and separate

upper and lower piece. If it takes more than 5~6 hours, it is difficult to separate the lower and upper specimen due to strong adhesion. Cure the specimen in the water for ten days and after curing, grind the bottom and upper surface of the specimen. In the case of water pressure applied specimens, water injection holes were drilled after curing due to the low permeability of the specimen.

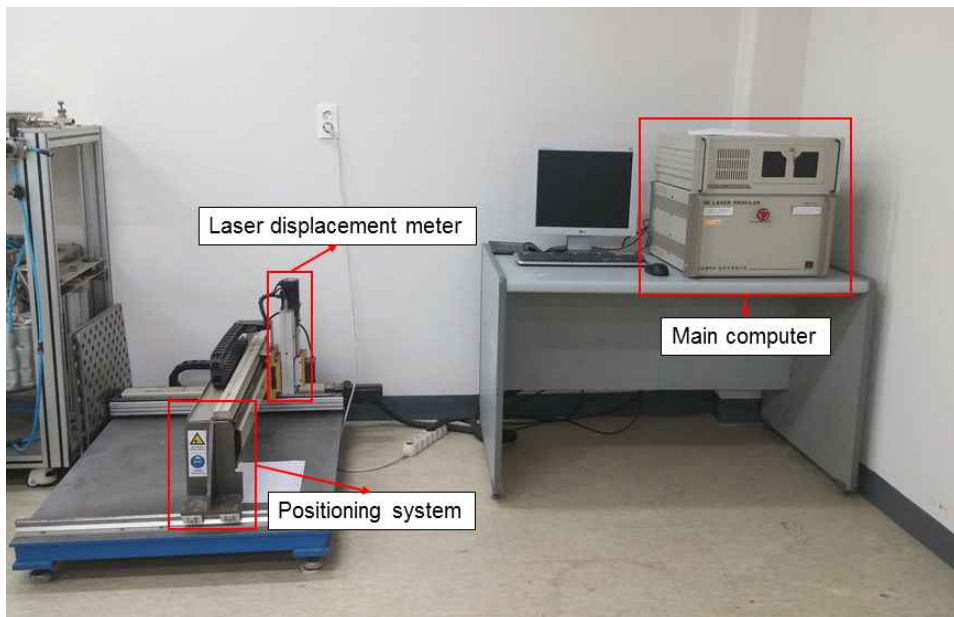
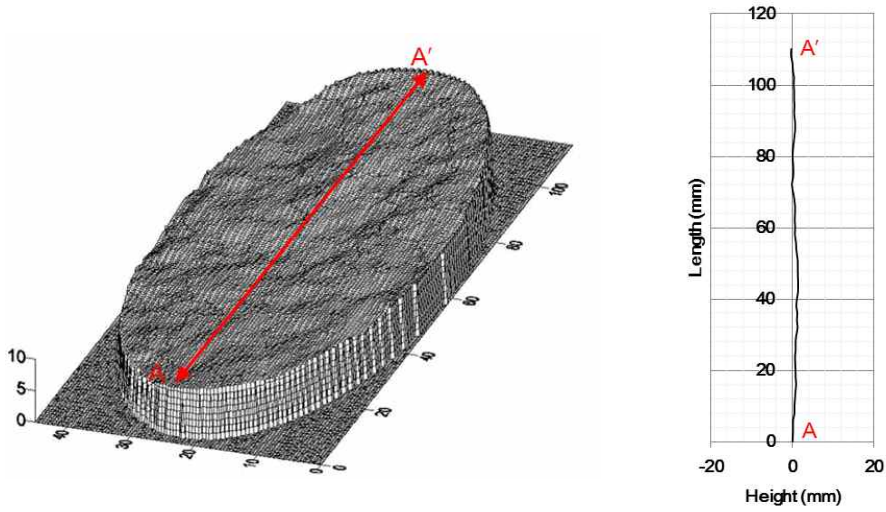
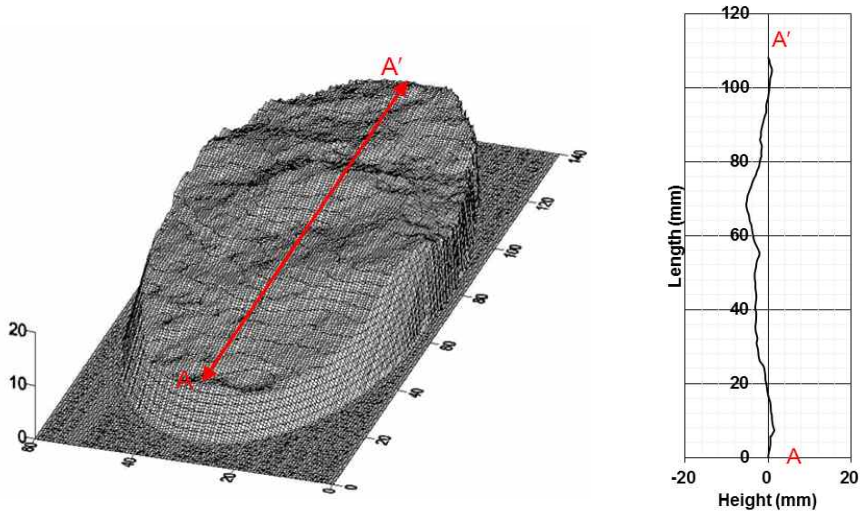


Fig. 3.1.3 A configuration of 3 dimensional laser roughness profiling machine.



(a)



(b)

Fig. 3.1.4 Three dimensional profiles of discontinuities of cement-mortar specimens and the profiles of center lines (A-A') used in the numerical simulation: (a) $JRC = 2.05$ and (b) $JRC = 11.63$.



Fig. 3.1.5 Aluminum replica of rock joint surface and a pair of cast with lower piece of the specimen: (a) an inclined cast combined with aluminum replica of rock joint surface and (b) a cylindrical cast with lower piece made by cement-mortar.

3.2 Testing apparatus and testing conditions

3.2.1 Testing apparatus

In this study, a series of shear tests were performed in the triaxial compression chamber to reproduce in-situ condition (Fig. 3.2.1(a)). MTS 816 system was used for the tests, which composed of a triaxial compression chamber, a servo-controlled hydraulic ram for axial loading and confining pressure intensifier with an accuracy of 0.1 MPa, band heater for heating, temperature control system and data acquisition (DAQ) system to record the data in real-time. In MTS 816 system, tests are carried out inside a triaxial compression chamber, and hence various stress, temperature and water pressure conditions can be controlled as intended.

The maximum capacity of a loadcell placed inside the chamber is 100 tonf and inside the triaxial compression chamber temperature, confining pressure and water pressure can be controlled. The maximum pressure capacity of the triaxial compression chamber is 69 MPa. Axial displacement of the specimen was measured through the linear variable differential transformer (LVDT) placed on the axial actuator and the lateral displacement was measured through the circumferential extensometer installed around the specimen. All the measured data including axial load, confining pressure, temperature and displacement were recorded in real-time through DAQ system with the interval of 0.2 seconds. Heat to control temperature is applied by band heater around the chamber (Fig. 3.2.1(a)). During the test, triaxial compression chamber is filled with hydraulic oil and heat from band heater is transferred to the specimen through the oil. MTS 816 control system compare the difference between the temperature of a band heater and thermocouples installed inside the chamber and apply heat to reach up to the target temperature. Heating rate also can be controlled and the maximum temperature of the chamber is 165°C.

500D syringe pump made by ISCO was used to apply water pressure on the discontinuity surface during the tests. 500D syringe pump consists of a frame, a piston to control water pressure and a controller to apply constant fluid flow and fluid pressure. The capacity of constant fluid flow is in the range of 0.001-200 ml/min and the maximum fluid pressure is 25.9 MPa (2750 psi) with an accuracy of $\pm 0.5\%$ of the full scale. The maximum storage capacity of syringe pump is 507 ml and syringe pump can apply the water pressure without fluctuation. Fig. 3.2.1(b) shows the view of experimental set-up inside the triaxial compression chamber when water

pressure was applied and Fig. 3.2.2 shows the overall view of MTS 816 system with 500D syringe pump.

High-temperature heat shrinkage tube made from perfluoroalkoxy (PFA) was used as a membrane of the specimen to prevent that confining oil permeates into the specimen. Initial diameter of the tube is 57 mm and if hot air above 90°C through heat gun is applied, the diameter is contracted to 49 mm. Due to plasticity, the tube is not able to be expanded again after shrinkage and the maximum temperature is 260°C.

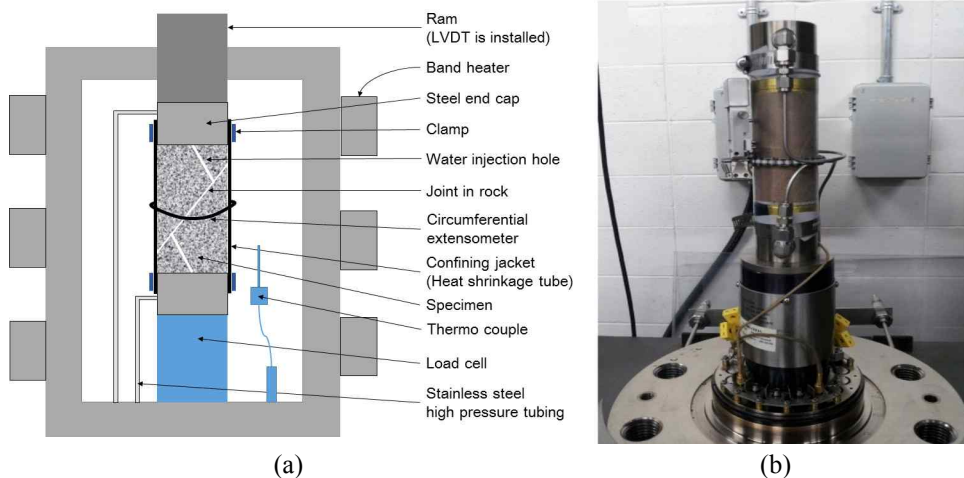


Fig. 3.2.1 A schematic diagram of experiment and the view of experimental set-up of water pressure applied test: (a) a schematic diagram of experiment inside the triaxial compression chamber and (b) the view of experimental set-up inside the chamber when water pressure was applied.

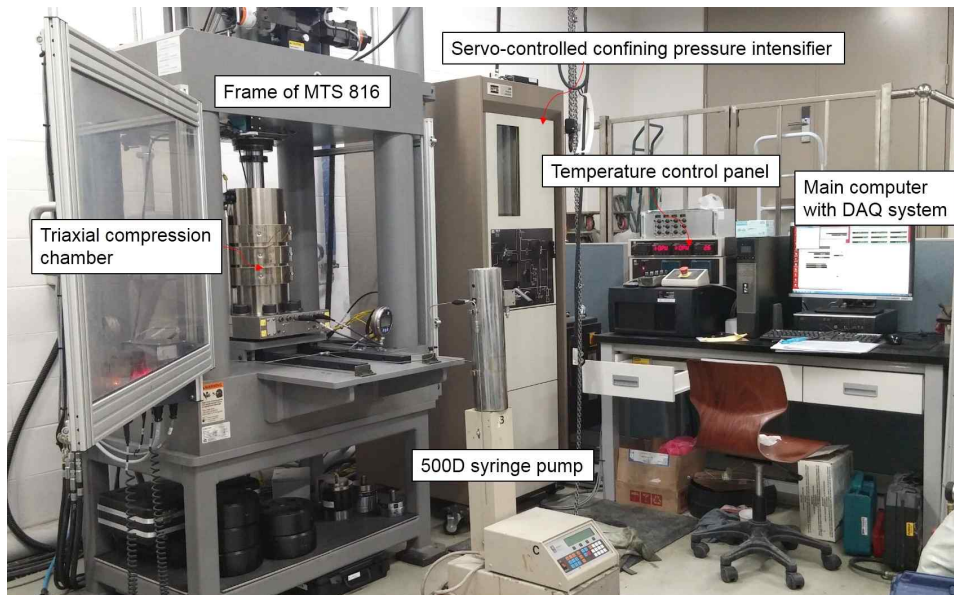


Fig. 3.2.2 Overall view of MTS 816 system with 500D syringe pump after setup in use.

3.2.2 Testing method for saw-cut specimens

Multistage triaxial compression tests were performed under various confining stress, temperature and water pressure applied conditions. In multistage triaxial compression test, a full failure envelope can be generated using a single specimen and thus scatter of the results can be reduced (Kovari et al., 1983). However, in the case of the specimen having rough surfaces, failure of the asperities can occur under high confining pressure, and as a result, the roughness can be degraded as shearing proceeds. In this study, multistage triaxial compression tests can be applied on the saw-cut specimens because shear displacement does not induce change of roughness. Multistage triaxial compression method have been widely applied on shear

tests for planar discontinuities due to the simplicity and consistency of the test results (Jaeger, 1959; Liz and Reddish, 2005).

Testing conditions including confining pressure, temperature and water pressure were decided considering in-situ conditions at depth below than 300 m. The confining pressure was 5, 10 and 15 MPa for granite. In the case of diorite and sandstone, stage of 20 MPa was added to increase the reliability of failure criterion. When water pressure of 1 MPa was applied, 6, 11, 16 and 21 MPa of confining pressure were applied to compare the results under the same initial effective normal stress of discontinuity surface.

In the first stage of the test, axial load and confining pressure increased simultaneously to 5 MPa. After reaching hydrostatic state, the confining pressures were maintained, and the axial load increased. Constant axial displacement with the rate of 0.4 mm/min was applied. The displacement rate is in the range of $10^{-2}\sim 10^{-5}$ sec⁻¹ of strain rate, which was suggested by the standard method for multistage triaxial compression tests of International Society for Rock Mechanics (ISRM) (Kovari et al., 1983). During the tests, the effective normal stress was not kept constant but varied according to the magnitude of the confining pressure. If shearing occurred along the discontinuity, the slope of the curve from axial displacement versus axial stress decreased. Once the change of the slope was observed, axial displacement was held, and then, confining pressure increased to the next step. After the confining pressure had reached up to the next level, axial displacement increased again. Fig. 3.2.3 shows the relation between axial stress and confining pressure obtained from multistage triaxial compression test of the LY-M-1 specimen.

In the case of tests where water pressure was involved, water pressure

was maintained constant during the tests. Four different water pressures (0, 0.1, 0.5, 2.0 MPa) were applied on granite saw-cut specimens and in the case of diorite and sandstone specimens, 0 and 1 MPa of water pressures were applied. Fig. 3.2.4 shows an example of stress path of effective normal stress and shear stress plane of saw-cut granite A-M-2 specimen when 2 MPa of water pressure was applied under 10 MPa of confining pressure. To avoid water leakage, firstly, confining pressure exceeding water pressure was applied (Point 2 in Fig. 3.2.4). In the case of the experiments at the dry condition, after target confining pressure, axial load increased and if the Mohr's circle reached on the failure criterion line, then slip occurred (Point 3 in Fig. 3.2.4). However, when water pressure applied after target confining pressure, effective normal stress decreased (Point 3' in Fig. 3.2.4), and the axial load was raised to the slippage point (Point 4 in Fig. 3.2.4).

Room temperature and 80°C were chosen as temperature conditions considering the temperature of rock mass in the vicinity of the canister at high-level radioactive repository (Kwon and Cho, 2009). Richter and Simmons (1974) reported that thermal cracking was observed on granite specimens when the heating rate exceeded 2°C/min. Lee (1993) also carried out a series of experiments at various heating rates to investigate the effect of thermal shock on Iksan granite in Korea and no damage on the specimen occurred when the heating rate was less than 3°C/min. Therefore, in this study, heating rate was controlled to be within the range of 2~3°C/min to heat up to 80°C. Heating was conducted at unconfined state and to prevent thermal gradient in the specimen, specimens were kept constant at the elevated temperature of 80°C for 60 minutes before the tests.

For each condition, 2~3 specimens were prepared. Table 3.2.1 shows the

testing conditions, the number of specimens at each condition and specimen identifications. The identifications of specimens were named to represent specimen information, and the meaning of each symbol is as below.

Rock type : A - Daejeon granite / D - Goheung diorite / LY - Linyi sandstone

Testing condition : M - room temperature / Dry surface.

HM - room temperature / Water pressure is applied.

TM - elevated temperature, 80°C / Dry surface.

THM - elevated temperature, 80°C / Water pressure is applied.

Serial number of specimens : from 1 to 6

For example, “D-HM-2” means the test was performed on the specimen of ‘diorite’ at ‘room temperature’ and ‘water pressure applied condition’, and the specimen was prepared ‘secondly’ for the described condition. And therefore, totally, 15 specimens for granite and 6 specimen each for diorite and sandstone were tested to investigate shear characteristics of saw-cut rock surfaces in multistage triaxial compression test.

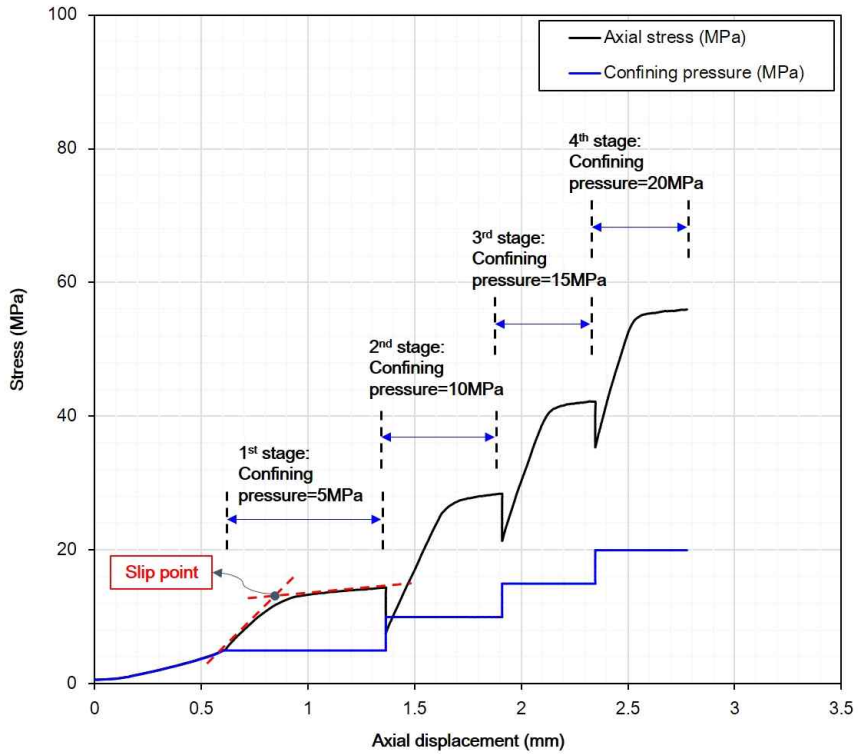


Fig. 3.2.3 Relation between axial stress, confining pressure and shear displacement of LY-M-1 and decision of slip point by using bilinear decay method.

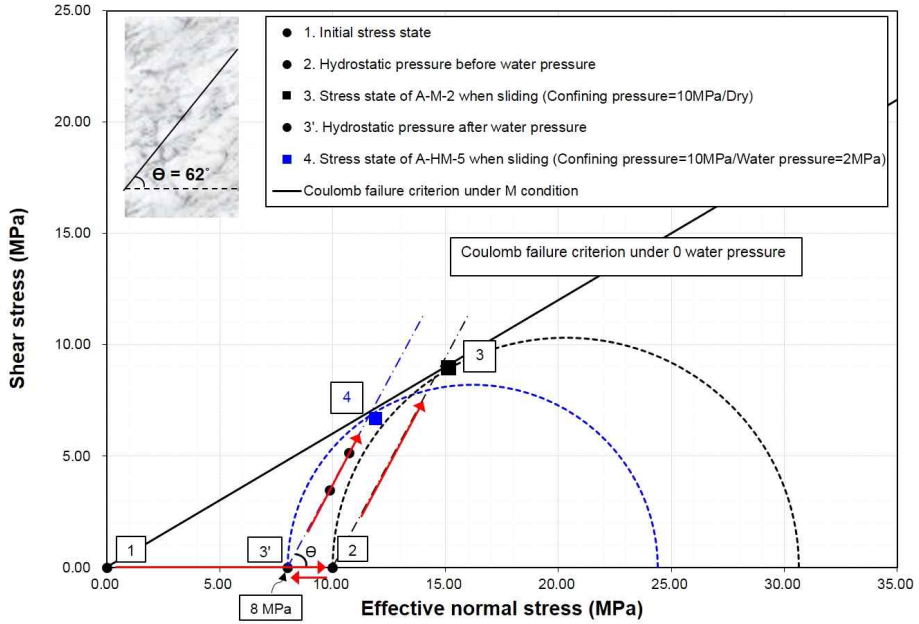


Fig. 3.2.4 Stress path of A-M-2 (confining pressure: 10 MPa/room temperature/Dry) and A-HM-5 (confining pressure: 10 MPa/room temperature/water pressure: 2 MPa). After target confining pressure (point 2), water pressure was applied (point 3').

Table 3.2.1 Number of specimens and specimen identifications (IDs).

Rock type	Temperature (°C)	Water pressure (MPa)	Confining pressure (MPa)	Number of specimens / Specimen IDs
Daejeon granite	20	0	5, 10, 15	2 / A-M-1~2
		0.1		2 / A-HM-1~2
		0.5		2 / A-HM-3~4
		2.0		2 / A-HM-5~6
	80	0		2 / A-TM-1~2
		0.1		3 / A-THM-1~3
		0.5		2 / A-THM-4~5
Goheung diorite	20	0	5, 10, 15, 20	2 / D-M-1~2
		1.0	6, 11, 16, 21	2 / D-HM-1~2
	80	0	5, 10, 15, 20	2 / D-TM-1~2
Linyi sandstone	20	0	5, 10, 15, 20	2 / LY-M-1~2
		1.0	6, 11, 16, 21	2 / LY-HM-1~2
	80	0	5, 10, 15, 20	2 / LY-TM-1~2
Cement-mortar (JRC=2.05)	20	0	0.5, 1, 2, 10, 15, 20	16 / S-M-1~16
		3	3.5, 4, 5, 10, 15, 20	12 / S-HM-1~12
	80	0	0.5, 1, 2, 10, 15, 20	9 / S-TM-1~9
Cement-mortar (JRC=11.63)	20	0	0.5, 1, 2, 10, 15, 20	12 / R-M-1~12
		3	3.5, 4, 5, 10, 15, 20	12 / R-HM-1~12
	80	0	0.5, 1, 2, 10, 15, 20	11 / R-TM-1~11

3.2.3 Testing method for cement-mortar specimens

In the case of the specimens including rough discontinuities, degradation and damage on asperities can occur as shear displacement increases as mentioned above. Thus, conventional triaxial compression test was conducted on cement-mortar specimens with various testing conditions. Firstly, axial load and confining pressure increased simultaneously up to the target stress

while maintaining hydrostatic pressure conditions. The confining pressure was kept constant after reaching the target pressure, and the axial load increased with constant axial displacement rate. Axial displacement rate was 0.4 mm/min, the same with the rate of the tests for saw-cut specimens. After peak axial stress, tests were continued until additional axial displacement of 1~1.5 mm increased additionally to observe post peak behavior.

Cement-mortar specimens have advantages on reproducibility, and thus the tests were performed under more various testing conditions compared with rock specimens. To investigate shear behavior at diverse normal stresses, confining pressures of 0.5, 1.0, 2.0, 10, 15 and 20 MPa were applied.

The syringe pump controlled water pressure to be constant and water pressure of 3 MPa was applied to consider the depth conditions. Confining pressures of 3.5, 4.0, 5.0, 10, 15 and 20 MPa were applied to prevent water leakage for water pressure applied tests.

For each condition, 2~4 specimens were prepared. The information of testing conditions, number of specimens at each condition and specimen identifications are summarized in Table 3.2.1. The information of identification of specimens was named in the same way of saw-cut specimens and the meaning of each symbol is as below.

Joint roughness : S - JRC = 2.05 / R - JRC = 11.63

Testing condition : M - room temperature / Dry surface.

HM - room temperature / Water pressure is applied.

TM - elevated temperature, 80°C / Dry surface.

Serial number of specimen : from 1 to 16

Therefore, for the specimens including smooth surfaces ($JRC=2.05$), 37 tests were carried out and 35 specimens having rough surfaces ($JRC=11.63$) were tested by using conventional triaxial compression tests to investigate shear characteristics of rock discontinuities under various testing conditions.

4. Experimental results

Test results were analyzed in a variety of ways including effective normal stress, peak shear stress, peak friction angle, normal and shear stiffness and dilation angle of discontinuities to investigate shear characteristics under each testing condition. First, normal stress (σ_n) and shear stress (τ) acting on discontinuities were calculated through equations (4.1) and (4.2):

$$\sigma_n = \frac{1}{2}[(\sigma_a + P_c) - (\sigma_a - P_c)\cos 2\theta] \quad (4.1)$$

$$\tau = \frac{1}{2}(\sigma_a - P_c)\sin 2\theta \quad (4.2)$$

where, σ_a is peak axial stress, P_c is confining pressure, P_p is water pressure on rock discontinuity and θ is 28° , the angle between core axis and rock discontinuity. When water pressure was acting on the discontinuity surface, the theory of effective stress should be applied, and equation (4.3) shows the relation:

$$\sigma_{neff} = \sigma_n - \alpha P_p \quad (4.3)$$

where, σ_{neff} is effective normal stress, α is biot coefficient, and P_p is water pressure acting on discontinuity surface. In this study, α was assumed as 1 and many previous researchers also reported that biot coefficient of rock discontinuity was equal to 1 (Barton and Choubey, 1977; Aydan et al.,

1995; Aydan, 1998). Then, to investigate peak friction coefficients of discontinuities under each testing condition, Mohr-Coulomb's failure criterion was used. In Mohr-Coulomb's equation, relation between effective normal stress and peak shear stress is expressed to have linear relation simply. Peak friction angles for each test were obtained by using linear regression method and apparent cohesion, c , was assumed as zero because discontinuities in this study were unweathered and clean.

However, according to Patton (1966b), in the case of rough discontinuities, shear stress increases non-linearly because of asperity degradation. Thus, for cement-mortar specimens, it was more reasonable to investigate the peak friction angles at low and high normal stresses separately considering asperity degradation. In this study, when the confining pressure was less than 2 MPa, effective stresses when slip occurred were in the range of 3.29 and 7.21 MPa (Table 4.4.1 and 4.5.1), and at higher confining pressure, effective normal stresses exceeded 17 MPa in the results of both rough specimens ($JRC=2.05$ and 11.63). Additionally, Barton (1973) and Handayan et al. (1990) reported that although discontinuities are in a state of shear, on the asperity scale, local tensile failures can be predominant. Therefore, considering the tensile strength of cement-mortar specimens (9.22 MPa, Table 3.1.1), transition normal stress between low and high normal stress was determined as 10 MPa.

In the case of cement-mortar specimens, peak shear stress was observed clearly when the specimen slipped along the discontinuity, but for saw-cut specimens, shear stress increased continuously even after slip occurred. If the discontinuity surface maintains flatness ideally even after slip occurred, shear stress will converge on a peak value. However, in realistic cases, as shear

displacement increases, shear surface is damaged, and due to the damage, shear stress shows a gradual increase (Engelder, 1992). This phenomenon is called as ‘slip-hardening’ and was also observed in the tests of saw-cut specimens. Therefore, it was difficult to decide where slip occurred and ‘Bilinear decay rate method’ was adopted to overcome this problem. Bilinear decay rate method was suggested by Tunbridge (1989) to decide shut-in pressure in hydrofracture tests, and if a graph consists of two straight line, their intersection is the shut-in pressure. An example of the decision of slip point through the intersection of two straight lines is shown in Fig. 3.2.3. Additionally, Park et al. (2007) and Lee (2011) carried out shear tests at constant normal stiffness condition, and the peak friction coefficients could be varied with the initial effective normal stress. In their studies, the peak friction coefficient was the coefficient of friction where maximum shear stress (τ_p) was obtained at each testing condition, and the peak friction coefficient of rough discontinuities could be dependent on initial effective normal stress but independent on normal stiffness variations at constant normal stiffness condition. That means peak friction angle obtained from Mohr-Coulomb’s failure criterion can change along with effective normal stress and therefore, the peak friction coefficients of rough discontinuities of cement-mortar specimens were investigated depending on initial effective normal stress in this study. In the case of saw-cut specimens, the peak friction coefficients were not varied with the change of normal stress because of flat surfaces.

Normal and shear displacement (Δu and Δv) of discontinuities were calculated through equation 4.9 and 4.10 (Goodman, 1992) and Fig. 4.1.1(a) shows a schematic longitudinal section diagram of the deformation of the

specimen with positive shear and normal direction.

$$\Delta u = \Delta z \cos\theta + \Delta x \sin\theta \quad (4.9)$$

$$\Delta v = -\Delta z \sin\theta + \Delta x \cos\theta \quad (4.10)$$

In the equations, Δz is axial displacement and Δx is lateral displacement of the specimen. Lateral displacement was converted from the length of radial expansion obtained from circumferential extensometer. During shear tests, radial expansion was assumed to arise only from the slip along discontinuities on the dip direction of the discontinuities. On the cross-section plane of the specimen in Fig. 4.1.1(b), half length of the radial expansion (blue line) was considered as lateral displacement in this study. From the results, dilation angle and normal and shear stiffness of rock discontinuities were also measured. Dilation angle was obtained from the graph of normal displacement versus shear displacement, and the results were compared with the results of an empirical model proposed by Barton and Choubey(1977) (equation 4.11). In this study, the test results of cement-mortar specimens were compared to the dilation angle (d_n) of rough discontinuities obtained from the equation (4.11).

$$d_n = \frac{12 JRC(\log_{10}(JCS/\sigma_n))^2}{JRC + 8.4 \log_{10}(JCS/\sigma_n)} \quad (4.11)$$

where, JRC is the joint roughness coefficient and JCS is joint wall compressive strength.

Normal and shear stiffness were determined based on the section where the slopes of the graphs of normal displacement versus normal stress and shear displacement versus shear stress are relatively linear before peak shear stress. In the whole tests, contraction on the discontinuity surfaces was observed with comparatively constant normal stiffness values before peak shear stress. Dilation started after slip occurred, and shear stiffness dropped drastically (Fig. 4.1.2(b)). Therefore, shear tests inside the triaxial compression chamber in this study were analogous to those under constant normal stiffness (CNS) conditions.

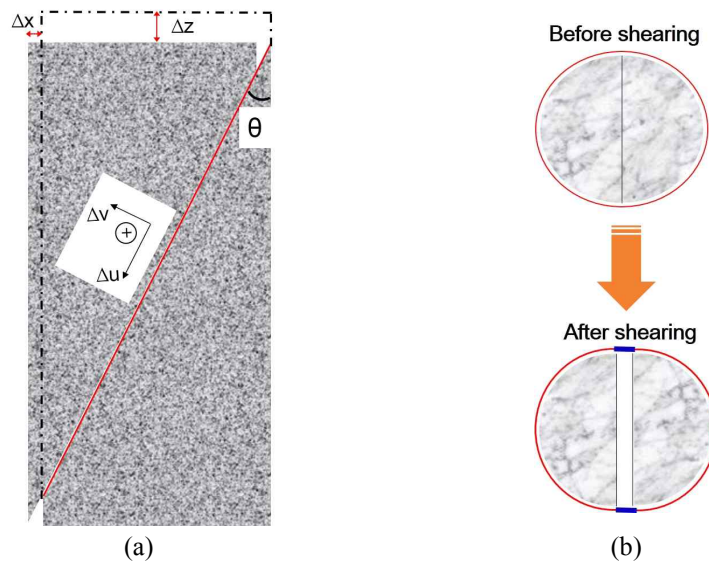
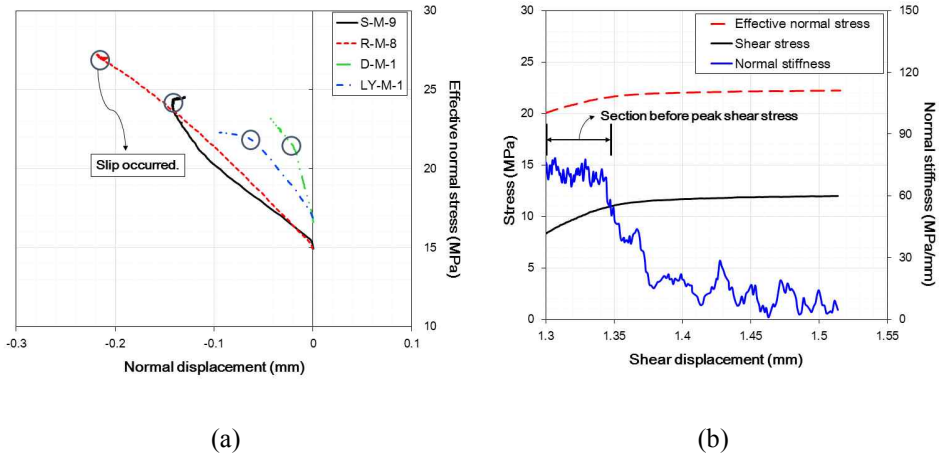


Fig. 4.1.1 Schematic diagram for calculation of normal and shear displacement on rock discontinuities: (a) a longitudinal section view of the specimen after slip with positive normal and shear direction and (b) a conceptual cross-section view before and after shearing (Red line is the length of initial circumference of the specimen and after shearing, blue line is the length of expansion induced by slip on the discontinuities.).



(a) (b)

Fig. 4.1.2 relation between stress and displacement: (a) curve of effective normal stress and normal displacement of S-M-9, R-M-8, D-M-1 and LY-M-1 specimens (confining pressure = 15 MPa / room temperature / Dry condition). Black circle shows where slip occurred. (b) graph of effective normal stress, shear stress and normal stiffness versus shear displacement of LY-M-1 specimen. Before peak shear stress, normal stiffness was within a relatively constant range.

4.1 Saw-cut Daejeon granite

4.1.1 Test results at room temperature and dry conditions

Rock powder and slickenside were observed on the saw-cut surfaces after the whole tests as a proof of shear behavior along the saw-cut surfaces (Fig. 4.1.3), and slip-hardening behavior was observed. At room temperature on dry condition, peak friction angle of granite saw-cut surfaces was 31.7° from linear regression method and the correlation coefficient of the line was 0.9879. Peak friction angle showed a similar value compared with basic friction angle of 30° obtained from tilt tests on flat dry surfaces. The whole test results at each testing condition were shown in Fig. 4.1.4, Fig. 4.1.5 and Table 4.1.1. Relations between shear stress, effective normal stress and shear displacement at each testing condition were shown separately in Appendix. Fig. 4.1.5 shows peak friction angle at each testing condition and Fig. 4.1.6 illustrates the relation between effective normal stress, shear stress and shear displacement at room temperature and dry condition. Effective normal stress increased gradually with the increase of shear displacement even after slip occurred along the discontinuity due to slip-hardening effect. To confirm the decrease of the slope, 0.5~1.0 mm of additional shear displacement increased after slip at each confining pressure stage (Fig. 4.1.6). When the confining pressure raised to next stage, axial displacement was held and thus, in some cases, shear stress and shear displacement decreased slightly due to the upthrust force by the increase of confining pressure.

Dilation did not occur on the saw-cut surfaces during sliding, but

variations of normal and shear stiffness of the discontinuities were investigated. As described above, shear tests inside the triaxial chamber in this study were analogous to the tests under constant normal stiffness condition. Therefore, relations between normal and shear stiffness and effective confining pressure were plotted together to investigate the effect of initial effective normal stress (Fig. 4.1.7), and effective confining pressure means the confining pressure which excludes water pressure. As initial effective confining pressure increased, initial effective normal stress on the saw-cut surfaces also increased and hence, effective confining pressure corresponded to initial effective normal stress. At room temperature on dry condition, normal and shear stiffness increased along with the increase of effective confining pressure which means the increase of initial effective normal stress.

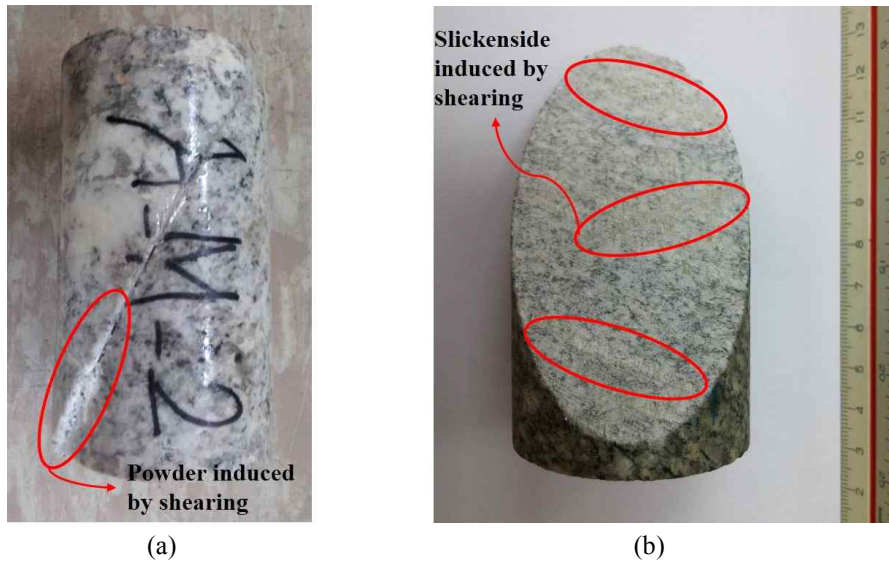


Fig. 4.1.3 A-M-2 specimen after the test (20°C / Dry surface): (a) powder induced by shearing on the saw-cut surface and (b) slickenside induced by shearing on the saw-cut surface.

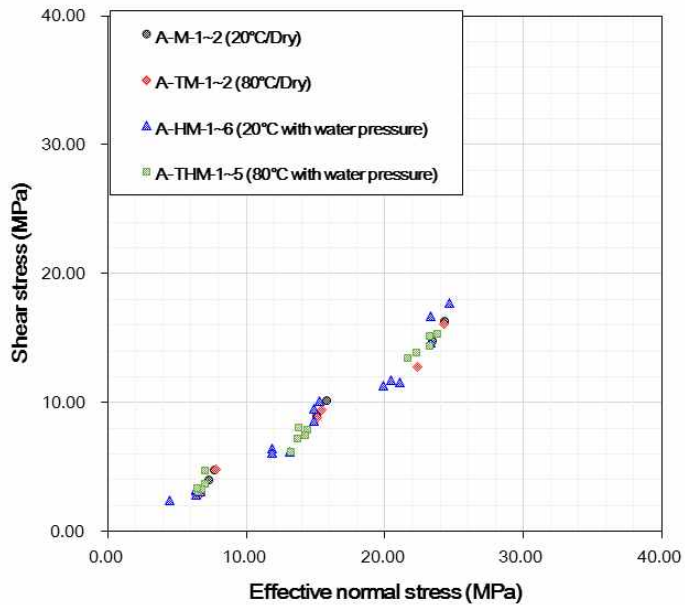


Fig. 4.1.4 Relation between shear stress and effective normal stress acting on Daejeon granite saw-cut surfaces on various testing conditions.

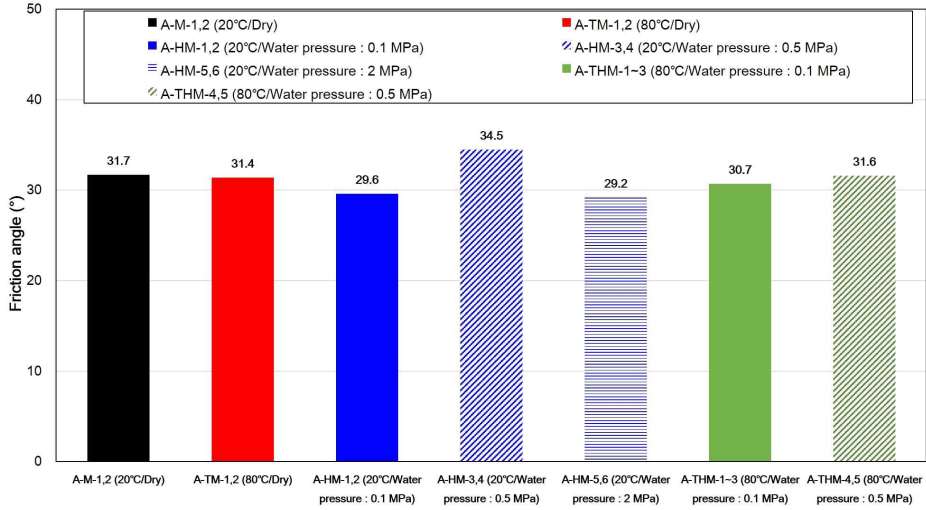


Fig. 4.1.5 Peak friction angles of Daejeon granite saw-cut surfaces on various testing conditions.

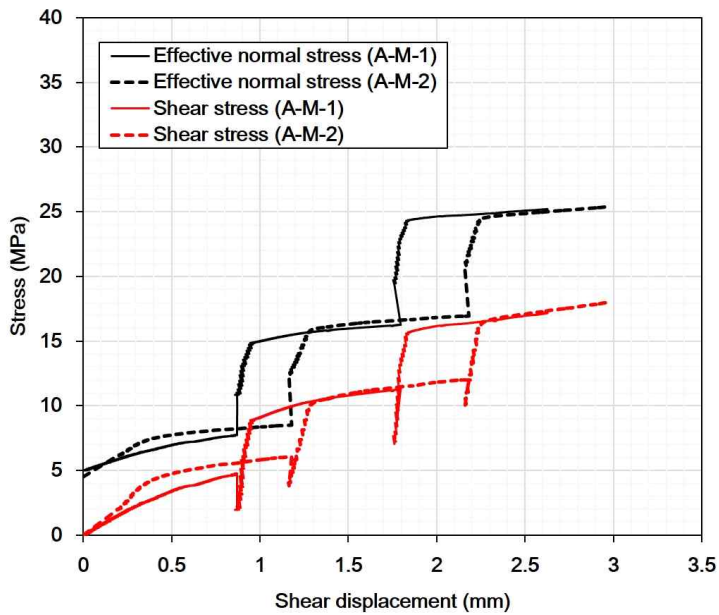
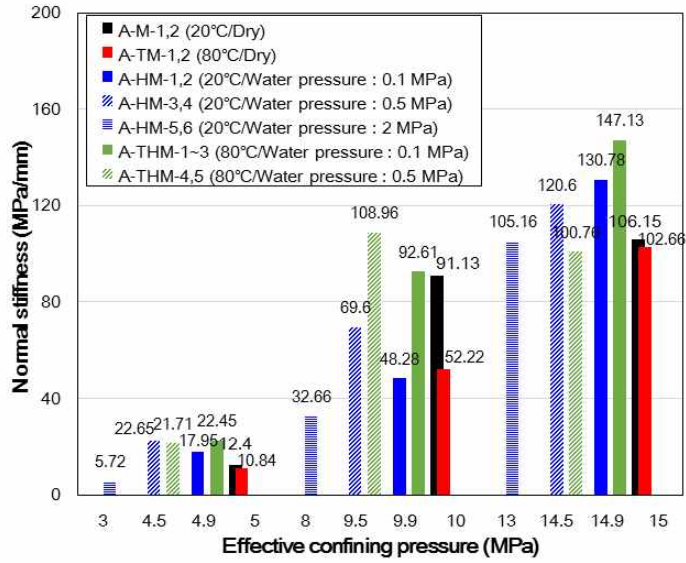
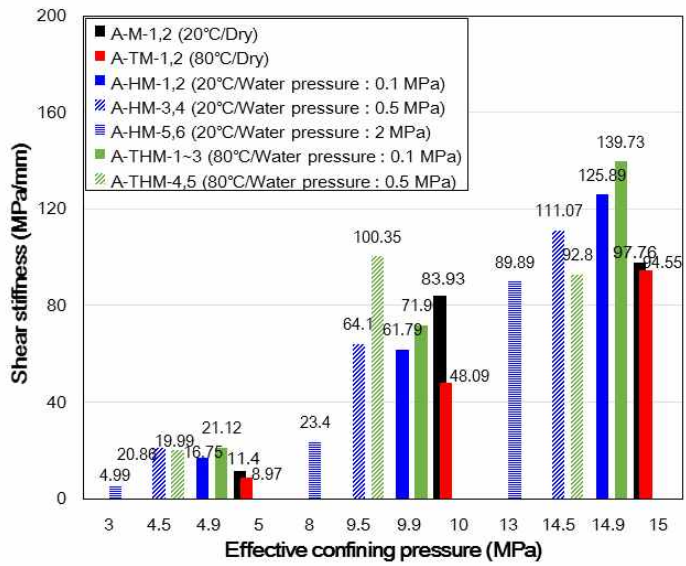


Fig. 4.1.6 Relation between effective normal stress, shear stress and shear displacement of A-M-1 and A-M-2 at room temperature on dry condition.



(a)



(b)

Fig. 4.1.7 Relation between normal, shear stiffness and initial effective confining pressure of Daejeon granite saw-cut surfaces on various testing conditions: (a) normal stiffness and (b) shear stiffness.

Table 4.1.1 Results of shear tests by using multistage triaxial compression test method on Daejeon granite saw-cut surfaces on various testing conditions.

Testing condition	Sample no.	Confining pressure (MPa)	Effective normal stress (MPa)	Peak shear stress (MPa)	Peak friction coefficient	Normal stiffness (MPa/mm)	Shear stiffness (MPa/mm)	Friction angle (°) (coefficient of friction)
M (20°C / Dry)	A-M-1	5	7.31	3.99	0.55	9.22	8.45	31.7 (0.6176)
		10	15.16	8.94	0.59	113.05	104.12	
		15	23.50	14.77	0.63	112.22	103.35	
	A-M-2	5	7.73	4.73	0.61	15.58	14.35	
		10	15.82	10.08	0.64	69.2	63.73	
		15	24.38	16.24	0.67	100.07	92.16	
TM (80°C / Dry)	A-TM-1	5	7.77	4.79	0.62	13.27	10.19	31.4 (0.6094)
		10	15.11	8.85	0.59	27.9	25.69	
		15	22.39	12.80	0.57	102.51	94.41	
	A-TM-2	5	6.71	2.97	0.44	8.4	7.74	
		10	15.45	9.44	0.61	76.54	70.49	
		15	24.28	16.07	0.66	102.8	94.68	
HM (20°C / water pressure: 0.1 MPa)	A-HM-1	5	6.41	2.84	0.44	5.44	5.44	29.6 (0.5670)
		10	13.17	6.15	0.47	5.75	39.96	
		15	21.07	11.60	0.55	137.88	137.88	
	A-HM-2	5	6.68	3.09	0.46	30.46	28.05	
		10	14.85	8.57	0.58	90.8	83.62	
		15	23.34	14.61	0.63	123.68	113.9	
HM (20°C / water pressure: 0.5 MPa)	A-HM-3	5	6.34	3.18	0.50	25.29	23.29	34.5 (0.6880)
		10	15.32	10.08	0.66	70.24	64.69	
		15	24.71	17.68	0.72	119.8	110.33	
	A-HM-4	5	6.40	3.29	0.51	20	18.42	
		10	14.85	9.52	0.64	68.96	63.51	
		15	23.34	16.70	0.72	121.4	111.8	

Table 4.1.1 Continued.

Testing condition	Sample no.	Confining pressure (MPa)	Effective normal stress (MPa)	Peak shear stress (MPa)	Peak friction coefficient	Normal stiffness (MPa/mm)	Shear stiffness (MPa/mm)	Friction angle (°) (coefficient of friction)
HM (20°C / water pressure: 2.0 MPa)	A-HM-5	5	4.47	2.42	0.54	5.72	4.99	29.2 (0.5586)
		10	11.90	6.39	0.54	33.83	29.51	
		15	19.90	11.32	0.57	109.76	95.76	
	A-HM-6	-	-	-	-	-	-	
		10	11.86	6.06	0.51	31.48	17.28	
		15	20.46	11.72	0.57	100.55	84.01	
THM (80°C / water pressure: 0.1 MPa)	A-THM-1	5	7.03	3.68	0.52	26.84	24.72	30.7 (0.5936)
		10	14.44	7.86	0.54	86.41	29.58	
		15	23.22	14.40	0.62	142.71	131.43	
	A-THM-2	5	6.56	3.11	0.47	16.79	16.79	
		10	13.20	6.20	0.47	126.88	126.88	
		15	22.28	13.87	0.62	160.37	160.37	
	A-THM-3	5	6.81	3.30	0.48	23.72	21.84	
		10	14.23	7.50	0.53	64.53	59.42	
		15	23.78	15.37	0.65	138.32	127.39	
THM (80°C / water pressure: 0.5 MPa)	A-THM-4	5	7.00	4.71	0.67	29.51	27.17	31.6 (0.6149)
		10	13.81	8.10	0.59	129.08	118.88	
		15	21.66	13.46	0.62	78.9	72.67	
	A-THM-5	5	6.42	3.32	0.52	13.9	12.8	
		10	13.68	7.24	0.53	88.84	81.81	
		15	23.24	15.13	0.65	122.62	112.93	

4.1.2 Test results at 80°C

Peak friction angle at an elevated temperature of 80°C was 31.4° and correlation coefficient for linear regression line was 0.9685. Peak friction angle showed little change compared to the friction angle at room temperature. Effective normal stress and peak shear stress were also showed similar values compared with previous results. Stesky et al. (1974) carried out shear tests in a triaxial chamber, and the peak friction angle of Westerly granite saw-cut surfaces did not change less than 300°C. The effect of temperature increase on friction angle of KURT granite saw-cut surfaces in this study also showed same results.

Normal and shear stiffness increased with the increase of initial effective normal stress but showed little variation with increasing temperature (Fig. 4.1.7 and Table 4.1.1). Fig. 4.1.8 shows an example of relations between effective normal stress, shear stress and shear displacement of A-M-2 at room temperature and A-TM-2 at 80°C. The amount of stress increase due to slip hardening were similar, but at elevated temperature, stick-slip behavior was observed. Stesky (1978) reported that stick-slip is enhanced by high normal stresses, by low temperatures, by the presence of strong, brittle minerals, by the absence of gouge, and by lower surface roughness. In the case of Westerly granite saw-cut surfaces, stick-slip behavior was observed below than 265°C and 300 MPa (Stesky et al., 1974). On A-TM-2 specimen, at the first stage of confining pressure, stick-slip behavior was observed clearly, and the testing condition of A-TM-2 specimen corresponded to the condition as referred above.

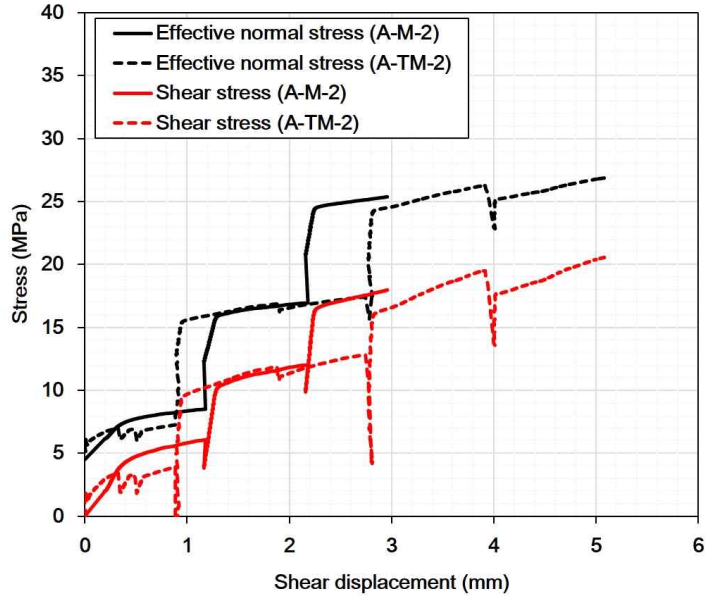


Fig. 4.1.8 Relation between effective normal stress, shear stress and shear displacement of A-M-2 (20°C / Dry) and A-TM-2 (80°C / dry condition).

4.1.3 Test results at room temperature with water pressure

Water pressures of 0.1, 0.5 and 2.0 MPa were applied on the saw-cut surfaces of A-HM-1~6 specimens at room temperature. Peak friction angles on each water pressure applied condition were 29.6°, 34.5° and 29.2° and correlation coefficients of each linear regression curve were higher than 0.95. When water pressure was 0.1 and 2.0 MPa, peak friction angle showed a slight decrease by 2.1° and 2.5° (Fig. 4.1.5). Although massive crystalline minerals including quartz and feldspar were observed, layer lattice minerals such as muscovite, biotite and chlorite were also included in the specimens, and the total weight amount was 13.8% (Table 3.1.2). Therefore, lubrication effect of water induced by minerals might have an effect on the granite saw-cut specimens in this study. Additionally, saw-cut surfaces

without polishing are not ideally flat and micro roughness also might affect the decrease of friction angle. Coulson (1972) investigated the shear strength depending on surface roughness and reported that the shear strength of rough surfaces are smaller than that of smooth surfaces when the surfaces were wet. The applied water pressure reduced normal stress following effective stress law, and as a result, shear stress also showed a decrease.

Fig. 4.1.9 shows a relation between effective normal stress, shear stress and shear displacement of A-HM-2, 4 and 5 (20°C / water pressure: 0.1, 0.5, 2.0 MPa). In A-M-4, 5 and 6 specimens, stick-slip behavior was observed, and Mehrishal et al. (2016) also reported that stick-slip behavior appeared on moist ground surfaces during shear tests for marble and travertine under constant normal load condition. Normal and shear stiffness increased along with the increase of confining pressure (Fig. 4.1.7), but the effect of water on saw-cut surfaces was not clear. In the case of A-HM-5 and 6 specimens (room temperature, water pressure: 2 MPa), normal and shear stiffness showed smaller values compared with other cases and the reason is that initial effective normal stress on saw-cut surfaces was lower due to the water pressure of 2 MPa.

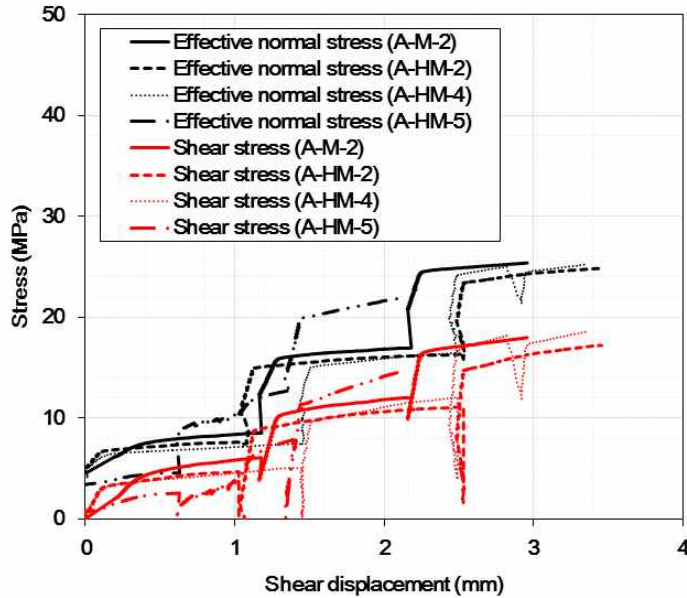


Fig. 4.1.9 Relation between effective normal stress, shear stress and shear displacement of A-M-2 (20°C / Dry) and A-HM-2, 4 and 5 (20°C / water pressure: 0.1, 0.5, 2.0 MPa).

4.1.4 Test results at 80°C with water pressure

In this study, water pressures of 0.1 and 0.5 MPa were applied on the saw-cut surfaces at 80°C. Peak friction angles were 30.7° and 31.6° at each condition and compared with A-M-1 and 2, peak friction angle did not show much variation. Stesky et al. (1974) performed a series of shear tests using faulted Westerly granites with different temperature and water pressure conditions. In his results, friction coefficients of Westerly granite little affected by water pressure up to 265°C. Therefore, the results of Daejeon granite in this study showed the same tendency compared with previous studies.

Normal and shear stiffness increased with the increase of initial effective

normal stress but did not show much variation upon elevated temperature and presence of water pressure in this study. The effect of different water pressure was not also clear (Fig. 4.1.7), and stick-slip behavior was not observed at this testing condition.

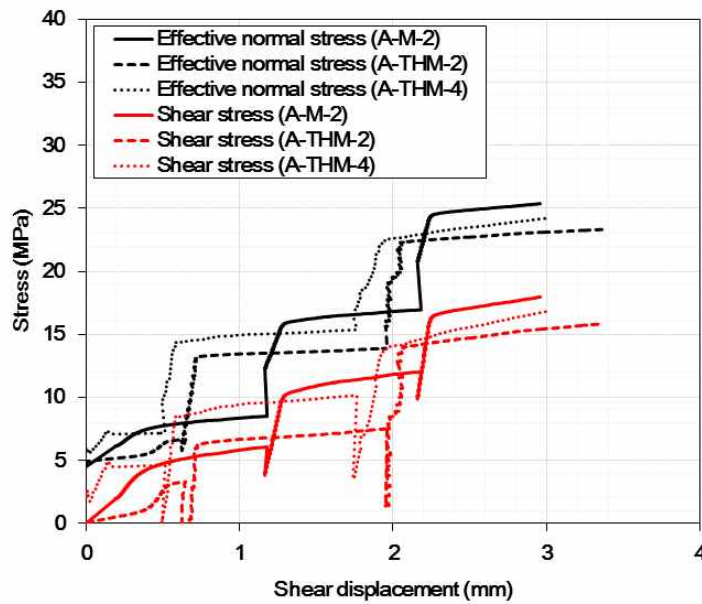


Fig. 4.1.10 Relation between effective normal stress, shear stress and shear displacement of A-M-2 (20°C / Dry) and A-THM-2 and 4 (80°C / water pressure: 0.1, 0.5 MPa).

4.2 Saw-cut Goheung diorite

4.2.1 Test results at room temperature and dry conditions

Rock powder and slickenside were observed clearly after the tests along the shear direction on the saw-cut surfaces (Fig. 4.2.1), and slip-hardening behavior was also observed (Fig. 4.2.4). Peak friction angle of diorite saw-cut surfaces at room temperature on dry condition was 27.1° (Fig. 4.2.3). Peak friction angle of diorite was a little smaller than that of Daejeon granite and Fig. 4.2.2 shows the relation between effective normal stress and shear stress of Goheung diorite saw-cut surfaces under various testing conditions.

Normal and shear stiffness were investigated, and they increased with the increase of confining pressure (Fig. 4.2.5). The increasing tendency was similar to that of granite saw-cut surfaces. However, normal and shear stiffness values were much higher than those of granite saw-cut surfaces, and the amount was in the range of 30~40%. The reason for the higher values might be related with greater Young's modulus of the diorite (Table 3.1.1). Young's modulus is known to increase with the increase of confining pressure in a triaxial compression condition (Lee, 1993). However, friction angle and shear stress are lower than the results of granite at the same confining pressure. It means that friction of the discontinuities is not always proportional to the elastic properties of the discontinuities such as stiffness and Young's modulus.



Fig. 4.2.1 Slickenside along the shear direction on the saw-cut surface of Goheung diorite: (a) D-M-2 specimen (room temperature/dry condition) and (b) D-HM-2 specimen (room temperature/water pressure: 1 MPa).

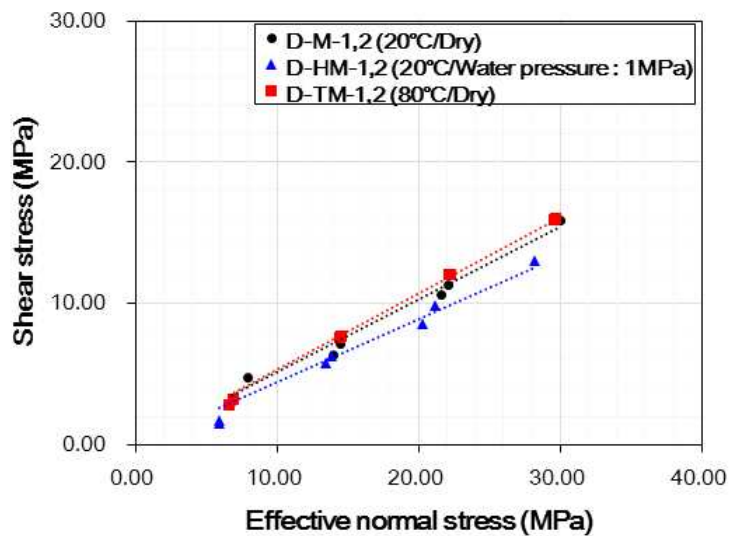


Fig. 4.2.2 Relation between shear stress and effective normal stress acting on Goheung diorite saw-cut surfaces on various testing conditions and linear regression line for peak friction angle.

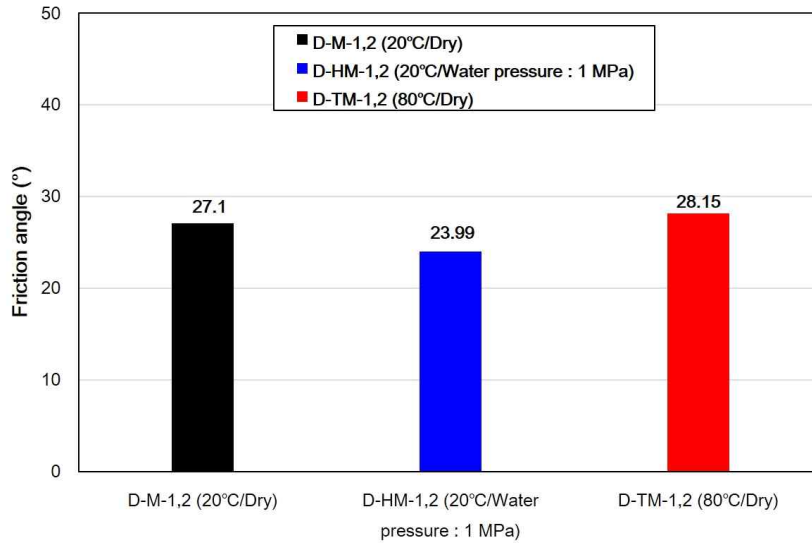


Fig. 4.2.3 Peak friction angles of Goheung diorite saw-cut surfaces on various testing conditions.

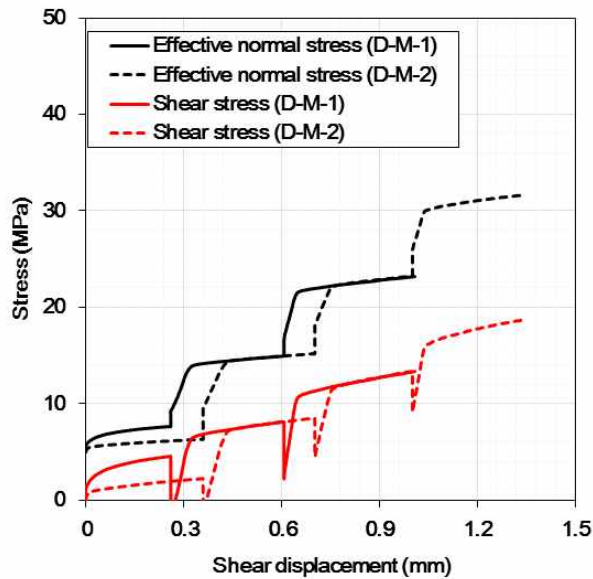
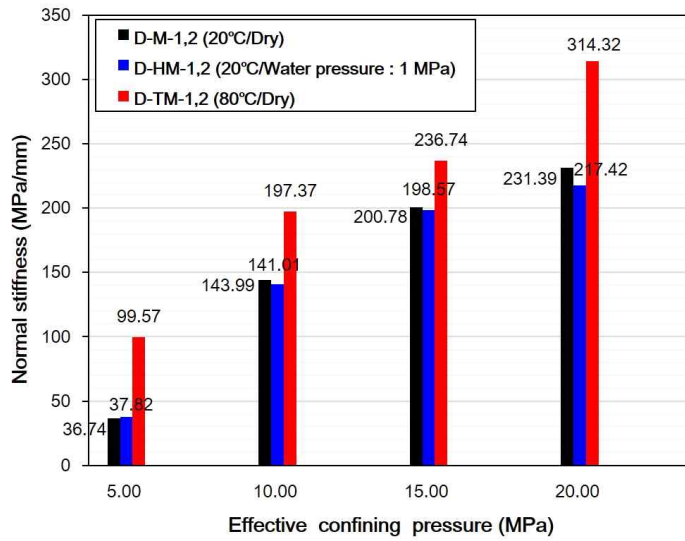
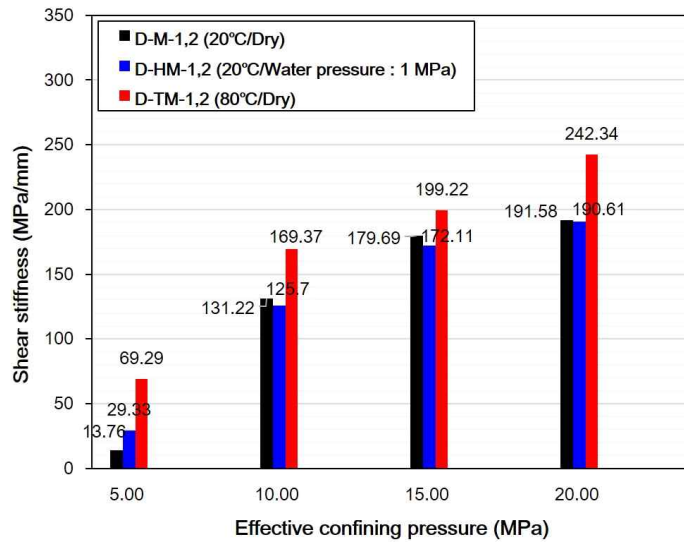


Fig. 4.2.4 Relation between effective normal stress, shear stress and shear displacement of D-M-1 and D-M-2 at room temperature on dry saw-cut surfaces.



(a)



(b)

Fig. 4.2.5 Relation between normal, shear stiffness and initial effective confining pressure of Goheung diorite saw-cut surfaces on various testing conditions: (a) normal stiffness and (b) shear stiffness.

Table 4.2.1 Results of shear tests by using multistage triaxial compression test method on Goheung diorite saw-cut surfaces on various testing conditions.

Testing condition	Sample no.	Confining pressure (MPa)	Effective normal stress (MPa)	Peak shear stress (MPa)	Peak friction coefficient	Normal stiffness (MPa/mm)	Shear stiffness (MPa/mm)	Friction angle (°) (coefficient of friction)
M (20°C / Dry)	D-M-1	5	6.78	3.07	0.45	34.68	24.84	27.1 (0.5118)
		10	13.90	6.41	0.46	143.25	133.85	
		15	21.54	10.66	0.49	241.89	217.30	
	D-M-2	5	7.87	4.80	0.61	38.79	2.67	
		10	14.39	7.16	0.50	144.73	128.59	
		15	22.07	11.33	0.51	159.67	142.08	
		20	30.02	15.92	0.53	231.39	191.58	
TM (80°C / Dry)	D-TM-1	5	6.87	3.23	0.47	92.84	76.08	28.2 (0.5350)
		10	14.58	7.71	0.53	148.99	132.67	
		15	22.22	12.03	0.54	193.38	168.20	
		20	29.72	16.05	0.54	272.60	209.64	
	D-TM-2	5	6.60	2.75	0.42	106.31	62.51	
		10	14.46	7.54	0.52	245.75	206.07	
		15	22.17	11.98	0.54	280.11	230.23	
		20	29.57	15.89	0.54	356.04	275.04	
HM (20°C / water pressure: 1.0 MPa)	D-HM-1	6	5.97	1.72	0.29	28.54	20.90	24.0 (0.4451)
		11	13.49	5.79	0.43	120.78	109.14	
		16	20.25	8.59	0.42	230.37	196.69	
	D-HM-2	6	5.89	1.54	0.26	47.10	37.77	
		11	13.85	6.27	0.45	161.24	142.26	
		16	21.15	9.86	0.47	166.78	147.53	
		21	28.18	12.99	0.46	217.42	190.61	

4.2.2 Test results at 80°C

Peak friction angle at 80°C and dry condition was 28.2° with a high correlation but did not show much variation (Fig. 4.2.3) compared to the peak friction angle at room temperature. Unlike granite saw-cut surfaces, stick-slip behavior was not observed (Fig. 4.2.6), and effective normal and shear stress when slip occurred did not vary much with temperature increase (Fig. 4.2.2 and Table 4.1.1).

Normal and shear stiffness were investigated and showed the same increasing tendency depending on confining pressure compared to the results at room temperature on dry saw-cut surfaces. Normal and shear stiffness at 80°C increased by 10.9~37.1% compared to the results at room temperature under each confining pressure, and normal stiffness showed a little higher value than shear stiffness (Fig. 4.2.5 and Table 4.1.1). Generally, when temperature increases, elastic properties including uniaxial compressive strength and Young's modulus were reduced due to thermal cracking of minerals (Lee, 1993; Araujo et al., 1997; Dwivedi et al., 2008). However, Wai and Lo (1982) carried out a series of laboratory tests to investigate the effect of temperature on strength and deformation of rocks up to 250°C, and for granitic gneiss, the deformation modulus increased slightly up to 120°C. Homand-Etienne and Houpert (1989) also reported that Young's modulus of Remiremont granite specimens increased by 3~4% until 200°C. Youn and Lee (1996) performed uniaxial compression tests for Pocheon granite specimens at various temperature conditions until 600°C and observed that Young's modulus showed a slight increase up to 200°C. They reported that this might be due to the closure of pore due to thermal loading. The

increase of normal and shear stiffness in this study might occur due to the same reason.

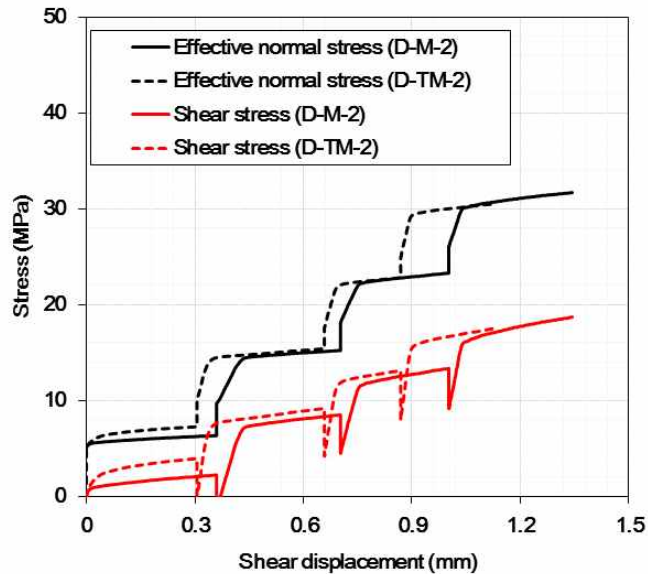


Fig. 4.2.6 Relation between effective normal stress, shear stress and shear displacement of D-M-2 at room temperature and D-TM-2 at 80°C on dry saw-cut surfaces.

4.2.3 Test results at room temperature with water pressure

When water pressure of 1 MPa was applied on saw-cut diorite specimens, peak friction angle was 24.0° (correlation coefficient: 0.9745) and decreased by 3.1°. Effective normal stress and peak shear stress when slip occurred also decreased compared to the results on dry conditions and stick-slip behavior was not observed (Fig. 4.2.7). In the XRD test results of Goheung diorite (Table 3.1.2), layer lattice minerals including montmorillonite (4.4%), talc (3.7%), biotite (3.2%) and chlorite (1.7%) were

detected, and these minerals might affect the decrease of the peak friction angle. For further analysis, scanning electron microscope (SEM) was used to observe the saw-cut surface after experiments and the results will be introduced in chapter 4.6. Additionally, micro roughness of saw cut surfaces also might affect the decrease of friction angle when the surfaces were wet.

Compared to the stiffness of dry surfaces, normal stiffness showed a slight decrease by 1.1~6.0% at each confining pressure, but the amount of decrease was negligible (Fig. 4.2.5). Shear stiffness also showed same tendency and the decreasing amount was in the range of 0.5~4.2%. Thus, normal and shear stiffness was not influenced by water unlike the peak friction angle within the range of the water pressure in this study.

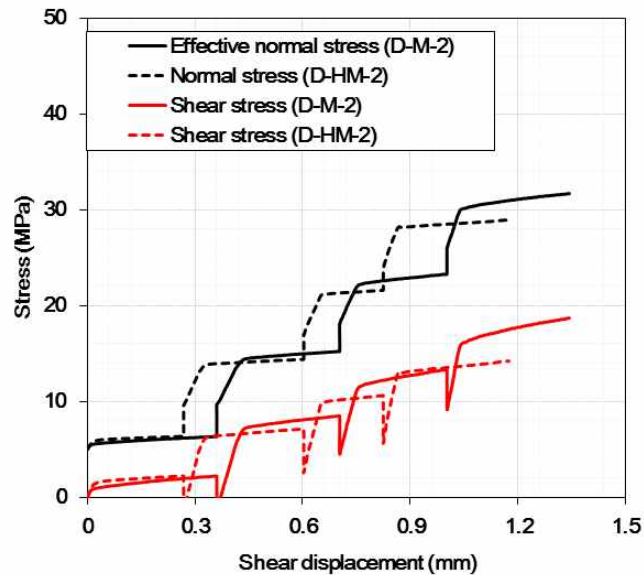


Fig. 4.2.7 Relation between effective normal stress, shear stress and shear displacement of D-M-2 (room temperature, dry condition) and D-HM-2 (room temperature, water pressure: 1.0 MPa).

4.3 Saw-cut Linyi sandstone

4.3.1 Test results at room temperature and dry conditions

Peak friction angle of Linyi sandstone saw-cut surfaces was 28.2° having a high correlation coefficient of 0.9936 (Fig. 4.3.2). Rock powder induced by shearing and slickenside were clearly seen on the saw-cut surfaces along shear direction after the tests. Fig. 4.3.3 shows the peak friction angle with testing conditions and Table 4.3.1 provides test results of Linyi sandstone saw-cut surfaces. Slip-hardening behavior was also observed, but the degree of hardening was not so significant compared to the results of other rocks (Fig. 4.3.4). Thus, it can be considered rock powder of sandstone is much softer than that of other rocks.

Normal and shear stiffness increased with the increase of confining pressure (Fig. 4.3.5) at room temperature on dry condition, and the tendency is similar to that of other rocks. However, the normal and shear stiffness of saw-cut surfaces of Linyi sandstone was lower than those of other rocks. For instance, at the confining pressure of 15 MPa and room temperature, average shear stiffness was 68.07 MPa/mm for Linyi sandstone (Fig. 4.3.5), 176.69 MPa/mm for Goheung diorite (Fig. 4.2.5) and 106.15 MPa/mm for Daejeon granite (Fig. 4.1.7). This also might be caused by the difference of Young's modulus as explained above and normal stiffness showed higher values than shear stiffness from the whole tests in this study.



Fig. 4.3.1 Saw-cut surface of Linyi sandstone specimen (LY-M-1): (a) before shearing and (b) after shearing. Slickenside were observed over the whole saw-cut surface along the shear direction.

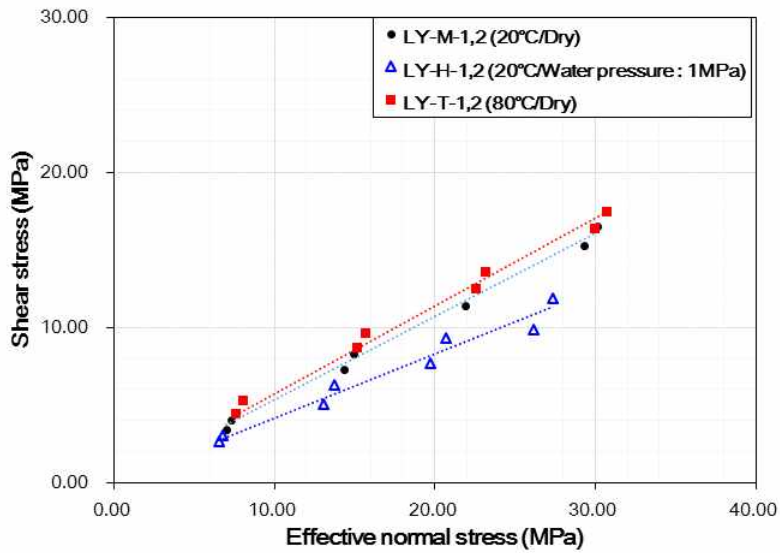


Fig. 4.3.2 Relation between shear stress and effective normal stress acting on Linyi sandstone saw-cut surfaces on various testing conditions and linear regression line for peak friction angle.

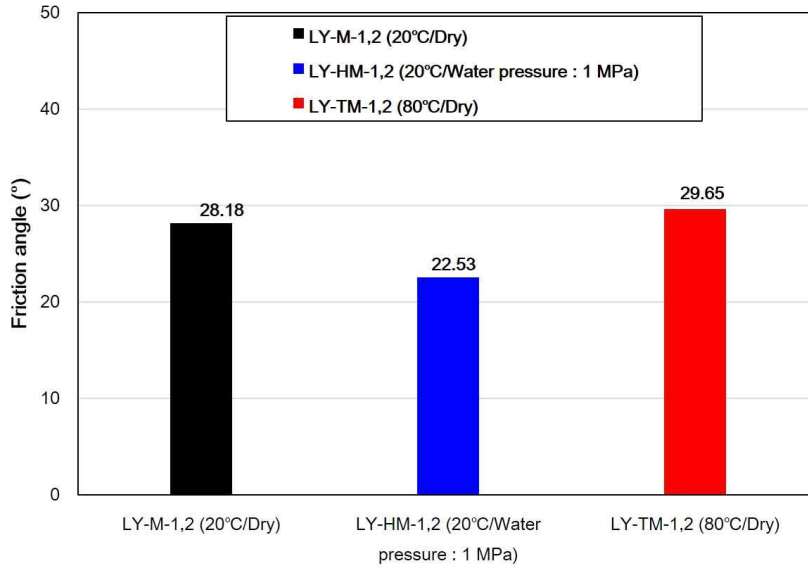
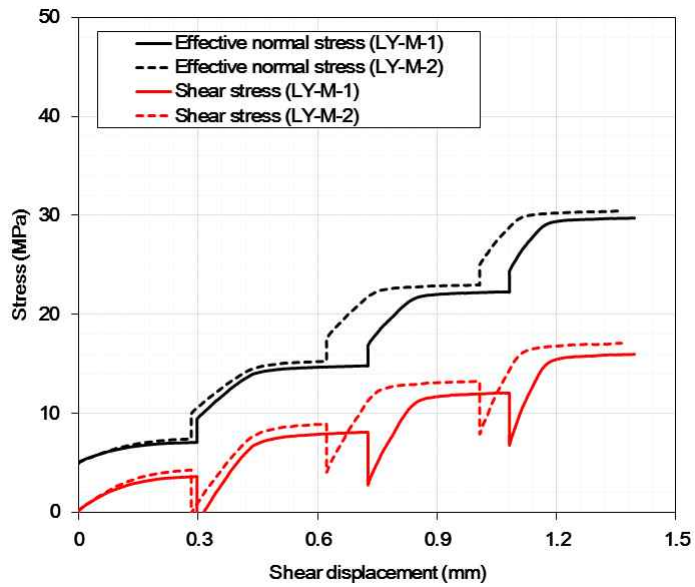
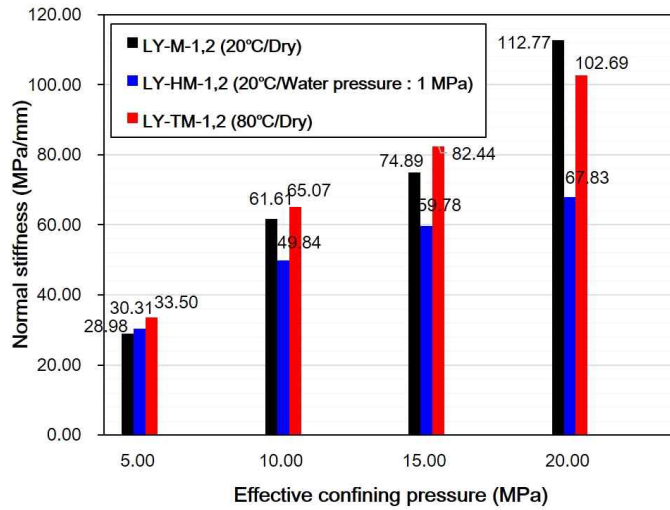
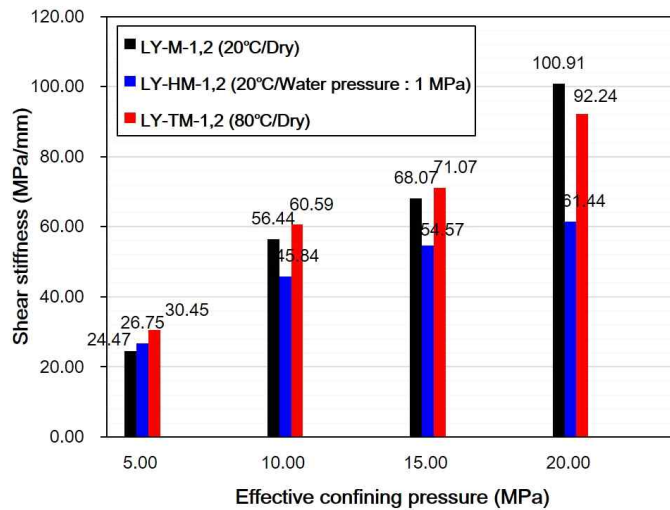


Fig. 4.3.3 Peak friction angles of Linyi sandstone saw-cut surfaces on various testing conditions.





(a)



(b)

Fig. 4.3.5 Relation between normal, shear stiffness and initial effective confining pressure of Linyi sandstone saw-cut surfaces on various testing conditions: (a) normal stiffness and (b) shear stiffness.

Table 4.3.1 Results of shear tests by using multistage triaxial compression test method on Linyi sandstone saw-cut surfaces on various testing conditions.

Testing condition	Sample no.	Confining pressure (MPa)	Effective normal stress (MPa)	Peak shear stress (MPa)	Peak friction coefficient	Normal stiffness (MPa/mm)	Shear stiffness (MPa/mm)	Friction angle (°) (coefficient of friction)
M (20°C / Dry)	LY-M-1	5	6.99	3.42	0.49	28.44	22.67	28.2 (0.5358)
		10	14.35	7.30	0.51	64.32	59.36	
		15	21.87	11.38	0.52	74.19	68.27	
	LY-M-2	15	29.32	15.26	0.52	118.22	107.46	
		5	7.34	4.02	0.55	29.53	26.27	
		10	14.90	8.27	0.56	58.89	53.53	
		15	22.56	12.55	0.56	75.58	67.87	
TM (80°C / Dry)	LY-TM-1	20	30.08	16.56	0.55	107.32	94.37	29.7 (0.5692)
		5	8.07	5.30	0.66	33.65	30.70	
		10	15.69	9.60	0.61	60.48	56.91	
		15	23.18	13.57	0.59	73.98	66.56	
	LY-TM-2	20	30.69	17.49	0.57	91.97	83.59	
		5	7.59	4.45	0.59	33.34	30.21	
		10	15.17	8.72	0.57	69.66	64.27	
HM (20°C / water pressure: 1.0 MPa)	LY-HM-1	15	22.54	12.53	0.56	90.90	75.58	22.5 (0.4148)
		20	29.97	16.35	0.55	113.42	100.89	
		6	6.53	2.62	0.40	26.77	23.53	
		11	13.06	5.08	0.39	45.22	42.44	
	LY-HM-2	16	19.71	7.66	0.39	48.72	46.08	
		21	26.17	9.87	0.38	59.45	56.10	
		6	6.79	3.07	0.45	33.85	29.96	
LY-HM-2	11	13.76	6.30	0.46	54.46	49.25		
	16	20.68	9.34	0.45	70.84	63.06		
		21	27.36	11.91	0.44	76.21	66.77	

4.3.2 Test results at 80°C

Peak friction angle at 80°C on dry condition was 29.7° with a high correlation coefficient of 0.9895 and showed a slight increase (Fig. 4.3.3) at elevated temperature condition. Stick-slip behavior and slip hardening were not observed during the tests (Fig. 4.3.6). The results showed the same tendency with the results of Lockner et al (1982). Peak shear stress and effective normal stress also did not vary with increasing temperature (Fig. 4.3.2) in this study and hence, the temperature of 80°C did not affect peak friction angle of Linyi sandstone saw-cut surfaces. Normal and shear stiffness increased with the increase of confining pressure but did not show much change compared to the results at room temperature.

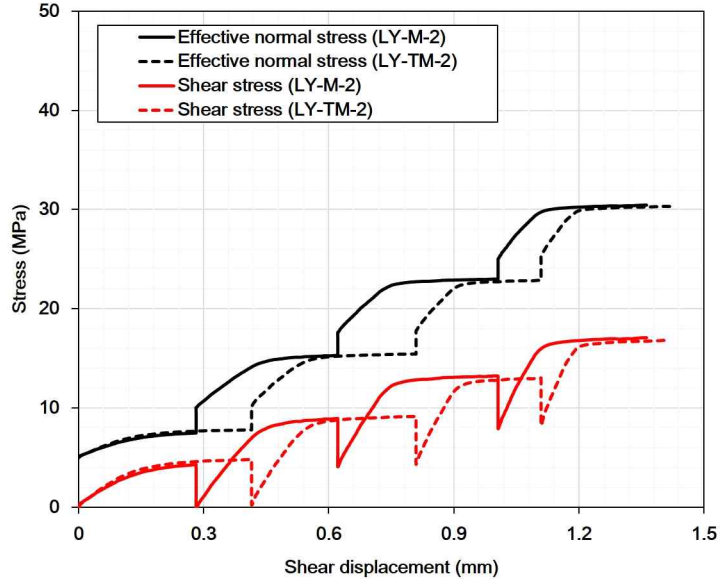


Fig. 4.3.6 Relation between effective normal stress, shear stress and shear displacement of LY-M-2 at room temperature and LY-TM-2 at 80°C on dry saw-cut surfaces.

4.3.3 Test results at room temperature with water pressure

When water pressure of 1 MPa was applied on the saw-cut surfaces, peak friction angle of Linyi sandstone was 22.5° and decreased by 5.7° than the peak friction angle obtained at room temperature on dry surfaces. In XRD analyses (Table 3.1.2), laumontite was included in layer lattice minerals, but the weight ratio is only 3.5%. Although calcite (1.7%) has massive crystal structure, Ulusay and Karakul (2015) reported that basic friction angle of limestone, composed of calcite, decreased when wet and submerged conditions. Therefore, the presence of laumontite and calcite could affect the decrease of peak friction angle. Additionally, after the tests, much fine powder was observed on the saw-cut surfaces compared to the surfaces of the other tests. For further analysis, SEM observation was performed for the saw-cut surfaces, and the results will be introduced in chapter 4.6.

Normal and shear stiffness also decreased when water pressure was applied on the saw-cut surfaces of Linyi sandstone (Fig. 4.3.5). At all confining pressures, the amount of decrease of normal stiffness was in the range of 19.1~39.9% and for shear stiffness, 18.8~39.1% compared to those in dry condition. As confining pressure increased, the difference in stiffness between dry and water pressure applied condition showed increasing tendency. In common with other test results of Linyi sandstone saw-cut surfaces, stick-slip behavior was not observed, but slight slip hardening behavior was observed during shearing when water pressure was applied.

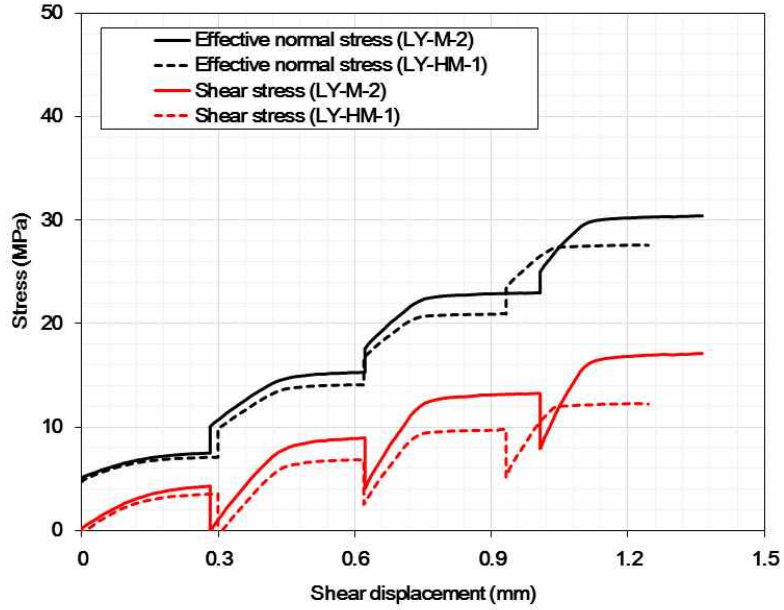


Fig. 4.3.7 Relation between effective normal stress, shear stress and shear displacement of LY-M-2 (at room temperature/dry condition) and LY-HM-1 (at room temperature/water pressure: 1.0 MPa).

4.4 Cement-mortar including a smooth discontinuity

4.4.1 Test results at room temperature and dry conditions

To investigate the effect of roughness, cement-mortar specimens which had two different rough discontinuities were produced, and joint roughness was measured by the method proposed by Tse and Cruden (1979) as explained above. Fig. 4.4.1 shows the rough surface of the S-M-10 specimen before and after the shear test at room temperature and 10 MPa of confining pressure on dry condition. After the test, rock powder and slickenside were observed along the shearing direction on the surface, especially on the asperity part. The results for smooth discontinuities (JRC=2.05) of cement-mortar specimens are shown in Table 4.4.1 and Fig. 4.4.2. Peak friction angle obtained from linear regression line at the total normal stress was 35.0° , which is almost analogous to 34.4° obtained from tilt tests and this might be due to low JRC value (Fig. 4.4.2). At the normal stress less than 10 MPa, peak friction angle was 48.3° , and at high normal stress over 10 MPa, 28.3° (Fig. 4.4.3). This non-linearity of shear behavior can be more clearly seen in the relationship between the peak friction coefficient and the initial effective normal stress (Fig. 4.4.4) which was equivalent to confining pressure. As the initial effective normal stress increased, the peak friction coefficients decreased. However, when the initial effective normal stress exceeded 10 MPa, the coefficients did not show much variation within the range of 0.65~0.80 which is analogous to basic friction angle of 34.4° (friction coefficient: 0.68). That means at low normal stresses asperities play a major role in shear behavior, but after the failure

of asperities, the effect of basic friction angle is dominant on shearing.

Fig. 4.4.5 shows the relation between normal and shear stiffness and initial effective normal stress, and normal and shear stiffness increased with increasing initial effective normal stresses. However, when initial effective normal stress was greater than 10 MPa, the increasing amounts of normal stiffness were not noticeable. Especially, at low normal stress, shear stiffness showed remarkably small values which are in the range of 3.93 and 11.49, and this might be due to the low level of roughness. Shear stiffness showed lower values than normal stiffness and shear stiffness also showed the same tendency compared to the normal stiffness.

Fig. 4.4.6 shows the relationship between effective normal stress, shear stress, normal displacement and shear displacement of the test results at room temperature, dry condition, and various confining pressures. As shear displacement increased, effective normal stress and shear stress increased, and both values became constant after peak values (Figs. 4.4.6 (a) and (b)). In the general constant normal stiffness conditions, shear stress shows hardening behavior with the increase of normal stiffness due to the constraint of dilation (Son, 2005; Lee, 2011). However, in this study, normal stiffness was kept quite constant just before peak shear stress, and after that, normal stiffness dropped rapidly (Fig. 4.1.2). Therefore, the normal and shear stress became comparatively stable after slip occurred and stress hardening tendency was not observed. In Fig. 4.4.6(c), initially, 0.1~0.2 mm of contraction was observed on the discontinuities, and after peak shear stress, dilation occurred at relatively constant normal stress conditions. This tendency was observed from the whole tests of cement-mortar specimens at every testing condition, and the total graphs of the relation between dilation

and stresses were listed in Appendix. Dilation angle decreased as effective normal stress increased (Fig. 4.4.7) and the decreasing amount was reduced. This might result from the asperity degradation, and the test results showed similar values compared to the dilation angle calculated by Barton and Choubey's empirical equation (4.7).

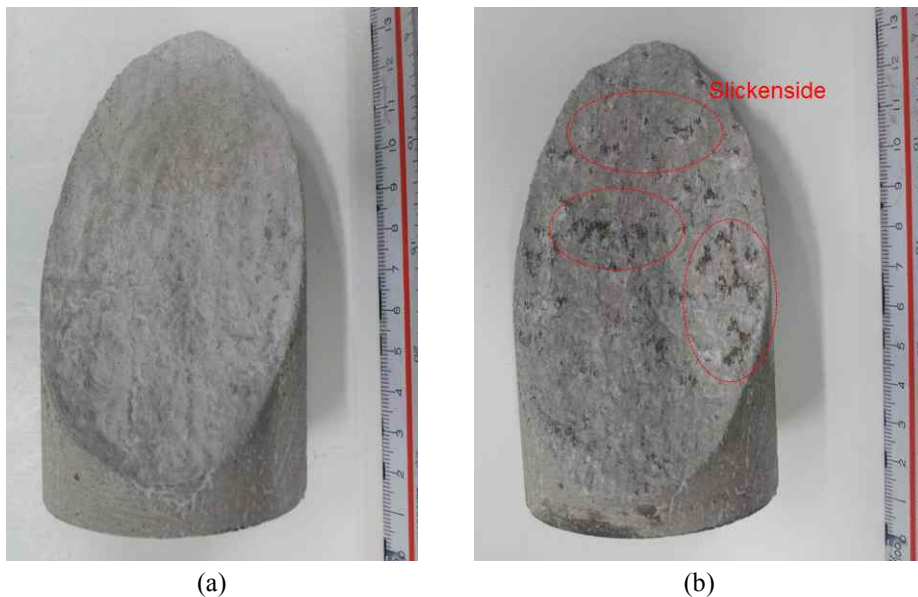


Fig. 4.4.1 Discontinuity surface of S-M-10 specimen (JRC=2.05/at room temperature/dry condition/confining pressure: 10 MPa): (a) before shearing and (b) after sliding. Slickenside was observed along the shear direction in places where asperity was.

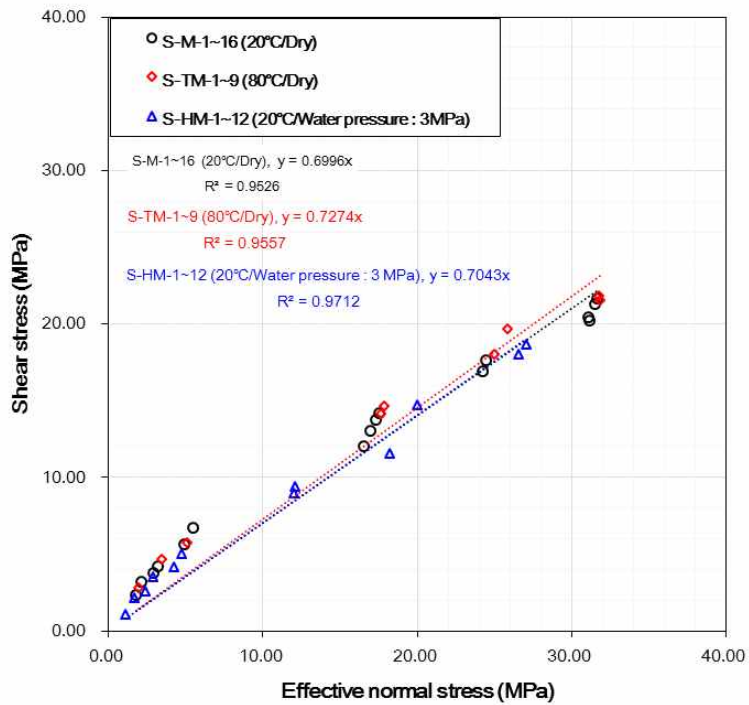


Fig. 4.4.2 Relation between shear stress and effective normal stress acting on cement-mortar specimens including smooth discontinuities ($JRC=2.05$) on various testing conditions and linear regression lines for peak friction angles.

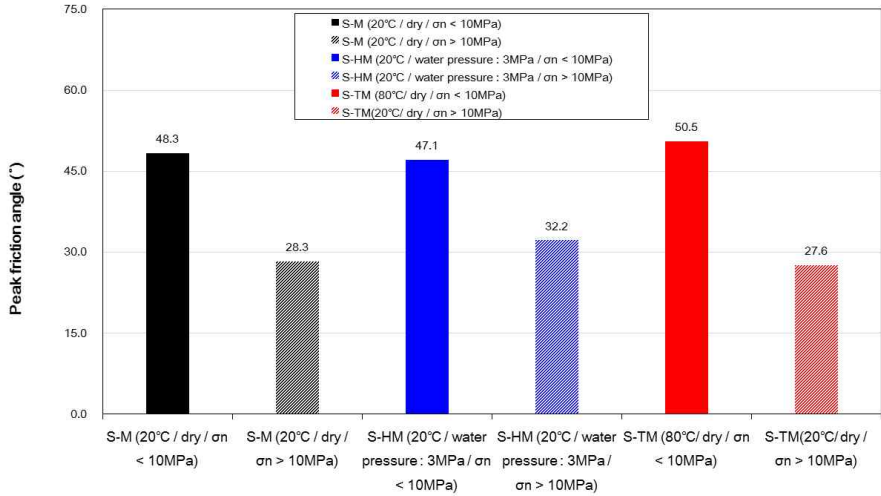


Fig. 4.4.3 Peak friction angles of cement-mortar specimens including smooth discontinuities (JRC=2.05) depending on normal stress and various testing conditions.

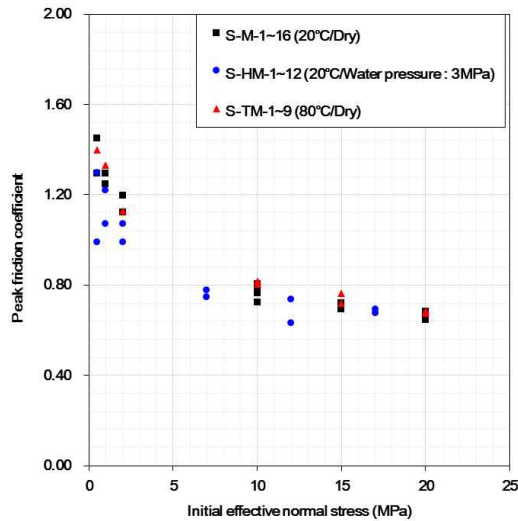


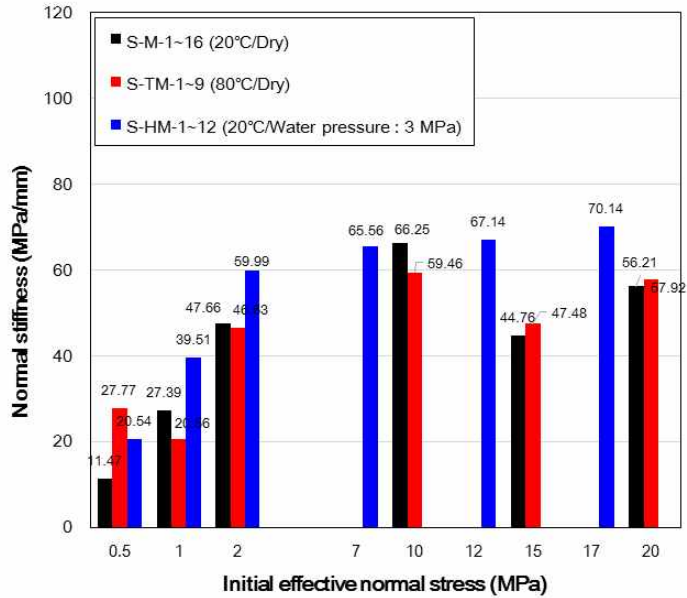
Fig. 4.4.4 Relation between the peak friction coefficient and initial effective normal stress of cement-mortar specimens including smooth discontinuities (JRC=2.05) under various testing conditions.

Table 4.4.1 Results of shear tests on smooth discontinuities (JRC=2.05) of cement-mortar specimens on various testing conditions.

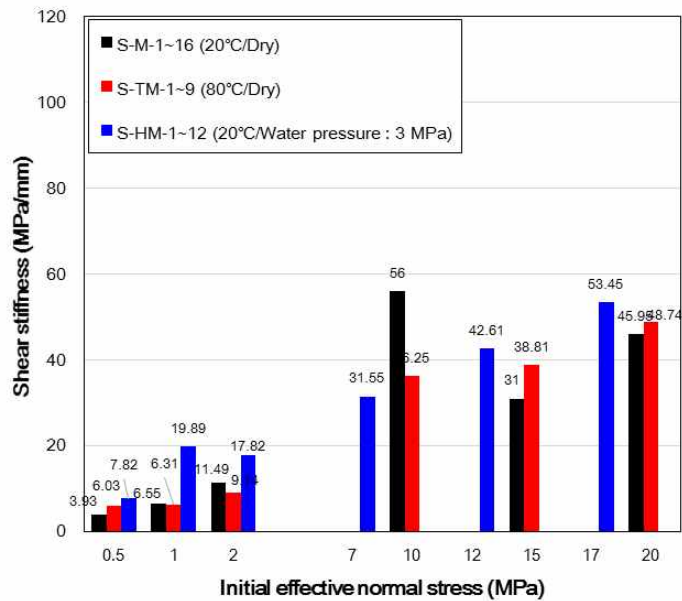
Testing condition	Sample no.	Confining pressure (MPa)	Effective normal stress (MPa)	Peak shear stress (MPa)	Peak friction coefficient	Normal stiffness (MPa/mm)	Shear stiffness (MPa/mm)	Dilation angle (°)	Peak friction angle (°) (coefficient of friction)			Cohesion (MPa) ($\sigma_n > 10$ MPa)
									Total	$\sigma_n < 10$ (MPa)	$\sigma_n > 10$ (MPa)	
M (20°C / Dry)	S-M-1	0.50	1.80	2.33	1.29	11.47	3.93	4.43	35.0 (0.6989)	48.3 (1.1211)	28.3 (0.5399)	3.98
	S-M-2	0.50	2.20	3.19	1.45	-	-	-				
	S-M-3	1.00	2.99	3.73	1.25	27.39	6.55	3.96				
	S-M-4	1.00	3.24	4.19	1.29	-	-	3.02				
	S-M-5	2.00	4.99	5.60	1.12	47.66	11.49	3.34				
	S-M-6	2.00	5.55	6.65	1.20	-	-	2.35				
	S-M-7	10.00	17.36	13.75	0.79	65.61	56.00	1.34				
	S-M-8	10.00	17.57	14.13	0.80	69.92	44.61	1.40				
	S-M-9	10.00	17.02	13.00	0.76	63.21	33.84	2.26				
	S-M-10	10.00	16.61	12.02	0.72	40.41	31.00	0.80				
	S-M-11	15.00	24.49	17.63	0.72	49.11	29.03	1.07				
	S-M-12	15.00	24.29	16.87	0.69	54.85	49.99	-				
	S-M-13	20.00	31.55	21.26	0.67	53.23	48.79	0.81				
	S-M-14	20.00	31.71	21.61	0.68	61.46	53.00	-				
	S-M-15	20.00	32.14	21.03	0.65	59.67	46.85	1.24				
	S-M-16	20.00	31.20	20.19	0.65	50.46	35.14	-				
TM (80°C / Dry)	S-TM-1	0.50	1.98	2.77	1.40	27.77	6.03	5.23	36.0 (0.7274)	50.5 (1.2127)	27.6 (0.5238)	5.22
	S-TM-2	1.00	3.49	4.65	1.33	20.56	6.31	3.69				
	S-TM-3	2.00	5.08	5.73	1.13	46.63	9.14	3.77				
	S-TM-4	10.00	17.62	14.16	0.80	64.16	48.75	2.64				
	S-TM-5	10.00	17.89	14.62	0.82	54.76	23.75	2.11				
	S-TM-6	15.00	25.01	18.04	0.72	55.80	43.92	0.85				
	S-TM-7	15.00	25.81	19.68	0.76	39.15	33.70	1.91				
	S-TM-8	20.00	31.78	21.80	0.69	67.43	53.17	1.18				
	S-TM-9	20.00	31.84	21.57	0.68	48.41	44.30	-				

Table 4.4.1 Continued.

Testing condition	Sample no.	Confining pressure (MPa)	Effective normal stress (MPa)	Peak shear stress (MPa)	Peak friction coefficient	Normal stiffness (MPa/mm)	Shear stiffness (MPa/mm)	Dilation angle (°)	Peak friction angle (°) (coefficient of friction)		
									Total	$\sigma_n < 10$ (MPa)	$\sigma_n > 10$ (MPa)
HM (20°C / water pressure: 3MPa)	S-HM-1	3.50	1.11	1.10	0.99	-	-	-	35.2 (0.7043)	47.1 (1.0778)	32.2 (0.6308)
	S-HM-2	3.50	1.68	2.18	1.30	20.54	7.82	4.29			
	S-HM-3	4.00	2.40	2.57	1.07	30.93	7.21	3.88			
	S-HM-4	4.00	2.90	3.54	1.22	48.09	32.56	3.32			
	S-HM-5	5.00	4.21	4.17	0.99	74.52	18.09	2.31			
	S-HM-6	5.00	4.72	5.06	1.07	45.45	17.55	2.68			
	S-HM-7	10.00	12.01	8.97	0.75	64.36	28.03	1.94			
	S-HM-8	10.00	12.05	9.38	0.78	66.75	35.07	2.36			
	S-HM-9	15.00	20.02	14.75	0.74	59.65	39.13	1.26			
	S-HM-10	15.00	18.25	11.56	0.63	74.63	46.08	1.09			
	S-HM-11	20.00	26.57	18.00	0.68	78.71	60.87	1.02			
	S-HM-12	20.00	27.03	18.70	0.69	61.56	46.03	0.33			



(a)



(b)

Fig. 4.4.5 Relation between normal, shear stiffness and initial effective normal stress of cement-mortar specimens including smooth discontinuities (JRC=2.05) under various testing conditions: (a) normal stiffness and (b) shear stiffness.

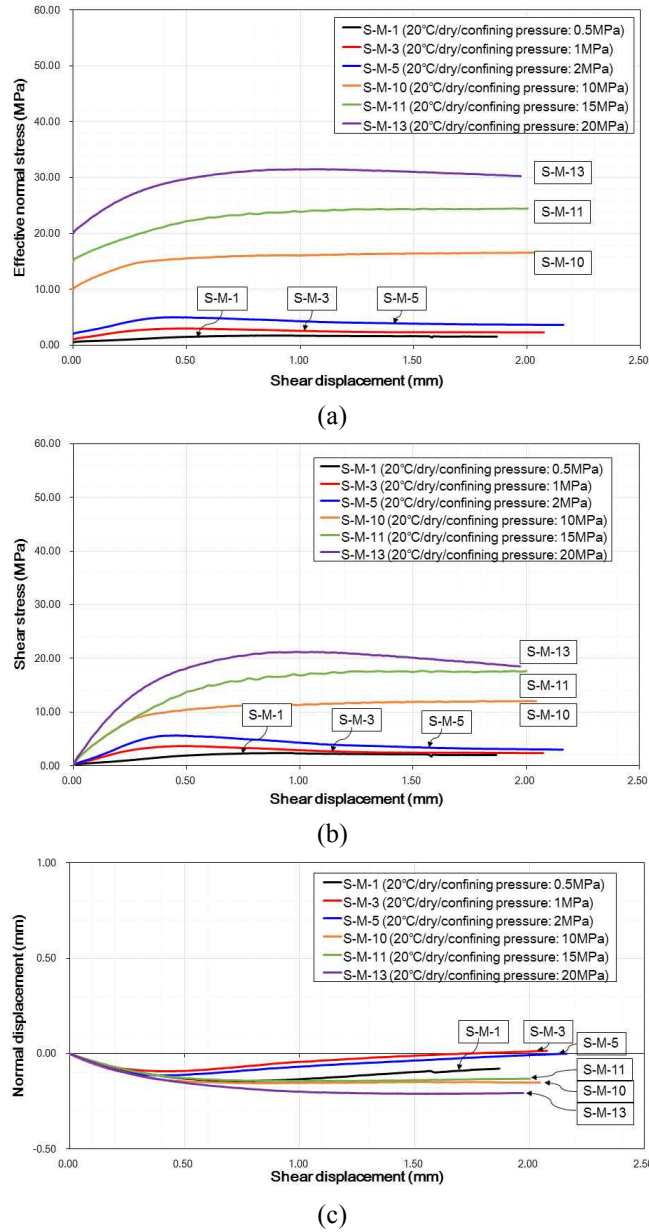


Fig. 4.4.6 Relation between effective normal stress, shear stress, normal displacement and shear displacement of S-M-1, 3, 5, 10, 11, 13 specimens (confining pressure: 0.5, 1, 2, 10, 15, 20 MPa/20°C/dry condition): (a) effective normal stress, (b) shear stress, and (c) normal displacement along with shear displacement.

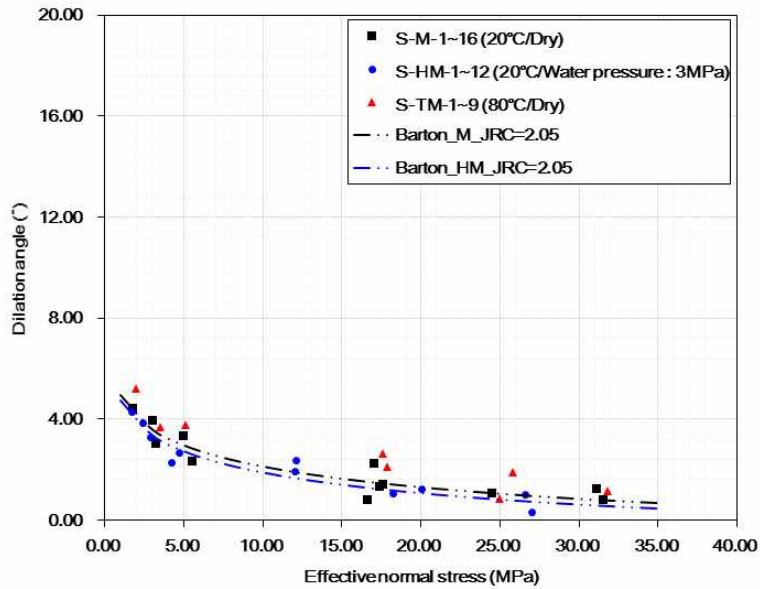


Fig. 4.4.7 Relation between dilation angle and effective normal stress of cement-mortar specimens including smooth discontinuities (JRC=2.05) under various testing conditions.

4.4.2 Test results at 80°C

The temperature was maintained at 80°C during the tests and peak friction angle obtained from the whole normal stress range was 36.0°, showing not much variation (Fig. 4.4.2). At low normal stress, peak friction angle was 50.5°, and at high normal stress, peak friction angle was 27.6° and cohesion was 5.22 MPa (Fig. 4.4.3 and Table 4.4.1). Effective normal stress and shear stress also did not change much and thus, at an elevated temperature of 80°C, the effect of temperature was not significant to the friction properties in this study. In Fig. 4.4.5, normal and shear stiffness did

not vary much compared to the results at room temperature. In Fig. 4.4.7, dilation angle showed similar values compared to the results at room temperature.

4.4.3 Test results at room temperature with water pressure

Water pressure of 3 MPa was applied on the discontinuity surface and maintained constant during the tests. Peak friction angle at the total normal stress was 35.2° and showed not much change (Fig. 4.4.2). At low normal stress less than 10 MPa, peak friction angle decreased to 47.1° , by 1.2° , compared to the result at room temperature and dry conditions. In the XRD test results (Table 3.1.2), only a small amount of calcite which can reduce friction angle was observed, and therefore, the effect of mineralogy might not be significant. However, as explained above, Barton (1973) referred the possibility of local tensile failure in asperity scale and as a result when joints were in wet condition shear strength could be reduced by 5~30%. Li et al. (2005) observed that the residual friction angle of fractured sandstone decreased by 10.1~25.8% when the specimens were saturated. In this study, the tensile strength was reduced from 9.22 MPa to 7.32 MPa when saturated, and thus, the decrease of tensile strength might affect the reduction of peak friction angle at low normal stress. However, at high normal stress exceeding 10 MPa, peak friction angle was 32.2° and showed a slight increase. When wet condition, basic friction angle from tilt tests increased (Table 3.2.1), and hence, after the failure of asperities at high normal stress, basic friction angle might dominate shear behavior. In Fig. 4.4.4, this tendency can be observed more clearly from the peak friction

coefficient.

Sheng and Reddish (2005) carried out multistage triaxial tests on fractured jointed coal specimens, and they also observed a decrease of residual friction angle when the specimens were saturated. They proposed a hypothesis that the roughness of saturated rocks became smoother because saturated rocks can deform much more than dry rocks. As a result, residual friction angle can decrease. However, in this study, normal and shear stiffness increased with the increase of confining pressure but did not show any clear effect of water pressure (Fig. 4.4.5). Therefore, their hypothesis was not applicable to the results of this study.

Dilation angle when water pressure was applied showed a slight decrease (Fig. 4.4.7). The test results showed a good agreement with Barton and Choubey's empirical model, and Barton (1973) emphasized that for saturated joints, input parameters including JCS and basic friction angle should be measured at wet condition. In the previous tests, JCS decreased when wet condition (Table 3.1.1) and the reduction of dilation angle in the test results might also be influenced by the change of surface strength.

4.5 Cement-mortar including a rough discontinuity

4.5.1 Test results at room temperature and dry conditions

For the specimens including rough discontinuities ($JRC=11.63$), marks of slickenside were mainly observed where big asperities were placed (Fig. 4.5.1). Peak friction angle at the whole normal stress was 41.5° (Fig. 4.5.2 and Table 4.5.1), and showed an increase compared to the peak friction angle of smooth discontinuities ($JRC=2.05$). At normal stress less than 10 MPa, peak friction angle was 54.9° (Fig. 4.5.3 and Table 4.5.1), and at high normal stress, 29.6° . The increase of roughness caused the increase of peak friction angle, but interestingly, the peak friction angle at high normal stress did not show much change. That proves as the normal stress acting on the discontinuity rises, asperities are sheared off rather than sliding along the asperities. As a result shear behavior is affected by the basic friction angle (Byerlee, 1978; Stesky, 1978, Guo and Qi, 2015). The peak friction coefficients were also plotted with initial effective normal stress (Fig. 4.5.4), and decreased with increasing initial effective normal stress. This result shows well the non-linearity of shear behavior depending on normal stress, and at high normal stress, the peak friction coefficients did not show much change as explained above.

Normal and shear stiffness increased with the increase of initial effective normal stress (Fig. 4.5.5). Compared to the stiffness of smooth discontinuities, at low normal stress, both stiffness of rough discontinuities was greater than those of smooth discontinuities. However, at high normal stress, normal and shear stiffness did not show much difference between the

two different discontinuities and it might be caused by the breakage of asperities.

Fig. 4.5.6 shows the relationship between effective normal stress, shear stress, normal displacement on shear displacement. After peak shear stress, the effective normal stress became quite stable, and normal displacement began to increase (Fig. 4.5.6 (c)). As normal stress increased, dilation along the discontinuities diminished due to the asperity degradation, and the test results of dilation angle showed a good agreement with the empirical model of Barton and Choubey (1977). Additionally, the difference of dilation angle between smooth and rough discontinuities became smaller with increasing normal stress as asperities sheared off.

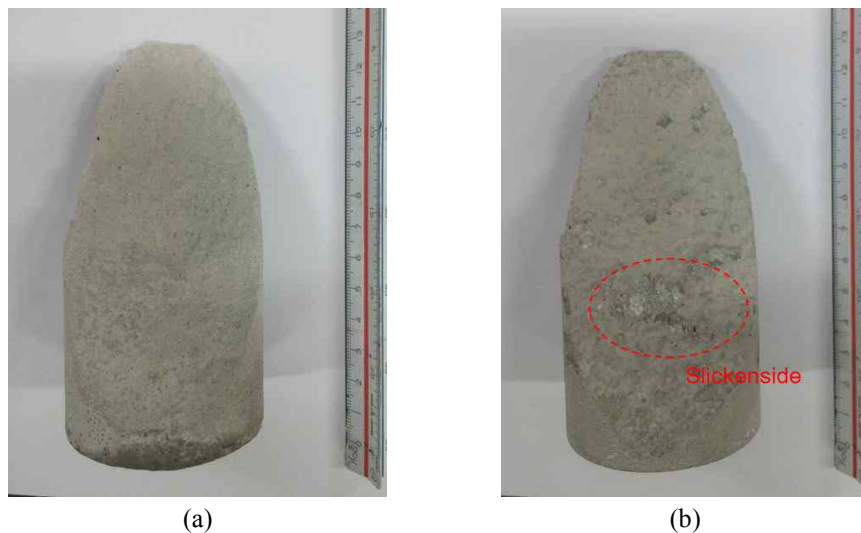


Fig. 4.5.1 Discontinuity surface of R-M-5 specimen (JRC=11.63/at room temperature/dry condition/confining pressure: 2 MPa): (a) before shearing and (b) after sliding. Marks of slickenside were observed along the shear direction in places where asperity was.

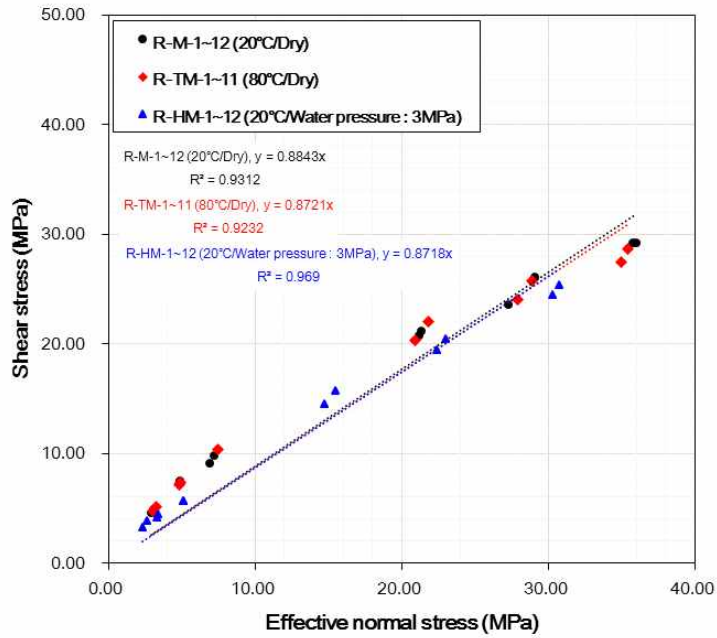


Fig. 4.5.2 Relation between shear stress and effective normal stress acting on cement-mortar specimens including rough discontinuities (JRC=11.63) on various testing conditions and linear regression lines for peak friction angles.

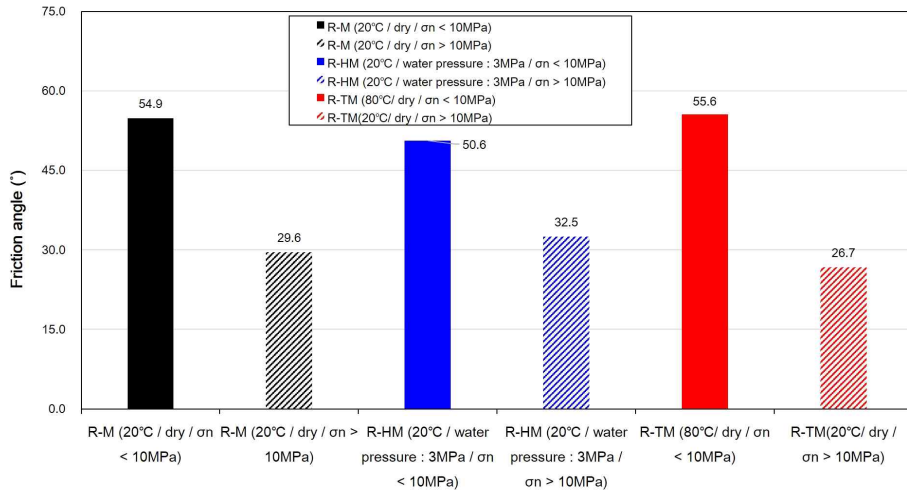


Fig. 4.5.3 Peak friction angles of cement-mortar specimens including rough discontinuities (JRC=11.63) depending on normal stress and various testing conditions.

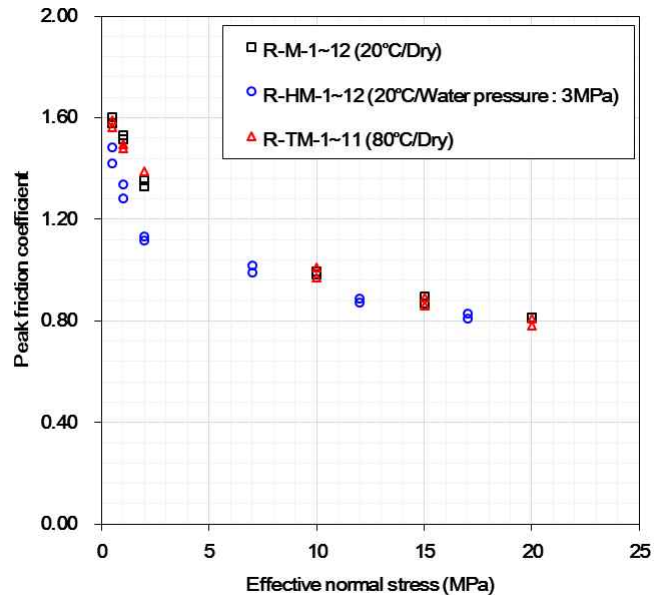
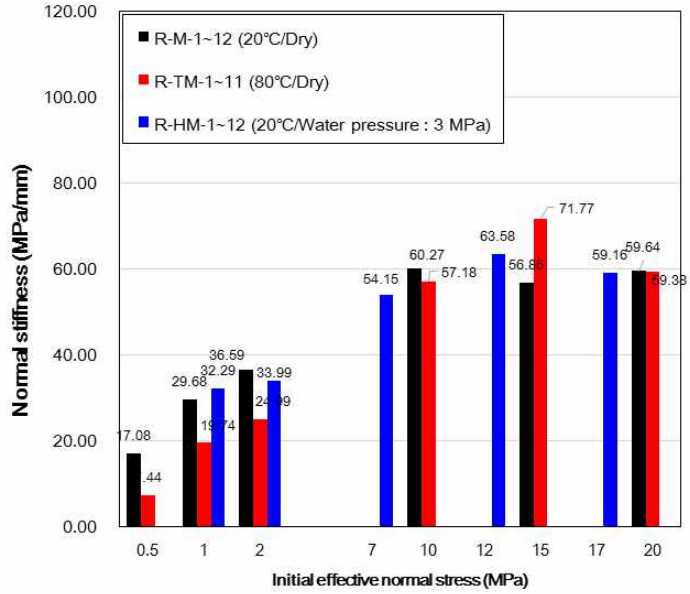
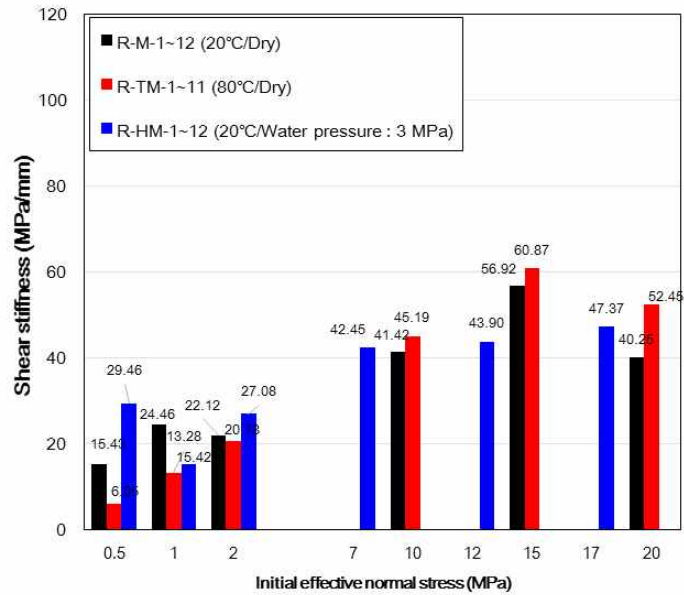


Fig. 4.5.4 Relation between the peak friction coefficient and the initial effective normal stress of cement-mortar specimens including rough discontinuities (JRC=11.63) under various testing conditions.



(a)



(b)

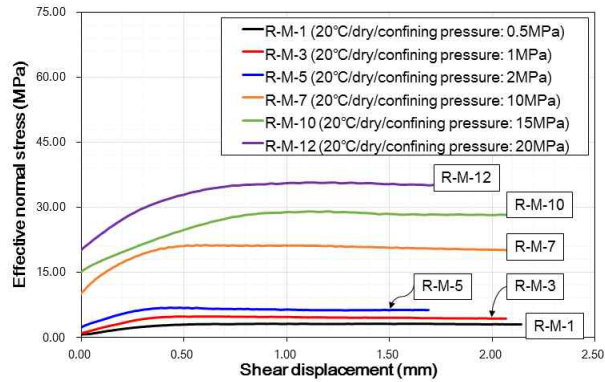
Fig. 4.5.5 Relation between normal, shear stiffness and initial effective normal stress of cement-mortar specimens including rough discontinuities (JRC=11.63) under various testing conditions: (a) normal stiffness and (b) shear stiffness.

Table 4.5.1 Results of shear tests on rough discontinuities (JRC=11.63) of cement-mortar specimens on various testing conditions.

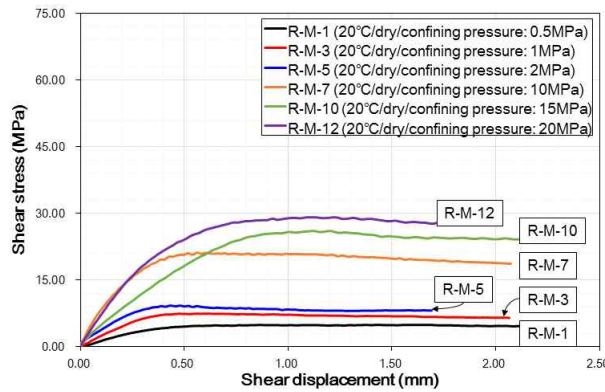
Testing condition	Sample no.	Confining pressure (MPa)	Effective normal stress (MPa)	Peak shear stress (MPa)	Peak friction coefficient	Normal stiffness (MPa/mm)	Shear stiffness (MPa/mm)	Dilation angle (°)	Peak friction angle (°) (coefficient of friction)			Cohesion (MPa) ($\sigma_n > 10$ MPa)
									Total	$\sigma_n < 10$ (MPa)	$\sigma_n > 10$ (MPa)	
M (20°C / Dry)	R-M-1	0.50	3.06	4.90	1.60	16.84	15.43	13.79	41.5 (0.8843)	54.9 (1.4221)	29.6 (0.5680)	8.88
	R-M-2	0.50	2.90	4.58	1.58	17.32	8.22	-				
	R-M-3	1.00	4.86	7.37	1.52	29.68	24.46	11.97				
	R-M-4	1.00	4.86	7.45	1.53	25.40	48.48	9.42				
	R-M-5	2.00	6.88	9.15	1.33	24.72	22.12	9.83				
	R-M-6	2.00	7.21	9.77	1.36	48.46	20.62	8.78				
	R-M-7	10.00	21.33	21.20	0.99	64.76	41.42	4.18				
	R-M-8	10.00	21.16	20.78	0.98	55.77	58.10	3.08				
	R-M-9	15.00	27.23	23.62	0.87	58.51	56.92	-				
	R-M-10	15.00	29.10	26.13	0.90	55.18	39.65	2.53				
	R-M-11	20.00	36.00	29.26	0.81	40.47	40.25	2.20				
	R-M-12	20.00	35.78	29.17	0.82	78.81	62.18	2.63				
TM (80°C / Dry)	R-TM-1	0.50	3.03	4.74	1.56	10.23	8.64	12.04	41.1 (0.8721)	55.6 (1.4586)	26.7 (0.5025)	10.5
	R-TM-2	0.50	3.26	5.18	1.59	4.64	3.46	18.04				
	R-TM-3	1.00	4.81	7.12	1.48	22.07	14.31	9.39				
	R-TM-4	1.00	4.94	7.39	1.50	17.4	12.25	10.92				
	R-TM-5	2.00	7.45	10.36	1.39	24.99	20.78	7.37				
	R-TM-6	10.00	21.81	22.00	1.01	67.88	53.48	3.61				
	R-TM-7	10.00	20.93	20.35	0.97	46.48	36.89	3.81				
	R-TM-8	15.00	28.85	25.74	0.89	77.16	67.39	3.07				
	R-TM-9	15.00	27.90	24.00	0.86	66.37	54.35	2.57				
	R-TM-10	20.00	35.45	28.65	0.81	69.86	62.8	2.67				
	R-TM-11	20.00	34.99	27.42	0.78	48.9	42.09	2.43				

Table 4.5.1 Continued.

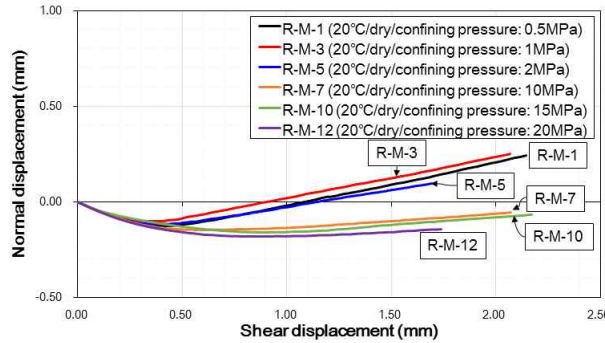
Testing condition	Sample no.	Confining pressure (MPa)	Effective normal stress (MPa)	Peak shear stress (MPa)	Peak friction coefficient	Normal stiffness (MPa/mm)	Shear stiffness (MPa/mm)	Dilation angle (°)	Peak friction angle (°) (coefficient of friction)		
									Total	$\sigma_n < 10$ (MPa)	$\sigma_n > 10$ (MPa)
HM (20°C / water pressure: 3MPa)	R-HM-1	3.50	2.29	3.25	1.42	-	29.46	14.27	41.1 (0.8718)	50.6 (1.2185)	32.5 (0.6376)
	R-HM-2	3.50	2.60	3.86	1.48	-	-	-			
	R-HM-3	4.00	3.36	4.49	1.34	26.00	16.01	6.62			
	R-HM-4	4.00	3.26	4.18	1.28	38.58	14.82	10.14			
	R-HM-5	5.00	5.06	5.73	1.13	53.16	39.11	8.88			
	R-HM-6	5.00	5.09	5.68	1.12	14.82	15.04	7.33			
	R-HM-7	10.00	14.68	14.56	0.99	56.11	45.55	4.06			
	R-HM-8	10.00	15.43	15.72	1.02	52.19	39.35	4.99			
	R-HM-9	15.00	22.36	19.50	0.87	66.53	43.69	1.89			
	R-HM-10	15.00	22.98	20.42	0.89	60.62	44.10	2.07			
	R-HM-11	20.00	30.25	24.47	0.81	58.94	51.47	1.66			
	R-HM-12	20.00	30.70	25.40	0.83	59.38	43.27	1.18			



(a)



(b)



(c)

Fig. 4.5.6 Relation between effective normal stress, shear stress, normal displacement and shear displacement of R-M-1, 3, 5, 7, 10, 12 specimens (confining pressure: 0.5, 1, 2, 10, 15, 20 MPa/20°C/dry condition): (a) effective normal stress, (b) shear stress, and (c) normal displacement along with shear displacement.

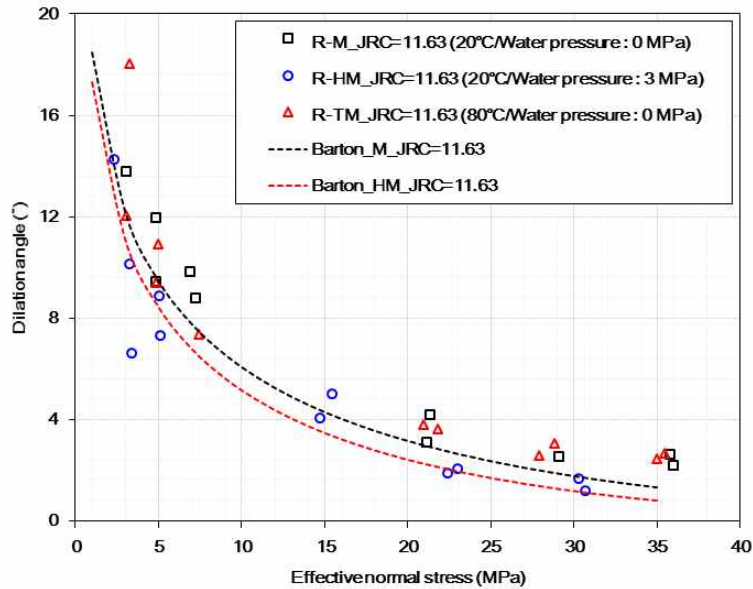


Fig. 4.5.7 Relation between dilation angle and effective normal stress of cement-mortar specimens including rough discontinuities (JRC=11.63) under various testing conditions.

4.5.2 Test results at 80°C

The results of peak friction angles depending on normal stress range were listed in Table 4.5.1 and Fig. 4.5.3 and they were 41.1° (at the whole normal stress), 55.6° (at low normal stress), and 26.7° (at high normal stress), respectively. Peak friction angle, effective normal stress, and shear stress did not show remarkable change at an elevated temperature of 80°C, and hence, the temperature of 80°C did not affect much on the shear behavior. The same tendency of non-linearity of shear behavior was also observed. This can be seen more clearly in Fig. 4.5.4, and at low normal stress, the peak friction coefficients show a notable difference compared to the coefficients at dry condition. However, as effective normal stress

increased, the difference became smaller as a result of the failure of asperities as explained above.

In Fig. 4.5.5, normal and shear stiffness increased with increasing initial normal stress but did not show much variation with increasing temperature. Dilation angle did not show clear change at elevated temperature (Fig. 4.5.7) and the effect of temperature on dilation at 80°C was negligible in this study.

4.5.3 Test results at room temperature with water pressure

Peak friction angles under water pressure applied conditions were 41.1° at the whole normal stress, 50.6° at the low normal stress below than 10 MPa, and 32.5° at high normal stress greater than 10 MPa, respectively (Table 4.5.1). Compared to the dry condition, at low normal stress, peak friction angle decreased by 3.7° (Fig. 4.5.3) and increased slightly. The amount of decrease was much more noticeable than the result of smooth discontinuities and Barton (1973) stated that the effect of wet condition on friction strength increases with the increase of roughness. Therefore, the effect of water can increase depending on the roughness of discontinuities and normal stress level.

Normal and shear stiffness increased as initial effective normal stress increased, but did not show any clear change compared to the results at dry conditions (Fig. 4.5.5). Dilation angles when 3 MPa of water pressure was applied showed smaller values than those at dry conditions (Fig. 4.4.7). In the empirical formula (equation (4.11)), as numerator consists of multiplication JRC and JCS, the effect of decreasing JCS becomes greater

when the roughness increases. The test results showed a good agreement with the empirical formula and the same reason might affect the decrease of dilation angles.

4.6 Scanning electron microscope analysis

Peak friction angles of the saw-cut surfaces of Goheung diorite and Linyi sandstone showed a noticeable decrease when water pressure was applied. According to previous studies (Horn and Deere, 1962; Morrow et al., 2000; Ulusay and Karakul, 2015), the decrease might be caused by minerals and surface damage. Therefore, to investigate the cause of the change of the peak friction angle depending on testing conditions, it was necessary to observe the discontinuity surfaces at a microscopic scale before and after the tests. For that reason, field-emission scanning electron microscope (FE-SEM) observation and analysis were conducted in this study.

FE-SEM analysis is widely used to obtain the microscopic images with high magnification and high resolution, such as pore distributions (Sondergeld et al., 2010), mineral structure and identification (Ji et al., 2012; Ma et al., 2014; Cai et al., 2014) and rock surface damage detection (He et al., 2016). SEM analytical experiments were carried out at the Research Institute of Advanced Materials at Seoul National University. The equipment used in this study was MERLIN Compact FE-SEM made by Zeiss, as shown in Fig. 4.6.1. The highest resolution of the machine is 1.0 nm at 15 kV, and the image sizes of up to 32k by 32k pixels is available.

In the case of cylindrical shape specimens, the maximum available sample diameter is 2.5 cm, and the height should be less than 1 cm. Thus, the specimens of diorite and sandstone before the tests were prepared to meet the required size firstly for comparison. After the tests at dry conditions and at water pressure applied conditions, the saw-cut surfaces of diorite and sandstone specimens were drilled with a core bit having 2.5 cm

diameter. Coring was carried out at the position which slickenside was observed clearly. Fig. 4.6.2 shows the locations of coring on the saw-cut surfaces (red circles) and prepared specimens for SEM observation. After coring, the surfaces of all the samples were coated with platinum to raise the conductivity using a coater (MSC-101) in a vacuum state before SEM observation (Fig. 4.6.3).



Fig. 4.6.1 Zeiss Merlin Compact Field-Emission scanning electron microscope used in this study.

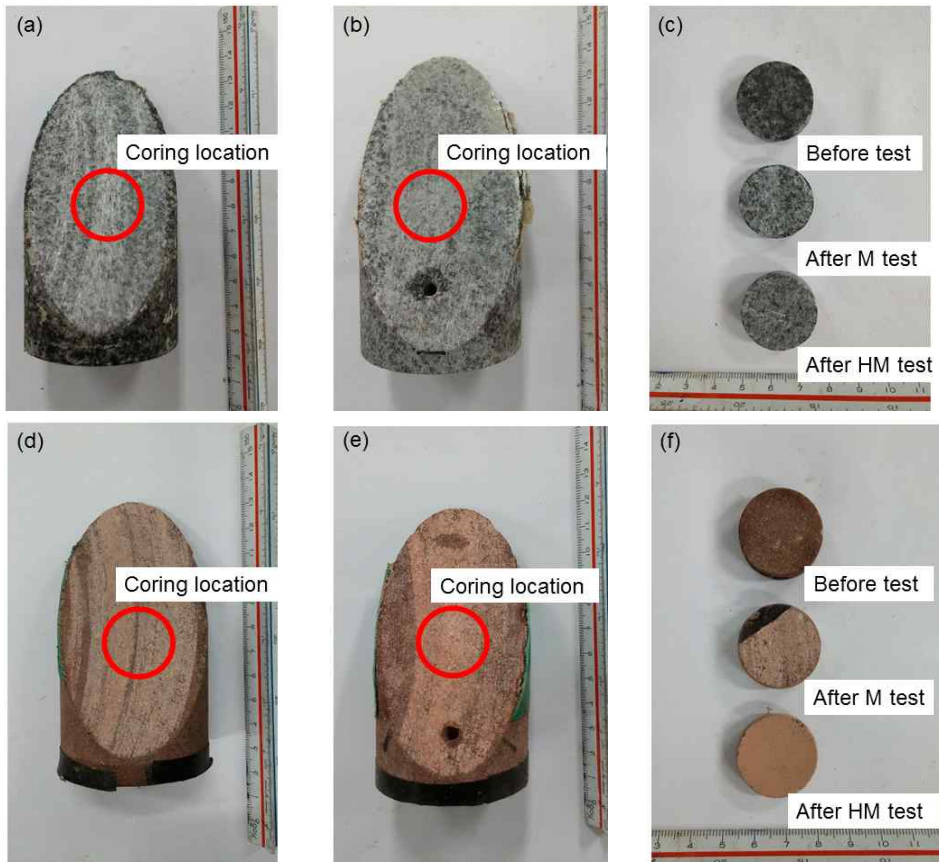


Fig. 4.6.2 Saw-cut surfaces after the tests and cored samples for SEM observation of Goheung diorite ((a), (b), (c)) and Linyi sandstone ((d), (e), (f)): (a) D-M-1, (b) D-HM-1, (c) cored samples of Goheung diorite, (d) LY-M-1, (e) LY-HM-1, and (f) cored samples of Linyi sandstone.



Fig. 4.6.3 A coater (MSC-101) and Linyi sandstone samples for the SEM tests: (a) a coater and (b) Linyi sandstone samples after platinum spraying treatments.

4.6.1 Goheung Diorite

Fig. 4.6.4 shows the SEM images of Goheung diorite samples at each testing conditions at a magnification of 100 and 500. In Figs. 4.6.4(a) and (b) before the tests, mineral grains having flat surfaces are tightly packed, and cracks and pores can hardly be observed. After the tests in a dry condition, a slight slickenside trace was observed, but it was difficult to state any clear changes were induced by shearing in the image at a magnification of 100 (Fig. 4.6.4(c)). While, in Fig. 4.6.4(d) at a magnification of 500, slickenside traces and a small amount of pulverized mineral grain was observed more clearly. These powdered grains were considered to be produced by shearing along the discontinuity. In Figs. 4.6.4 (e) and (f), after the test at water pressure applied condition, these types of traces and pulverized grains were observed much more clearly. In Fig. 4.6.4(e) and (f), the image of the surface is much flatter compared to that

of Fig. 4.6.4(c) at the dry condition. Furthermore, even at a magnification of 100, a small amount of mineral grain were observed. Fig. 4.6.5 presents the images of the D-HM-1 specimen after the test at a higher magnification of 1000 and 20000. In Fig. 4.6.5(a), pulverized mineral grains and microcracks on a mineral were observed. Additionally, minerals having thin layer lattice structure were also observed on the sheared surface (Fig. 4.6.5(b)), which were detected in the XRD analysis (Table 3.1.2). Thus, these images present that the wet surfaces might be more weakened than the dry surfaces when shearing occurred. The presence of layer lattice structured minerals also might influence on the decrease of peak friction angle as many previous researchers found (Nascimento, 1981; Morrow et al., 2000; Ulusay and Karakul, 2015).

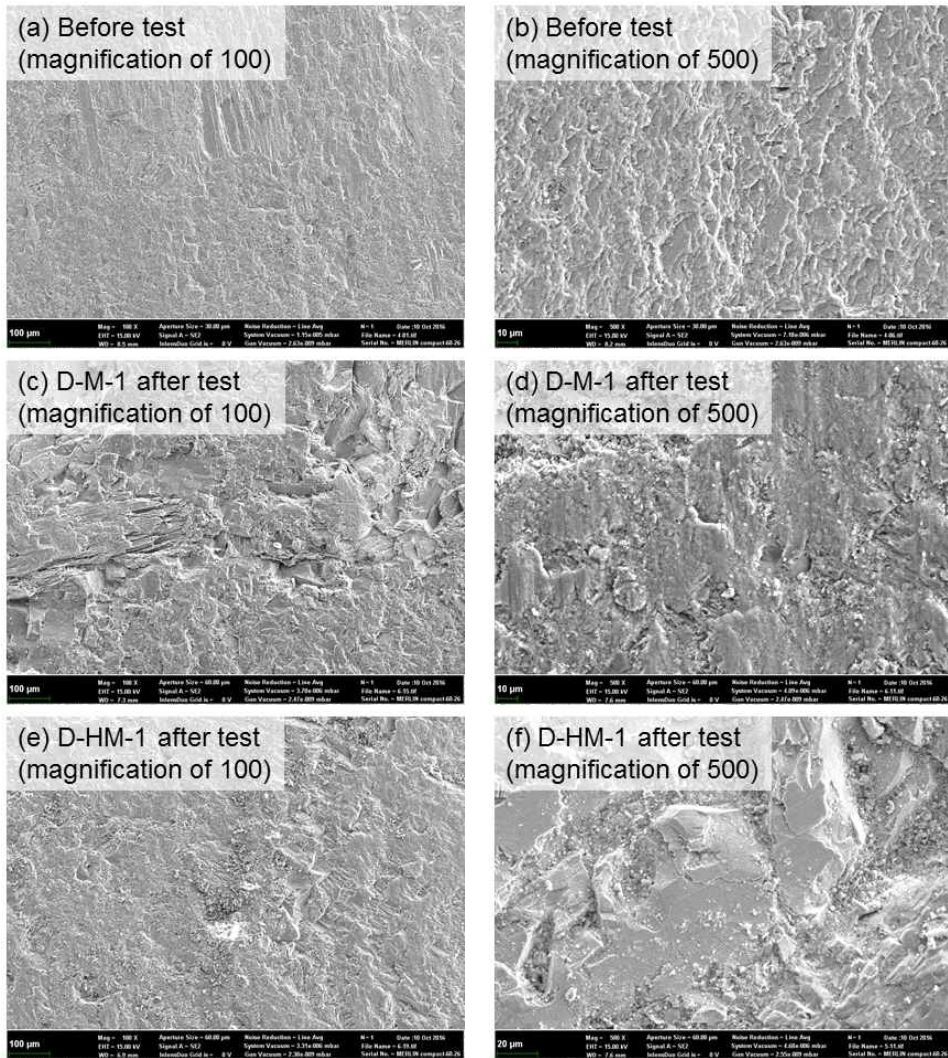


Fig. 4.6.4 SEM images of Goheung diorite saw-cut surfaces: (a) and (b) before test ($100\times/500\times$, respectively), (c) and (d) D-M-1 after test at room temperature and dry conditions ($100\times/500\times$, respectively), and (e) and (f) D-HM-1 after test at 3 MPa of water pressure applied conditions ($100\times/500\times$, respectively).

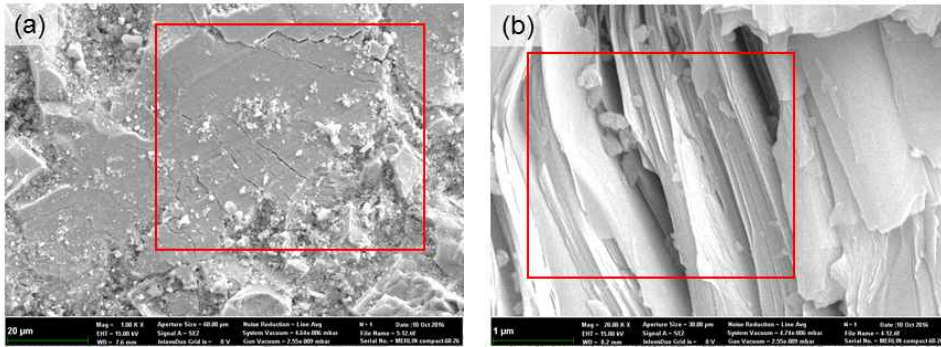


Fig. 4.6.5 SEM images of microcracks and lattice structures in Goheung diorite saw-cut surfaces after the test at a 3 MPa of water pressure applied condition: (a) microcracks on a mineral grain (1000×) and (b) layer lattice structure mineral (20000×).

4.6.2 Linyi sandstone

The structure of Linyi sandstone appeared markedly different compared to those of Goheung diorite. In Figs. 4.6.6(a) at a magnification of 100 before the tests, the mineral grains are loosely packed, and small size of grains are cemented with bigger size of minerals weakly (Fig. 4.6.6(b)), even before the tests. After the test in a dry condition, as bumpy minerals were sheared off (Fig. 4.6.6(c)), the surface became flatter than before the test. As a result, separated powdered grains were found easily (Fig. 4.6.6(d)), and much more powdered grains were observed than the saw-cut surface of diorite, even in naked eyes (Fig. 4.6.2(d)). The changes appeared much more remarkably when the surface was wet. In Fig. 4.6.6(e), as the minerals were completely pulverized, it was difficult to find the shape of the minerals, and only smooth surface and small size of powdered grains were observed. At a magnification of 500 (Fig. 4.6.6(f)), microcracks were

found on the wide range of surface. That means the surface might be damaged and softened much more severely during shearing when the surface was wet than the dry surface. Decreased normal and stiffness also can be another proof for the weakening of the surface (Fig. 4.3.5). Fig. 4.6.7 shows the images of LY-HM-1 after the test at a wet condition at a higher magnification. At a magnification of 5000 (Fig. 4.6.7(a)), apparent microcracks were observed on the surface, and at a magnification of 20000, the weakly cemented minerals were found easily (Fig. 4.6.7(b)). Although in the XRD analysis (Table 3.1.2), only small amount of minerals which can reduce the peak friction angle were detected, it was found that water might weaken the bond strength of grains and decrease the surface strength from the SEM analysis. Barton (1976) noted that the presence of moisture could enhance the formation of fine gouge and it will have the obvious softening effect. The same phenomenon was observed on the surface of Linyi sandstone through SEM observation, and those factors may affect the decrease of the peak friction angle of Linyi sandstone at wet conditions in this study.

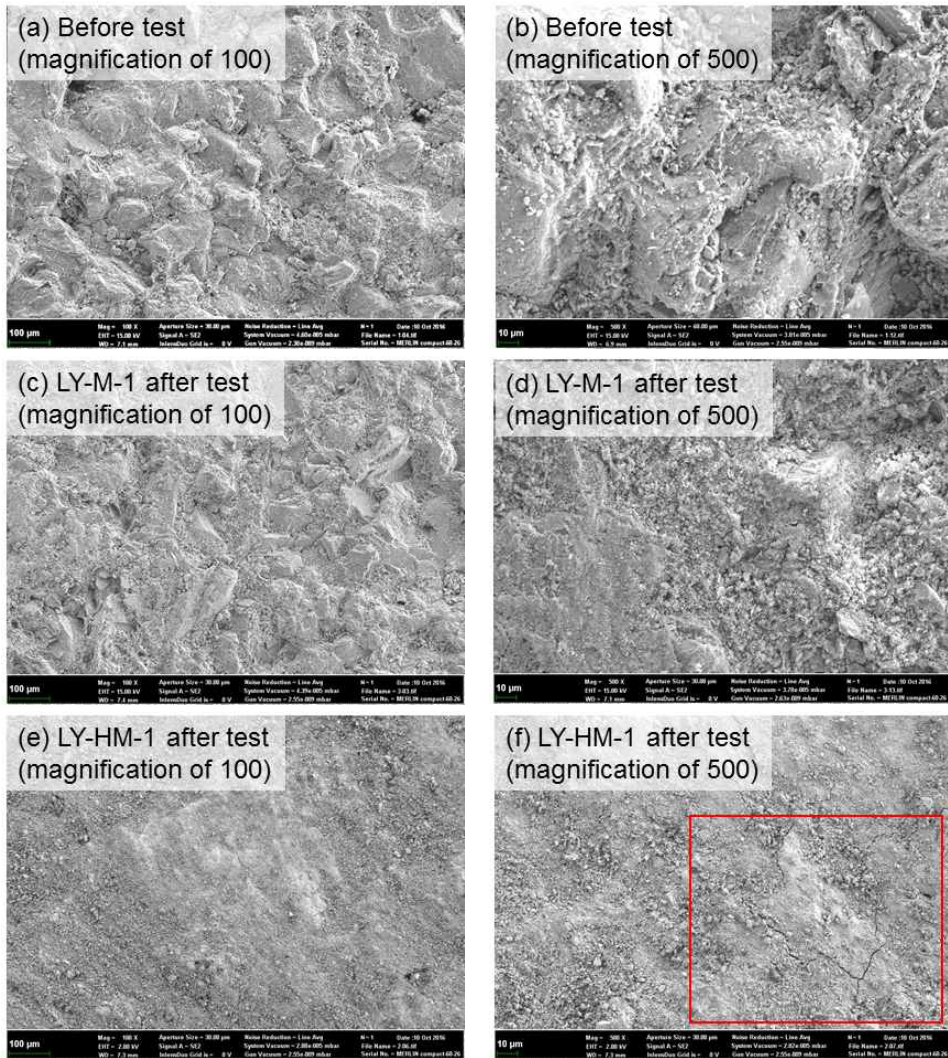


Fig. 4.6.6 SEM images of Linyi sandstone saw-cut surfaces: (a) and (b) before test ($100\times/500\times$, respectively), (c) and (d) LY-M-1 after test at room temperature and dry conditions ($100\times/500\times$, respectively), and (e) and (f) LY-HM-1 after test at 3 MPa of water pressure applied conditions ($100\times/500\times$, respectively). In a red rectangle in (f), microcracks were observed.

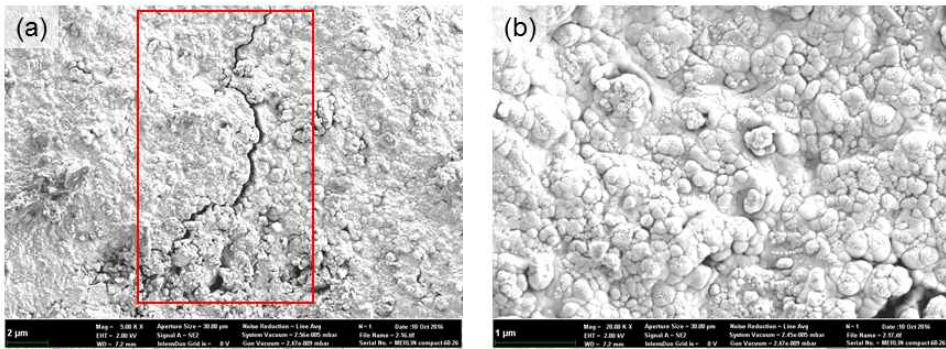


Fig. 4.6.7 SEM images of Linyi sandstone saw-cut surfaces after the tests at 3 MPa of water pressure applied conditions: (a) microcracks at the saw-cut surfaces (5000×) and (b) mineral grains at a magnification of 20000.

5. Numerical simulation

5.1 Introduction

Distinct Element Method (DEM) assumes rock as an assembly of separate particles, and the mechanical behavior of rock is governed by the properties of particles and bonds between the particles. In this case, the breakage of bonding between each particle can be expressed as damage or cracks of materials, and non-linear behavior of rocks can be simulated successfully. The particle flow code (PFC) is a DEM based simulation tool developed by ITASCA Consulting Group, and in PFC 2D, particles comprising rocks are assumed as rigid circular disks. Many studies were carried out to evaluate the applicability of PFC2D in the shear behavior of rock (Kulatilake et al., 2001; Park and Song, 2009; Bahaaddini et al., 2013), but few simulations have been reported under coupled condition. Thus, the main purpose of this study is to reproduce the experimental results and examine the effects of thermal and hydraulic condition on shear characteristics of rock by using PFC2D.

In PFC, the particles behave independently, and the mechanical behavior of rock is simply determined by the algorithm of Newton's second law of motion for particles and a force-displacement law for the contact of particles. The bond between particles is broken when the applied stress exceeds the normal/shear strength of the bond, and the breakage of the bond can represent the crack occurrence explicitly. Thus, it is important to determine the micro-properties of the bonds and particles for modeling mechanical behavior, crack propagation and asperity degradation in rocks

realistically. Two types of bonding models are provided in PFC: a contact-bonded model and parallel bonded model. In both bonded-models, the bonds are broken when the stress acting on the bonds exceed the bond strength. For a parallel bonded model, micro-properties including normal/shear bond strength, normal/shear bond stiffness, and bond radius are necessary. In a parallel bonded model, force and bending moment can be calculated at the imaginary circular section including contact point. In a contact-bonded model, the radius of an imaginary circular section is assumed as zero, and hence, only force can be transmitted during simulation. Therefore, micro-properties of bond stiffness and bond radius are not necessary for a contact-bonded model. However, even after breakage of bonds, macro stiffness may not decrease significantly because contact stiffness at the active contact remains. While, in a parallel bonded model, macro stiffness consists of contact stiffness and bond stiffness, and therefore, macro stiffness decreases if bond breakage occurs (Cho et al., 2007).

In this study, a parallel bonded-model was applied to construct a numerical model in PFC 2D. In Goheung diorite and Linyi sandstone specimens, although peak friction angle showed a decrease, the decrease was not induced by mechanical behavior but minerals. Mineralogical behavior such as adsorption and dissolution is difficult to simulate in PFC, but mechanical behavior such as asperity degradation can be expressed successfully in shear tests (Park and Song, 2009). Thus, in this study, only the simulation of cement-mortar specimens including discontinuities was simulated. The micro-properties were calibrated against the macro-properties of cement-mortar specimens in Table 3.1.1 by trial and error method. Table 5.1.1 lists the determined micro-properties and the macro-properties obtained

from numerical simulation by PFC2D.

Table 5.1.1 Mechanical, thermal and hydraulic micro-properties of particles, parallel bonds and smooth joint contacts of cement-mortar specimens and the macro properties tested from the simulation of uniaxial compression test by PFC2D.

Micro-properties	Value
Particle density (kg/m ³)	2650
Minimum particle size (mm)	0.24
Particle size ratio	1.66
Number of particles	17848
Friction coefficient of particles	0.6
Young's modulus of particles (MPa)	42.0×10 ³
Parallel bond elastic modulus (MPa)	9.5×10 ³
Parallel bond stiffness ratio	0.85
Parallel-bond radius multiplier	1.0
Parallel normal bond strength (MPa)	51.0
Parallel normal bond strength standard deviation	5.1
Parallel shear bond strength (MPa)	51.0
Parallel shear bond strength standard deviation	5.1
Smooth joint micro-properties	
Smooth joint normal stiffness (MPa/mm)	100
Smooth joint shear stiffness (MPa/mm)	50
Smooth joint coefficient of friction	0.68
Smooth joint dilation angle	0.0
Thermal micro-properties	
Coefficient of linear thermal expansion (10 ⁻⁶ /°C)	10.0
Specific heat at constant volume (J/kg°C)	976.94
Hydraulic micro-properties	
Initial hydraulic aperture (m)	2.2×10 ⁻⁶
Infinite hydraulic aperture (m)	2.2×10 ⁻⁷
Bulk modulus of the fluid (GPa)	2.15
Macro-properties	
Uniaxial compressive strength (MPa)	81.5
Young's modulus (MPa)	35.9×10 ³
Poisson's ratio	0.34
Brazilian tensile strength (MPa)	13.8

5.2 Smooth joint model

Two methods has been generally applied to model shear tests in PFC: bond removal method and smooth joint model. In bond removal method, bonds between particles lying on a discontinuity are removed, and many previous researchers have applied this approach (Cundall, 1999; Jing and Stephansson, 2007; Park and Song, 2009). However, even flat discontinuity have an inherent micro-scale roughness due to the circular shape, non-uniform size and distribution of particles. Therefore, this results in unrealistic shear behaviors, such as drastic shear stress drop after peak shear stress and stress concentration at the bonds of some interlocking particles (Pierce et al., 2007; Mas Ivars et al., 2011; Bahaaddini et al., 2013, 2014, and 2015). In order to overcome this problem, the smooth joint model was newly developed for simulation of rock discontinuities in PFC. Fig. 5.2.1 shows a schematic diagram of the particles assigned smooth joint contacts. Once a specified smooth joint is identified, then the local particle contact orientation is forced to be arranged parallel to the smooth joint. Then, the particles that lie upon the opposite sides of a specified discontinuity can overlap and slide past each other, rather than move around one another (Pierce et al., 2007).

The smooth joint model is assumed as a circular shaped disk, and the geometry is defined by the center point, the radius and the normal vector orientation of the disk. Micro-properties of the smooth joint model including normal/shear stiffness, the coefficient of friction and dilation angle should be defined. The relationship between force and displacement is governed by Coulomb sliding model with dilation. Thus, when a certain normal force

(F_n) is applying, the greatest magnitude of shear force (F_s^*) of a smooth joint contact is defined by equation (5.1).

$$F_s^* = \mu F_n \quad (5.1)$$

In equation (5.1), μ is the friction coefficient of a smooth joint contact, and sliding occurs when a shear force acting on a smooth joint contact exceeds F_s^* . In this study, the micro-properties were determined against the multistage triaxial compression test results of the cement-mortar specimens including a flat discontinuity, and the determined parameters were listed in Table 5.1.1. Fig. 5.2.2(a) shows the numerical model used in the validation process. Fig. 5.2.2(b) is the relation between shear stress and effective normal stress comparison of the laboratory test and the numerical simulation.

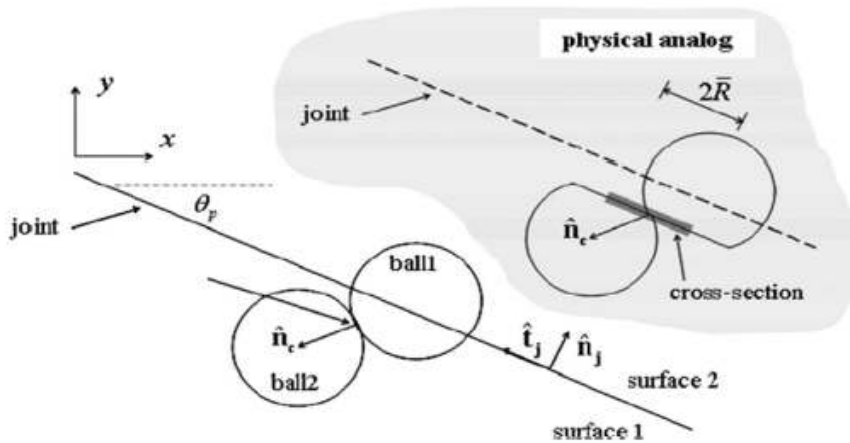


Fig. 5.2.1 A schematic diagram of the particles assigned smooth joint contacts (from Mas Ivars et al., 2011).

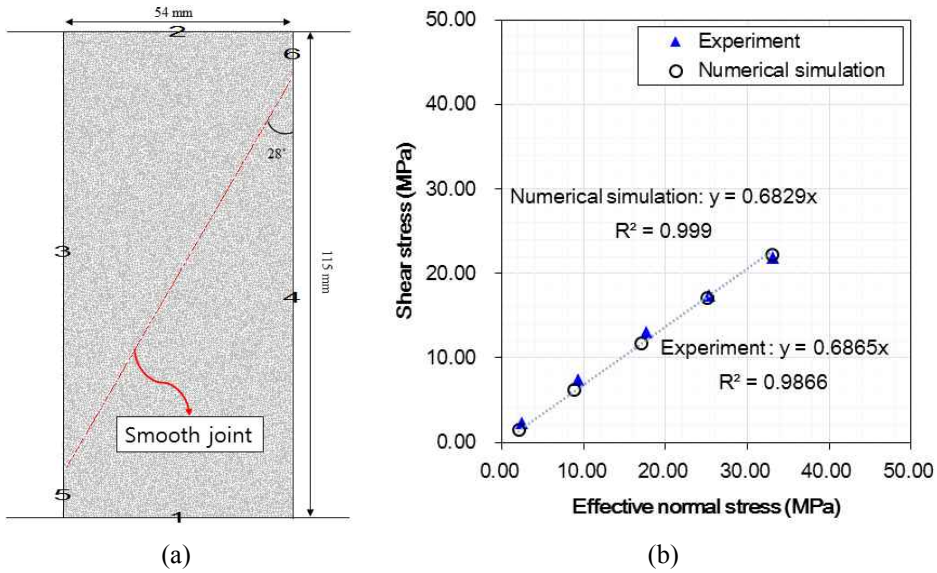


Fig. 5.2.2 A numerical model used in the validation process and the result: (a) a numerical model including a flat discontinuity and (b) relationship between shear stress and effective normal stress from a multi-stage triaxial compression test and a numerical simulation on a flat discontinuity.

5.3 TM coupling simulation in PFC2D

The thermal option of PFC2D allows development of thermally induced displacements and forces. Heat is only transferred by conduction by assuming that strain changes play a negligible role in influencing temperature (Carslaw and Jaeger, 1959). The model is regarded as a network of heat reservoirs (each particle) and thermal pipes (contacts). Each particle is associated with a temperature, a mass, a volume, a specific heat and a linear thermal expansion coefficient.

In case that the temperature changes, firstly, thermally induced strains and expansion occur by the change of the particle radii (ΔR) through equation (5.2). Then, thermal expansion accounts for the normal component of the force vector (ΔF_n) by effectively changing the bond length as shown in equation (5.3).

$$\Delta R = \alpha R \Delta T \quad (5.2)$$

$$\Delta F_n = -K_n A (\alpha L \Delta T) \quad (5.3)$$

In equation (5.2) and (5.3), α is the linear thermal expansion coefficient, ΔT is the temperature change, K_n is the parallel bond normal stiffness, A is the area of the parallel bond cross-section, and L is the bond length and ΔT temperature change. The force increment generated by thermal expansion is then added to the current value of the force vector. When simulating a granular material, the value of linear thermal expansion coefficient of material should correspond to that of each particle. That

means thermal heterogeneity of rock specimens can be easily modeled by changing the micro-properties of particles (ITASCA, 2008; Wanne & Young, 2008; Lee et al., 2012). However, the emphasis of this study is not the investigation of thermal heterogeneity, but the effect of thermal expansion on roughness change and thermal stress. In the XRD analysis (Table 3.1.2), dolomite is accounted for 70% of cement-mortar. Walter and Wilard (1944) stated that linear thermal expansion coefficient of dolomite is in the range of 8.1×10^{-6} and $10 \times 10^{-6}/^{\circ}\text{C}$, and therefore, the values of α for every particle were assumed as $10 \times 10^{-6}/^{\circ}\text{C}$ in this study (Table 5.1.1).

5.4 HM coupling simulation in PFC2D

Cundall (2000) introduced a developed code for simulation of fluid flow in PFC, and various studies have been carried out to simulate the hydro-mechanical coupled behavior in rocks using this algorithm (Hazzard et al., 2002; Shimizu, 2004). In the fluid flow algorithm, the fluid network consists of lines connecting the centers of all particles in contact, green lines in Fig. 5.4.1. These lines generate a series of enclosed domains (Fig. 5.4.1, green polygons), and the centers of the domains are assumed as reservoirs which can store fluid pressures (Fig. 5.4.1, blue circles). The reservoirs are linked by flow channels (Fig. 5.4.1, blue lines), which are perpendicular to the particle contacts. The increment of fluid pressures (ΔP) are calculated from the fluid bulk modulus (K_f), the volume of the domain (V_d) and the volumetric flow rate (Q) through equation (5.4):

$$\Delta P = \frac{K_f}{V_d} (\sum Q \Delta t - \Delta V_d) \quad (5.4)$$

where, ΔV_d is the change in the volume of the domain due to mechanical loading, and Δt is time step. In the simulation, the volumetric flow rate is calculated assuming laminar flow between two parallel plates having smooth surfaces. If a fluid pressure of a reservoir is applied on the surrounding particles, then deformation and movements of the particles affect the contact normal force and the increase of contact normal force induces the decrease of aperture asymptotically. Therefore, it is important to define hydraulic micro-properties such as the size of aperture and bulk modulus of the fluid

to model the fluid flow in rock mass realistically. The properties are usually determined by a permeability test (Jung et al., 2013; Yoon et al., 2015; Zhou et al., 2016). However, in this study, the water pressure was maintained constant during the laboratory tests, and the fluid flow during the test is out of the scope of this study. Therefore, the hydraulic properties were assumed referring to Zhou et al. (2016), and the determined micro-properties were listed in Table 5.1.1. During the simulation, the water pressure was only applied on the area nearby the discontinuity and maintained constant.

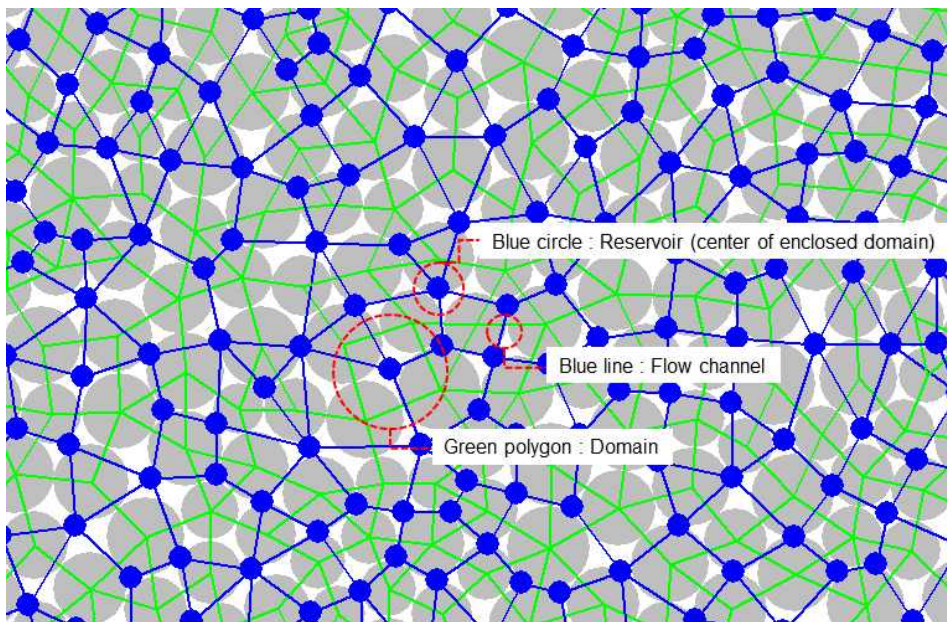
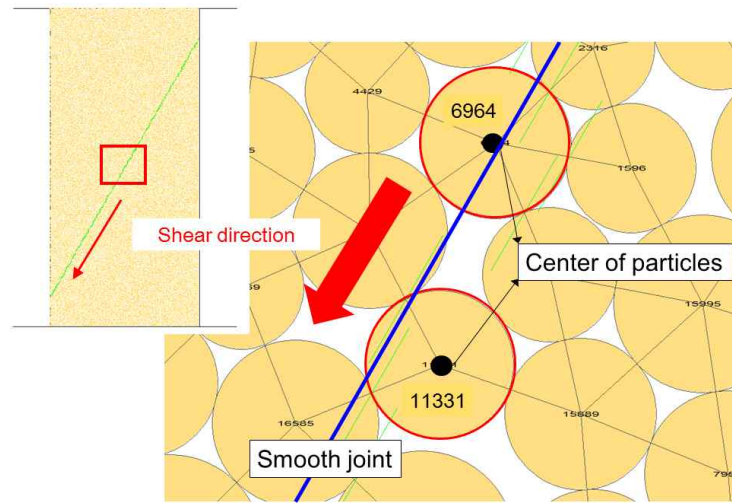


Fig. 5.4.1 A numerical model assigned a fluid network system. Green polygons denotes domains, and blue circles denote reservoirs, which are placed in the center of domains, and blue lines are flow channels connecting reservoirs.

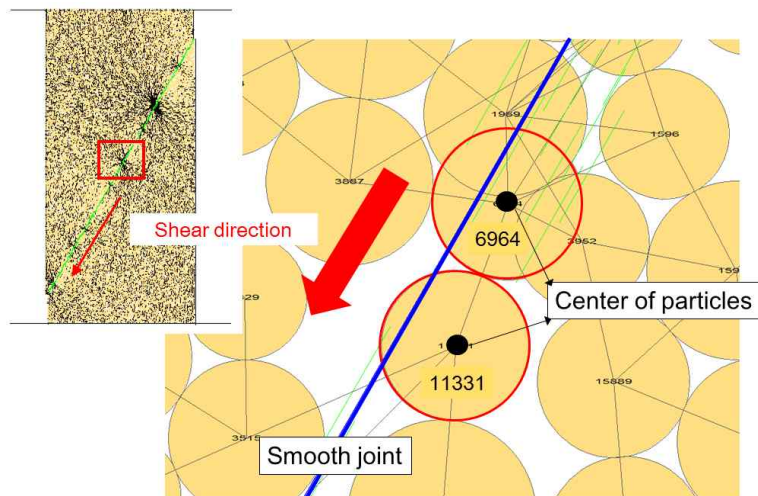
5.5 Numerical model generation

A series of short smooth joint lines with a length of 0.5 mm were connected to generate a discontinuity in the intact numerical model (Fig. 5.5.1). The coordinates of the smooth joint lines were obtained from the center lines of each discontinuity surface, A-A' lines in Fig. 3.1.4(a) and (b). However, when the shear displacement exceeds the minimum particle diameter, some particles of which the centers lying on the opposite side of the discontinuity may move to the same side, and the particles make new contacts with other balls. In that case, smooth joint contacts are not assigned to the newly generated contacts and the particle interlocking induces unrealistic stress concentration (Bahaaddini et al., 2013).

In this study, the same phenomenon was observed in the numerical simulation of the shear test even on flat discontinuity. In Fig. 5.5.1(a), ball 6964 and ball 11331 lie on the opposite side of the smooth joint before shearing. However, after 1 mm of shear displacement, the two balls are placed on the same side of the smooth joint, and hence a smooth joint is not assigned even new contact is generated. Therefore, at this contact, contact forces are concentrated (Fig. 5.5.1(b)), and as a result, unrealistic shear behavior was observed.



(a)



(b)

Fig. 5.5.1 Enlarged view of particle interlocking in a smooth joint model of a flat discontinuity: (a) before shearing and (b) after 1 mm shear displacement.

To solve this problem, Bahaaddini et al. (2013) proposed a new approach to generating a numerical model with a separated shear box. In this study, to make the shear behavior realistically, a similar procedure was

applied in model generation.

1) Material vessels generation: Each upper and lower model consists of four walls. For instance, the lower model consists of wall 1, 4, 5 and 8 in Fig. 5.5.2(a). In PFC, only one side of a wall is active (Itasca, 2008), and therefore, two walls (wall 7 and 8) are required.

2) Lower model generation: After material vessels generation, a lower model is generated (Fig. 5.5.2(b)). The minimum particle size was 0.24 mm (Table 5.1.1), and seven measurement circles are installed to check equilibrium state.

3) Upper model generation: An upper model is generated in the same way of a lower model generation (Fig. 5.5.2(c)).

4) Acquisition of the information of an upper model: To combine the upper and the lower model, firstly, obtain the coordinates and the radius of the particles of the upper model.

5) Combination of the lower and the upper model: Generate particles using the information of the particles of the upper model onto the lower model (Fig. 5.5.2(d)).

6) Applying smooth joints: After generation of a completed model, delete wall 7 and 8, and insert a smooth joint model along the discontinuity.

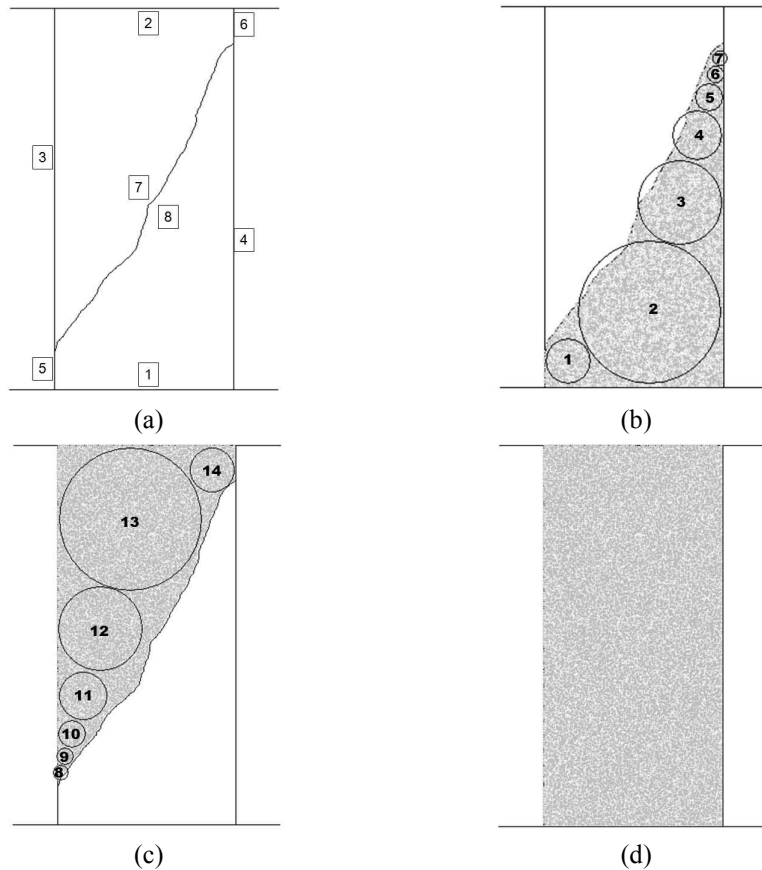


Fig. 5.5.2 Procedure of a numerical model generation (JRC=11.63): (a) material vessels generation, (b) lower model generation, (c) upper model generation, and (d) combination of the lower and the upper model.

From this procedure, a total of 17848 particles were generated, and after that smooth joint contacts were inserted along with the coordinates of the discontinuities. A series of numerical simulations were performed in the same process with laboratory tests at each testing condition, and Fig. 5.5.3 shows the flowchart of the numerical simulation. In the case of the simulations at room temperature and dry conditions, firstly, axial loading and confining pressure were applied to the target pressure maintaining hydrostatic

state by controlling wall velocity. Axial loading was controlled by wall 1 and 2, and confining pressure was controlled by wall 3, 4, 5 and 6 (Fig. 5.5.2(a)). After hydrostatic state, axial loading was applied until the axial displacement reached at 1.5 mm to investigate the shear behavior after peak shear stress. In the simulations at an elevated temperature of 80°C, heating was firstly applied to all the particles simultaneously, and then loading was applied. During the heating process, walls were not constrained to prevent thermal stress, which was the same state compared to that of the laboratory tests.

For HM simulation, reservoirs are only generated at the spaces which are surrounded by the particles connected by bonds. In the model generation procedure, lower and upper models were generated separately, and hence, the particles lying on the smooth joint line have neither contacts nor bonds at the initial stage (Fig. 5.5.4(a)). Therefore, firstly, hydrostatic pressures were applied to make contacts, and weak parallel bonds were installed where the particles were newly contacted along the smooth joint line (Fig. 5.5.4(b)). The parallel bonds were weak not enough to affect the shear behavior and were broken immediately after loading started. After this procedure, flow network could be created successfully even on the discontinuity. In the numerical simulation, water pressure was applied in the vicinity along the discontinuity, and the width was 1.0 cm (Fig. 5.5.5) considering low permeability of the specimen.

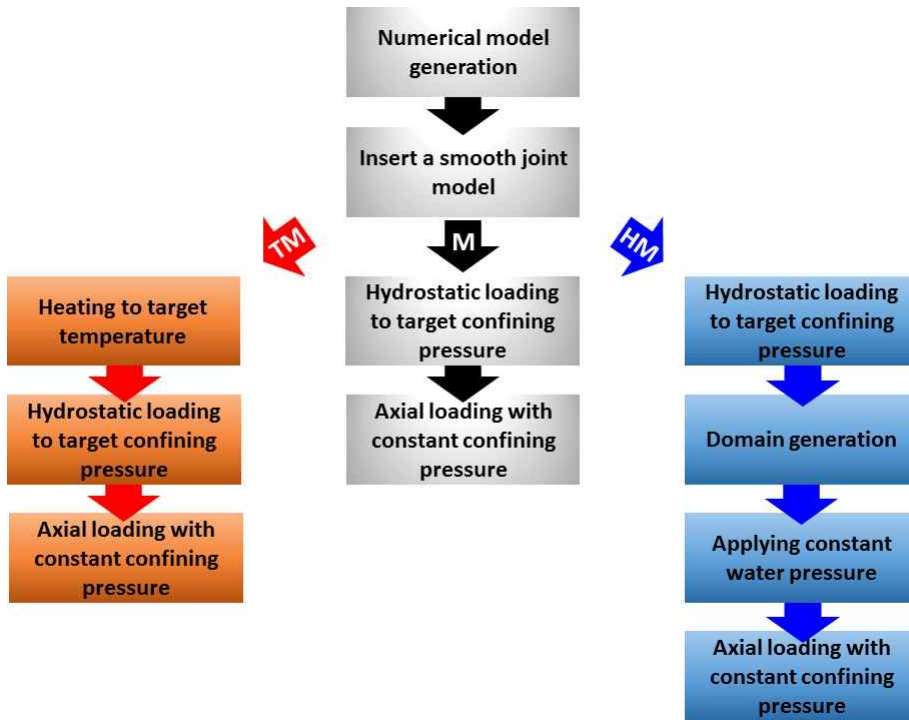
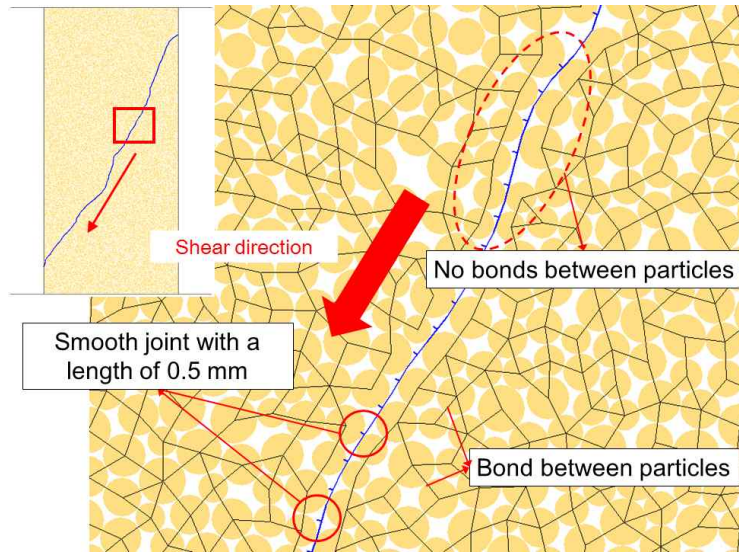
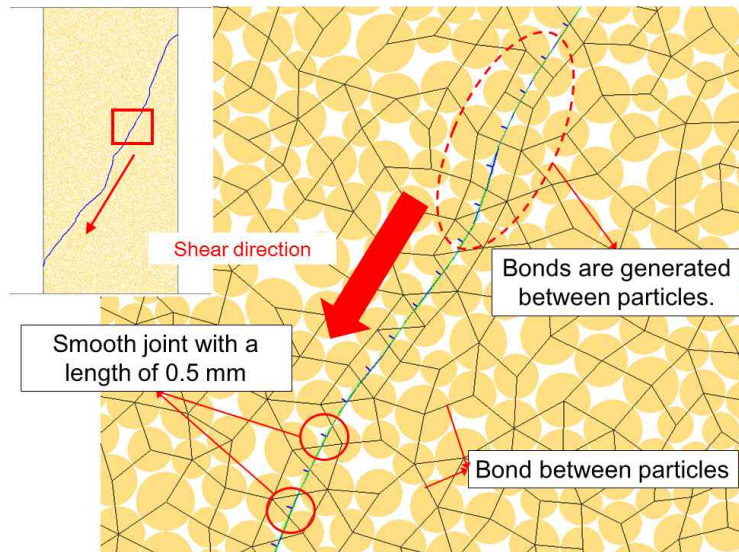


Fig. 5.5.3 Flowchart of numerical simulation at each testing conditions. In the flow chart, ‘M’ means the simulation at room temperature and dry conditions, ‘TM’ is the simulation at 80°C and dry conditions, and ‘HM’ means the simulation at room temperature with 3 MPa of water pressure.



(a)



(b)

Fig. 5.5.4 Enlarged view of bonds between particles: (a) initial stage and (b) after hydrostatic pressure. At the initial stage, particles lying on the smooth joint line have neither contacts nor bonds. However, after hydrostatic pressure, contacts are generated and weak parallel bonds are installed on that particles for flow network generation.

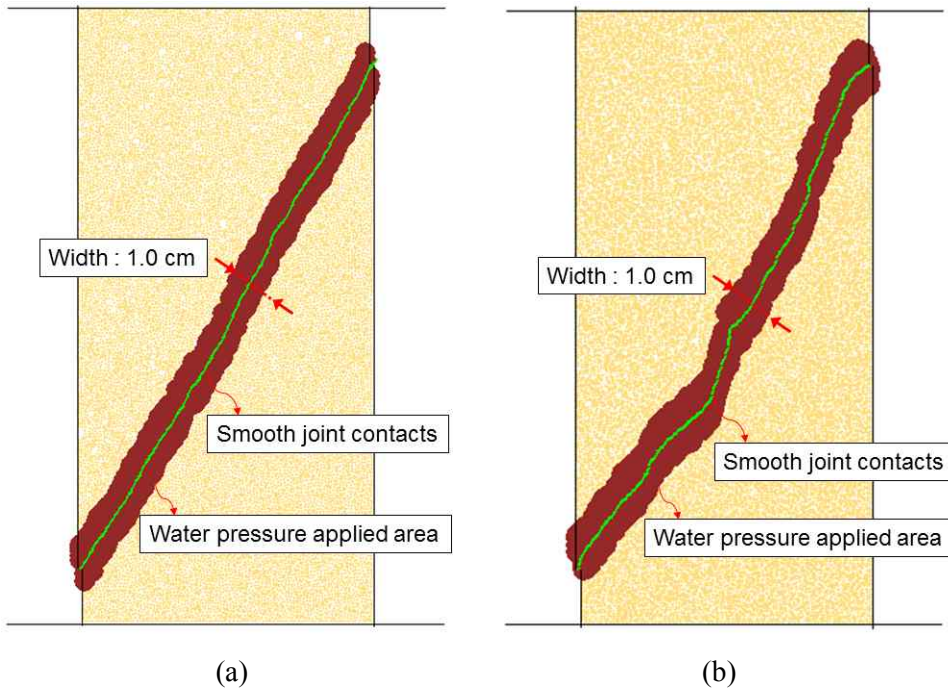


Fig. 5.5.5 Numerical models with a smooth discontinuity ($JRC=2.05$) and a rough discontinuity ($JRC=11.63$): (a) $JRC=2.05$ and (b) $JRC=11.63$. Green lines are smooth joint contacts (discontinuity), and brown colored region denotes the area where water pressure was applied with a width of 1.0 cm.

5.6 Simulation results

5.6.1 Simulation results of a smooth discontinuity

(1) Results at room temperature and dry conditions

A series of numerical simulations in PFC2D were performed under various testing conditions. The shear properties including effective normal stress, shear stress and dilation in the numerical simulations were calculated in the same way of the experiments analysis. Fig. 5.6.1 shows an example of the comparison between the numerical simulation and the experiment of a smooth discontinuity ($JRC=2.05$) when the confining pressure is 10 MPa at room temperature and dry condition. The results obtained from the numerical simulations showed a good match with the experimental data (Figs. 5.6.1 and 5.6.2). Table 5.6.1 provides the results of the numerical simulation, and the peak friction angles were investigated divided into two groups depending on the normal stress (Fig. 5.6.3). Compared to the experimental results, the values of peak friction angle showed similar results, and forth by 10 MPa, peak friction angle decreased. At low normal stress below than 10 MPa, peak friction angle was 45.1° , and at high normal stress greater than 10 MPa, 31.5° . The decreased peak friction angle at higher normal stress approximates 34.3° , the basic friction angle of a numerical model including a flat joint (Fig. 5.2.2(b)). Peak shear stress was observed when shear displacement reached at 0.1~0.6 mm (Fig. 5.6.5(b)). The microcracks were initiated at 40~60% of the peak shear stress, and after peak shear stress, the number of microcracks increased rapidly (Fig. 5.6.4) at every confining pressure.

Microcracks and contact forces at each confining pressures at a shear

displacement of 1.2 mm were compared to investigate the asperity degradation (Figs. 5.6.6 and 5.6.7). As confining pressure increased, the number of microcracks along the discontinuity increased. Especially, at low normal stress less than 10 MPa, microcracks were rarely observed, and that means sliding were predominant than shearing accompanying with asperity degradation. However, at high normal stress greater than 10 MPa, both the number of microcracks and the damaged area (red and black color in Fig. 5.6.6) increased. This observation corresponds well to the experimental results and also proves asperity degradation can occur at high normal stress greater than 10 MPa in this study.

Additionally, contact forces were concentrated on where the uphill slopes of the asperities are placed at low normal stress condition. However, at high normal stress, the contact force was distributed comparatively evenly along the discontinuity, because after asperity degradation, the contact area increased. Patton (1966b) classified asperity into first-order (waviness) and second-order (unevenness) categories. Barton (1973) noted that the second-order asperity is sheared off as the normal stress increases, and the first-order asperity plays as a critical factor in shear behavior. While, locally, the failure of second-asperity can be occurred by tensile failure (Handanyan et al., 1990), and tensile cracks accounted for more than 80% of the total number of cracks at each confining pressure (Table 5.6.1). Therefore, the results of numerical simulation in this study matched well with those explanations.

As confining pressure increased, effective normal stress was raised together, and contraction was observed before peak shear stress (Fig. 5.6.5). After peak shear stress, effective normal stress and shear stress became

stable, same with experimental results, and dilation started. Normal and shear stiffness increased with the increase of the confining pressure (Fig. 5.6.8), and normal stiffness showed higher values than shear stiffness. Dilation was also investigated, and dilation angle decreased as the confining pressure increased. The results of dilation angle showed a good agreement compared to the results of the empirical equation of Barton and Choubey (1977) (Fig. 5.6.9).

Table 5.6.1 Results of the numerical simulations on smooth discontinuities (JRC=2.05) at various testing conditions.

Testing condition	Confining pressure (MPa)	Effective normal stress (MPa)	Peak shear stress (MPa)	Peak friction coefficient	Normal stiffness (MPa/mm)	Shear stiffness (MPa/mm)	Dilation angle (°)	Number of cracks after 1.2 mm of shear displacement		Peak friction angle (°) (coefficient of friction)			Cohesion (MPa) ($\sigma_n > 10$ MPa)
								Tensile crack	Shear crack	Total	$\sigma_n < 10$ (MPa)	$\sigma_n > 10$ (MPa)	
M (20°C / Dry)	0.50	1.70	1.92	1.13	55.82	28.30	4.82	2.00	0.00	36.1 (0.7297)	45.1 (1.0026)	31.5 (0.6130)	3.1
	1.00	2.73	2.84	1.04	48.95	28.36	4.32	2.00	0.00				
	2.00	4.74	4.61	0.97	50.92	29.09	3.25	9.00	0.00				
	10.0	18.43	14.30	0.78	65.31	44.06	1.28	85.00	7.00				
	15.0	26.46	19.61	0.74	71.02	48.11	0.95	88.00	18.00				
	20.0	33.95	23.81	0.70	75.03	52.42	0.76	158.00	36.00				
TM (80°C / Dry)	0.50	1.70	1.92	1.13	52.32	28.09	4.70	2	0	36.4 (0.7364)	45.1 (1.0031)	32.9 (0.6472)	2.4
	1.00	2.72	2.83	1.04	51.04	26.57	4.14	2	0				
	2.00	4.74	4.62	0.97	72.51	12.60	3.76	13	0				
	10.0	18.39	14.27	0.78	67.90	44.73	1.46	95	11				
	15.0	26.47	19.59	0.74	72.22	45.83	0.88	104	23				
	20.0	34.44	24.65	0.72	72.14	51.08	0.73	168	43				
HM (20°C / water pressure : 3MPa)	3.50	1.77	2.13	1.21	43.82	2.10	4.99	2.00	0.00	36.7 (0.7453)	45.8 (1.0285)	32.4 (0.6345)	2.4
	4.00	2.78	3.02	1.09	44.48	20.60	4.12	2.00	0.00				
	5.00	4.76	4.71	0.99	64.88	30.89	3.11	9.00	0.00				
	10.0	13.47	11.02	0.82	73.68	35.62	1.91	42.00	3.00				
	15.0	21.30	15.91	0.75	84.56	42.94	1.39	105.00	13.00				
	20.0	29.32	21.12	0.72	86.55	44.66	0.90	127.00	20.00				

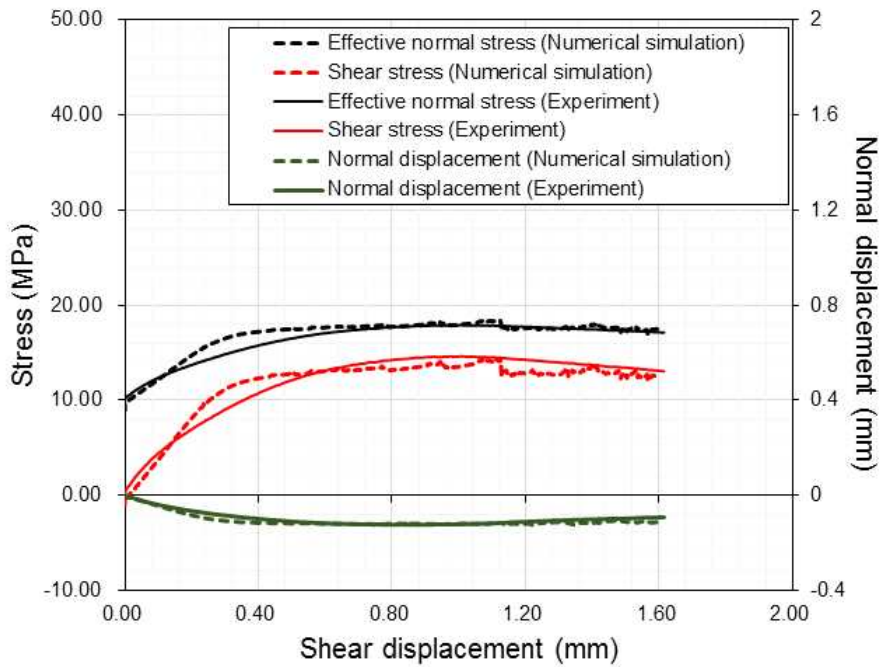


Fig. 5.6.1 Effective normal stress, shear stress, normal displacement versus shear displacement of cement-mortar specimens including smooth discontinuities ($JRC=2.05$) when the confining pressure was 10 MPa at room temperature and dry conditions in both experimental test and the numerical simulation (PFC2D).

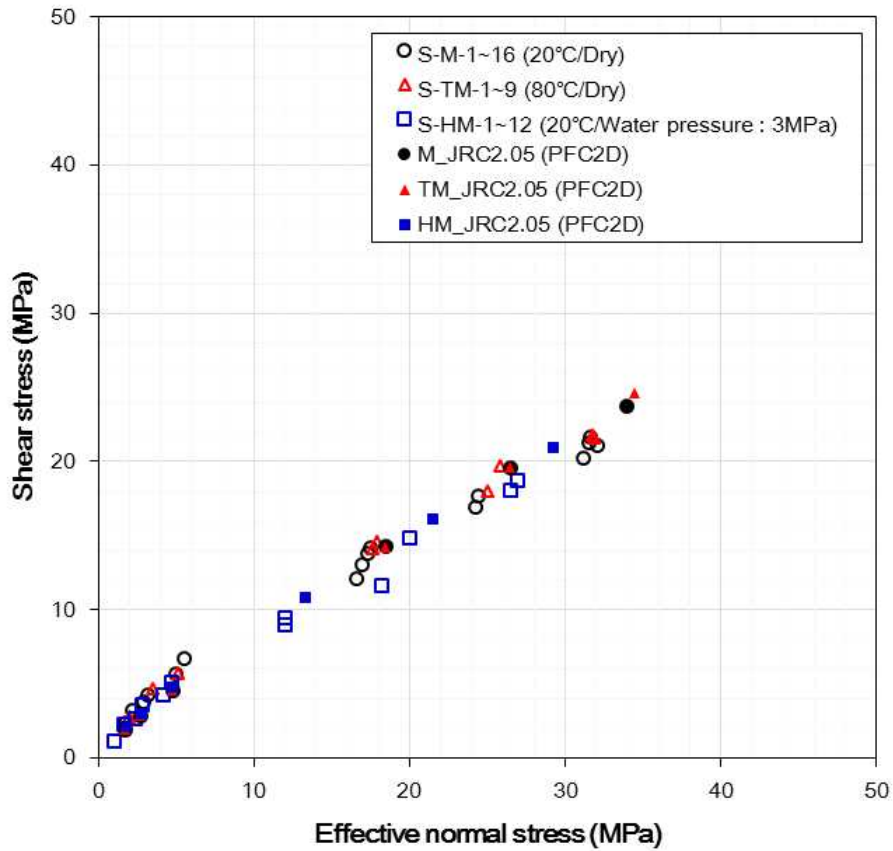


Fig. 5.6.2 Relation between effective normal stress and shear stress of cement-mortar specimens including smooth discontinuities (JRC=2.05) at various testing conditions in both experimental tests and the numerical simulation (PFC2D).

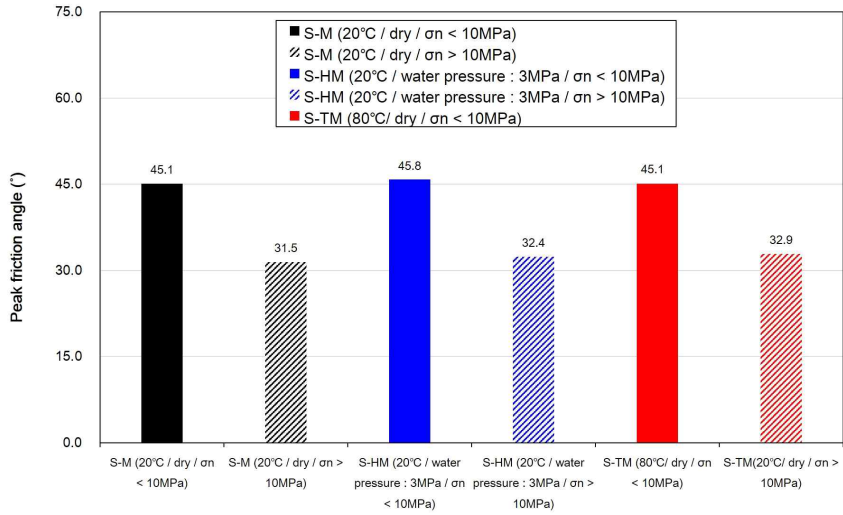


Fig. 5.6.3 Peak friction angles of cement-mortar specimens including smooth discontinuities ($JRC=2.05$) depending on normal stress and various testing conditions obtained from the numerical simulations.

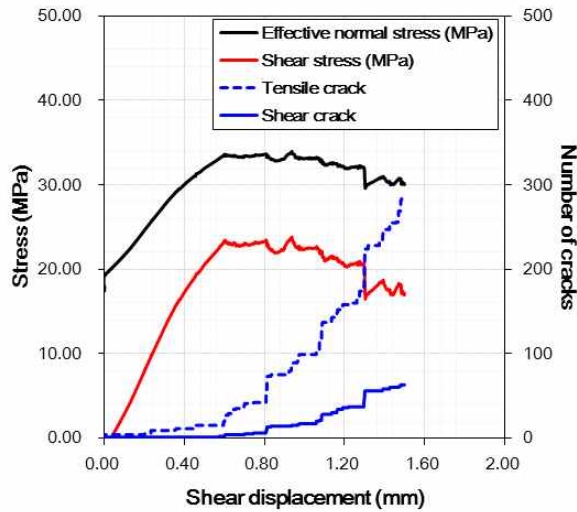
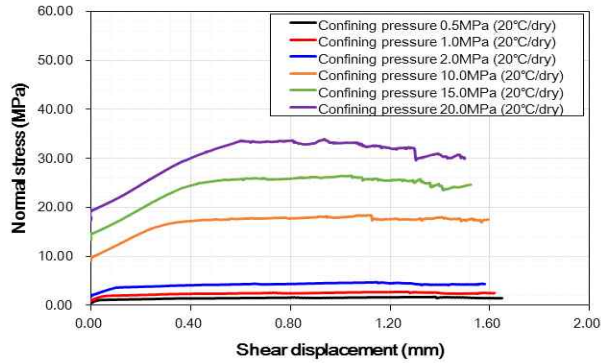
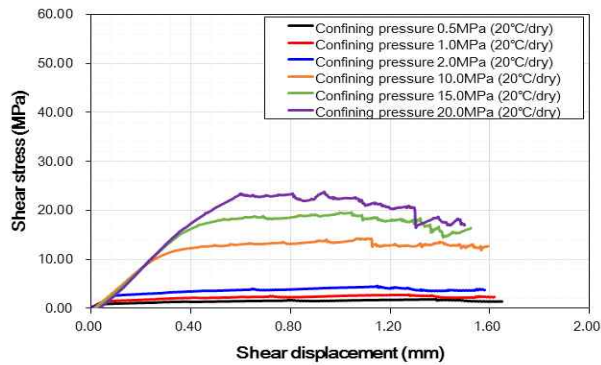


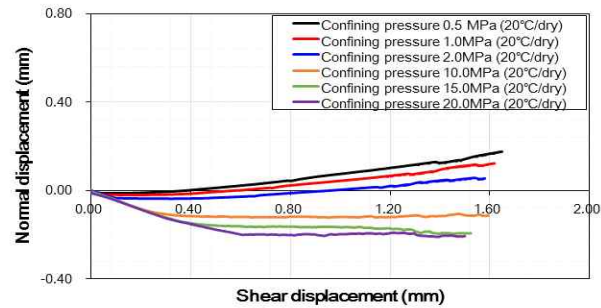
Fig. 5.6.4 Effective normal stress, shear stress and cumulative crack numbers versus shear displacement of cement-mortar specimens including a smooth discontinuity ($JRC=2.05$) when the confining pressure was 20 MPa at room temperature and dry conditions in the numerical simulation.



(a)



(b)



(c)

Fig. 5.6.5 Effective normal stress, shear stress, normal displacement versus shear displacement of cement-mortar specimens including smooth discontinuities ($JRC=2.05$) at various testing conditions in the numerical simulations (confining pressure: 0.5, 1, 2, 10, 15, 20 MPa/20°C/dry condition): (a) effective normal stress, (b) shear stress, and (c) normal displacement versus shear displacement.

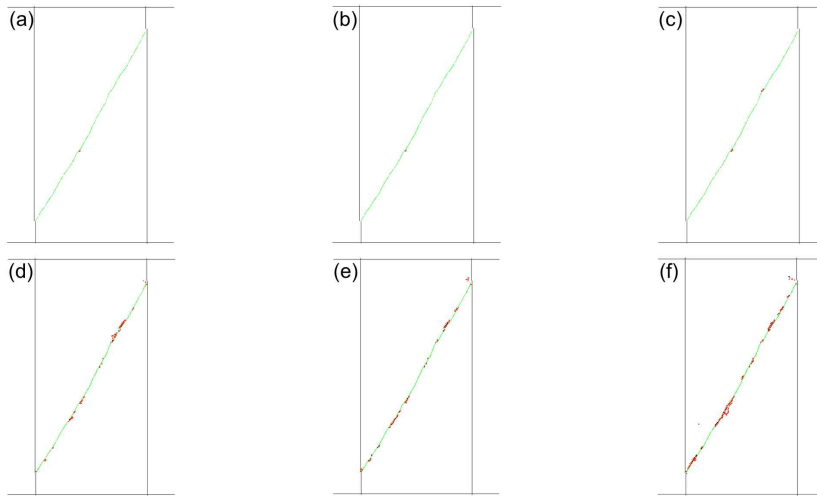


Fig. 5.6.6 Microcracks at a shear displacement of 1.2 mm on smooth discontinuities ($JRC=2.05$) at room temperature and dry condition depending on confining pressure: (a) 0.5 MPa, (b) 1.0 MPa, (c) 2.0 MPa, (d) 10.0 MPa, (e) 15.0 MPa, and (f) 20.0 MPa (red : tensile crack, black : shear crack).

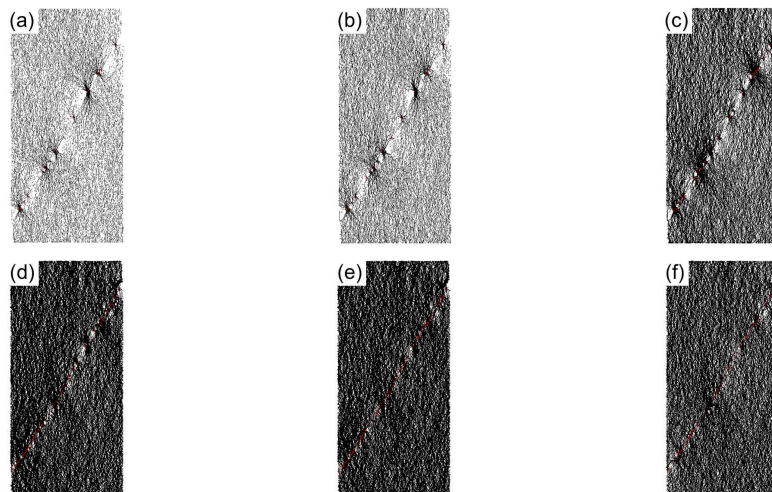
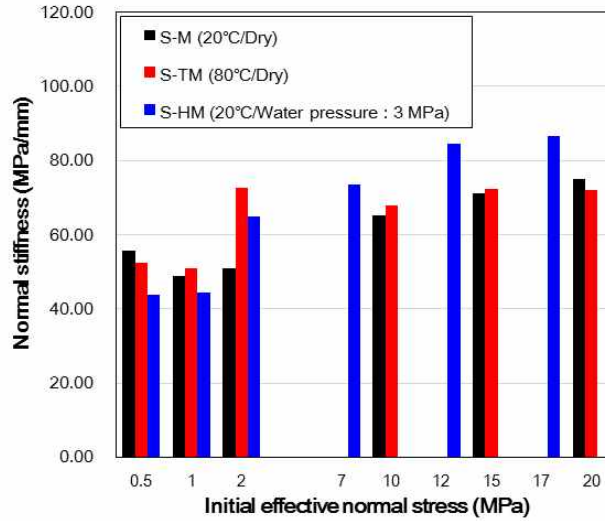
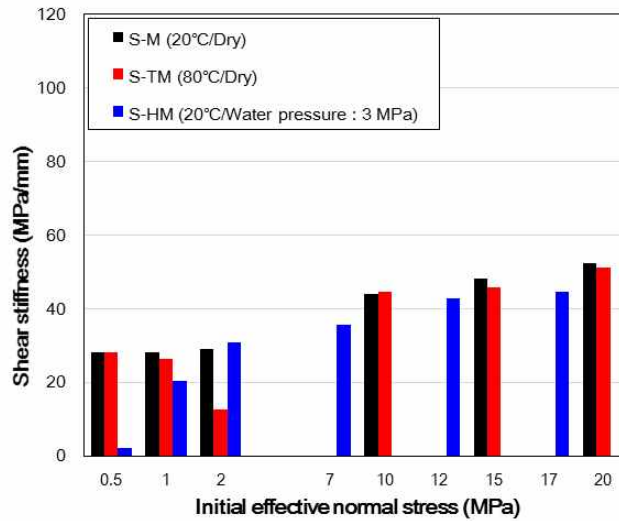


Fig. 5.6.7 Contact forces (black in compression and red in tension) at a shear displacement of 1.2 mm on smooth discontinuities ($JRC=2.05$) at room temperature and dry condition depending on confining pressure: (a) 0.5 MPa, (b) 1.0 MPa, (c) 2.0 MPa, (d) 10.0 MPa, (e) 15.0 MPa, and (f) 20.0 MPa.



(a)



(b)

Fig. 5.6.8 Relation between normal, shear stiffness and initial effective normal stress of cement-mortar specimens including smooth discontinuities (JRC=2.05) at various testing conditions obtained from the numerical simulations.: (a) normal stiffness and (b) shear stiffness.

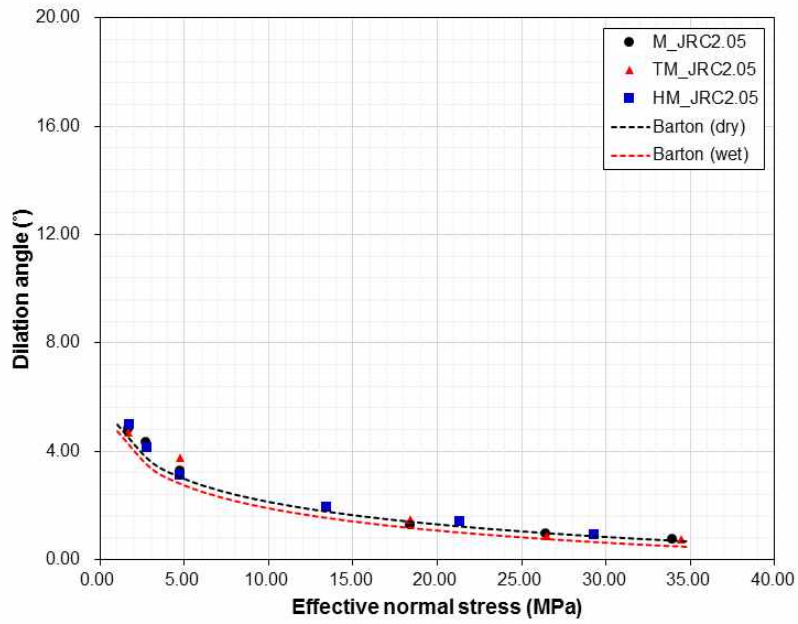


Fig. 5.6.9 Relation between dilation angle and effective normal stress of cement-mortar specimens including smooth discontinuities (JRC=2.05) at various testing conditions obtained from the numerical simulations.

(2) Results at 80°C

After heating the particles up to 80°C, confining pressures were applied, and then loading was started. Peak friction angle at low normal stress was 45.1°, and 32.9° at high normal stress greater than 10 MPa. Peak friction angle did not show any variations at an elevated temperature of 80°C in this study (Fig. 5.6.3). The other results including shear and normal stiffness, dilation angle and number of cracks also did not show much variation compared to the results at room temperature in this study (Figs. 5.6.8 and 5.6.9). This tendency also coincides well with the experimental results.

(3) Results at room temperature with water pressure

3 MPa of water pressure was applied along the discontinuity after applying confining pressure in the numerical simulation (Fig. 5.6.5). Peak friction angle at low normal stress was 45.8°, and 32.4° at high normal stress greater than 10 MPa. Unlike the experimental results, it did not show any change compared to the results of the numerical simulation at the dry condition. However, in the experimental results, the decreasing amount was not also high, and the effect of water can increase on more rough discontinuities (Barton, 1973).

The decrease of effective normal stress due to 3 MPa of water pressure was well simulated (Fig. 5.6.2). Normal stiffness, shear stiffness, and dilation angle did not show much variation (Figs. 5.6.8 and 5.6.9). At low normal stress, the number of cracks also did not show much difference. However, at high normal stress, the number of cracks was less than the results of the other conditions. The reason is the lower initial effective normal stresses than those of the other conditions due to the water pressure.

5.6.2 Simulation results of a rough discontinuity

(1) Results at room temperature and dry conditions

Fig. 5.6.10 shows an example of the comparison between the numerical simulation and the experiment of a rough discontinuity (JRC=11.63) when the confining pressure is 10 MPa at room temperature and dry condition. The results of the numerical simulations showed a good agreement with those of experiments (Fig. 5.6.10 and Fig. 5.6.11). However, after peak shear stress, a slight softening behavior of shear stress was observed especially at high normal stress greater than 10 MPa, which might be due to the failure of the undulating rough discontinuities (Figs, 5.6.10 and 14).

At low normal stress below than 10 MPa, peak friction angle was 51.9° , and at high normal stress, 30.0° (Table 5.6.2 and Fig. 5.6.12). The peak friction angle at low normal stress was higher than that of a smooth discontinuity, by 6.8° , which was almost the same amount of experiments, by 6.6° . The peak friction coefficient, the ratio of the peak shear stress to the normal stress, was also increased compared to the results of smooth discontinuities, by 0.08~0.29, which was caused by the rougher discontinuity (Table 5.6.2). While, at high normal stress greater than 10 MPa, the peak friction angle did not show much difference compared to that of a smooth discontinuity, 31.5° . Fig. 5.6.13 shows the relationship between effective normal stress, shear stress, the number of cracks and shear displacement. Microcracks started to occur when the shear stress reached 57% of the peak shear stress, and after peak shear stress, the number of microcracks increased rapidly. In Fig. 5.6.15, at the low normal stress below than 10 MPa, only a few microcracks were observed on the uphill slope of the

discontinuities, where the contact forces were concentrated. However, effective normal stress and shear stress increased with the increase of confining pressure (Figs. 5.6.14(a) and (b)), and as a result, undulating asperities were sheared off by tensile failure (Figs. 5.6.15 (c), (d) and (e)). The distribution of the contact forces also became relatively even along the discontinuity (Figs. 5.6.16 (c), (d) and (e)). Therefore, same with the experimental results, it can be concluded that at high normal stress greater than 10 MPa, the second-order asperities were broken, and after asperity degradation, the effect of the first-order asperity and basic friction angle increases.

Normal and shear stiffness increased with the increase of the confining pressure (Fig. 5.6.17), and normal stiffness showed higher values than shear stiffness. Before peak shear stress, contraction occurred on the discontinuity, and after peak shear stress, dilation was initiated (Fig. 5.6.14(c)). The dilation angles at low normal stress below than 10 MPa matched well with the experimental results and the empirical equation (4.11). However, at high normal stress, the dilation angles in the numerical simulations were overestimated (Fig. 5.6.18). Unlike the experimental results, effective normal stress showed softening behavior after peak shear stress, and therefore, normal displacement increased gradually with decreasing constraint.

Table 5.6.2 Results of the numerical simulations on rough discontinuities (JRC=11.63) at various testing conditions.

Testing condition	Confining pressure (MPa)	Effective normal stress (MPa)	Peak shear stress (MPa)	Peak friction coefficient	Normal stiffness (MPa/mm)	Shear stiffness (MPa/mm)	Dilation angle (°)	Number of cracks after 1.2 mm of shear displacement		Peak friction angle (°) (coefficient of friction)		
								Tensile crack	Shear crack	Total	$\sigma_n < 10$ (MPa)	$\sigma_n > 10$ (MPa)
M (20°C / Dry)	0.50	3.52	4.96	1.41	43.06	12.53	14.60	19	2	40.2 (0.8457)	51.9 (1.2732)	30.0 (0.5776)
	1.00	4.89	6.49	1.33	47.60	18.39	11.12	45	7			
	2.00	7.18	8.72	1.22	43.79	25.92	9.44	65	7			
	10.0	21.67	19.98	0.92	58.18	25.92	5.87	155	34			
	15.0	30.37	26.24	0.86	66.10	50.88	5.53	247	50			
	20.0	36.52	28.41	0.78	79.49	54.02	4.69	592	113			
TM (80°C / Dry)	0.50	3.49	4.94	1.42	41.06	6.70	14.45	19	2	40.6 (0.8562)	52.5 (1.3031)	31.3 (0.6074)
	1.00	4.98	6.62	1.33	50.36	14.57	10.85	44	8			
	2.00	8.09	10.28	1.27	59.35	19.46	9.48	81	10			
	10.0	21.81	20.24	0.93	56.23	41.56	5.44	320	61			
	15.0	30.27	26.13	0.86	63.37	48.76	5.65	425	102			
	20.0	37.23	29.56	0.79	74.26	52.84	5.59	568	120			
HM (20°C / water pressure : 3MPa)	3.50	3.65	5.19	1.42	39.97	7.89	13.24	19	2	40.8 (0.8632)	51.8 (1.2698)	28.4 (0.5409)
	4.00	4.94	6.52	1.32	54.38	13.62	10.70	58	8			
	5.00	7.28	8.79	1.21	51.67	21.67	8.25	69	7			
	10.0	16.75	16.73	1.00	61.13	41.24	5.47	134	24			
	15.0	24.62	21.27	0.86	73.64	39.11	5.76	203	36			
	20.0	31.28	24.58	0.79	86.93	40.03	5.64	303	39			

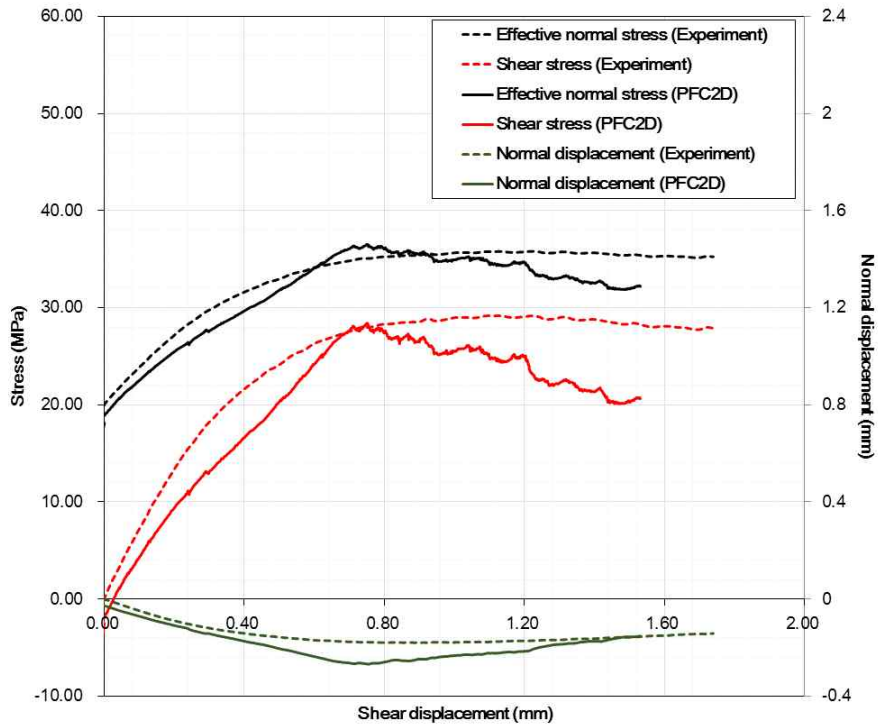


Fig. 5.6.10 Effective normal stress, shear stress, normal displacement versus shear displacement of cement-mortar specimens including rough discontinuities ($JRC=11.63$) when the confining pressure was 20 MPa at room temperature and dry conditions in both experimental test and the numerical simulation (PFC2D).

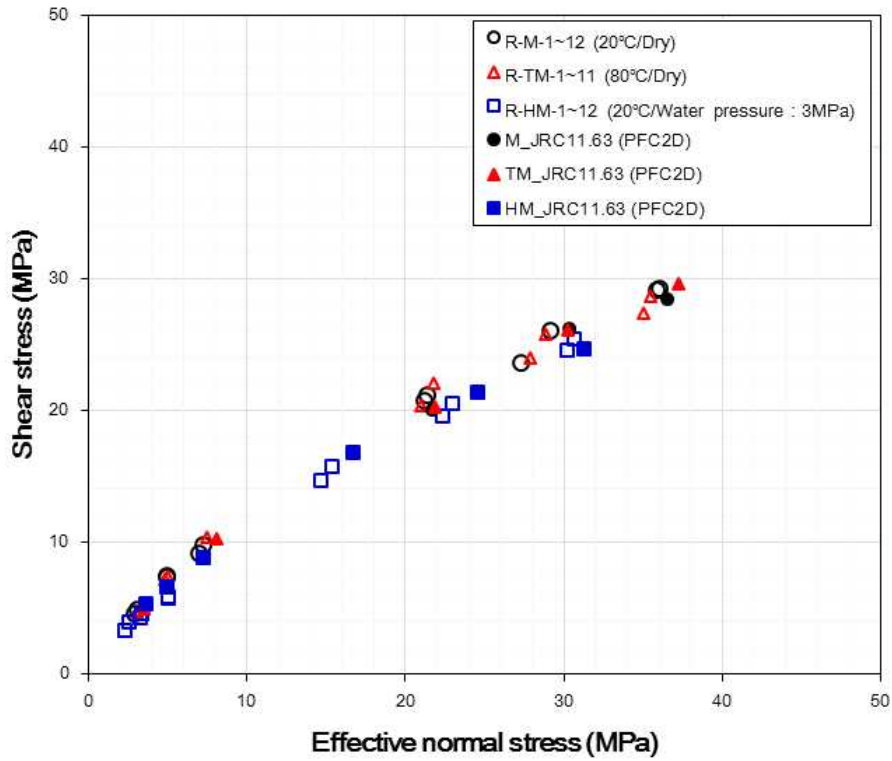


Fig. 5.6.11 Relation between effective normal stress and shear stress of cement- mortar specimens including rough discontinuities (JRC=11.63) at various testing conditions in both experimental tests and the numerical simulation (PFC2D).

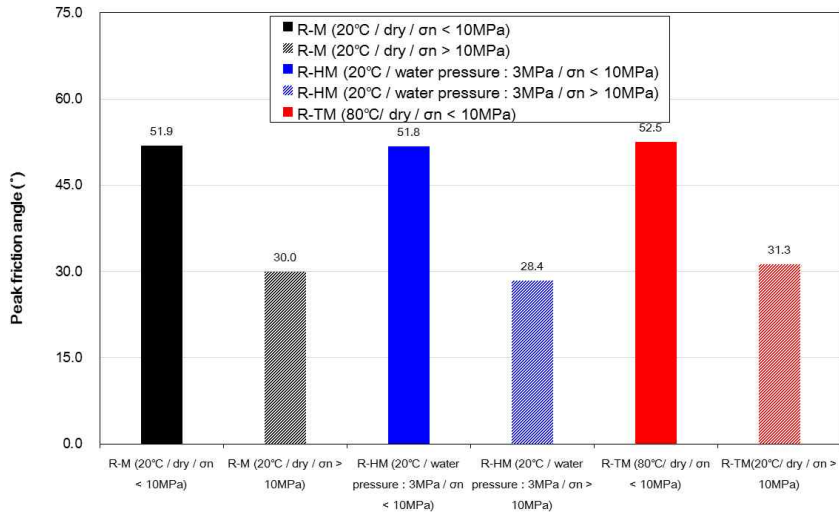


Fig. 5.6.12 Peak friction angles of cement-mortar specimens including rough discontinuities ($JRC=11.63$) depending on normal stress and various testing conditions obtained from the numerical simulations.

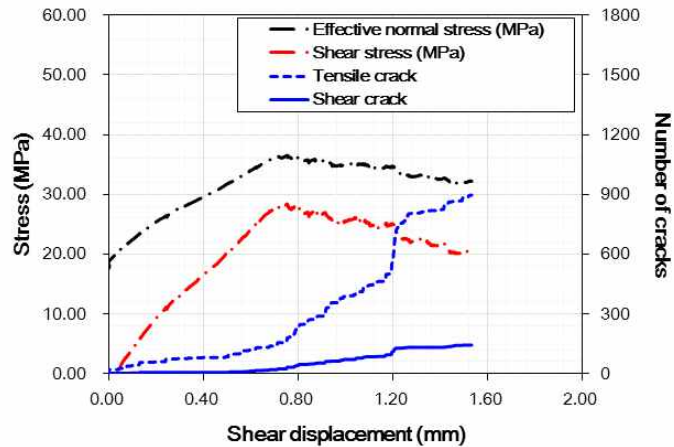
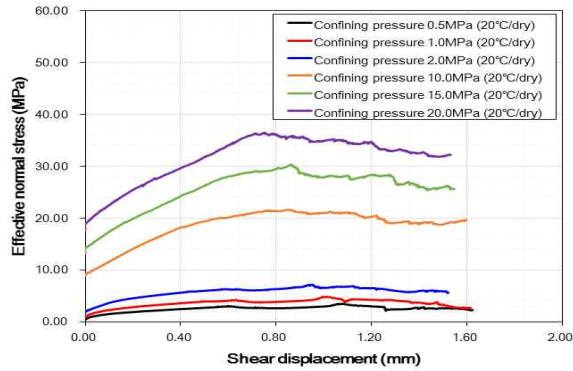
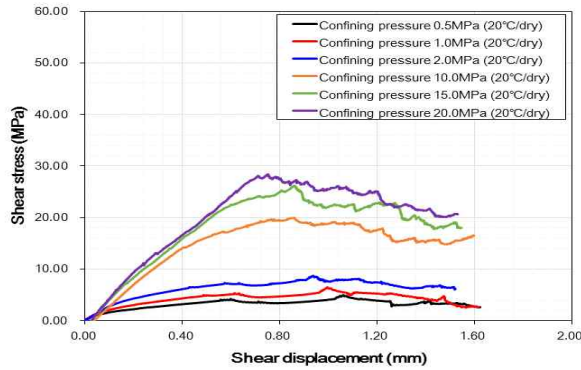


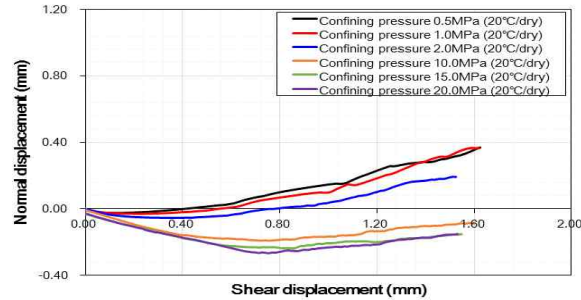
Fig. 5.6.13 Effective normal stress, shear stress and cumulative crack numbers versus shear displacement of cement-mortar specimens including a rough discontinuity ($JRC=11.63$) when the confining pressure was 20 MPa at room temperature and dry conditions in the numerical simulation.



(a)



(b)



(c)

Fig. 5.6.14 Effective normal stress, shear stress, normal displacement versus shear displacement of cement-mortar specimens including rough discontinuities ($JRC=11.63$) at various testing conditions in the numerical simulations (confining pressure: 0.5, 1, 2, 10, 15, 20 MPa/20°C/dry condition): (a) effective normal stress, (b) shear stress, and (c) normal displacement versus shear displacement.

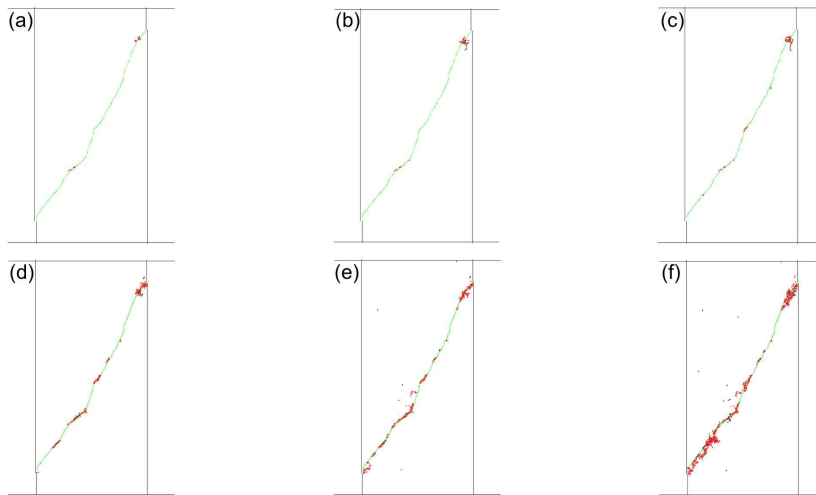


Fig. 5.6.15 Microcracks at a shear displacement of 1.2 mm on rough discontinuities (JRC=11.63) at room temperature and dry condition depending on confining pressure: (a) 0.5 MPa, (b) 1.0 MPa, (c) 2.0 MPa, (d) 10.0 MPa, (e) 15.0 MPa, and (f) 20.0 MPa (red : tensile crack, black : shear crack).

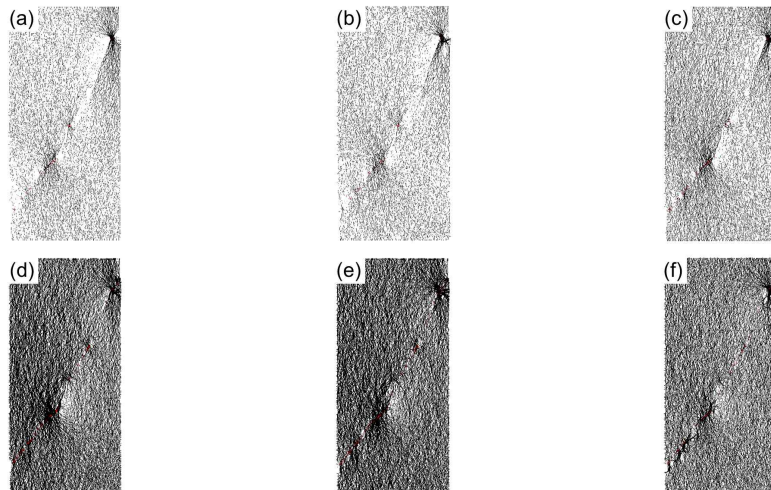
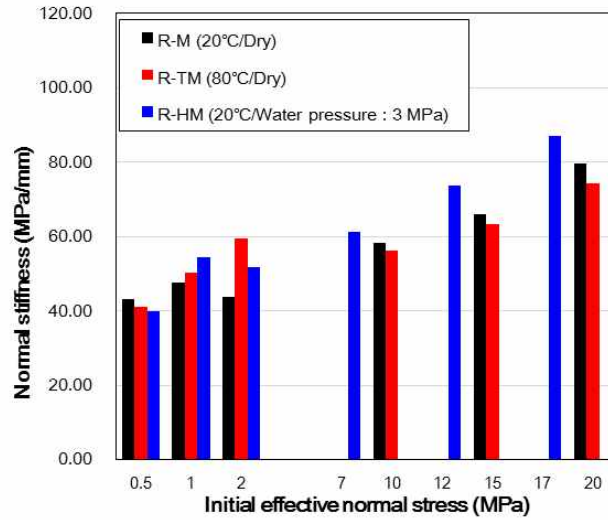
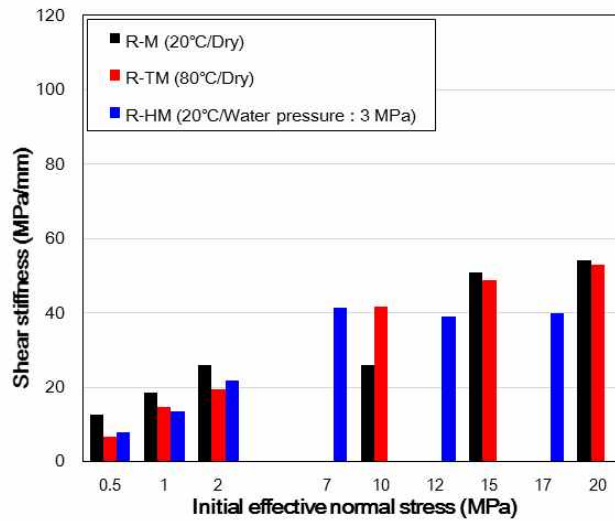


Fig. 5.6.16 Contact forces (black in compression and red in tension) at a shear displacement of 1.2 mm on rough discontinuities (JRC=11.63) at room temperature and dry condition depending on confining pressure: (a) 0.5 MPa, (b) 1.0 MPa, (c) 2.0 MPa, (d) 10.0 MPa, (e) 15.0 MPa, and (f) 20.0 MPa.



(a)



(b)

Fig. 5.6.17 Relation between normal, shear stiffness and initial effective normal stress of cement-mortar specimens including rough discontinuities (JRC=11.63) at various testing conditions obtained from the numerical simulations.: (a) normal stiffness and (b) shear stiffness.

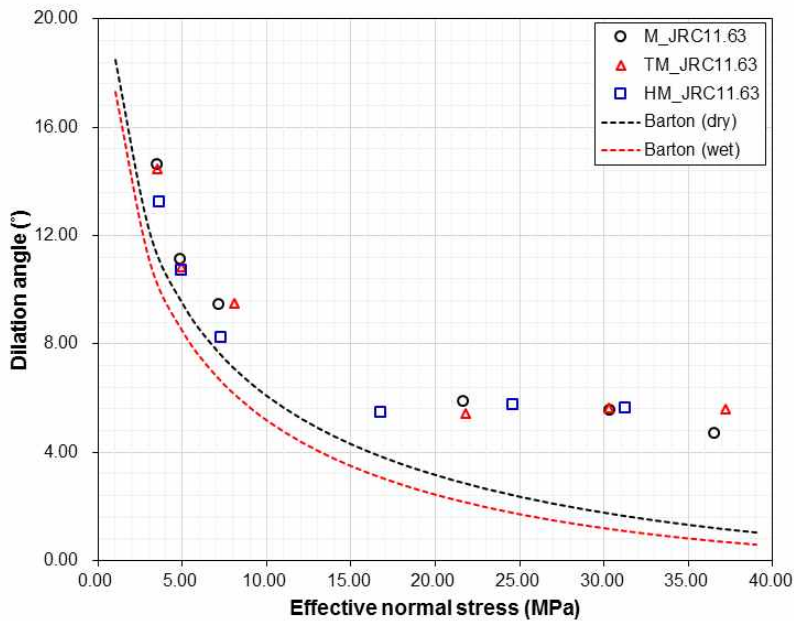


Fig. 5.6.18 Relation between dilation angle and effective normal stress of cement-mortar specimens including rough discontinuities (JRC=11.63) at various testing conditions obtained from the numerical simulations.

(2) Results at 80°C

Same with the experimental results, the peak friction angle did not vary with the temperature rise to 80°C in the numerical simulation at both low normal stress and high normal stress conditions (Fig. 5.6.12). The number of microcracks also increased as the confining pressure increased, and more than 80% of the cracks occurred by tensile failure (Table 5.6.2). However, it was difficult to find the effect of temperature increase up to 80°C on the number of cracks in this study. Normal and shear stiffness and dilation also did not change much, same with the experimental results (Figs. 5.6.17 and 5.6.18).

(3) Results at room temperature with water pressure

When water pressure of 3 MPa was applied on the area nearby the rough discontinuity (Fig. 5.5.5), peak friction angle at the low normal stress below than 10 MPa was 51.8° and did not change. In the experimental results, the reason for the reduction of the peak friction angle under the wet condition was explained due to the decrease of the tensile strength. The tensile strength of the numerical model was 13.8 MPa at the dry condition (Table 5.1.1), which was a higher value than that of an experiment, 9.22 MPa at the dry condition and 7.32 MPa at the wet condition. Therefore, this may affect the peak friction angle in the numerical simulation, since the second-asperities can be broken by tensile failure locally (Barton, 1973; Handayan et al., 1990). Yang et al. (2001) also noted that the second-order asperity cannot be neglected at low normal stress through a series of shear tests using synthetic rock specimen. However, in PFC, it is difficult to match the both uniaxial compressive strength and tensile strength (Cho et al., 2007; Park and Song, 2009). Although Cho et al. (2007) have proposed a clumped-particle model which groups particles to behave as a rigid body, it is not appropriate to apply this model to the simulation of shear behavior due to the unbreakable clumped particles. Additionally, the existence of calcite also could influence on the peak friction angle (Table 3.1.2), however, in PFC, the effect of mineralogy can not be simulated. Therefore, in the further study, it will be necessary to examine the effect of the decline of tensile strength under wet condition and the mineralogy.

At high normal stress greater than 10 MPa, the peak friction angle was 28.4°, which was almost the same value obtained at the dry condition. Effective normal stress when the shear stress reached the peak shear stress

decreased by 4.9 to 5.4 MPa than the results at the dry condition, and thus the theory of effective stress was well simulated (Table 5.6.2). The number of microcracks and normal and shear stiffness increased with the increase of confining pressure, and did not show much change when water pressure was applied (Fig. 5.6.17). Dilation angle was reduced when the confining pressure increased, but it was hard to clarify the effect of water pressure in the numerical simulation.

6. Discussion

6.1 Effect of temperature

From the experimental results, shear characteristics of the rock discontinuities including peak friction angle, normal and shear stiffness, and dilation angle were investigated. Table 6.1.1 provides the summarized test results depending on the rock types with the information of testing conditions, and Fig. 6.1.1 presents the relation between shear stress and effective normal stress of all the tested specimens.

In the case of the saw-cut surfaces, the peak friction angles were in the range of 27.1° and 31.7° at room temperature and dry conditions. To investigate the effect of the temperature, temperature of the specimens were maintained constant at 80°C during the tests in this study. Temperature condition of 80°C was decided considering the temperature of rock mass in the vicinity of a canister at high-level radioactive repository. At the elevated temperature of 80°C, the peak friction angle showed no change (Daejeon granite) or increased slightly (Goheung diorite, Linyi sandstone, Cement-mortar specimens) (Table 6.1.1). Friedman et al. (1974) carried out shear tests on sandstone specimens including a single saw-cut discontinuity. The friction coefficient increased progressively from 0.58 at 25°C to 0.72 at 410°C due to the glass-indurated quartz gouge. While, in the case of sandstone specimens, the peak friction angle did not change at an elevated temperature of 150 and 240°C (Lockner et al., 1982). Patterson and Wong (2005) also noted that up to around 427°C or 527°C (700K or 800 K), the friction characteristics of igneous or metamorphic rocks was not greatly

affected by the increase in temperature. Therefore, the results of this study showed a similar tendency with their reports, and the other properties including normal stiffness, shear stiffness, and dilation angle also did not show remarkable variations at 80°C. However, at a higher temperature, substantial decreases of friction angles are often seen (Paterson and Wong, 2005), and therefore, further studies should be considered.

6.2 Effect of water

When the water pressure was applied on the discontinuity surfaces, shear characteristics showed a decreasing tendency depending on rock types and surface roughness. In Table 6.1.1, two kinds of blue arrows (\downarrow and \Downarrow) were marked when the peak friction angle and cohesion decreased. Each arrow means the peak friction angle decreased by less than 10% (\downarrow), or by more than 10% (\Downarrow) compared to the peak friction angles of at room temperature and dry conditions. For the saw-cut specimens, the decreasing amount of Daejeon granite was in the range of 2.1° and 2.5°, and Goheung diorite and Linyi sandstone showed a noticeable reduction by 3.1° and 5.7°. In the case of cement-mortar specimens, the peak friction angles decreased at low normal stress condition, and the amount was 1.2° and 4.3° at different rough surfaces. Fig. 6.1.2 shows the ratio of the friction coefficients under dry and wet conditions obtained from this study and the previous researches. The causes of the reduction in the peak friction angles can be analyzed in the next three ways.

- 1) effect of layer lattice mineral
- 2) weak bond strength of grains
- 3) decrease of the tensile strength

The first and the second one can be applied to the saw-cut specimens, while the third one can be implemented to the cement-mortar specimens including rough discontinuities. In the XRD analysis (Table 3.1.2), layer lattice minerals such as muscovite, biotite, chlorite, montmorillonite, and talc were observed in Daejeon granite and Goheung diorite specimens, and the weight ratio was more than 10%. Layer lattice minerals readily adsorb water due to negative charged surfaces, and the water can act as a lubricant on the sliding surface (Horn and Deere, 1962; Morrow et al., 2000; Ulusay and Karakul, 2015). Especially, clay minerals such as montmorillonite show a significant decrease when the surface is wet. In the research of Pellet et al. (2013), the friction angle of Marl obtained from a series of direct shear tests was reduced by 10° , and the shear strength decreased by approximately 50% when the discontinuity was saturated. SEM observation also confirmed the existence of layer lattice minerals in Goheung diorite (Fig. 4.6.5(b)).

The second reason, weak bond strength, can be applied to Linyi sandstone. After the tests at water pressure applied condition, comparatively an amount of powder was observed on the sheared surfaces even to the naked eyes. In SEM observation, weakly cemented grains were well observed, and the sheared surface was much smoother than the surface at dry condition (Fig. 4.6.6). Microcracks were also found, and that means the surface was damaged and softened more. Decrease of normal and stiffness can be another proof for that. Those factors may affect the decrease of the

peak friction angles of Linyi sandstone specimens.

Reduction of the tensile strength can account for the case of the cement-mortar specimens. The results were analyzed by using the bilinear criterion of Patton (1966b), and the reduction of peak friction angle was observed at the low normal stress below than 10 MPa. Even during shearing, asperity can be failed by tensile failure (Handayan et al., 1990; Bahaaddini et al., 2013), where stress concentrated locally. Generally, the tensile strength of rocks decreases when the specimens were saturated. Several ways can explain the mechanisms for strength reduction: (1) fracture energy reduction; (2) pore pressure increase; and (3) chemical and corrosive deterioration (Van Eeckhout, 1976). Shucaï et al. (2004) found that when the saturated specimen is in loading condition, volume contraction of the pore fluids is less than that of bulk rock so that pore fluids accelerates crack growth through CT real-time testing. That means saturation can decrease fracture energy for rock failure. Pore pressure also can reduce the strength by the theory of effective stress, and chemical and corrosive deterioration affect the strength when soluble minerals are included. In this study, the tensile strength of cement-mortar specimens decreased by 1.9 MPa, and this might decrease the peak friction angle. Additionally, the reduction appeared much remarkably on the rougher discontinuities, and the tendency corresponded well to the results of Barton (1973). At high normal stress greater than 10 MPa, the peak friction angle did not show much variation because the asperities were sheared off. In that case, basic friction angle can be a predominant factor in shear behavior.

However, the rock types were not sufficient to assure the effect of water. Even a certain rock specimen have a similar mineral composition, the

results of the shear behavior can appear differently. Therefore, shear tests should be performed to investigate the geological characteristics at the different locations. The number of the tests for each rock were also insufficient due to the lack of the specimens. For practical use, quantification is imperatively necessary, and thus, further tests should be necessary.

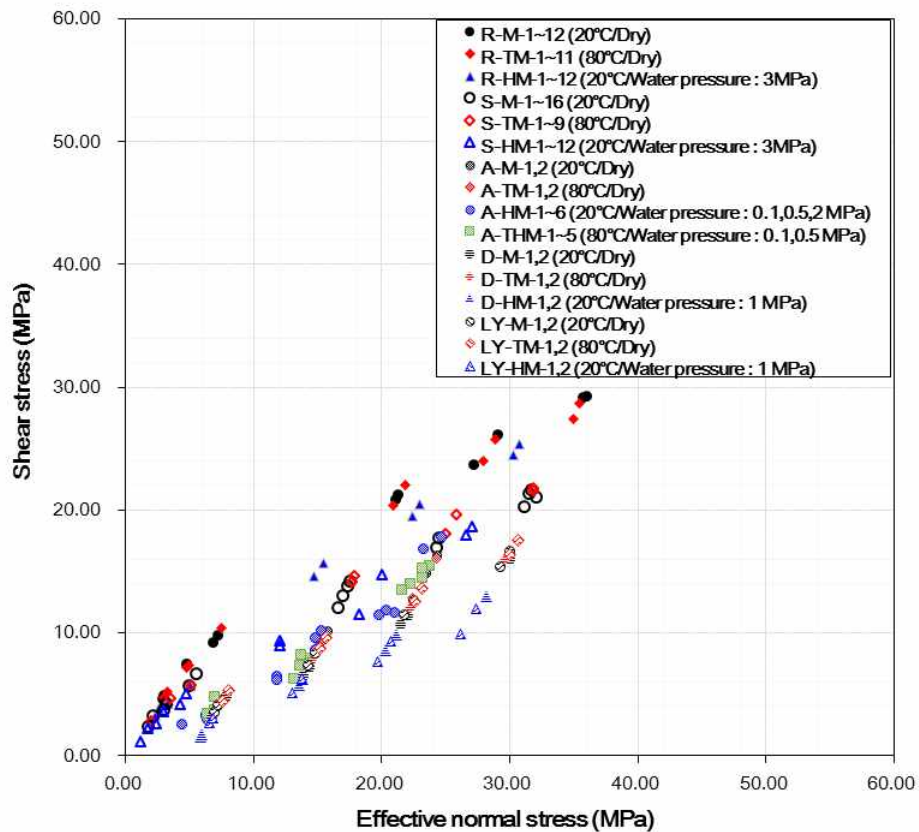


Fig. 6.1.1 Relation between effective normal stress and shear stress of discontinuities of Daejeon granite, Goheung diorite, Linyi sandstone and cement-mortar specimens at various testing conditions.

Table 6.1.1 Summary of a series of shear tests for peak friction angle and cohesion of Daejeon granite, Goheung granite, Linyi sandstone and Cement-mortar specimens. In the table, ‘↓’ means that the peak friction angle decreased by less than 10%, and ‘↓↓’ by more than 10% compared to the peak friction angles at room temperature and dry conditions.

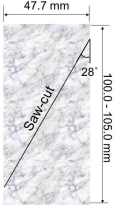
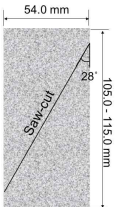
Rock type (JRC)	Specimen number	Testing condition	Normal stress (MPa)	Friction angle (°) (coefficient of friction)	Cohesion (MPa)
Daejeon Granite (saw-cut) 	A-M-1,2	20°C / Dry	$0 \leq \sigma_n$	31.7 (0.6176)	0
	A-TM-1,2	80°C / Dry		31.4 (0.6094) (-)	0
	A-HM-1,2	20°C / water pressure : 0.1 MPa		29.6 (0.5670) (↓)	0
	A-HM-3,4	20°C / water pressure : 0.5 MPa		34.5 (0.6880) (-)	0
	A-HM-5,6	20°C / water pressure : 2.0 MPa		29.2 (0.5586) (↓)	0
	A-THM-1~3	80°C / water pressure : 0.1 MPa		30.7 (0.5936) (-)	0
	A-THM-4,5	80°C / Water pressure : 0.5 MPa		31.6 (0.6149) (-)	0
Goheung Diorite (saw-cut) 	D-M-1,2	20°C / Dry	$0 \leq \sigma_n$	27.1 (0.5118)	0
	D-TM-1,2	80°C / Dry		28.2 (0.5350) (-)	0
	D-HM-1,2	20°C / water pressure : 1.0 MPa		24.0 (0.4451) (↓↓)	0

Table 6.1.1 Continued.

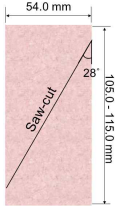
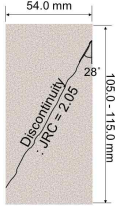
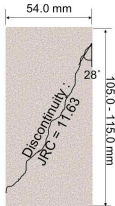
Rock type (JRC)	Specimen number	Testing condition	Normal stress (MPa)	Friction angle (°) (coefficient of friction)
Linyi Sandstone (saw-cut) 	LY-M-1,2	20°C / Dry	$0 \leq \sigma_n$	28.2 (0.5358)
	LY-TM-1,2	80°C / Dry		29.7 (0.5692) (-)
	LY-HM-1,2	20°C / water pressure : 1.0 MPa		22.5 (0.4148) (↓)
Cement-mortar (JRC=2.05) 	S-M-1~16	20°C / Dry	$\sigma_n \leq 10$	48.3 (1.1211)
			$10 \leq \sigma_n$	28.3 (0.5399)
	S-TM-1~9	80°C / Dry	$\sigma_n \leq 10$	50.5 (0.7274) (-)
			$10 \leq \sigma_n$	27.6 (0.5238) (-)
S-HM-1~12	20°C / water pressure : 3.0 MPa	$\sigma_n \leq 10$	47.1 (1.0778) (↓)	
		$10 \leq \sigma_n$	32.2 (-) (0.6308)	
Cement-mortar (JRC=11.63) 	R-M-1~12	20°C / Dry	$\sigma_n \leq 10$	54.9 (1.4221)
			$10 \leq \sigma_n$	29.6 (0.5680)
	R-TM-1~11	80°C / Dry	$\sigma_n \leq 10$	55.6 (1.4586) (-)
			$10 \leq \sigma_n$	26.7 (0.5025) (-)
R-HM-1~12	20°C / water pressure : 3.0 MPa	$\sigma_n \leq 10$	50.6 (1.2185) (↓)	
		$10 \leq \sigma_n$	32.5 (0.6376) (-)	

Table 6.1.2 Summary of a series of shear tests for peak friction angle depending on various testing conditions.

Friction angle		Experiments		Numerical simulation	
		Water pressure	Temperature increase	Water pressure	Temperature increase
Saw-cut (Granite, Diorite, Sandstone)		↓	—	—	—
Cement-mortar (JRC=2.05 and 11.63)	$\sigma_n \leq 10$	↓	—	—	—
	$10 \leq \sigma_n$	—	—	—	—

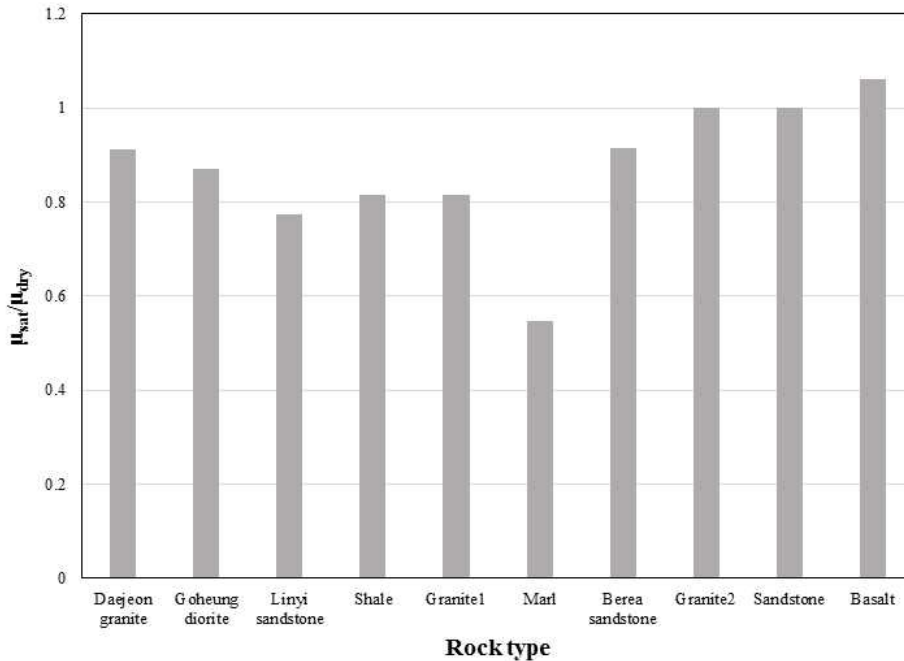


Fig. 6.1.2 Comparison of the ratio between the friction coefficients of flat discontinuities under dry and wet conditions depending on rock types: Shale, Granite (Rosengren, 1968), Marl (Pellet et al., 2013), Berea sandstone (Lee and Chang, 2015), Granite2 (Byerlee, 1967), Sandstone (Goodman and Onishi, 1972), Basalt (Duncan and Scheerman-Chase, 1965-66).

6.3 Comparison between experimental and simulation results

A series of numerical simulations using PFC2D were carried out to simulate the shear behavior on the discontinuities of cement-mortar specimens at various testing conditions. To overcome the particle interlocking problem, smooth joint model and separated vessel genesis procedure were adopted. The peak friction angles, normal and shear stiffness, and dilation angles were investigated and compared to the experimental results (Table 6.1.2).

The shear behavior including peak shear stress and stiffness matched well with the experimental data at room temperature and dry conditions. Propagation of microcracks was also examined during the simulations. During the simulation, contact forces were concentrated on the uphill slope asperities, and most of the cracks occurred by tensile failure. As the confining pressure increased, shearing accompanying with the failure of second-order asperities was predominant than sliding along the discontinuities, and hence, the number of the microcracks increased, extensively. The results corresponded well to the previous studies (Barton, 1973; Handayan et al., 1990; Bahaaddini et al., 2013). At the elevated temperature of 80°C, shear behavior did not show any difference same with the experimental results. Water pressure also applied in the area nearby the discontinuities, and the theory of effective stress was well simulated. Thus, based on the results, further numerical simulations can be performed at much more various conditions, such as higher temperature and water pressure conditions.

However, unlike the experimental results, the peak friction angle did not

change when water pressure was applied at low normal stress less than 10 MPa in both rough discontinuities. The higher tensile strength of PFC2D than that of the experimental results may be related to the disagreement. Post peak shear behavior of the rougher discontinuity (JRC=11.63) also showed a different tendency compared to the experimental results. This may be caused due to the 2-dimensional analysis, and thus, the further 3-dimensional simulation should be considered for more realistic simulation.

7. Conclusions

In this study, a series of shear tests in a laboratory scale and numerical simulation were performed to investigate the variations of shear characteristics of discontinuities under various thermal, hydraulic and mechanical conditions. The specimens were selected considering the regional characteristics, rock types, and roughness. Additionally, to comprehend the mechanisms of the variations of, XRD analysis and SEM observation were conducted. The main features of this study are as follow.

1) A series of shear tests were performed on saw-cut surfaces inside a triaxial chamber under various thermal, hydraulic and mechanical conditions. Saw-cut surfaces of Daejeon granite, Goheung diorite, and Linyi sandstone samples were used to examine the shear characteristics depending on rock types. Daejeon granite and Goheung diorite are representative plutonic rocks, and they were chosen as specimens considering the distinct characteristics of the sites. Daejeon granite was obtained at KURT, a research facility for a high-level radioactive repository (KURT), and the depth was in the range of 50 and 100 m. Goheung is a scheduled site for constructing a subsea tunnel, and Linyi sandstone was selected as a representative of sedimentary rock.

2) For Daejeon granite specimens, friction angles showed a slight decrease by 2.1 and 2.5° when water pressure was applied on the saw-cut surfaces. The decrease may be induced by the micro roughness of the saw-cut surfaces and the presence of layer lattice minerals which were

observed in the XRD test, however, due to large amounts of massive minerals, the reduction amount was not noticeable. Normal and shear stiffness did not show clear change.

3) A remarkable decrease of friction angles by 3.1° was observed for Goheung diorite when water pressure was applied. For diorite specimens, relatively a large amount of layer lattice minerals including clay minerals were found in XRD analysis and SEM observation. Those minerals can reduce the friction angles because of readily adsorption of water. Additionally, micro roughness of saw-cut surfaces also affect on the decrease of the friction angles. However, it was hard to find the effect of water pressure on normal and shear stiffness.

4) Friction angles of Linyi sandstone specimens decreased by 5.7° noticeably under water pressure applied conditions, but a different mechanism may affect. In XRD analysis, layer lattice minerals were rarely found. However, in SEM observation, a large amount of pulverized fine grains were observed on the saw-cut surface after the tests at water pressure applied conditions. Normal and shear stiffness also decreased when water pressure was applied. Thus, it can be deduced that bond strength of grains deteriorated due to the effect of water. As a result, detached soft powdered grains may reduce the shear characteristics of the saw-cut surfaces.

5) The friction angle of the saw-cut surfaces of the three rock types increased slightly or showed no change when the temperature was raised to 80°C . Temperature of 80°C was set considering the temperature of rock

mass in the vicinity of a canister at high-level radioactive waste repository. Normal and shear stiffness were not also varied clearly. Thus, the effect of temperature at 80°C was not significant on the shear behavior in this study.

6) Cement-mortar was used to reproduce identical rough discontinuities, and smooth and rough discontinuities (JRC=2.05 and 11.63) were prepared for the purpose of the investigation of the effect of roughness on shear characteristics. In the XRD analysis, only a small amount of layer lattice minerals were examined. Due to asperity degradation, friction angles were analyzed at low and high normal stress separately. The transition normal stress was 10 MPa considering the brazilian tensile strength.

7) When water pressure was applied, friction angle showed a slight decrease at the low normal stress below than 10 MPa in the case of smooth discontinuities. However, for rough discontinuities, the decrease was much larger due to the asperity degradation caused by the deterioration of tensile strength. At high normal stress greater than 10 MPa, friction angle showed almost similar values independent on roughness. That means at high normal stress the second-order asperities were failed, and hence, the effect of basic friction angle is predominant. It was difficult to find any clear change of normal and shear stiffness, while dilation angle decreased at water pressure applied conditions. This may be deduced by the reduction of joint wall compressive strength. At an elevated temperature of 80°C, shear characteristics were not also varied same with saw-cut specimens.

8) Numerical simulation using two-dimensional particle flow code was performed to reproduce the experimental results of cement-mortar specimens. Smooth joint model was used to generate a single discontinuity in the numerical model, and to avoid particle interlocking problem an improved model generation procedure was adopted.

9) In M and TM simulations, the results of experiments and numerical simulation showed a good agreement at room temperature and 80°C conditions. However, in the HM simulation, the friction angle of a rough discontinuity model did not reduce at low normal stress, unlike experimental results, due to the higher tensile strength in PFC. Dilation angles also showed larger values and the reason is presumed to have appeared because of two-dimensional simulation. Laboratory tests of saw-cut surfaces were not also able to be simulated because the effect of minerals can not be considered in PFC.

Reference

- Aydan, O. È., Shimizu, Y., Kawamoto, T., (1995) A portable system for in-situ characterization of surface morphology and frictional properties of rock discontinuities. Proceedings of 4th International Symposium on Field Measurements in Geomechanics, pp. 463-470, Bergamo, Italy.
- Aydan, Ö., (1998) Simple tests on the validation of the effective stress law for rock discontinuities. Proceedings of poromechanics, pp. 539-544, Belgium.
- Bahaaddini, M., Sharrock, G., Hebblewhite, B. K., (2013) Numerical direct shear tests to model the shear behaviour of rock joints. Computers and Geotechnics, 51, pp. 101-115.
- Bahaaddini, M., Hagan, P. C., Mitra, R., Hebblewhite, B. K., (2015) Parametric study of smooth joint parameters on the shear behaviour of rock joints. Rock Mechanics and Rock Engineering, 48(3), pp. 923-940.
- Bahaaddini, M., Hagan, P. C., Mitra, R., Khosravi, M. H., (2016) Experimental and numerical study of asperity degradation in the direct shear test. Engineering Geology, 204, pp. 41-52.
- Bernaix, J., (1969). New laboratory methods of studying the mechanical properties of rocks. International Journal of Rock Mechanics and Mining Sciences Geomechanics Abstracts, 6(1), pp. 43-90.

- Bilgin, H. A., Pasamehmetoglu, A. G., (1990) Shear behaviour of shale joints under heat in direct shear, *Rock Joints*, pp. 179-183.
- Broch, E., Franklin, J. A., (1972) The point-load strength test. In *International Journal of Rock Mechanics and Mining Sciences Geomechanics Abstracts* (Vol. 9, No. 6, pp. 669-676.
- Barton, N., (1973) Review of a new shear-strength criterion for rock joints. *Engineering geology*, 7(4), pp. 287-332.
- Barton, N., Choubey, V., (1977) The shear strength of rock joints in theory and practice. *Rock mechanics*, 10(1-2), pp. 1-54.
- Blanpied, M. L., Lockner, D. A., Byerlee, J. D., (1995) Frictional slip of granite at hydrothermal conditions. *Journal of Geophysical Research: Solid Earth*, 100(B7), pp. 13045-13064.
- Byerlee, J., (1978) Friction of rocks. *Pure and applied geophysics*, 116(4-5), pp. 615-626.
- Cai, C., Li, G., Huang, Z., Shen, Z., Tian, S., Wei, J., (2014) Experimental study of the effect of liquid nitrogen cooling on rock pore structure. *Journal of Natural Gas Science and Engineering*, 21, pp. 507-517.
- Carlsaw, H. S., Jaeger, J. C., (1959) *Conduction of heat in solids*. Oxford: Clarendon Press, 2nd ed.
- Cho, N. A., Martin, C. D., Segoo, D. C., (2007) A clumped particle model for rock. *International Journal of Rock Mechanics and Mining Sciences*, 44(7), pp. 997-1010.

- Colback, P.S.B., Wiid, B.L., (1965) The influence of moisture content on the compressive strength of rocks, Proceedings of Rock Mechanics Symposium, pp. 65-83.
- Coulson, J. H., (1972) Shear strength of flat surfaces in rock. In Stability of Rock Slopes, pp. 77-105.
- Cundall, P. A., (2000) Numerical experiments on rough joints in shear using a bonded particle model, Aspects of tectonic faulting, pp. 1-9.
- Cundall, P., (2000) Fluid formulation for PFC2D. Itasca Consulting Group: Minneapolis, Minnesota.
- Drennon, C. B., Handy, R. L., (1972) Stick-slip of lightly loaded limestone. International Journal of Rock Mechanics and Mining Sciences & Geomechanics Abstracts, 9(5), pp. 603-608.
- Donath, F. A., Fruth, L. S., Olsson, W. A., (1972) Experimental study of frictional properties of faults. In The 14th US Symposium on Rock Mechanics, pp. 189-222.
- Duncan, N., (1969) Engineering geology and rock mechanics, Vol. 2, Leonard Hill, London.
- Duncan, N., Sheerman-Chase, A., (1965-66), Planning, design and construction, rock mechanics in civil engineering works, Civil Engineering and public Works Review, 60: pp. 1751, 1755-1756; 61: pp. 57-59, 213-215, 217, 327-330, 431, 433, 613, 615-617, 751-753.

- Engelder, T., (1992) Stress regimes in the lithosphere, Princeton University Press.
- Friedman, M., Logan, J. M., Rigert, J. A., (1974) Glass-indurated quartz gouge in sliding-friction experiments on sandstone, Geological Society of America Bulletin, 85(6), pp. 937-942.
- Goldstein, M., Goosev, B., Pyrogovsky, N., Tulinov, R. Turovskaya, A., (1966) Investigation of mechanical properties of cracked rock, Proceeding of 1st International Society for Rock Mechanics Congress, pp. 521-524, Lisbon, Portugal.
- Guo, S., Qi, S., (2015) Numerical study on progressive failure of hard rock samples with an unfilled undulate joint, Engineering Geology, 193, pp. 173-182.
- Giardini, D., (2009) Geothermal quake risks must be faced, Nature, 462(7275), pp. 848-849.
- Goodman, R. E., Ohnishi, Y., (1973) Undrained shear testing of jointed rock. Rock Mechanics, 5(3), pp. 129-149.
- Goodman, R. E., (1992) Engineering Geology — Rock in engineering construction, Wiley.
- Gutierrez, M., Øino, L. E., Høeg, K., (2000) The effect of fluid content on the mechanical behaviour of fractures in chalk, Rock Mechanics and Rock Engineering, 33(2), pp. 93-117.

- Grasselli, G., (2001) Shear strength of rock joints based on quantified surface description, Ph.D. Thesis, Swiss Federal Institute of Technology, Lausanne, Switzerland.
- Griffiths, D. V., (1990) Failure criteria interpretation based on Mohr-Coulomb friction, *Journal of Geotechnical Engineering*, 116(6), pp. 986-999.
- Handanyan, J. M., Danek, E. R., Andrea, R. A. D., Sage, J. D., (1990) The role of tension in failure of jointed rock, *Rock joints*, Balkema, Rotterdam
- He, Z., Li, G., Tian, S., Wang, H., Shen, Z., Li, J., (2016) SEM analysis on rock failure mechanism by supercritical CO₂ jet impingement, *Journal of Petroleum Science and Engineering*, 146, pp. 111-120.
- Horn, H. M., Deere, D. U., (1962) Frictional characteristics of minerals, *Geotechnique*, 12(4), pp. 319-335.
- Hoskins, E. R., Jaeger, J. C., Rosengren, K. J., (1968) A medium-scale direct friction experiment, *International Journal of Rock Mechanics and Mining Sciences Geomechanics & Abstracts*, 5(2), pp. 143-152.
- ITASCA, 2008 ; Itasca Consulting Group., (2008) PFC 2D manual, version 4.0, Minneapolis, USA.
- Ivars, D. M., Pierce, M. E., Darcel, C., Reyes-Montes, J., Potyondy, D. O., Young, R. P., Cundall, P. A., (2011) The synthetic rock mass approach for jointed rock mass modelling, *International Journal of Rock Mechanics and Mining Sciences*, 48(2), pp. 219-244.

- Jaeger, J. C., (1959) The frictional properties of joints in rock, *Geofisica pura e applicata*, 43(1), pp. 148-158.
- Jaeger, J. C., Rosengren, K. J., (1969) Friction and sliding of joints, *Proceeding of Australian Institute of Mining and Metallurgy*, 229, pp. 93-104.
- Ji, L., Zhang, T., Milliken, K. L., Qu, J., Zhang, X., (2012) Experimental investigation of main controls to methane adsorption in clay-rich rocks, *Applied Geochemistry*, 27(12), pp. 2533-2545.
- Jing, L., Stephansson, O., (2007) *Fundamentals of discrete element methods for rock engineering: Theory and applications*. Elsevier.
- Johnson, W. H., Parsons, W. H., (1944) *Thermal expansion of concrete aggregate materials*. US Government Printing Office.
- Kim, T. and Jeon, S., (2011) Shearing behavior of a rupture surface of rock under thermo-hydro-mechanical coupled conditions, *International Journal of Geo-engineering*, 3(3), pp. 23-31.
- Kovari, K., Tisa, A., Einstein, H. H., Franklin, J. A., (1983) Suggested methods for determining the strength of rock materials in triaxial compression: revised version, *International Journal of Rock Mechanics and Mining sciences*, 20(6), pp. 283-290.
- Kulatilake, P. H. S. W., Shou, G., Huang, T. H., Morgan, R. M., (1995) New peak shear strength criteria for anisotropic rock joints, *International Journal of Rock Mechanics and Mining sciences & Geomechanics Abstracts*, 32(7), pp. 673-697.

- Kwon, S. K. and Cho, W. J., (2009) A sensitivity analysis of design parameters of an underground radioactive waste repository using a backpropagation neural network, *Tunnel & Underground Space*, 19(3), pp. 203-212.
- Ladanyi, B., Archambault, G., (1969) Simulation of shear behavior of a jointed rock mass, *Proceeding of 11th US Symposium on Rock Mechanics*.
- Lee, H., (1993) A study on thermal cracking and temperature dependence of strength and deformation behavior of rocks, Ph.D. Thesis, Seoul National University, Korea.
- Li, Z., Sheng, Y., Reddish, D. J., (2005) Rock strength reduction and its potential environmental consequences as a result of groundwater rebound. *Proceeding of 9th International Mine Water Congress*, pp. 513-519.
- Lee, Y., (2011) Experimental study on prediction of shear behavior of rock joints, Master Thesis, Seoul National University, Korea.
- Lockner, D. A., Summers, R., Moore, D., Byerlee, J. D. (1982) Laboratory measurements of reservoir rock from the Geysers Geothermal Field, California, *International Journal of Rock Mechanics and Mining Sciences & Geomechanics Abstracts*, 19(2), pp. 65-80.
- Lockner, D. A., Summers, R., Byerlee, J. D., (1986) Effects of temperature and sliding rate on frictional strength of granite, *Pure and applied geophysics*, 124(3), pp. 445-469.

- Lee, C., Lee, D., Jeon, S., (2013) The influence of excavation damaged zone on the mechanical and thermal behavior of cement mortar block around an opening, *KSCE Journal of Civil Engineering*, 17(6), pp. 1263-1274.
- Lee, S., Chang, C., (2013) Laboratory experiments on fracture shearing induced by pore pressure increase, *Proceeding of Fall joint conference of the geological science*, pp. 384, Jeju, Korea.
- Ma, Y., Zhong, N., Han, H., Li, D., Zhang, Y., Cheng, L., (2014) Definition and structure characteristics of pores in mylonitized organic-rich shales, *Science China Earth Sciences*, 57(12), pp. 3027-3034.
- Morrow, C., Radney, B., Byerlee, J., (1992) Frictional Strength and the Effective Pressure Law of Montmorillonite and Illite Clays, *International Geophysics*, 51, pp. 69-88.
- Morrow, C. A., Moore, D. E., Lockner, D. A., (2000) The effect of mineral bond strength and adsorbed water on fault gouge frictional strength, *Geophysical research letters*, 27(6), pp. 815-818.
- Mehrishal, S., Sharifzadeh, M., Shahriar, K., Song, J. J., (2016) An Experimental Study on Normal Stress and Shear Rate Dependency of Basic Friction Coefficient in Dry and Wet Limestone Joints, *Rock Mechanics and Rock Engineering*, pp. 1-23.

- Min, K. B., Stephansson, O., (2009) Shear-induced Fracture Slip and Permeability Change. Implications for Long-term Performance of a Deep Geological Repository, Swedish Radiation Safety Authority, No. SSM:2009-08.
- Nascimento, Úlpio., (1981) Lubricant and antilubricant effects of water, Memoria, pp. 3-11.
- Newland, P. L., Allely, B. H., (1957) Volume changes in drained triaxial tests on granular materials, *Geotechnique*, 7(1), pp. 17-34.
- Odera, A., Ohnaka, M., Mochizuki, H., Sammonds, P., (2001) Temperature and pore pressure effects on the shear strength of granite in the Brittle-Plastic Transition Regime, *Geophysical research letters*, 28(15), pp. 3011-3014.
- Olsson, W. A., (1974). Effects of temperature, pressure and displacement rate on the frictional characteristics of a limestone, *International Journal of Rock Mechanics and Mining Sciences & Geomechanics Abstracts*, 11(7), pp. 267-278.
- Pakpoom, N., (2013) Effect of temperatures on shear strength of fractures in granite, Master Thesis, Suranaree University of Technology, Thailand.
- Park, J. W., Song, J. J., (2009) Numerical simulation of a direct shear test on a rock joint using a bonded-particle model, *International Journal of Rock Mechanics and Mining Sciences*, 46(8), pp. 1315-1328.
- Patton, F. D., (1966a) Multiple modes of shear failure in rock and related materials, Ph.D. Thesis, University of Illinois.

- Patton, F. D., (1966b) Multiple modes of shear failure in rock, Proceeding of 1st ISRM Congress.
- Price, N. J., (1960) The compressive strength of coal measure rocks, Colliery Engineering, 37(437), pp. 283-292.
- Park, B. K., Lee, C. S., Jeon, S., (2007) Shear behavior of rough granite joints under CNS conditions, Tunnel & underground space, 17(3), pp. 203-215.
- Paterson, M. S., Wong, T. F., (2005) Experimental rock deformation-the brittle field, Springer Science Business Media.
- Pellet, F. L., Keshavarz, M., Boulon, M., (2013) Influence of humidity conditions on shear strength of clay rock discontinuities, Engineering Geology, 157, pp. 33-38.
- Pierce, M., Cundall, P., Potyondy, D., Mas Ivars, D., (2007) A synthetic rock mass model for jointed rock. Proceeding of 1st Canada-US Rock Mechanics Symposium, Vancouver, Canada.
- Plesha, M. E., (1987) Constitutive models for rock discontinuities with dilatancy and surface degradation, International Journal for Numerical and Analytical Methods in Geomechanics, 11(4), pp. 345-362.
- Richter, D., Simmons, G., (1974) Thermal expansion behavior of igneous rocks, International Journal of Rock Mechanics and Mining Sciences & Geomechanics Abstracts, 11(10), pp. 403-411.

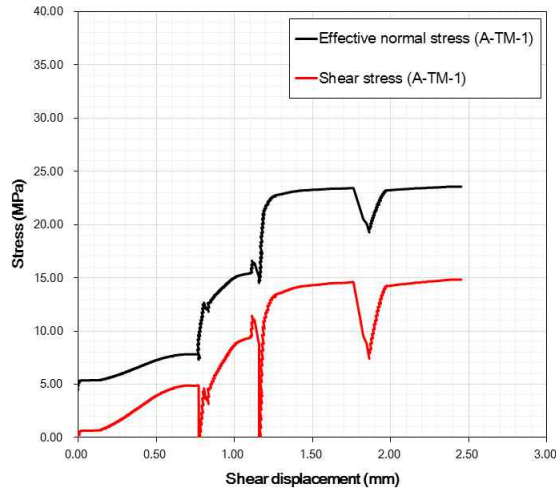
- Rosengren, K. J., (1968) Rock mechanics of the Black Star open cut, Mount Isa, Ph.D. Thesis, Australian National University.
- Saeb, S., (1990) A variance on the Ladanyi and Archambault's shear strength criterion, Rock Joints, pp. 701-705.
- Stesky, R. M., (1978) Rock friction-effect of confining pressure, temperature, and pore pressure, Pure and Applied Geophysics, 116(4-5), pp. 690-704.
- Stesky, R. M., Brace, W. F., Riley, D. K., Robin, P. Y., (1974) Friction in faulted rock at high temperature and pressure, Tectonophysics, 23(1-2), pp. 177-203.
- Son, B. K., (2005) Shear behavior of rock joint under constant normal stiffness condition, Ph. D. Thesis, Seoul National University.
- Sondergeld, C. H., Ambrose, R. J., Rai, C. S., Moncrieff, J., (2010) Micro-structural studies of gas shales, Proceeding of SPE Unconventional Gas Conference.
- Sheng, Li, Z., Y. and Reddish, D. J.. (2005) Rock strength reduction and its potential environmental consequences as a result of groundwater rebound, Proceeding of 9th International Mine Water Congress.
- Shimizu, Y., (2004) Fluid coupling in PFC2D and PFC3D, Proceeding of 2nd International PFC Symposium, Kyoto, Japan.

- Shucaï, L., Shuchen, L., Weishen, Z., Hao, J., Gang, W., (2004) CT real-time testing study on effect of water on crack growth in fractured rock mass, Chinese Journal of Rock Mechanics and Engineering, 23(21), pp. 3584-3590.
- Tse, R., Cruden, D.M., (1979) Estimating joint roughness coefficients, International Journal of Rock Mechanics and Mining Sciences & Geomechanics Abstracts, 16(5), pp. 303-307.
- Tunbridge, L.W., (1989) Interpretation of the shut-in pressure from the rate of pressure decay, International Journal of Rock Mechanics and Mining Sciences & Geomechanics Abstracts, 26(6), pp. 457-459.
- Ulusay, R., Karakul, H., (2016) Assessment of basic friction angles of various rock types from Turkey under dry, wet and submerged conditions and some considerations on tilt testing, Bulletin of Engineering Geology and the Environment, pp. 1-17.
- Van Eeckhout, E. M., (1976) The mechanisms of strength reduction due to moisture in coal mine shales, International Journal of Rock Mechanics and Mining Sciences & Geomechanics Abstracts, 13(2), pp. 61-67.
- Wai, R. S., Lo, K. Y., (1982) Temperature effects on strength and deformation behaviour of rocks in Southern Ontario, Canadian Geotechnical Journal, 19(3), pp. 307-319.
- Wanne, T. S., Young, R. P., (2008) Bonded-particle modeling of thermally fractured granite, International Journal of Rock Mechanics and Mining Sciences, 45(5), pp. 789-799.

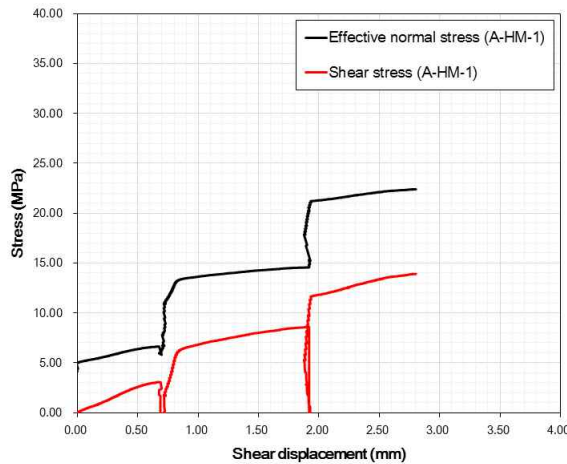
- Xia, C. C., Tang, Z. C., Xiao, W. M., Song, Y. L., (2014) New peak shear strength criterion of rock joints based on quantified surface description, *Rock Mechanics and Rock Engineering*, 47(2), pp. 387-400.
- Yang, Z. Y., Di, C. C., Yen. K. C., (2001) The effect of asperity order on the roughness of rock joints, *International Journal of Rock Mechanics and Mining Sciences*, 38(5), pp. 745-752.
- Yow, J. L., Hunt, J. R., (2002) Coupled processes in rock mass performance with emphasis on nuclear waste isolation, *International Journal of Rock Mechanics and Mining Sciences*, 39(2), pp. 143-150.
- Zhao, Z., Zhou, D., Pu, H., (2016) Shear behavior of heat-treated fractures in Beishan granite, *Proceeding of 9th Asian Rock Mechanics Symposium*, Bali, Indonesia.

Appendix A. Test results of saw-cut specimens

A.1 Daejeon granite saw-cut specimens

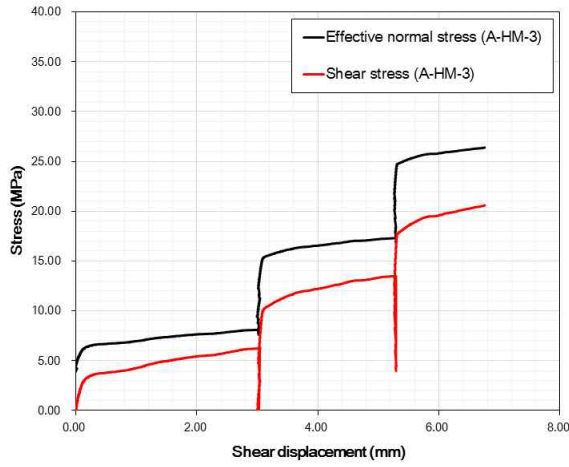


(a) Relation between effective normal stress, shear stress and shear displacement of A-TM-1 (80°C/dry condition)

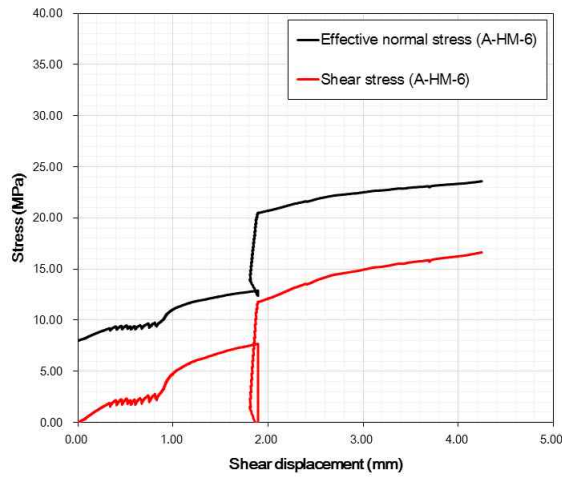


(b) Relation between effective normal stress, shear stress and shear displacement of A-HM-1 (20°C/water pressure : 0.1 MPa)

Fig. A.1 Test results of Daejeon granite saw-cut specimens.

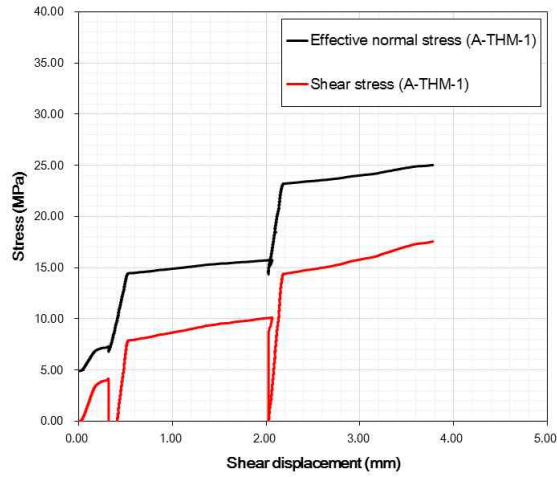


(c) Relation between effective normal stress, shear stress and shear displacement of A-HM-3 (20°C/water pressure : 0.5 MPa)

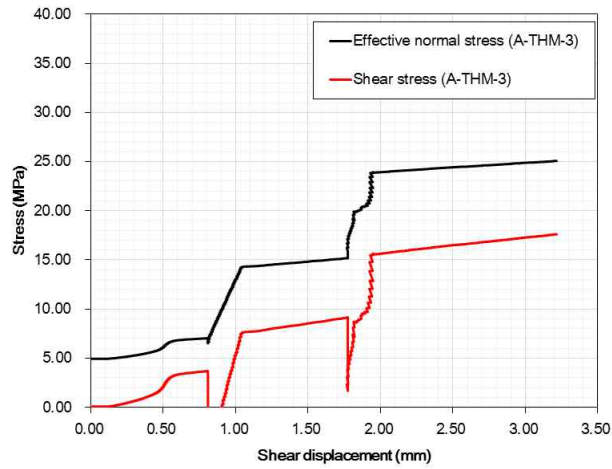


(d) Relation between effective normal stress, shear stress and shear displacement of A-HM-6 (20°C/water pressure : 2.0 MPa)

Fig. A.1 Continued.

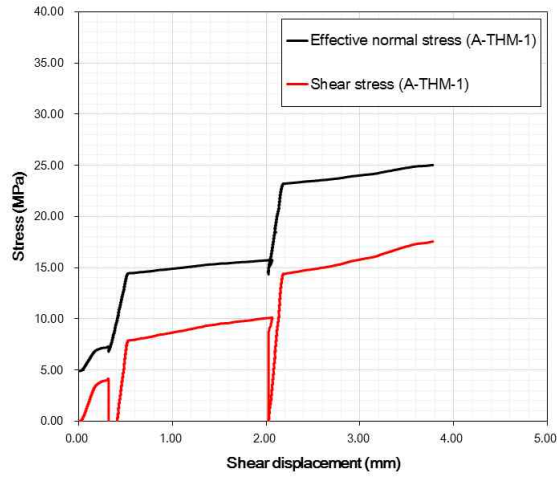


(e) Relation between effective normal stress, shear stress and shear displacement of A-THM-1 (80°C/water pressure : 0.1 MPa)

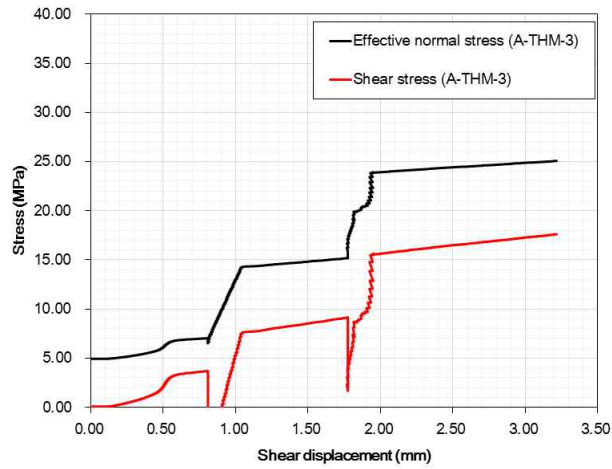


(f) Relation between effective normal stress, shear stress and shear displacement of A-THM-3 (80°C/water pressure : 0.1 MPa)

Fig. A.1 Continued.

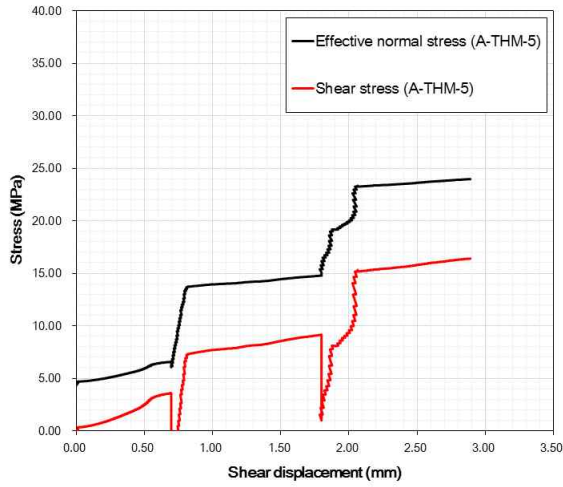


(e) Relation between effective normal stress, shear stress and shear displacement of A-THM-1 (80°C/water pressure : 0.1 MPa)



(f) Relation between effective normal stress, shear stress and shear displacement of A-THM-3 (80°C/water pressure : 0.1 MPa)

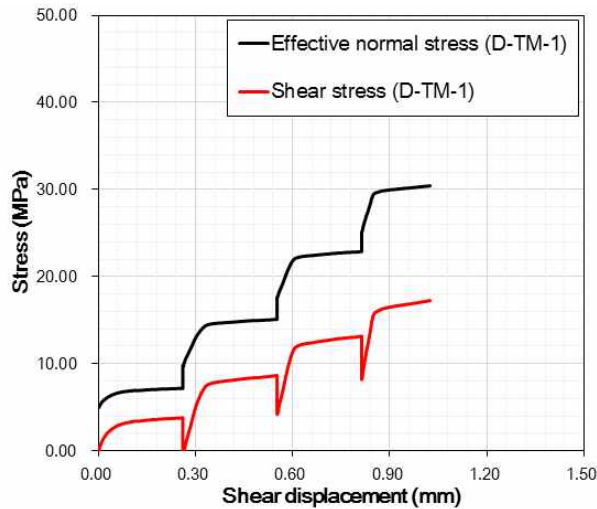
Fig. A.1 Continued.



(g) Relation between effective normal stress, shear stress and shear displacement of A-THM-5 (80°C/water pressure : 0.5 MPa)

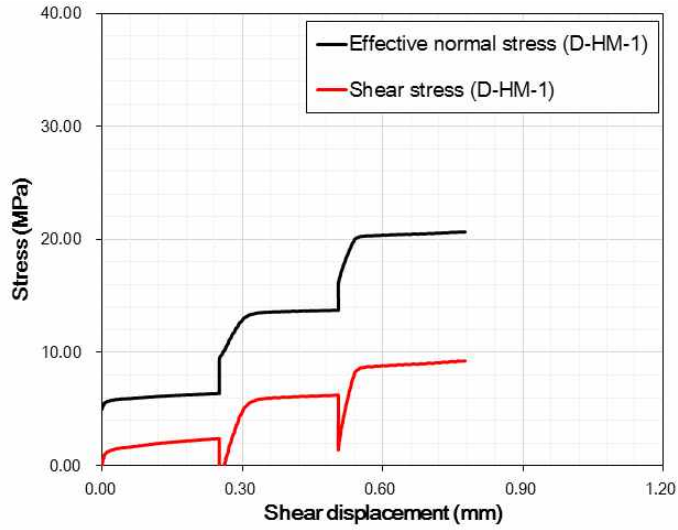
Fig. A.1 Continued.

A.2 Goheung diorite saw-cut specimens



(a) Relation between effective normal stress, shear stress and shear displacement of D-TM-1 (80°C/dry condition)

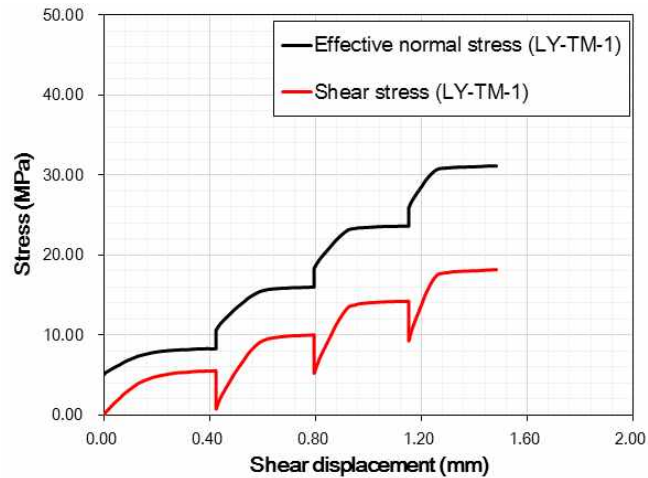
Fig. A.2 Test results of Goheung diorite saw-cut specimens.



(b) Relation between effective normal stress, shear stress and shear displacement of D-HM-1 (20°C/water pressure : 1.0 MPa)

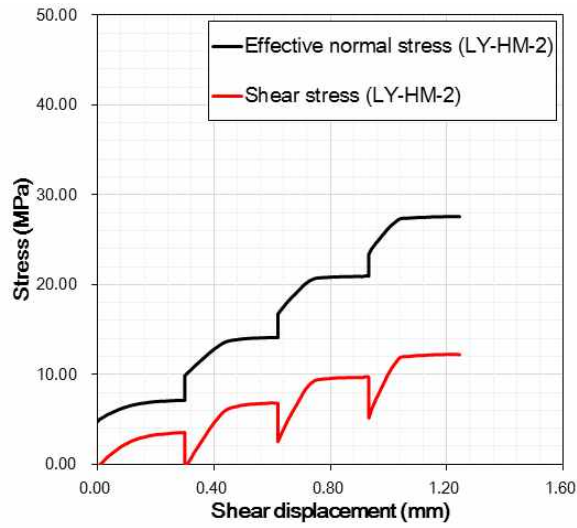
Fig. A.2 Continued.

A.3 Linyi sandstone saw-cut specimens



(a) Relation between effective normal stress, shear stress and shear displacement of LY-TM-1 (80°C/dry condition)

Fig. A.3 Test results of Linyi sandstone saw-cut specimens.

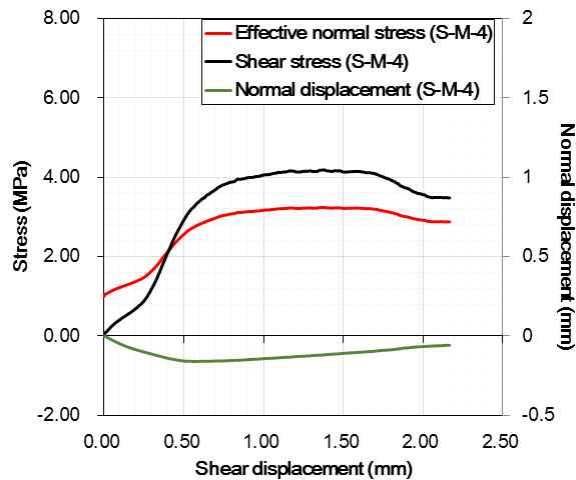


(b) Relation between effective normal stress, shear stress and shear displacement of LY-HM-2 (20°C/water pressure : 1.0 MPa)

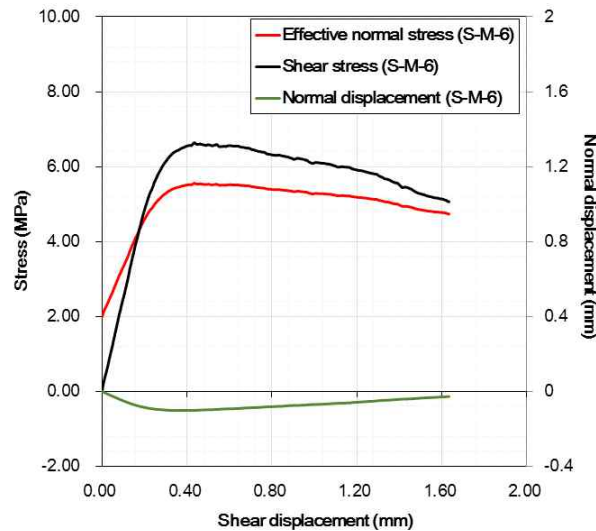
Fig. A.3 Continued.

Appendix B. Test results of cement-mortar specimens including a smooth discontinuity (JRC=2.05)

B.1 At room temperature and dry conditions

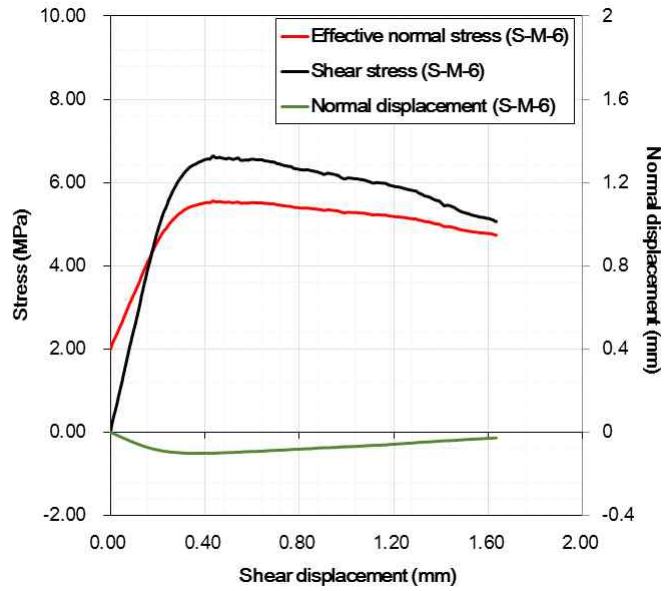


(a) S-M-2 (20°C/dry condition/confining pressure : 0.5 MPa)

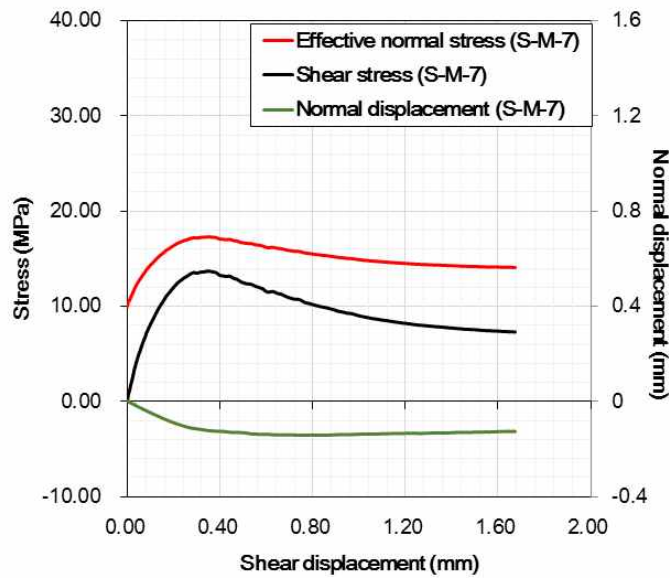


(b) S-M-4 (20°C/dry condition/confining pressure : 1.0 MPa)

Fig. B.1 Relation between effective normal stress, shear stress, normal displacement and shear displacement.

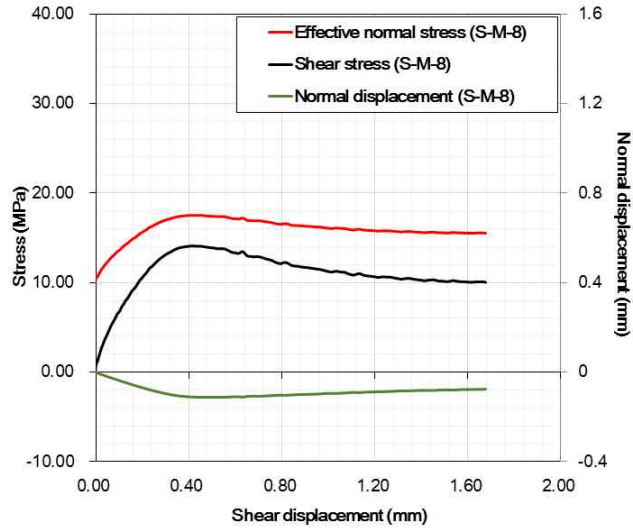


(c) S-M-6 (20°C/dry condition/confining pressure : 2.0 MPa)

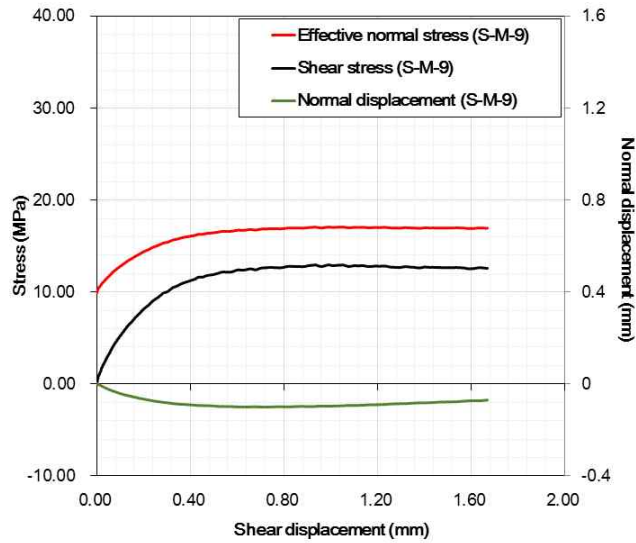


(d) S-M-7 (20°C/dry condition/confining pressure : 10.0 MPa)

Fig. B.1 Continued.

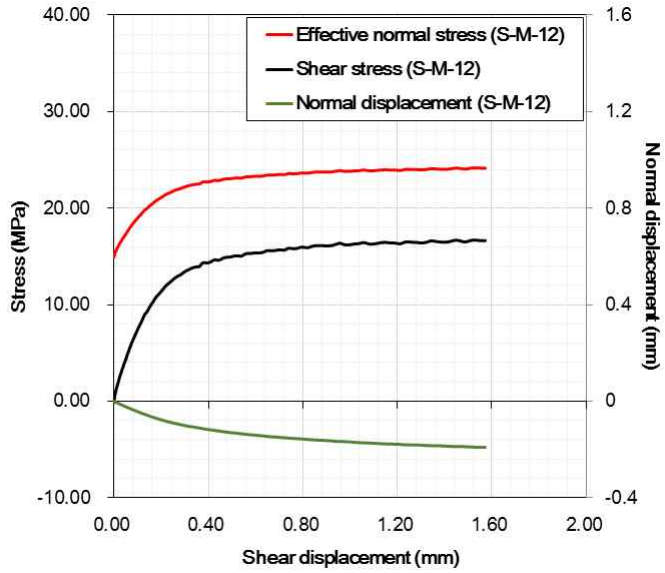


(e) S-M-8 (20°C/dry condition/confining pressure : 10.0 MPa)

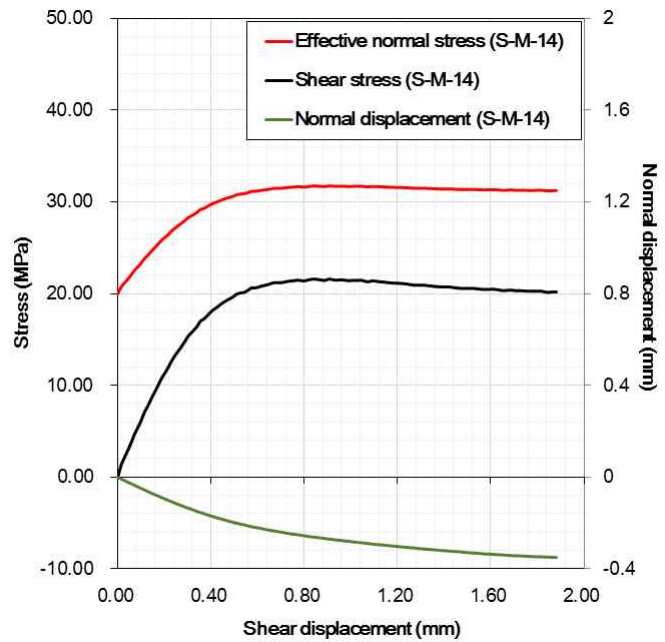


(f) S-M-9 (20°C/dry condition/confining pressure : 10.0 MPa)

Fig. B.1 Continued.

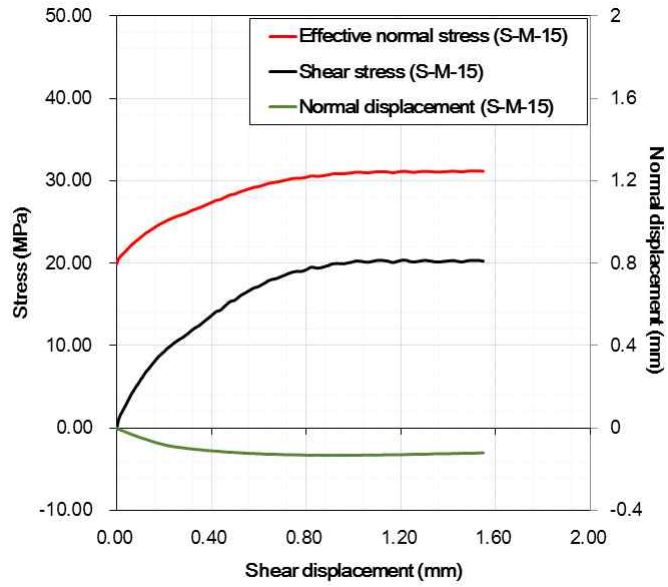


(g) S-M-12 (20°C/dry condition/confining pressure : 15.0 MPa)

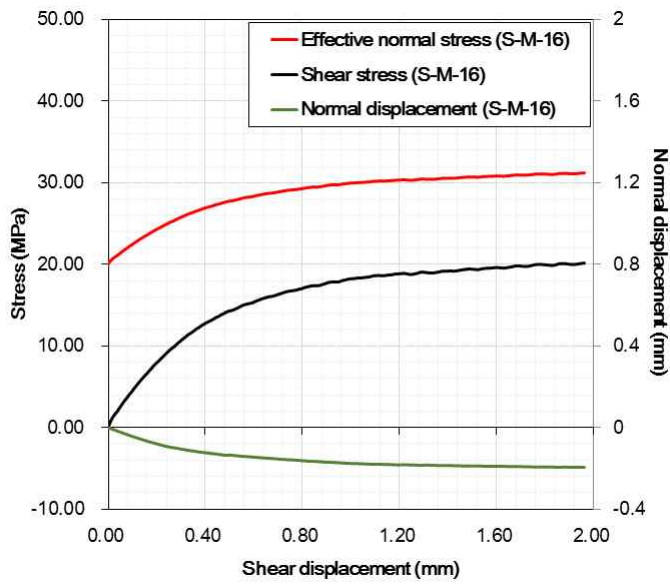


(h) S-M-14 (20°C/dry condition/confining pressure : 20.0 MPa)

Fig. B.1 Continued.



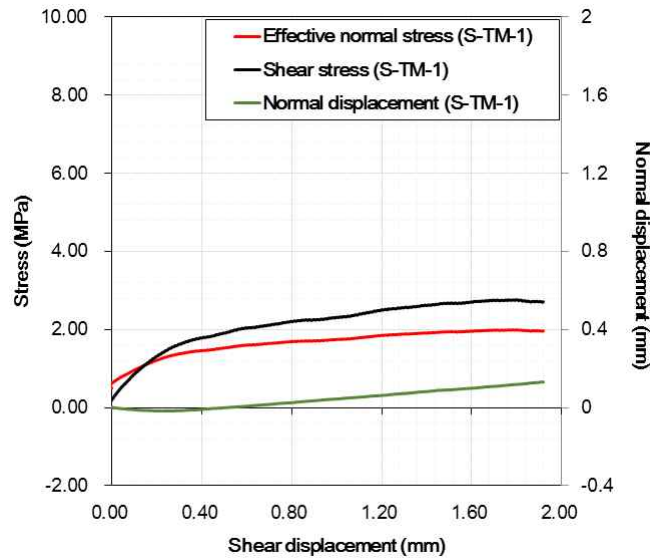
(i) S-M-15 (20°C/dry condition/confining pressure : 20.0 MPa)



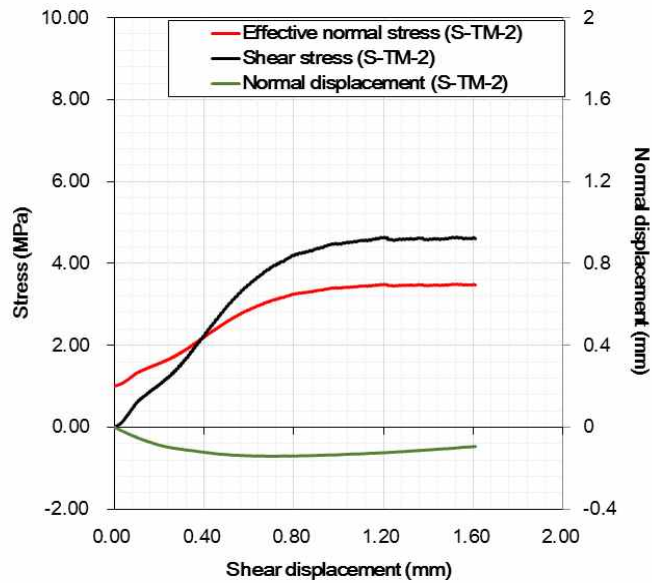
(j) S-M-16 (20°C/dry condition/confining pressure : 20.0 MPa)

Fig. B.1 Continued.

B.2 At 80°C and dry conditions

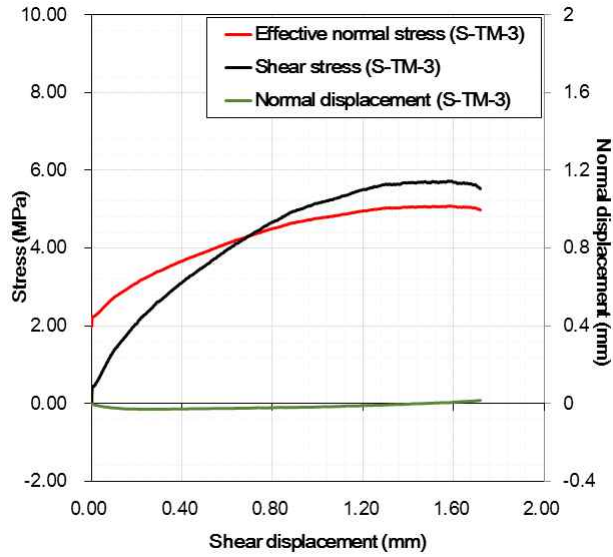


(a) S-TM-1 (80°C/dry condition/confining pressure : 0.5 MPa)

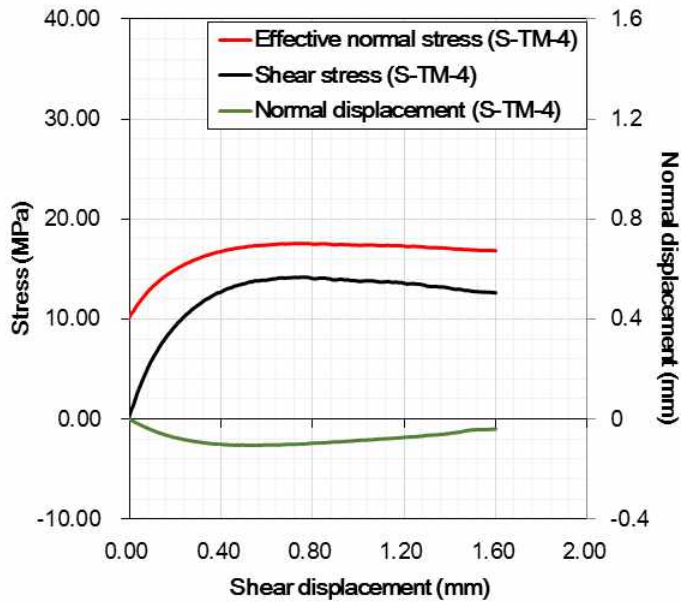


(b) S-TM-2 (80°C/dry condition/confining pressure : 1.0 MPa)

Fig. B.2 Relation between effective normal stress, shear stress, normal displacement and shear displacement.

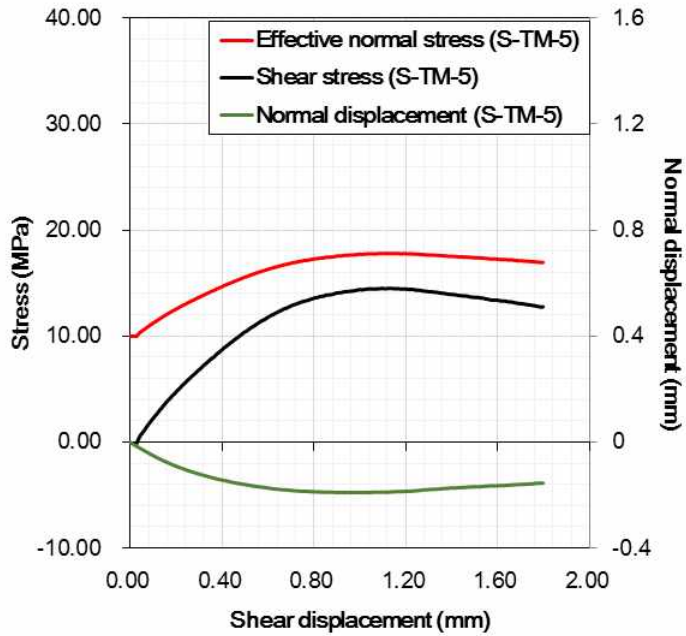


(c) S-TM-3 (80°C/dry condition/confining pressure : 2.0 MPa)

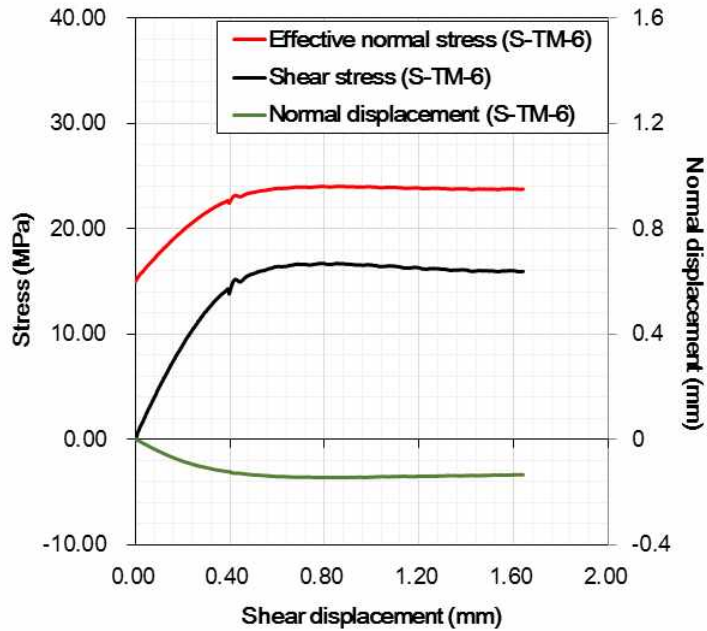


(d) S-TM-4 (80°C/dry condition/confining pressure : 10.0 MPa)

Fig. B.2 Continued.

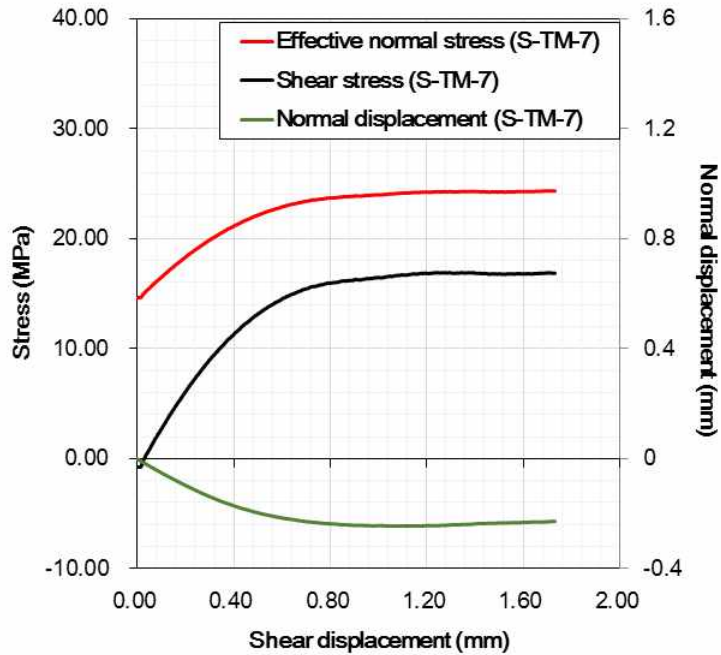


(e) S-TM-5 (80°C/dry condition/confining pressure : 10.0 MPa)

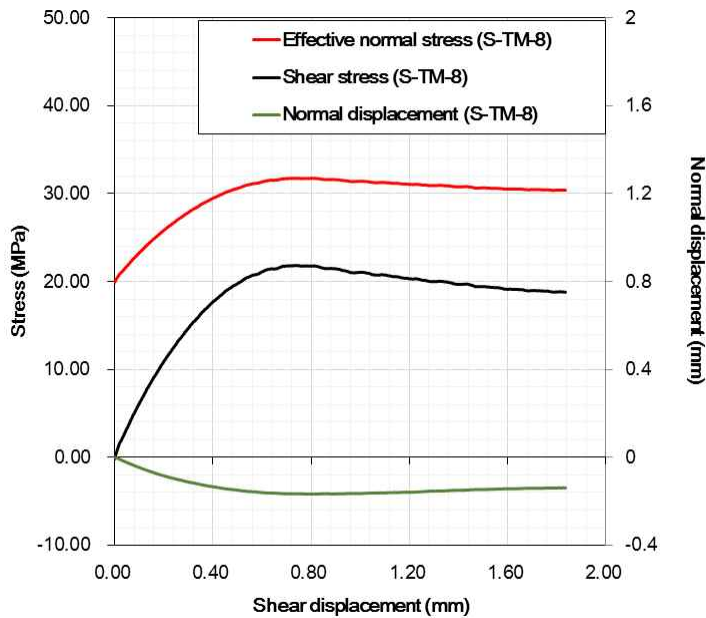


(f) S-TM-6 (80°C/dry condition/confining pressure : 15.0 MPa)

Fig. B.2 Continued.

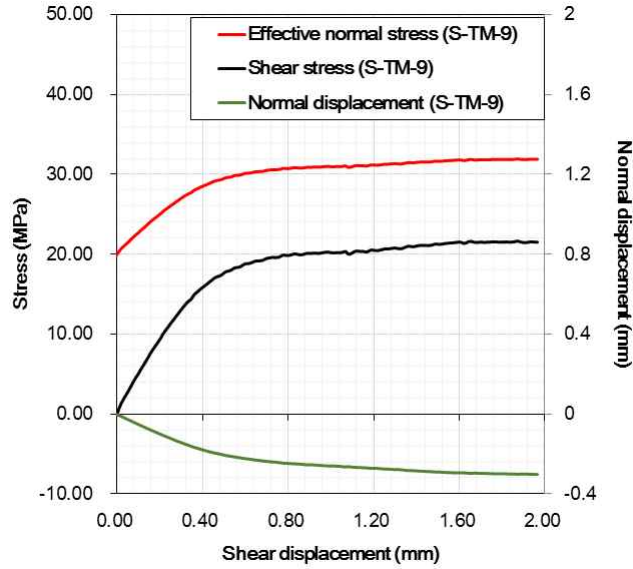


(g) S-TM-7 (80°C/dry condition/confining pressure : 15.0 MPa)



(h) S-TM-8 (80°C/dry condition/confining pressure : 20.0 MPa)

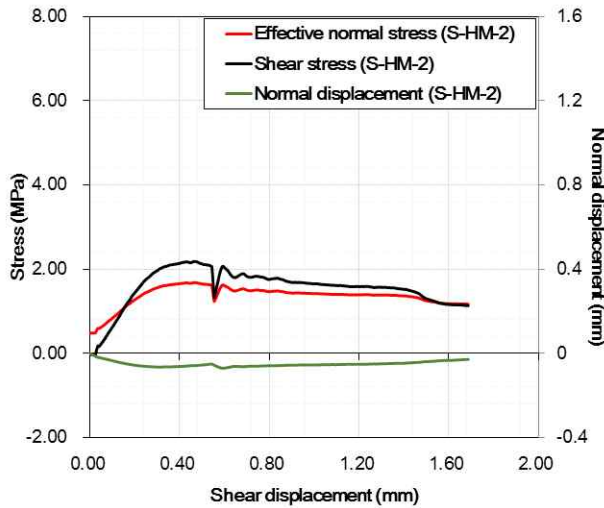
Fig. B.2 Continued.



(i) S-TM-9 (80°C/dry condition/confining pressure : 20.0 MPa)

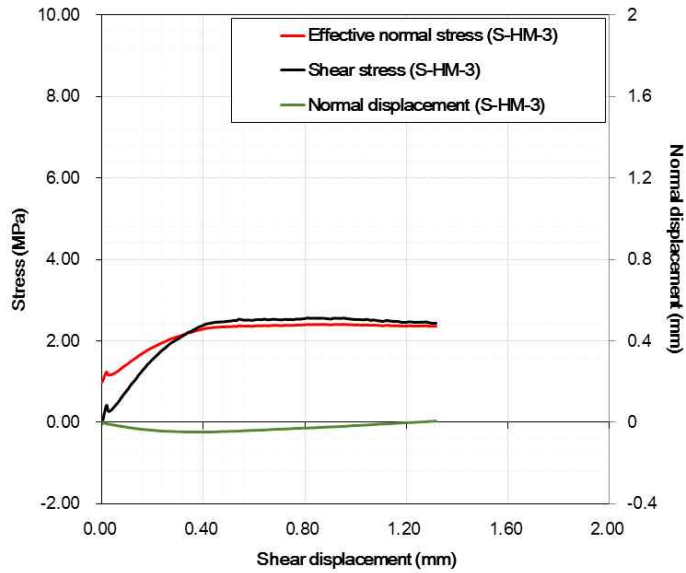
Fig. B.2 Continued.

B.3 At 20°C and water pressure (3.0 MPa) applied conditions

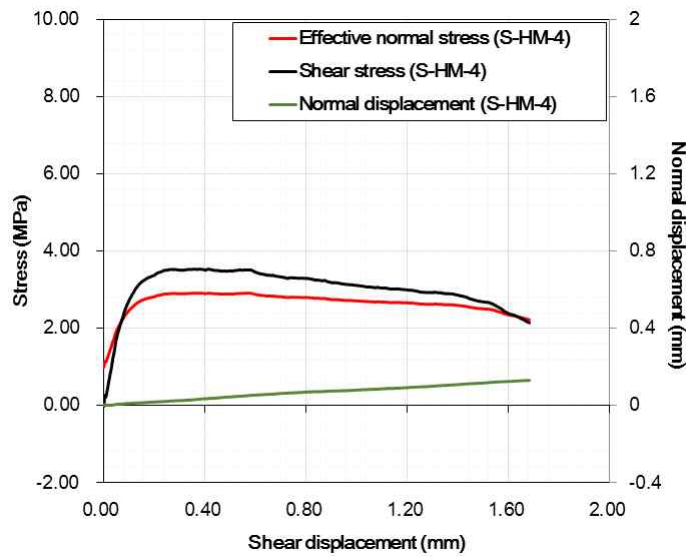


(a) S-HM-2 (20°C/dry condition/confining pressure : 3.5 MPa)

Fig. B.3 Relation between effective normal stress, shear stress, normal displacement and shear displacement.

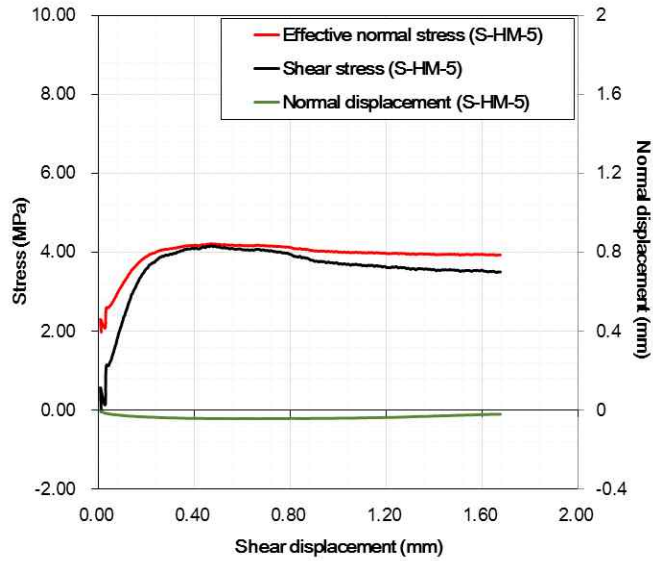


(b) S-HM-3 (20°C/dry condition/confining pressure : 4.0 MPa)

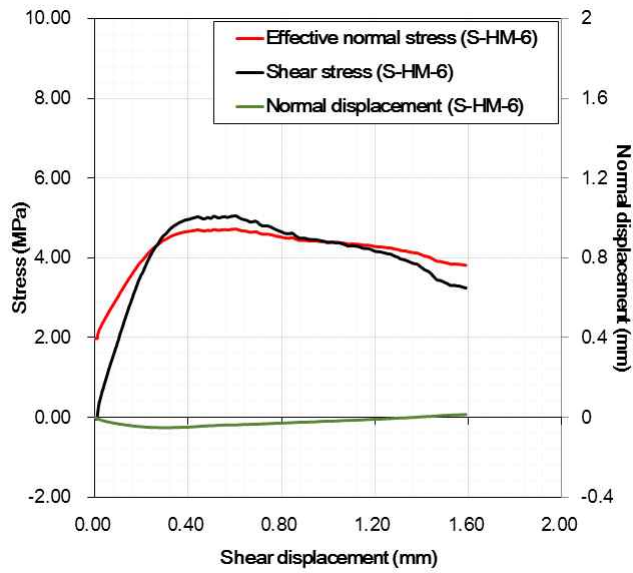


(c) S-HM-4 (20°C/dry condition/confining pressure : 4.0 MPa)

Fig. B.3 Continued.

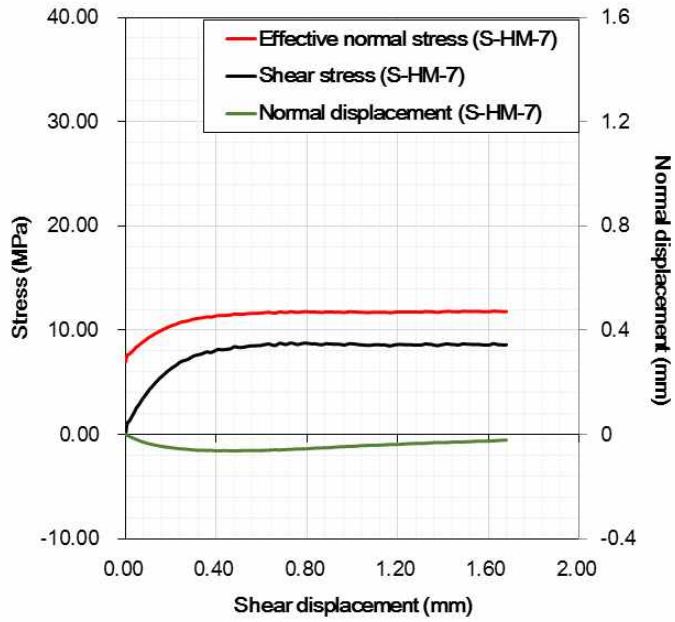


(d) S-HM-5 (20°C/dry condition/confining pressure : 5.0 MPa)

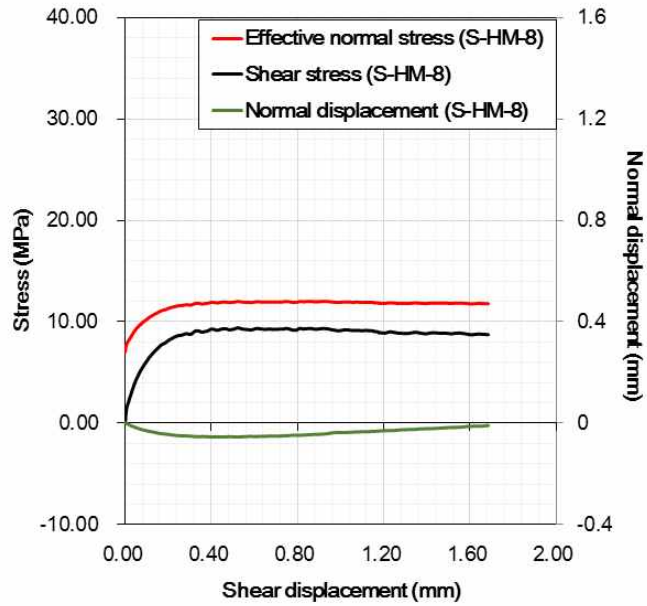


(e) S-HM-6 (20°C/dry condition/confining pressure : 5.0 MPa)

Fig. B.3 Continued.

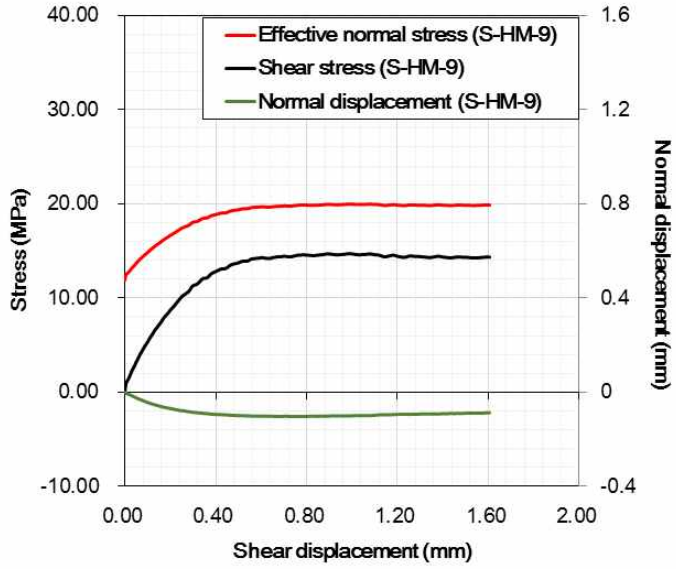


(f) S-HM-7 (20°C/dry condition/confining pressure : 10.0 MPa)

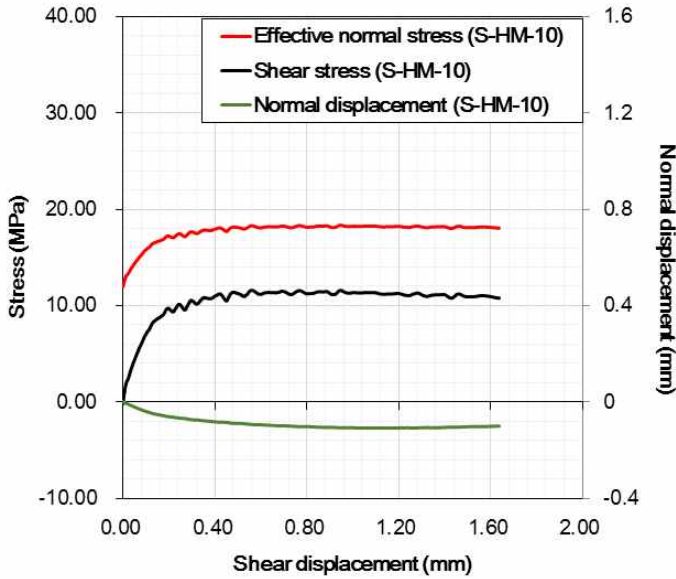


(g) S-HM-8 (20°C/dry condition/confining pressure : 10.0 MPa)

Fig. B.3 Continued.

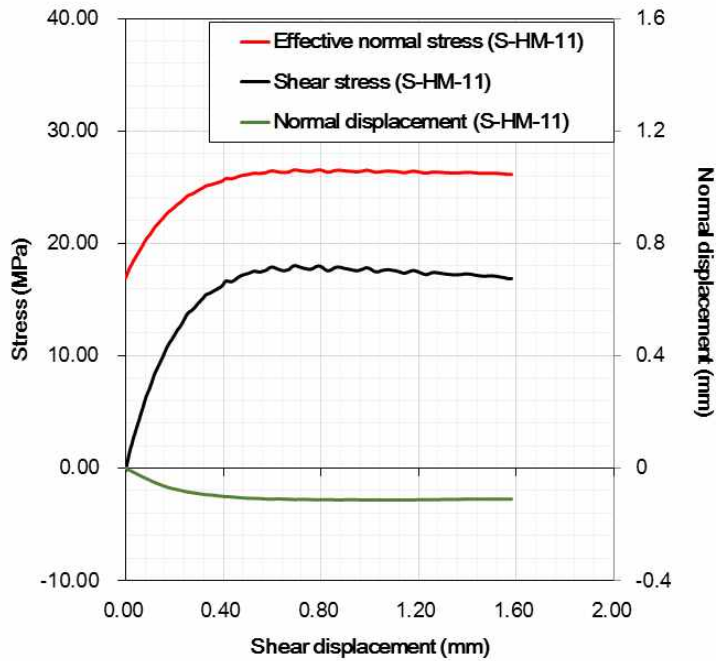


(h) S-HM-9 (20°C/dry condition/confining pressure : 15.0 MPa)

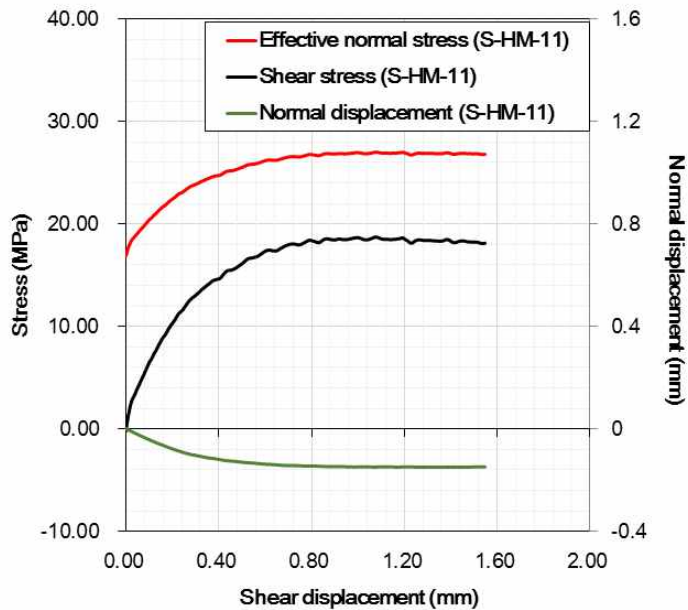


(i) S-HM-10 (20°C/dry condition/confining pressure : 15.0 MPa)

Fig. B.3 Continued.



(h) S-HM-11 (20°C/dry condition/confining pressure : 20.0 MPa)

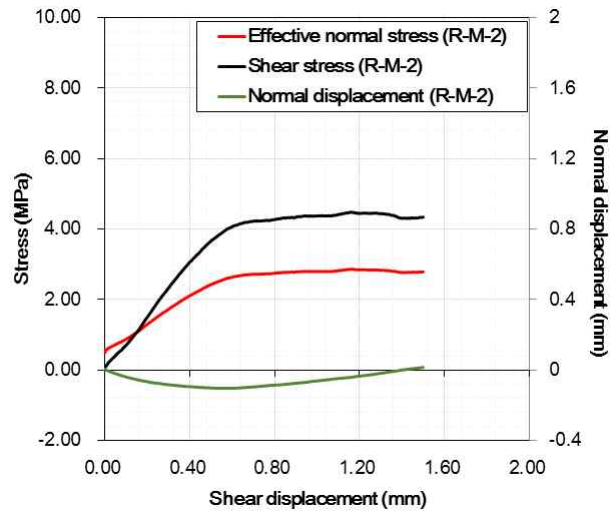


(i) S-HM-12 (20°C/dry condition/confining pressure : 20.0 MPa)

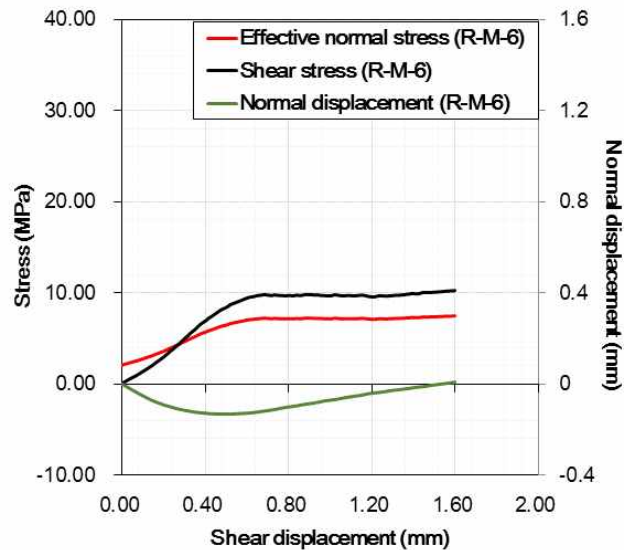
Fig. B.3 Continued.

Appendix C. Test results of cement-mortar specimens including a rough discontinuity (JRC=11.63)

C.1 At room temperature and dry conditions

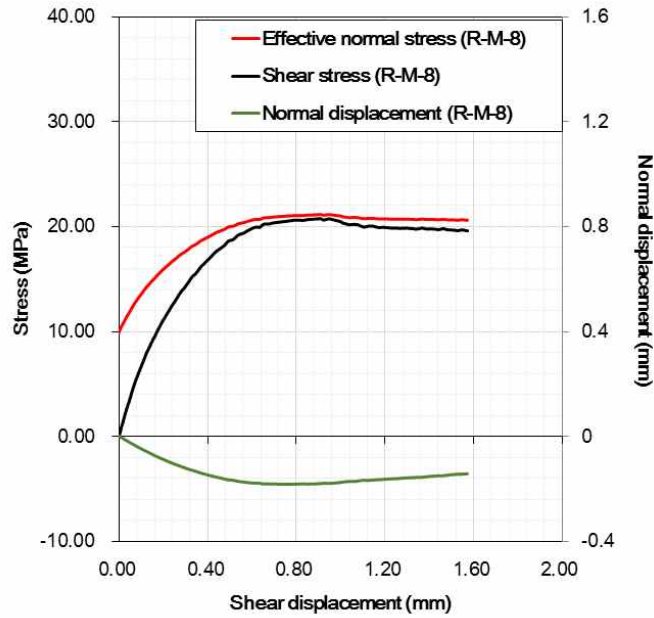


(a) R-M-2 (20°C/dry condition/confining pressure : 0.5 MPa)

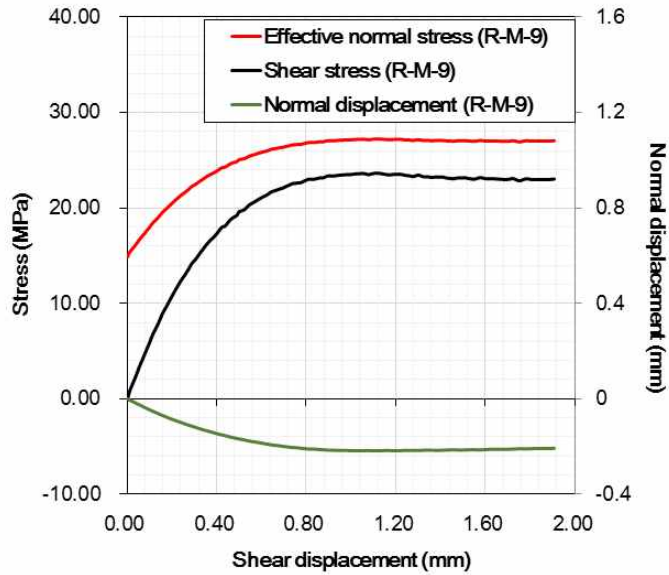


(b) R-M-6 (20°C/dry condition/confining pressure : 2.0 MPa)

Fig. C.1 Relation between effective normal stress, shear stress, normal displacement and shear displacement.



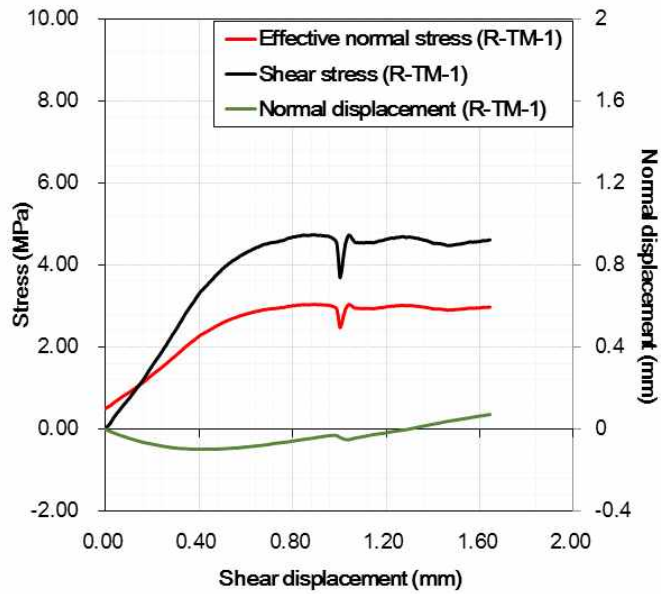
(c) R-M-8 (20°C/dry condition/confining pressure : 10.0 MPa)



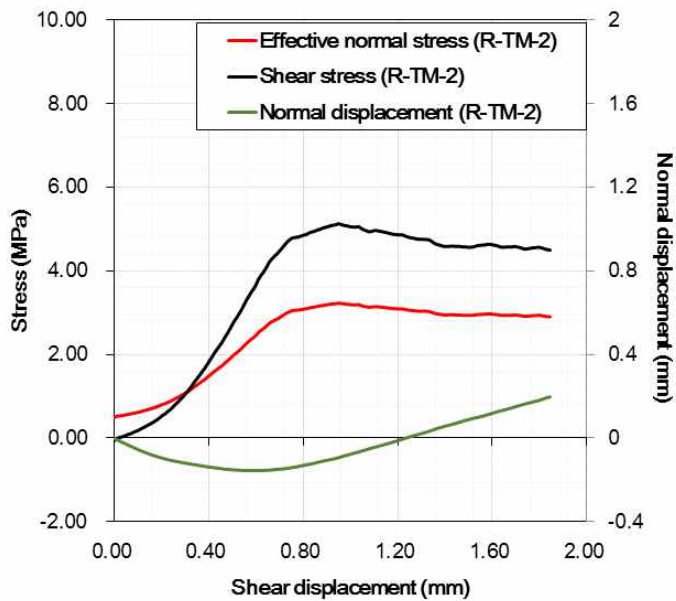
(d) R-M-9 (20°C/dry condition/confining pressure : 15.0 MPa)

Fig. C.1 Continued.

C.2 At 80°C and dry conditions

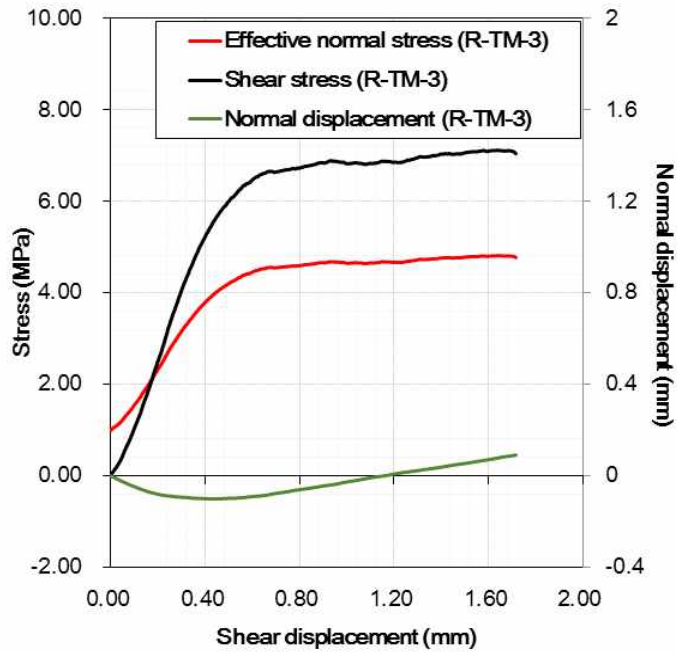


(a) R-TM-1 (80°C/dry condition/confining pressure : 0.5 MPa)

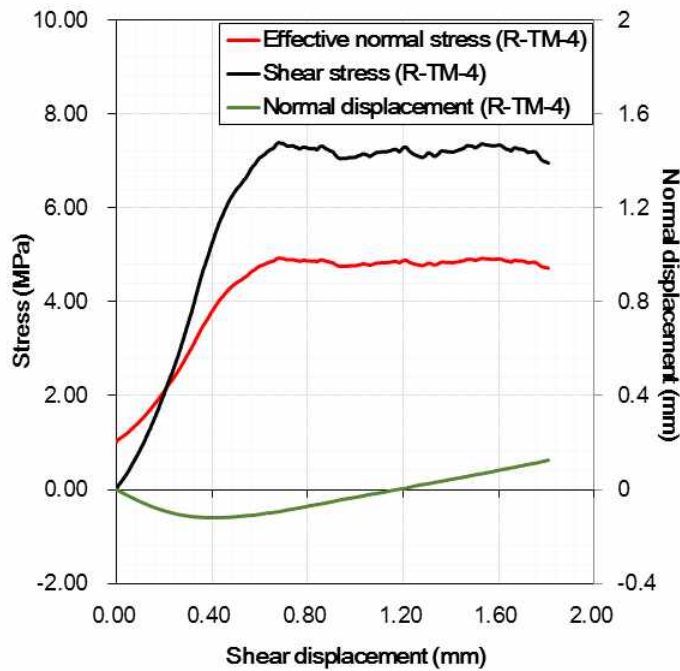


(b) R-TM-2 (80°C/dry condition/confining pressure : 0.5 MPa)

Fig. C.2 Relation between effective normal stress, shear stress, normal displacement and shear displacement.

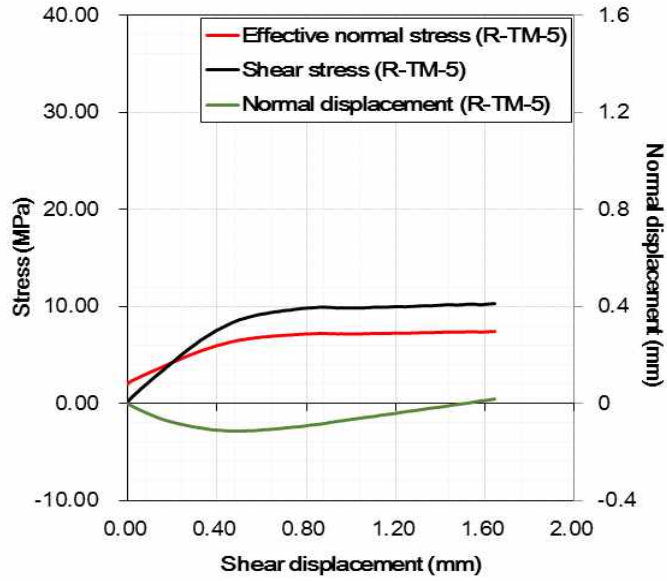


(c) R-TM-3 (80°C/dry condition/confining pressure : 1.0 MPa)

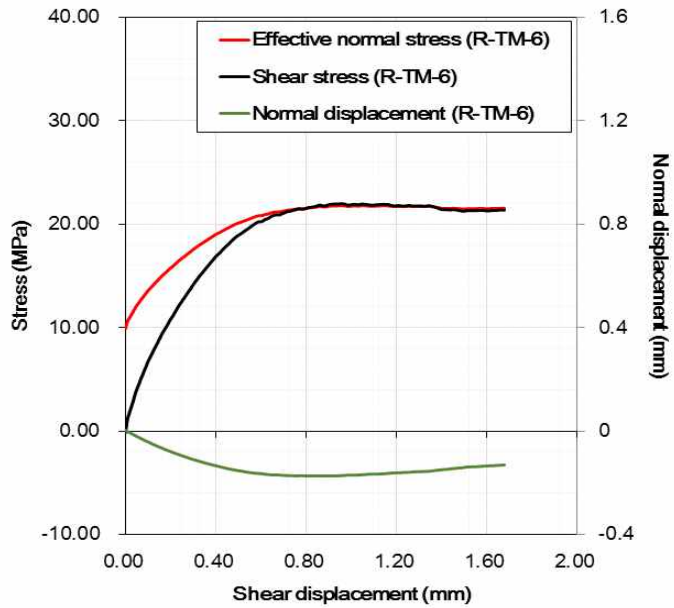


(d) R-TM-4 (80°C/dry condition/confining pressure : 1.0 MPa)

Fig. C.2 Continued.

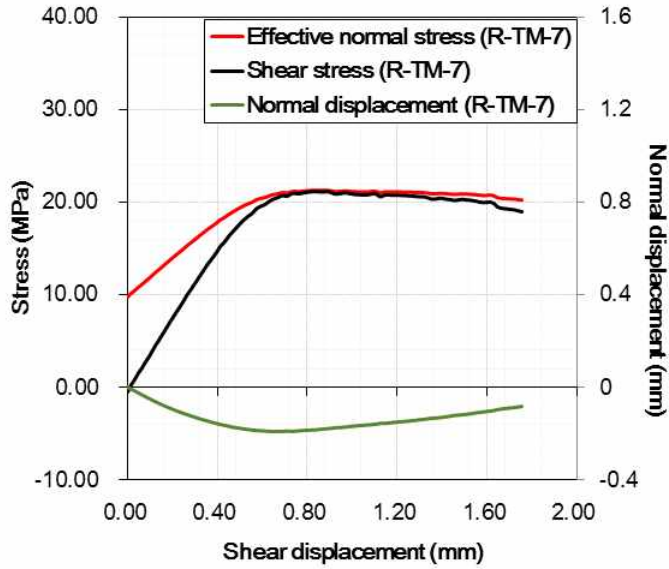


(e) R-TM-5 (80°C/dry condition/confining pressure : 2.0 MPa)

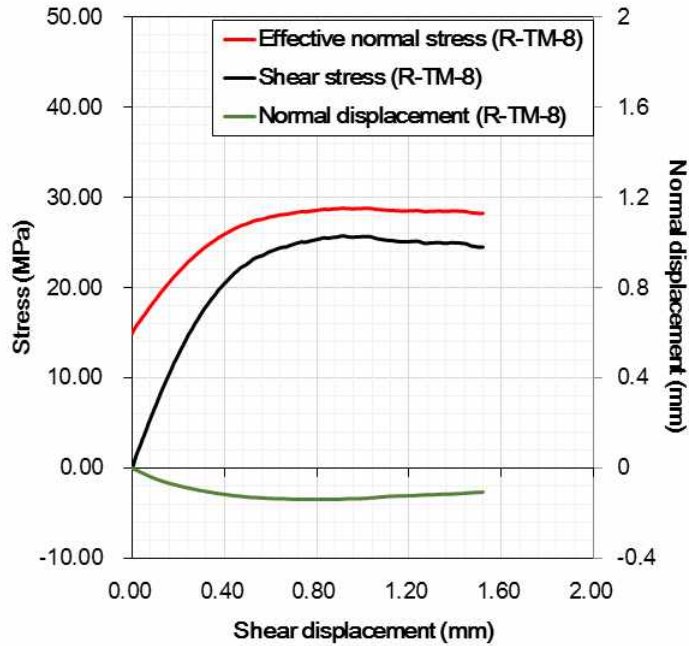


(f) R-TM-6 (80°C/dry condition/confining pressure : 10.0 MPa)

Fig. C.2 Continued.

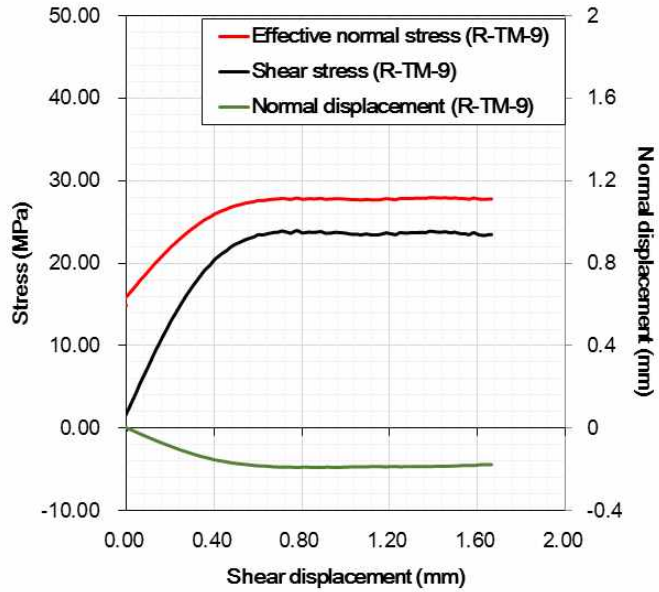


(g) R-TM-7 (80°C/dry condition/confining pressure : 10.0 MPa)

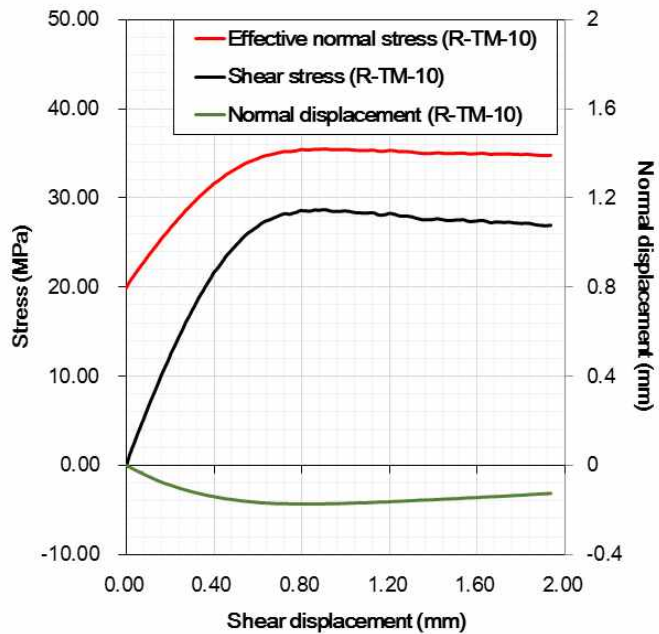


(h) R-TM-8 (80°C/dry condition/confining pressure : 15.0 MPa)

Fig. C.2 Continued.

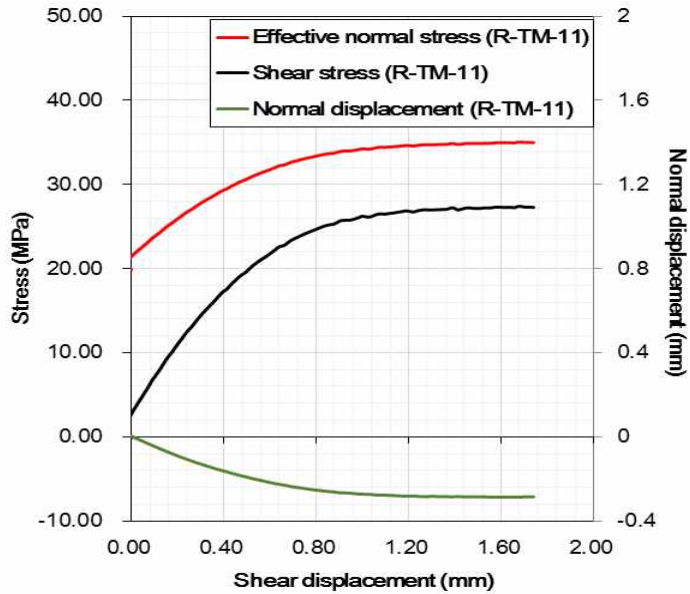


(i) R-TM-9 (80°C/dry condition/confining pressure : 15.0 MPa)



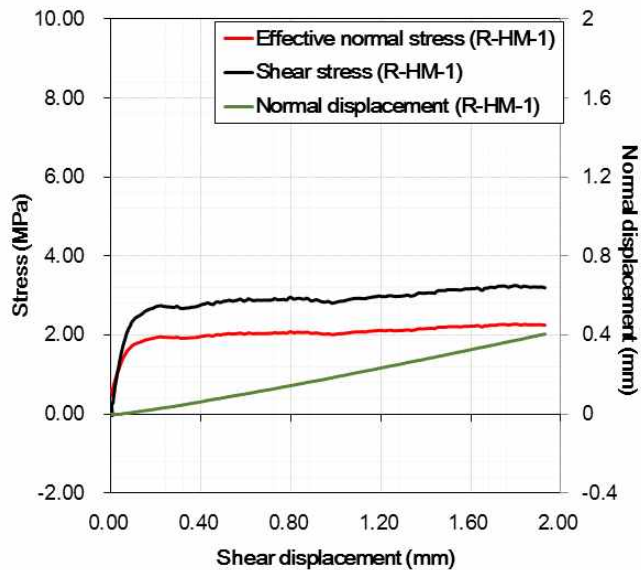
(j) R-TM-10 (80°C/dry condition/confining pressure : 20.0 MPa)

Fig. C.2 Continued.

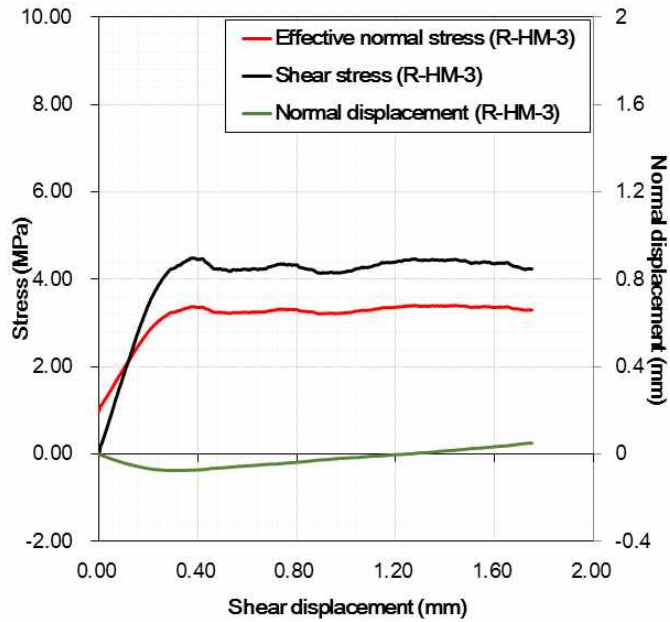


(k) R-TM-9 (80°C/dry condition/confining pressure : 20.0 MPa)
Fig. C.2 Continued.

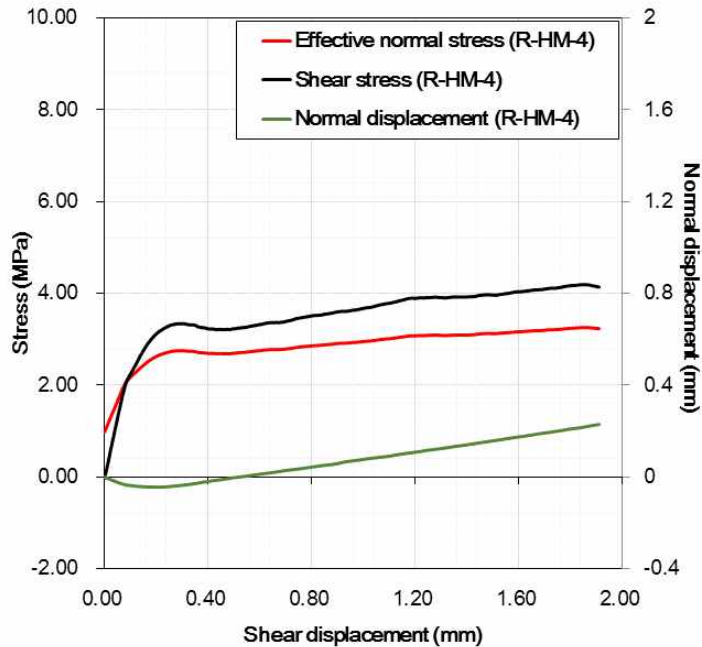
C.3 At 20°C and water pressure (3.0 MPa) applied conditions



(a) R-HM-1 (20°C/dry condition/confining pressure : 3.5 MPa)
Fig. C.3 Relation between effective normal stress, shear stress, normal displacement and shear displacement.

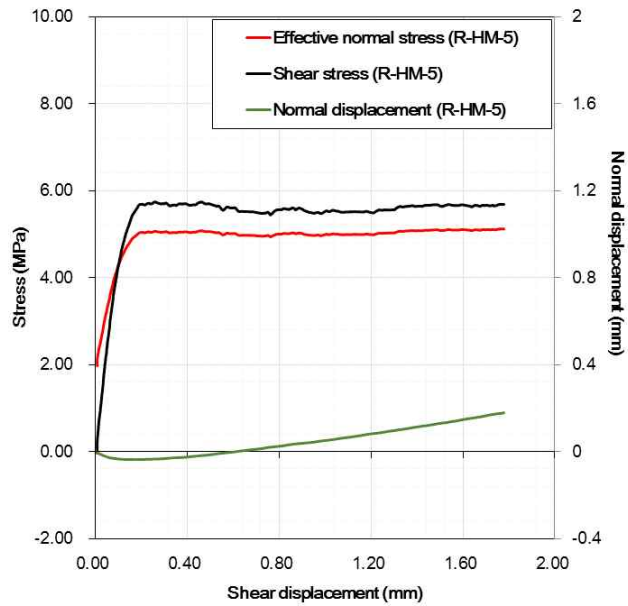


(b) R-HM-3 (20°C/dry condition/confining pressure : 4.0 MPa)

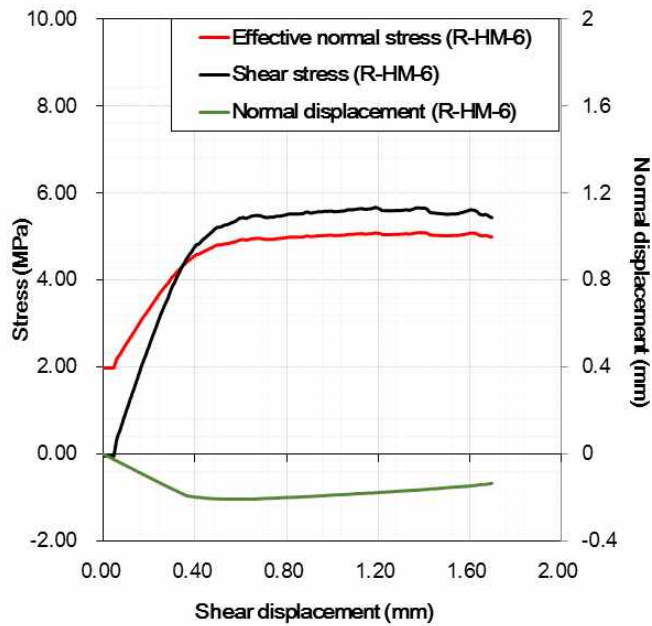


(c) R-HM-4 (20°C/dry condition/confining pressure : 4.0 MPa)

Fig. C.3 Continued.

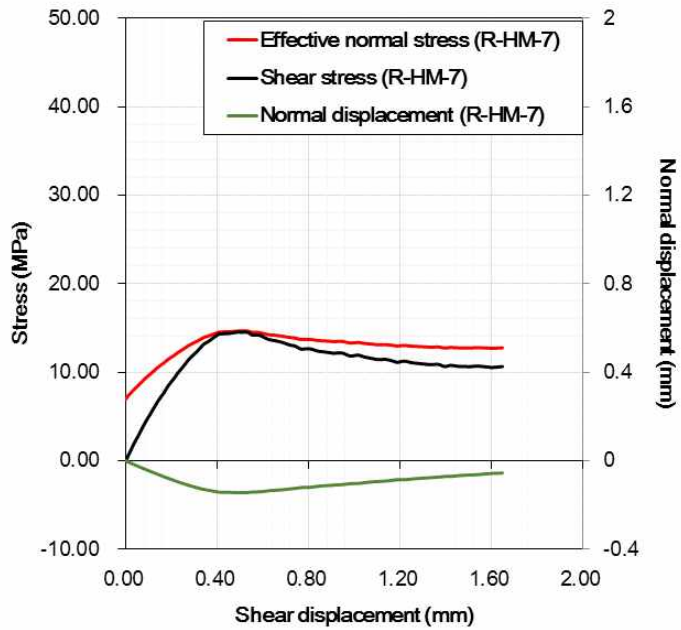


(d) R-HM-5 (20°C/dry condition/confining pressure : 5.0 MPa)

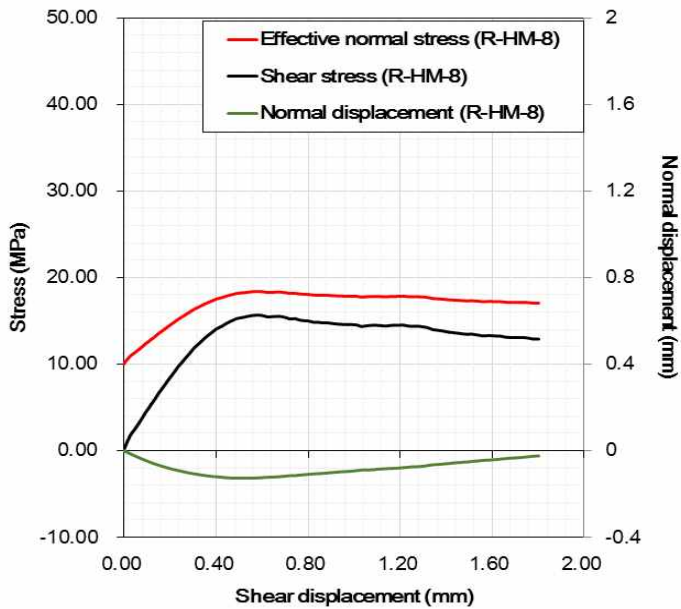


(e) R-HM-6 (20°C/dry condition/confining pressure : 5.0 MPa)

Fig. C.3 Continued.

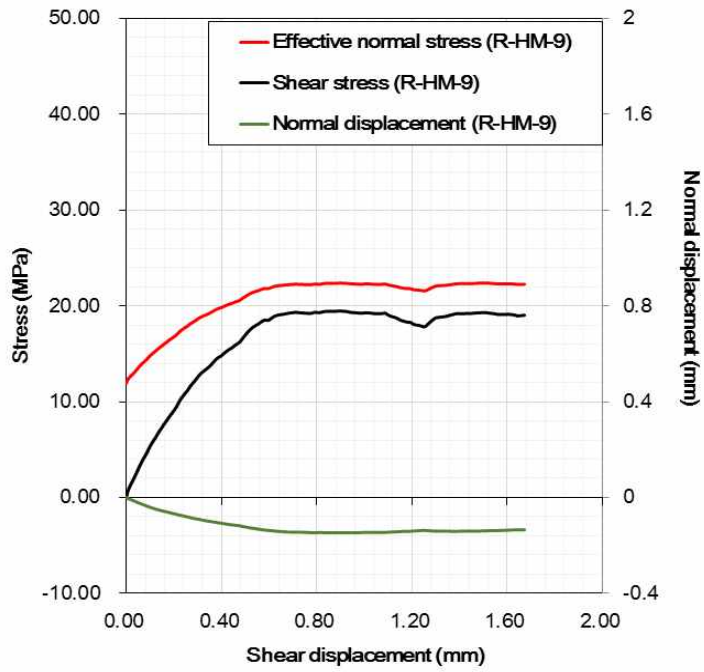


(f) R-HM-7 (20°C/dry condition/confining pressure : 10.0 MPa)

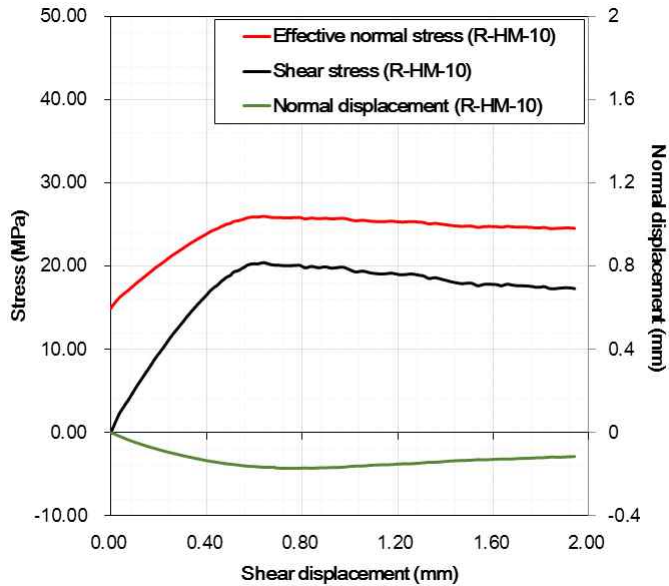


(g) R-HM-8 (20°C/dry condition/confining pressure : 10.0 MPa)

Fig. C.3 Continued.

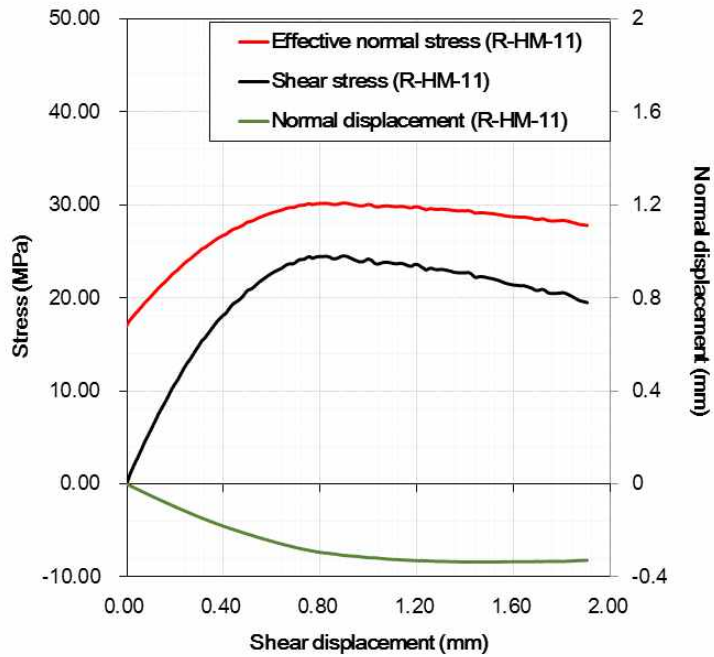


(h) R-HM-9 (20°C/dry condition/confining pressure : 15.0 MPa)

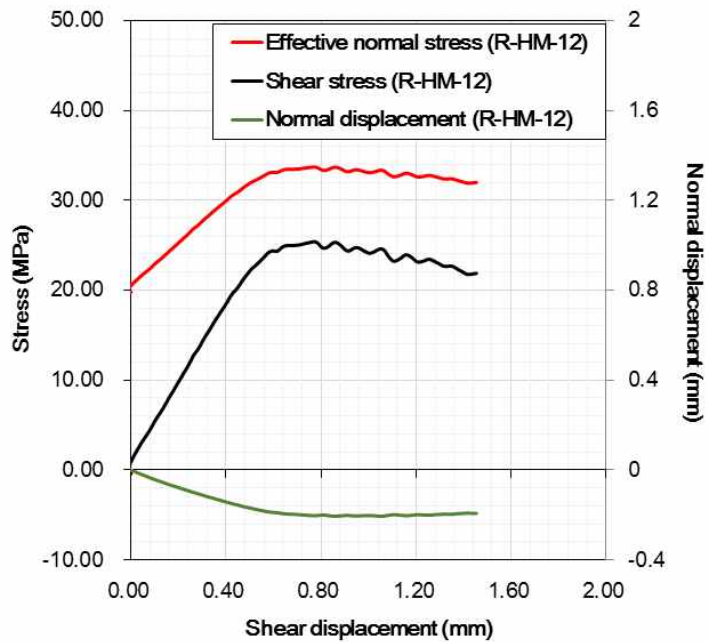


(i) R-HM-10 (20°C/dry condition/confining pressure : 15.0 MPa)

Fig. C.3 Continued.



(j) R-HM-11 (20°C/dry condition/confining pressure : 20.0 MPa)



(k) R-HM-12 (20°C/dry condition/confining pressure : 20.0 MPa)

Fig. C.3 Continued.

초 록

암반 내 불연속면은 연약면으로 작용하며, 따라서 지하 구조물의 안정성을 평가하는데 있어 불연속면의 거동을 이해하는 것은 필수적이다. 심부에서 불연속면의 전단 거동은 심도에 따른 상재하중, 지체응력, 지하수에 의한 수압 및 고온 조건의 상호 작용에 지표 부근 보다 더 큰 영향을 받게 된다. 이러한 상호 작용이 전단 거동에 미치는 영향을 파악하기 위해 많은 연구가 진행되었으나 그 결과들은 암종, 불연속면의 거칠기, 수직 응력, 온도 및 수압 조건에 따라 다양하게 나타났다. 또한, 대부분의 연구는 지각의 거동에 대해 이루어 졌기 때문에 수직응력, 온도 및 수압과 같은 시험 조건들이 극단적으로 높은 값에서 시험들이 수행되어 왔다. 따라서 공학적 조건에 적합한 상태에서 다양한 암종에 대한 마찰 특성의 변화를 평가하는 것이 필요하다.

다양한 열, 수리, 역학적 조건 하에서 전단 시험을 수행하였다. 톱으로 절단한 (saw-cut) 단일 불연속면을 포함하고 있는 세 가지 암종, 즉, 화강암, 섬록암, 린이 사암이 시료로 사용되었다. 시험 조건들은 방사성 폐기물 처분 시설, 지열 발전 및 석유 저류층과 같은 지하 구조물 인근의 현장 조건을 고려하여 결정하였다. 마찰각은 지질공학 분야에서 가장 널리 사용되어 온 기준 중 하나인 Mohr-Coulomb 파괴 기준을 사용하여 분석하였다.

Saw-cut 표면에 수압을 가했을 때 세 가지 암종 모두에서 마찰각이 감소하였으며, 마찰각의 감소에는 각기 다른 원인들이 작용하였다. XRD 분석과 SEM 관측 결과, 대전 화강암과 고흥 섬록암에서는 층상 구조 광물들을 발견하였다. 층상 구조 광물들은 물을 보다 쉽게 흡착하며 흡착된 물이 윤활제로 작용하기 때문에 마찰각이 감소할 수 있다. 린이 사암의 경우 XRD 분석 시 층상 구조 광물들은 거의 관찰되지 않았으나,

SEM 분석 시 수압을 가한 상태에서 실험을 진행한 후에 상당한 양의 분쇄된 고운 입자들이 발생하였음을 관찰하였다. 따라서 표면에서 분리된 고운 입자 가루들이 saw-cut 표면의 전단 강도를 감소시켰다고 판단할 수 있다. 반면, 온도를 80°C로 상승시켰을 경우 온도에 의한 전단 거동의 변화는 크지 않은 것으로 나타났다.

Saw-cut 시료들에 대한 시험 외에도 거칠기가 전단 거동에 미치는 영향을 파악하기 위한 시험이 수행되었다. 동일한 거칠기를 지닌 불연속면을 생성하기 위해 시멘트 모르타르가 사용되었으며, 두 가지 거칠기를 지닌 불연속면을 준비하였다 (JRC = 2.05, 11.63). 응력 수준에 따른 거칠기의 파괴를 고려하여 마찰각은 낮은 응력 수준과 높은 응력 수준으로 나누어 분석하였으며 Patton의 파괴 기준을 적용하였다. 수압을 가했을 때, 10 MPa 보다 낮은 수직응력 하에서 거친 불연속면의 마찰각이 더 크게 감소하는 것으로 나타났다. 이는 습윤 상태에서 인장강도가 저하되었기 때문인 것으로 판단된다. 따라서 습윤 상태에서 마찰각과 전단 강도의 저하는 거칠기가 커질 경우 더욱 크게 나타날 것으로 판단할 수 있다. 반면에 10 MPa 보다 높은 수직응력 하에서는 높은 수직응력으로 인해 거칠기가 이미 파괴되었기 때문에 마찰각은 거칠기와 관계없이 거의 유사한 값을 나타냈다. 온도를 80°C 로 상승시켰을 경우, saw-cut 시료와 마찬가지로 전단 특성의 변화는 크게 관찰되지 않았다.

시멘트 모르타르 시료의 전단 거동을 재현하기 위해 2차원 입자 결합 모델(particle flow code)를 활용하여 수치해석을 수행하였다. 수치해석 모델에 단일 불연속면을 생성하기 위해 smooth joint model을 적용하였다. 상온 건조 조건 및 80°C 건조 조건에서의 수치해석 결과는 실험결과와 잘 일치하는 것으로 나타났다. 그러나 HM 해석 시에는 마찰각 및 팽창각의 경우 실험 결과와 다소 차이를 보이는 것으로 나타났으며 향후 연구를 통해 해결해야 할 것으로 판단된다.

이 연구에서는 압중 변화 및 거칠기 변화에 따른 전단 거동 특성의 변화를 실내 시험 및 수치해석을 통해 연구하였다. 불연속면 표면에 물이 존재할 경우 압중 및 수직 응력의 크기에 따라 전단 강도가 저하되는 것으로 나타났으나 80°C로 온도를 증가시킬 경우 온도의 영향은 크지 않은 것으로 나타났다. 이 연구는 다양한 열, 수리, 역학적 조건 하에서 전단 거동 특성의 변화 및 그에 대한 원인을 이해하는데 기여할 수 있을 것으로 판단된다. 또한 이 연구를 통해 얻은 결과들은 향후 T-H-M 상호작용을 고려해야만 하는 지하 암반 구조물의 안정성 평가 및 설계에 활용될 수 있다.

주요어: 마찰각, 전단 시험, T-H-M 상호 작용, 삼축압축챔버, 개별요소법, 입자결합모델, smooth joint 모델.

학번 : 2007-21247